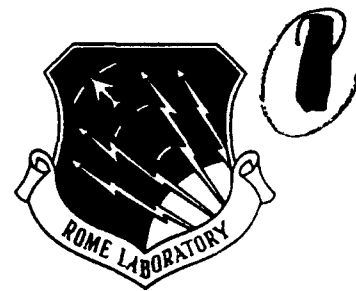


AD-A253 681



RL-IR-92-42, vol 1 (of two)
In-House Report
February 1992



PROCEEDINGS OF THE 1991 ANTENNA APPLICATIONS SYMPOSIUM

Paul Mayes, et al



APPROVED FOR PUBLIC RELEASE; DISTRIBUTION UNLIMITED.

Rome Laboratory
Air Force Systems Command
Griffiss Air Force Base, NY 13441-5700

92-13751



9 2 5 22 075

This report has been reviewed by the Rome Laboratory Public Affairs Office (PA) and is releasable to the National Technical Information Service (NTIS). At NTIS it will be releasable to the general public, including foreign nations.

RL-TR-92-42, Vol I (of two) has been reviewed and is approved for publication.

APPROVED:



DANIEL J. JACAVANCO, Acting Chief
Antenna and Components Division

APPROVED:



JOHN K. SCHINDLER, Director
Electromagnetics and Reliability Directorate

If your address has changed or if you wish to be removed from the Rome Laboratory mailing list, or if the addressee is no longer employed by your organization, please notify RL(ERAS) Hanscom AFB MA 01731-5000. This will assist us in maintaining a current mailing list.

Do not return copies of this report unless contractual obligations or notices on a specific document require that it be returned.

REPORT DOCUMENTATION PAGE			Form Approved OMB No. 0704-0188		
<small>Public reporting burden for this collection of information is estimated to average 1 hour per response, including the time for reviewing instructions, gathering and maintaining the data needed, and completing and reviewing the collection of information. Send comments regarding this burden estimate or any other aspect of this collection of information, including suggestions for reducing this burden, to Washington Headquarters Services, Directorate for Information Operations and Reports, 1215 Jefferson Davis Highway, Suite 1204, Arlington, VA 22202-4302, and to the Office of Management and Budget, Paperwork Reduction Project (0704-0188), Washington, DC 20503.</small>					
1. AGENCY USE ONLY (Leave blank)	2. REPORT DATE February 1992	3. REPORT TYPE AND DATES COVERED Final Report			
4. TITLE AND SUBTITLE Proceedings of the 1991 Antenna Applications Symposium			5. FUNDING NUMBERS PE 62702F PR 4600 TA 14 WU PF		
6. AUTHOR(S) Paul Mayes et al			Contract F30602-88-D-0028		
7. PERFORMING ORGANIZATION NAME(S) AND ADDRESS(ES) University of Illinois Champaign-Urbana, Illinois 61801			8. PERFORMING ORGANIZATION REPORT NUMBER		
9. SPONSORING/MONITORING AGENCY NAME(S) AND ADDRESS(ES) Rome Laboratory/ERAS Hanscom AFB, MA 01731-5000 Contract Manager: John Antonucci			10. SPONSORING/MONITORING AGENCY REPORT NUMBER RL-TR-92-42 (Volume I)		
11. SUPPLEMENTARY NOTES Volume I consists of pages 1 - 252; Volume II consists of pages 253 - 473					
12a. DISTRIBUTION/AVAILABILITY STATEMENT Approved for public release; distribution unlimited			12b. DISTRIBUTION CODE		
13. ABSTRACT (Maximum 200 words) The Proceedings of the 1991 Antenna Applications Symposium is a collection of state-of-the-art papers relating to phased array antennas, multibeam antennas, satellite antennas, microstrip antennas, reflector antennas, HF, VHF, UHF and various other antennas.					
14. SUBJECT TERMS Antennas Satellite antennas Broadband antennas		Microstrip Reflector HF VHF	UHF Multibeam antennas Array antennas	15. NUMBER OF PAGES 258	16. PRICE CODE
17. SECURITY CLASSIFICATION OF REPORT Unclassified	18. SECURITY CLASSIFICATION OF THIS PAGE Unclassified	19. SECURITY CLASSIFICATION OF ABSTRACT Unclassified	20. LIMITATION OF ABSTRACT SAR		

CONTENTS

WEDNESDAY, SEPTEMBER 25, 1991

PHASED ARRAY SIGNAL PROCESSING

- 1. * Keynote: "Beyond AWACS," by Gary Grann
- 2. "Advanced Architecture for a Monopulse Active Aperture Array - Part II," by W.J. Turcovski, P.D. Hrycak, J.B. Yon, M.J. Raginsky and P.J. Knowles 1
- 3. "Scan Correction Technique for Cylindrical Arrays," by J. B. Yon 17
- 4. "High Resolution Auroral Clutter Mapping Using the Verona Ava Linear Array Radar," by D.S. Choi, B. Weijers, R.J. Norris and N.B. Myers 30
- 5. * "Conformal Active Phased Array Demonstration Using Digital Attenuators," by J.D. Hanfling and O.J. Bedigian
- 6. "Adaptive Nulling and Spatial Spectral Estimation Using an Iterated Principal Components Decomposition," by D.O. Carhoun 44

ARRAYS

- 7. "Focal Arc Pattern Measurements," by P.R. Franchi and H. Tobin 54
- 8. "Engineering Analyses Associated With the Development of an Airborne Phased Array Radar Antenna," by C. H. Tang 65

* NOT INCLUDED IN THIS VOLUME

By _____	
Distribution/	
Availability Codes	
Dist	Avail and/or Special
A-1	

Contents

- | | | |
|-----|--|-----|
| 9. | "An Efficient, Low Cost Method of Modifying the E-3A Antenna Elevation Beam Offset Angle," by D.P. Parrish, P.S. Hacker, R.K. Vogelsang, J.R. Stepanek and K.G. Ramsey | 81 |
| 10. | "Circular Phased Array Development for Electronic Scanning of an Endfire Beam," by G.G. Sanford and P. Westfeldt, Jr | 97 |
| 11. | "Slot-Coupled Patch Arrays," by C.H. Chen, P.G. Ingerson and W.C. Wong | 118 |
| 12. | "Array Mutual Resistance Calculation From Far-Field Radiation Patterns," by D.D. de Schweinitz | 132 |
| 13. | "Nested Complementary Pair Arrays for Vehicular Applications," by K.G. Schroeder | 155 |

THURSDAY, SEPTEMBER 26, 1991

REFLECTORS AND LENSES

- | | | |
|-----|--|-----|
| 14. | "Transient Effects in Reflector Antennas," by R.C. Hansen | 169 |
| 15. | "Beamspace Low Sidelobe Pattern Synthesis," by D.J. Lawrence, W.T. Carey and J.A. Smolko | 188 |
| 16. | * "Design and Analysis of a Dual Reflector Multi-beam Torus Antenna," by S. Carrillo | |
| 17. | * "A High Efficiency Antenna for CONUS Coverage From Surveillance Spacecrafts," by C.W. Thousand and A.W. Love | |
| 18. | "Validation of Integral Equation Model With High-Dielectric Microstrip Rotman Lens Measurements," by A.F. Peterson and E.O. Rausch | 208 |
| 19. | "Advances in Lens-Fed Multibeam Technology," by G.J. Monser | 230 |
| 20. | * "The Horn Antenna With Large Beam Aspect Ratio," by C. Ming | |

* NOT INCLUDED IN THIS VOLUME

Contents

MICROWAVE AND MM WAVE

- | | | |
|-----|--|-----|
| 21. | "The Continuous Transverse Stub (CTS) Array:
Basic Theory, Experiment and Application,"
by W.W. Milroy | 253 |
| 22. | "A Center-Fed Planar Antenna Using a Surface/Leaky
Wave," by S. Carrillo and J. Ladds | 284 |
| 23. | "Offset Cassegrain With Triple Polarization
Gaussian Optics Lens Antenna Feed System for
High Power Ka-Band Weather Radar," by
E.L. Moore | 300 |
| 24. | "Performance of the TDRSS Space Deployable
Antenna," by M.J. Lynch | 313 |
| 25. | "TOPEX Spacecraft Dual-Frequency Radar
Altimeter Antenna," by A.R. Jablon | 334 |
| 26. | "Short Backfire Antenna Modeling With Dipole
or Waveguide Excitation," by G.P. Otto,
C. Lu and W.C. Chew | 349 |
| 27. | "Antenna and Radome Technology on Multiple
Landing System (MLS) in the Soviet Union,"
by H. Shnitkin | 363 |

FRIDAY, SEPTEMBER 27, 1991

BROADBAND AND OTHERS

- | | | |
|-----|--|-----|
| 28. | "Flush Mounted Four-Arm Spiral With Shallow
Backup Cavity," by J. Kobus and D. Munger | 374 |
| 29. | "Spiral Antennas Over Closely Spaced Ground,"
by D.W. Smith and P.E. Mayes | 404 |
| 30. | "Comparisons of Sinuous and Modulated Armwidth
Spiral Antennas for Wideband Dual-Polarized
Multi-Arm Applications," by P.G. Ingerson,
P.M. Ingerson and D.C. Senior | 434 |
| 31. | "Land Mobile Radio Propagation to Satellites,"
by A. Davidson | 455 |

* NOT INCLUDED IN THIS VOLUME

ADVANCED ARCHITECTURE FOR A MONOPULSE
ACTIVE APERTURE ARRAY - PART II [1]

William J. Turcovski
Peter D. Hrycak
James B. Yon
Mark J. Raginsky
P. J. Knowles

Westinghouse Electric Corporation
Electronic Systems Group
Design and Producibility Engineering Division
Baltimore, Maryland 21203

ABSTRACT

This paper is a follow-up to the one presented at the 1988 Antenna Applications Symposium where an Advanced Architecture for a monopulse active aperture array was presented. This architecture exploits the potential inherent in next generation T/R modules to reduce the number of elevation beamformers from three to two. The remaining two beamformers are relatively simple networks consisting of -3.01 dB Wilkinson Power Dividers, anti-symmetric in phase. This allows for simultaneous correction of the sum and difference beams with a single set of phase and amplitude controls found in the T/R modules. This paper describes the development of the conformal experimental hardware as it relates to a fuselage mount configuration. The architecture also compensates for conformal plane scan distortion by means of a single phase shifter located at the receive beamformer outputs.

1. Introduction

The objective of the Advanced Architectures for Airborne Arrays (A⁴) Program is to investigate array architectures for the next generation of airborne surveillance radars which will have the radiators, modules, beamformers, etc. integrated into the platform fuselage. This architecture exploits the potential inherent in the next generation T/R modules to simplify overall beamformer design and manufacture. The Phase I study focussed on the following subjects.

1. Elevation Monopulse Beamformer Architectures
 - a) Minimizing the number of networks.
 - b) Error correction to relax network precision.
2. Radiating Elements with Minimum Thickness
 - a) With bandwidth.
 - b) Minimizing VSWR with scan.
3. Achieving the Circulator Function
 - a) With better circulators.
 - b) With tuning.
 - c) With better amplifiers.

One of the major results of the Phase I study was the new architecture. The conventional approach employs 3 beamforming networks in the elevation plane: a uniform amplitude beamforming network used for transmit, a receive sum beamforming network, and a receive difference beamforming network as shown in Figure 1. On receive, one can correct errors within one beamforming network, via the phase and amplitude controls in the T/R modules, but the correction will induce errors into the other receive beamforming network. Therefore simultaneous correction

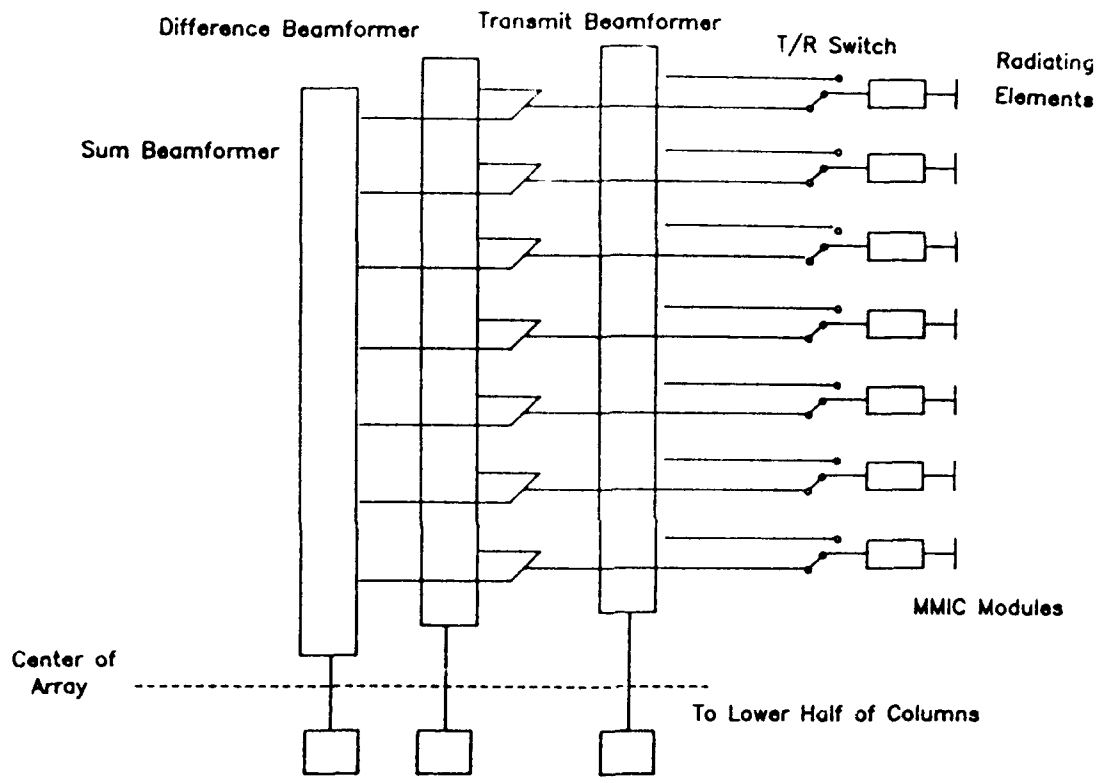


Figure 1. Conventional architecture

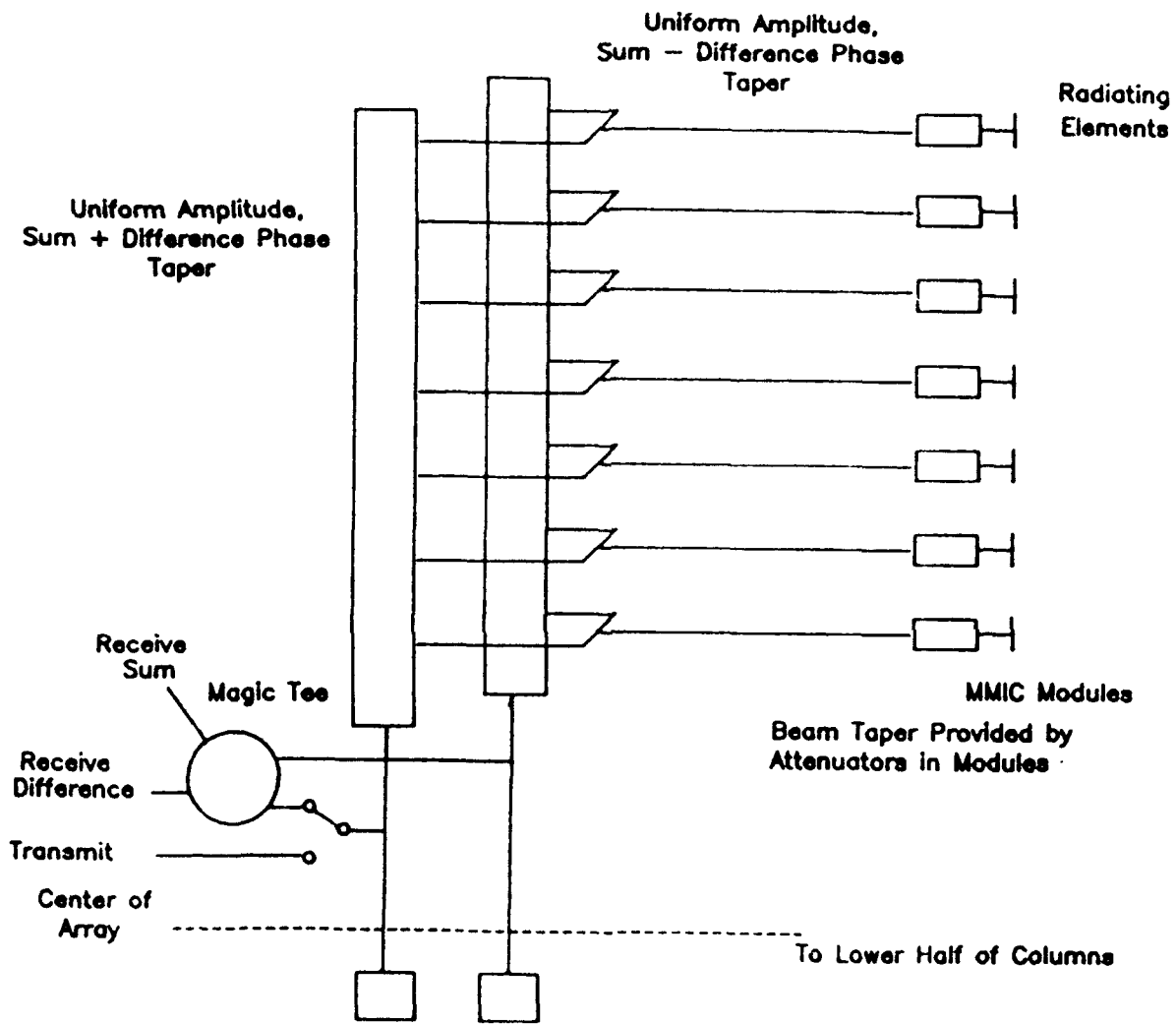


Figure 2. Advanced architecture

of both beams is impractical. The new architecture, shown in Figure 2, reduces the number of manifolds from 3 to 2 where a single beamforming network provides receive and transmit capability. This architecture also has the potential of compensating for errors in the receive sum and difference patterns simultaneously. The objective of Phase II is to demonstrate the key features of the Phase I architecture. This entails building a conformal beamformer which would feed a larger array (4x64).

2.0 Architectural Design

The advanced architecture consists of a magic tee (or hybrid ring), a transmit switch, two manifolds, and T/R modules. During receive, the hybrid ring separates the sum and differences signals from the $\Sigma + j\Delta$ manifold and $\Sigma - j\Delta$ manifold. The manifolds each consist of a 1:64 corporate network constructed of -3.01 dB couplers with a special phase taper applied at the output of each corporate feed. The special phase taper is anti-symmetric and is flipped on one manifold. Combining like ports, via the 2:1 combiners, produces partial amplitude tapering for the sum and difference distributions. The partial tapers are then further modified by a common amplitude taper, via trimmers, to establish the complete sum and difference tapers.

During transmit, the T/R modules operate in saturation. Therefore, a transmit feed that supplies equal signal level to each T/R module should be used. This is readily available by directly feeding the transmit signal into one of the manifolds as shown in Figure 2. The manifold supplies a uniform taper to the modules with a phase taper that could be compensated for by the T/R module phase shifters. Hence, the architecture that resulted from the Phase I study significantly simplifies the array architecture.

2.1 Manufactured Test Bed Array

The Phase II program involves the design and manufacture of ultra-low sidelobe monopulse receive sum and difference conformal array as shown in Figure 3. The advanced architecture test bed array was built to demonstrate the characteristics of the beamforming network (BFN) and patch radiators. The test bed array consists of four major sections, the hybrid ring, the conformal BFN, the "electronic" packages and the patch radiators. The BFN includes two manifolds which are punched from continuous flat brass and aluminum sheets. Each manifold is manufactured as a continuous piece. The electronic packages are passive networks consisting of splitters, combiners, phase trimmers and amplitude trimmers. The conformal BFN feeds a 4x64 array of conformal patch radiators. Phase and amplitude trimmers are used to simulate modules.

The overall dimensions of the radiating face and conformal beamformer are 114" x 59.5" x 8.3", which is commensurate with an array integrated into the fuselage of an aircraft. Behind this, the depth of the array is much greater than a production version because the T/R modules are simulated by commercial phase and amplitude trimmers.

3.0 Electrical Performance

The cylindrical elevation sum and difference distributions were derived from Taylor and Bayliss tapers, respectively. The sum distribution was derived from a -55 dB Taylor taper using an N bar of 8 and the difference from a -55 dB Bayliss taper using an N bar of 13. The linear tapers were projected onto the cylindrical surface and amplitude values found at the discrete element positions. Phase compensation was applied to each element to correct for the conformal surface at midband.

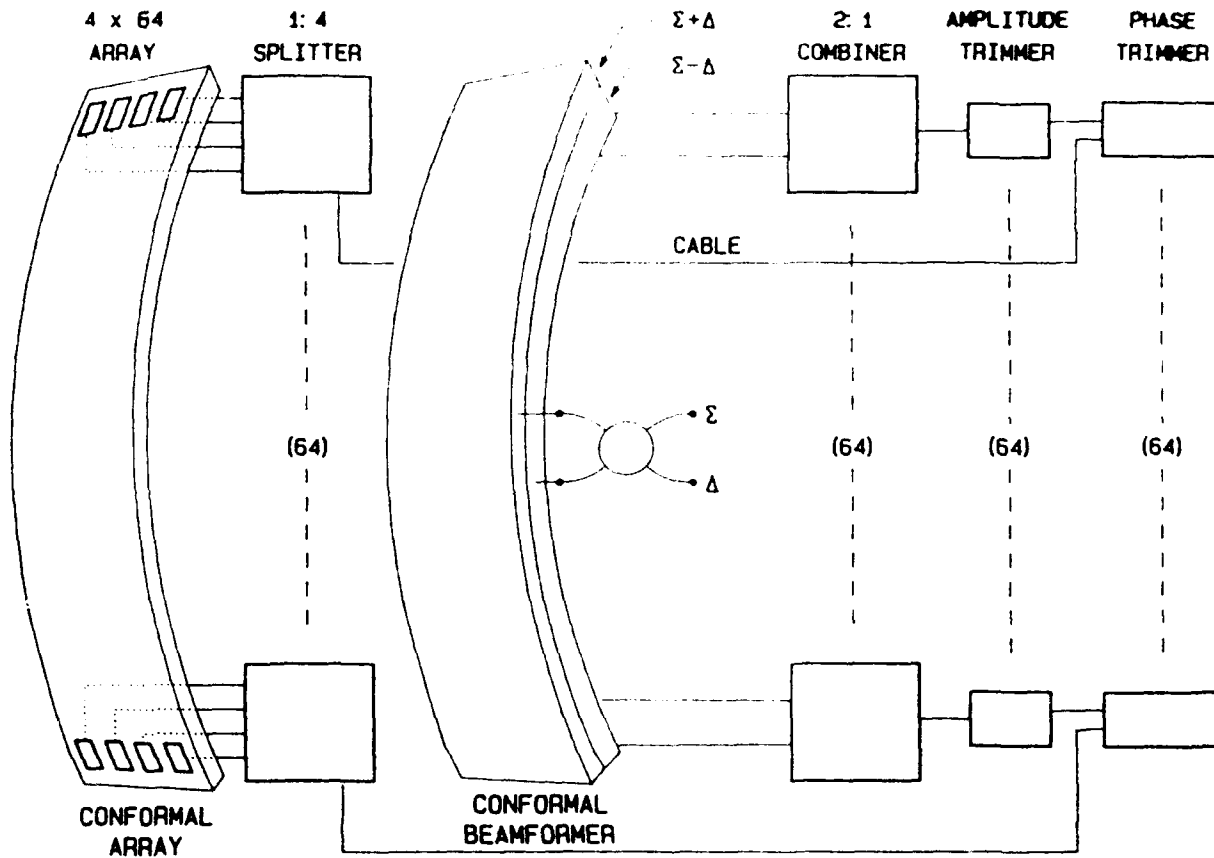


Figure 3. Architectural design

The special phase taper in each manifold and the common amplitude taper are a function of the chosen sum and difference distributions. To define how the phase taper and amplitude taper are calculated, let S_i and D_i represent the sum and difference excitations, respectively, on element i . Furthermore, both sum and difference distributions contain equal power. This is indicated by equation (1):

$$\Sigma (S_i)^2 = 1 \quad (1a)$$

$$\Sigma (D_i)^2 = 1 \quad (1b)$$

The phase and amplitude tapers are then computed by equation (2):

$$A_i \exp[j\phi_i] = S_i + jD_i \quad (2a)$$

$$A_i \exp[-j\phi_i] = S_i - jD_i \quad (2a)$$

Where ϕ_i represents the phase taper on port i of one manifold and port $65-i$ on the other manifold. Also, A_i represents the common amplitude taper on element i . The phase taper used in the test bed array is shown in Figure 4 and the amplitude taper is shown in Figure 5.

The radiating element is a patch radiator originally developed under IR&D and modified under this program for use in a conformal array. This radiator provides the column based architecture with horizontal polarization and with a scan capability of 60° in azimuth and 40° in elevation at S-band. It is unusual in that it has 15% bandwidth with only $.07\lambda$ thickness.

3.1 Conformal Plane Scanning

Scanning a cylindrical array in the conformal plane causes the sum and difference distributions to distort in the plane of the radiated plane wave. This distortion is the result of: 1) the skewing of the projected element spacing, and 2) the element pattern. The corrective technique consists of "mixing" a small portion of the sum illumination taper with the difference illumination taper, and vice versa, in such a way that the new radiated plane waves have minimal distortions for both sum and difference simultaneously [2].

Mixing the two illumination tapers is accomplished within the given architecture by a variable phase shifter between one of the manifolds and the hybrid ring. Analytically this produces new sum and difference distributions expressed by equation (3):

$$\text{new sum:} \quad \Sigma' = \sqrt{1 - B^2} * \Sigma \pm B * \Delta \quad (3a)$$

$$\text{new difference:} \quad \Delta' = \sqrt{1 - B^2} * \Delta \mp B * \Sigma \quad (3b)$$

where B is (percentage taper mix)/100 and the \pm corresponds to elevation scan direction. Furthermore, the variable phase shifter setting (θ) is analytically expressed as:

$$\theta = 2 * \sin^{-1}(B)$$

4.0 Phase and Amplitude Alignment

During the alignment process, the phase and amplitude trimmers are adjusted for either the sum or difference. By aligning one distribution the other is automatically aligned, however, the precision of the other

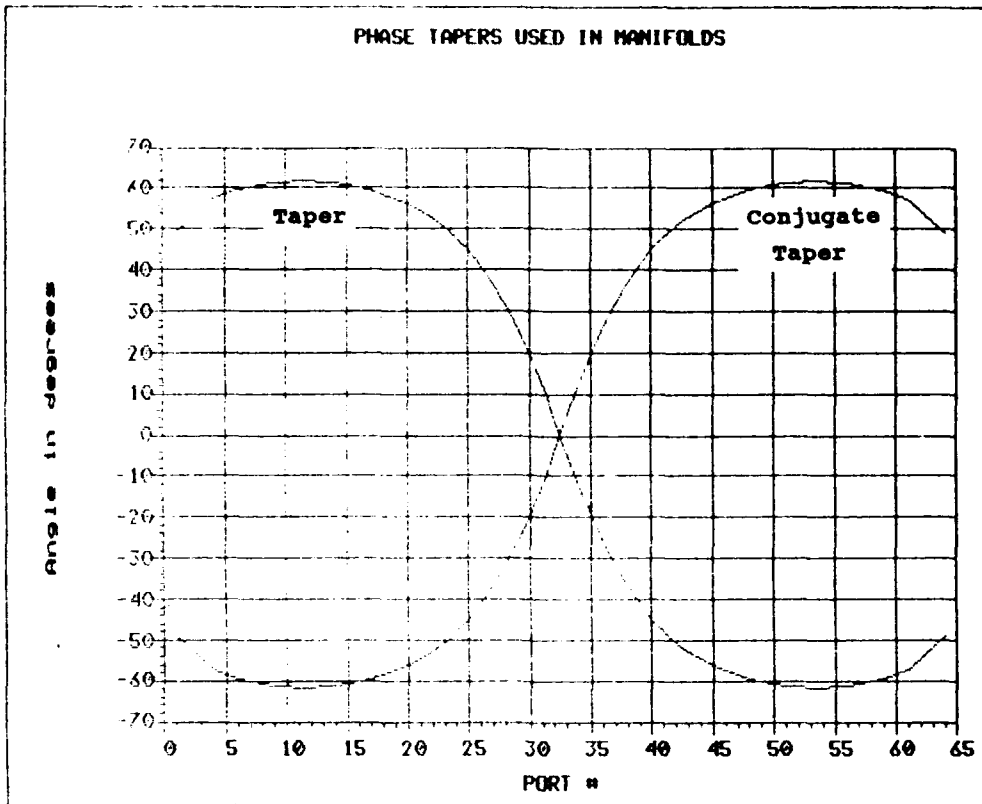


Figure 4. Phase tapers built into manifolds

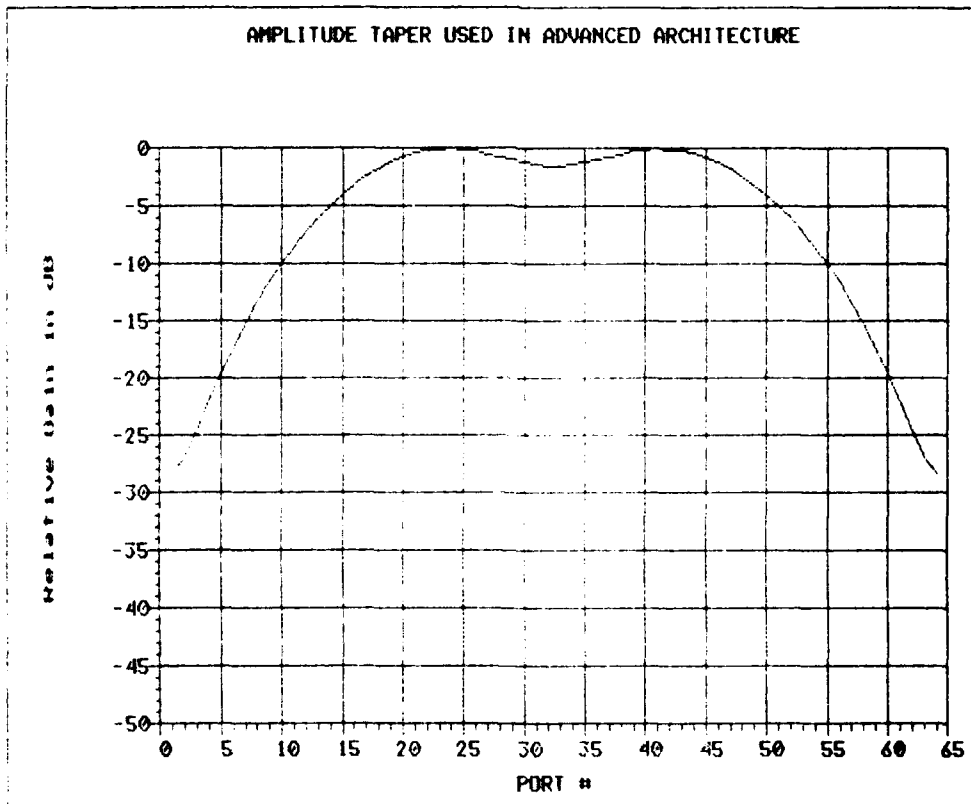


Figure 5. Common amplitude taper

depends on coupling accuracy. One objective was to see how compact the BFN could be made with acceptable line coupling. The phase and amplitude trimmers were adjusted to the settings shown in Figures 4 and 5 to achieve monopulse sum and difference receive beams. The sum distribution had been arbitrarily chosen for the tuning process. After tuning for the theoretical sum distribution, excitation measurements for both sum and difference distributions were collected and stored on disk.

Comparing the measured data with the theoretical, a significant systematic error was found in the difference taper. This occurred as a result of the two 1:64 manifolds not operating identically. Further analysis showed that one side of one layer had a distinct coupling problem due to long lengths of parallel stripline spaced too close together. This resulted from the size constraint put on the BFN.

When the coupling problem is resolved, the tuning process will correct both receive tapers simultaneously.

5.0 Pattern Predictions

Expected sum and difference elevation patterns were computed using measurements obtained during the beamformer network fabrication. These patterns provide expected range results except for range imperfections and element mismatches. Recent element pattern information were included to improve accuracy.

Sum and difference broadside data were collected. The measurements were taken before the 1:4 splitters, thus representing a 64:1 conformal array. Expected patterns are computed using using a 64:1 array having excitations equal to the measured data. Since patterns are only being

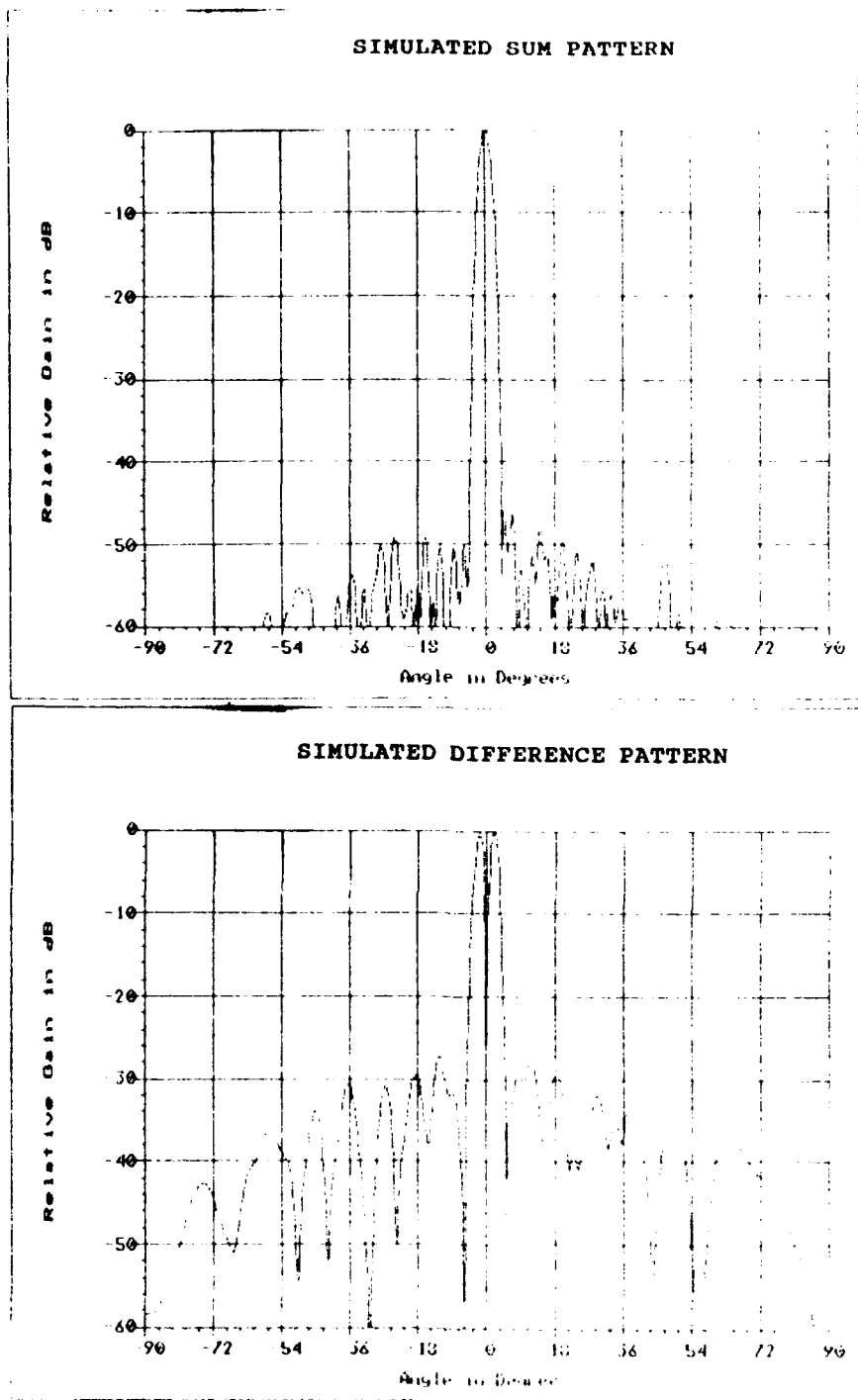


Figure 6. Simulated sum and difference broadside patterns

computed in elevation, the 64x4 array may be reduced to a 64x1. The expected broadside patterns at midband are shown in Figure 6. The sum pattern has an r.m.s. sidelobe level of -56.7 dB and sidelobes around -50 dB which closely resembles the design pattern (within 3 to 4 dB). Because of the stripline interaction (section 4), the difference pattern has an r.m.s. sidelobe level of -35.9 dB and sidelobes around -30 dB.

If corrective procedures are implemented it is estimated that the difference distribution errors would be lower than $\pm 5.0^\circ$ and $\pm .5$ dB. The pattern of such a distribution is shown in Figure 7. The r.m.s. sidelobe level has been lowered to -42.6 dB as well as the sidelobes to -35 dB. Table 1 summarizes the midband analysis.

	Pattern Analysis	
	RMS SL	SL level
-----	-----	-----
Sum	-56.7 dB	-50 dB
Difference	-35.9 dB	-30 dB
Modified Dif.	-42.6 dB	-35 dB

Table 1. Summary of midband pattern analysis.

6.0 Conclusion

The objective of phase II of Advanced Architectures for Airborne Arrays was to "reduce to practice" the architecture resulting from the phase I study with demonstration hardware. The hardware built for this phase of the program consisted of a 4x64 array of conformal patch radiators, a conformal beamformer with monopulse capability built as a continuous section, a novel, wideband "rat race" coupler, and phase and

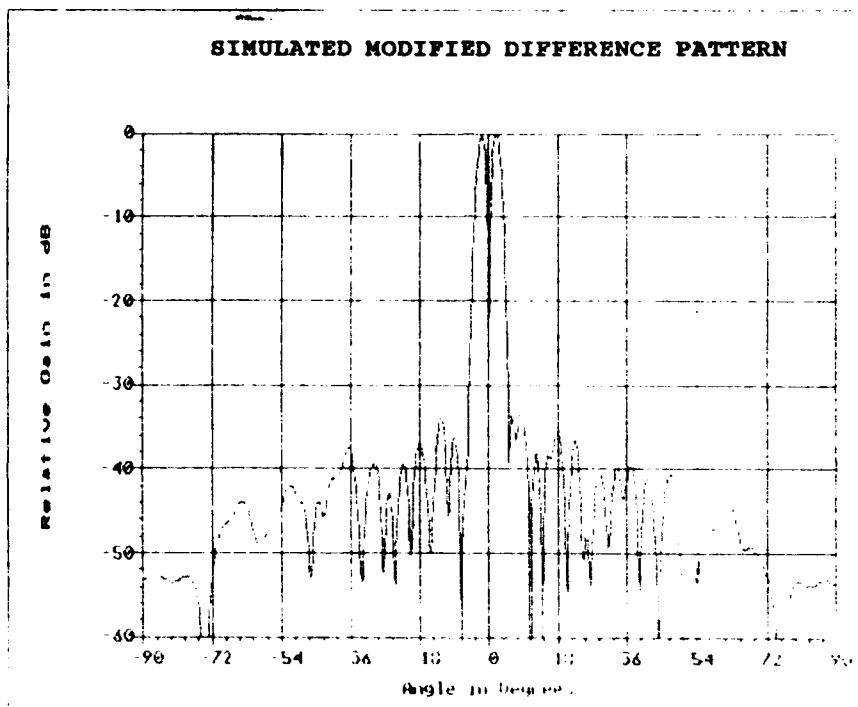


Figure 7. Simulated modified difference broadside pattern

amplitude trimmers that simulated the control inherent in the next generation T/R modules.

The program has demonstrated the critical aspects of the architecture:

1. A compact conformal radiator/distribution network.
2. A wide band patch radiator.
3. Reduction from 3 to 2 distribution networks.
4. Conformal plane phase compensation with a single phase shifter.

The greatest challenge in this program was in the manufacture of the dual layer package. The philosophy used in its construction was to manufacture the center conductor as a single piece in order to insure constancy in manufacture from unit to unit. However, the resulting dense packaging of the microwave network requires special measures to control coupling between adjacent lines. Further work is recommended to eliminate the difference pattern errors. Recommendations for improvement are:

Allowing the package width to grow for a conformal beamformer:

This would reduce the inter-line coupling. However, this solution would make the network inconsistent with the goal of staggering the columns between columns of radiators.

Introduction of mode suppression screws:

This would help reduce inter-line coupling. However, this would complicate the assembly of the columns and could force the lines further apart. The impact would then be to grow the width of the divider.

Build a planar beamformer with one of the edges being conformal to the fuselage:

We feel that this is the most feasible and manufacturable solution. Having the beamformer planar instead of conformal will simplify the overall manufacturing process since the assembly need not be done on a conformal surface. These manufacturing processes exist and need to be refined for the thinner center conductors and stripline ground plane spacings. In addition, a beamformer that is perpendicular to the plane of curvature will provide easier access to the T/R modules.

- 1 The work described herein was supported by the United States Air Force, Rome Laboratory through contract No. F19628-88-C-0016 and under the direction of Mr. John Antonucci.

- 2 * Yon, James, (1991) "Scan Correction Technique For Cylindrical Arrays", 1991 Antenna Applications Symposium

* This paper is based on work originally performed by Antonucci, J.D., and Franchi, P.R., (1987) "A Novel Method To Correct Radiation Distortion Of Conformal Antennas", RADC-TR-87-139, ADA193675

SCAN CORRECTION TECHNIQUE FOR CYLINDRICAL ARRAYS [1]

James B. Yon

Westinghouse Electric Corporation

Electronic Systems Group

Design and Producibility Engineering Division

Baltimore, Maryland 21203

ABSTRACT

Scanning in the curved plane of a cylindrical array causes the projected distribution to become skewed. This results in poor pattern performance such as broadened beamwidth, shallow difference beam null depth, and raised near-in sidelobes. Using traditional techniques to compensate for this distortion requires individual element control making the design too costly. A much less costly approach is achieved given a monopulse sum and difference architecture. By mixing a portion of the sum illumination taper with the difference illumination taper and vice versa, both patterns can simultaneously be corrected. This principle was first reported on by John Antonucci and Peter Franchi in a paper called "A Novel Method To Correct Radiation Pattern Distortion Of Conformal Antennas"[2]. Their study shows that by minimizing the skewness of the projected sum distribution the modified distributions greatly improve the sum pattern and somewhat improve the difference pattern. This paper carries their study one step further by optimizing the difference pattern to maximize null depth. This provides an optimal set of monopulse receive beams.

1.0 Introduction

Cylindrical arrays, with conformal scan capability, have existed for many years. However, such arrays typically scan using a commutator to rotate the distribution in the conformal plane. The disadvantages of this technique severely limit the application of cylindrical arrays. A major disadvantage results from radiation from only a fraction of the array. Furthermore, without additional beam sharing hardware, only discrete beam positions can be achieved through this technique.

An alternate approach to scanning cylindrical arrays has emerged with the advent of active phased array elements. Using amplitude and phase control on each element, conformal plane scan distortion can be compensated. However, the current cost of active phased arrays deters their use for low cost systems. Furthermore, the scan correction does not require the complexity of individual element control.

This paper discusses a technique for compensating for scan distortion given monopulse sum and difference distributions formed by a phased array conformal about an arc of a cylinder, as shown in Figure 1. This concept was first discussed in a paper called "A Novel Method To Correct Radiation Pattern Distortion Of Conformal Antennas"[2] and will be expanded upon to demonstrate a new technique.

2.0 Conformal Plane Scan Distortion

Scanning a cylindrical array in the conformal plane causes the sum and difference patterns to suffer serious degradation. This is the result of two characteristics inherent to conformal arrays. First, the element spacing along the projected plane wave becomes more nonuniform as the scan angle increases, as depicted in Figure 2. Secondly, every

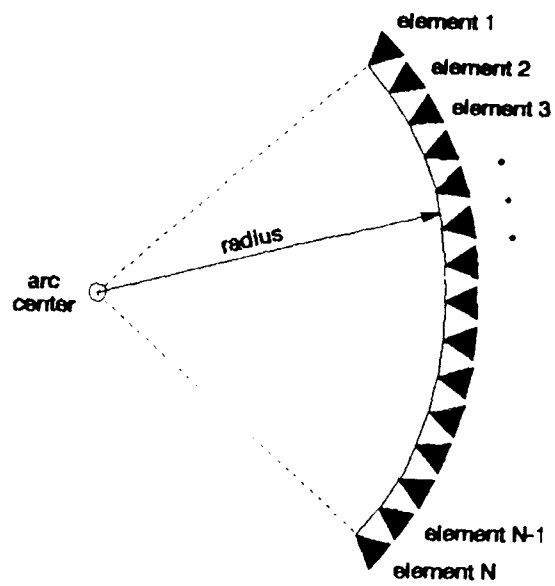


Figure 1. Conformal array about an arc of a cylinder

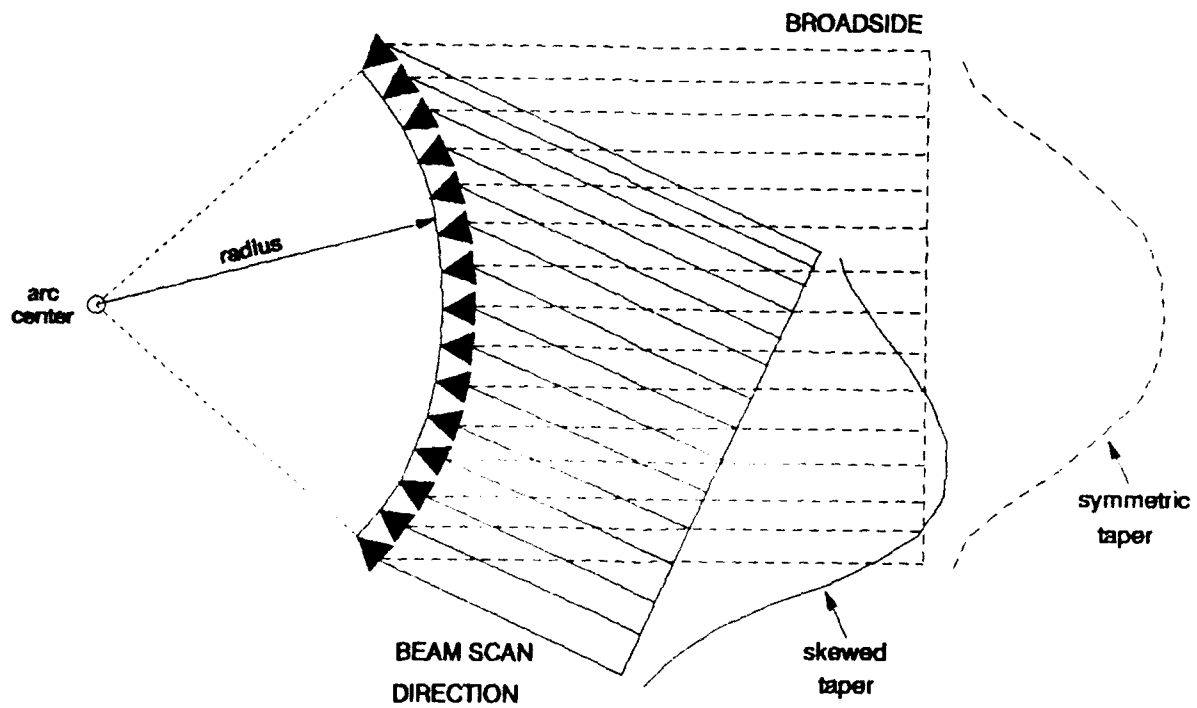


Figure 2. Effect of projected element spacing as array scans

element points in a different direction causing the element pattern of each element to have a different effect on the scanned pattern at a given direction, as shown in Figure 3.

To demonstrate the amount of degradation under consideration an arbitrary array is chosen having 64 elements with $\lambda/2$ spacing about a 60° arc. Figures 4 and 5 show typical low sidelobe sum and difference patterns, respectively, using an assumed cosine element pattern. In each figure, broadside and 40 degree scanned patterns are displayed as a reference pattern to show the distortion level. In general, the scanned patterns beamwidth broadens and near-in sidelobes rise. Also, the null depth becomes very shallow as the positive and negative regions of the distribution become unequal in projected size.

3.0 Correcting Scanned Pattern Distortion

A method of correcting for such pattern degradation is described in the paper referenced [2]. The method uses the fact that the change in the projected radiated sum taper due to scanning resembles a difference illumination taper. The reverse is almost true for the difference taper as well. Figure 6 shows typical scan distortion for sum and difference distributions. The corrective technique consists of combining a small portion of the sum signal with the difference signal, and vice versa. Analytically this produces new sum and difference distributions expressed by equation (1):

$$\text{new sum:} \quad \Sigma' = \sqrt{1 - B^2} * \Sigma + B\Delta \quad (1a)$$

$$\text{new difference:} \quad \Delta' = \sqrt{1 - B^2} * \Delta - B\Sigma \quad (1b)$$

where B is the ratio of taper mix. The "+" and "-" signs are reversed when scan direction is changed.

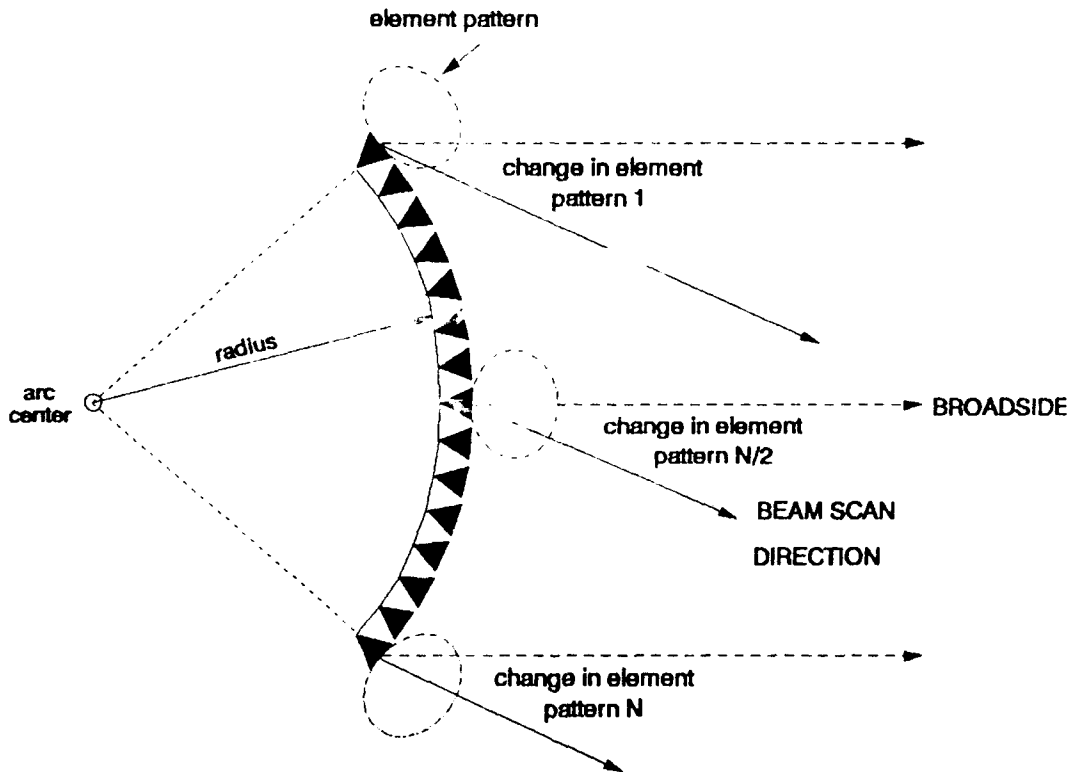
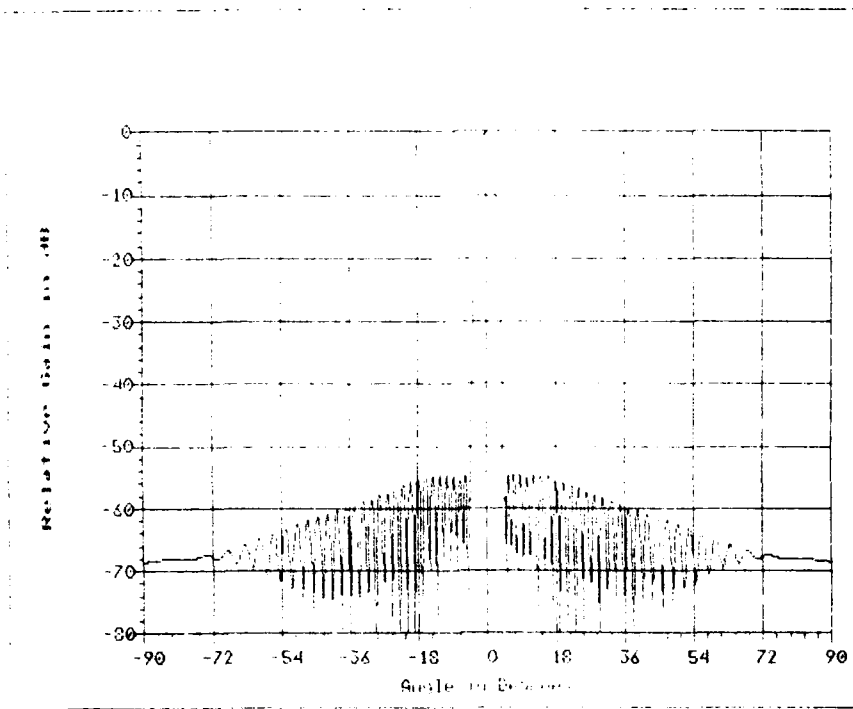
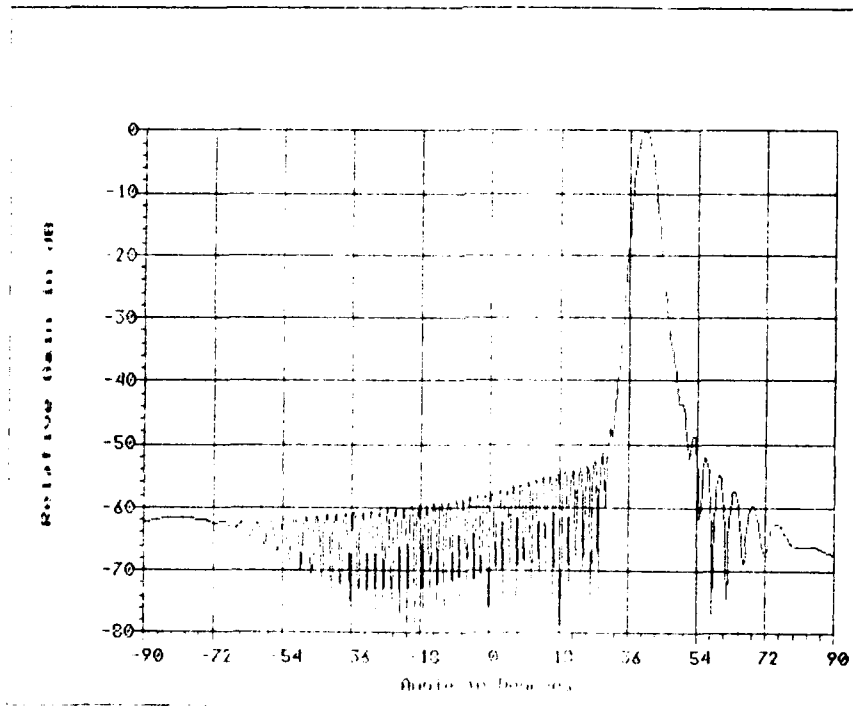


Figure 3. Effect of each element's pattern on the scanned beams

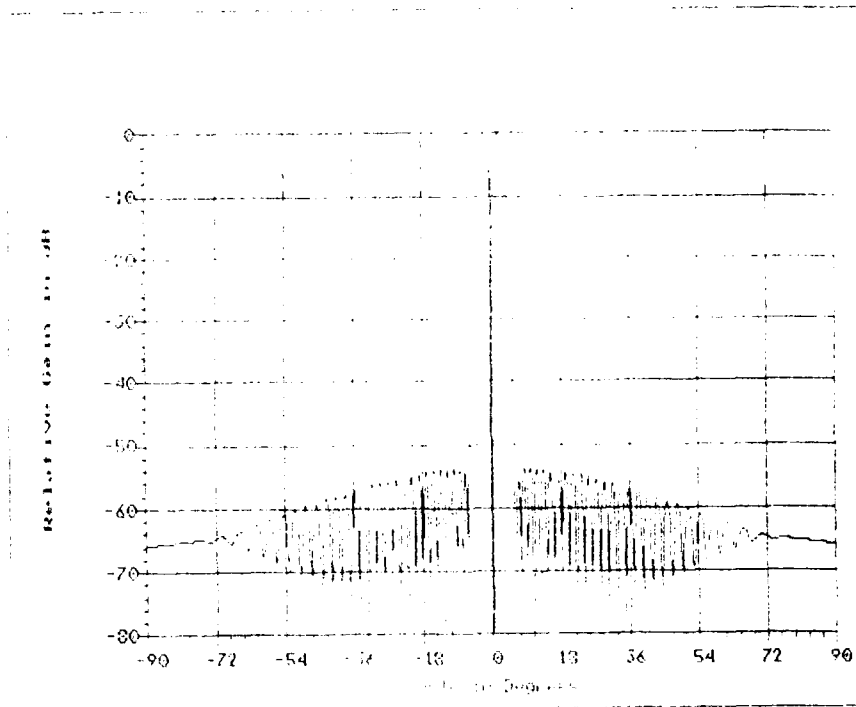


a) Broadside sum pattern

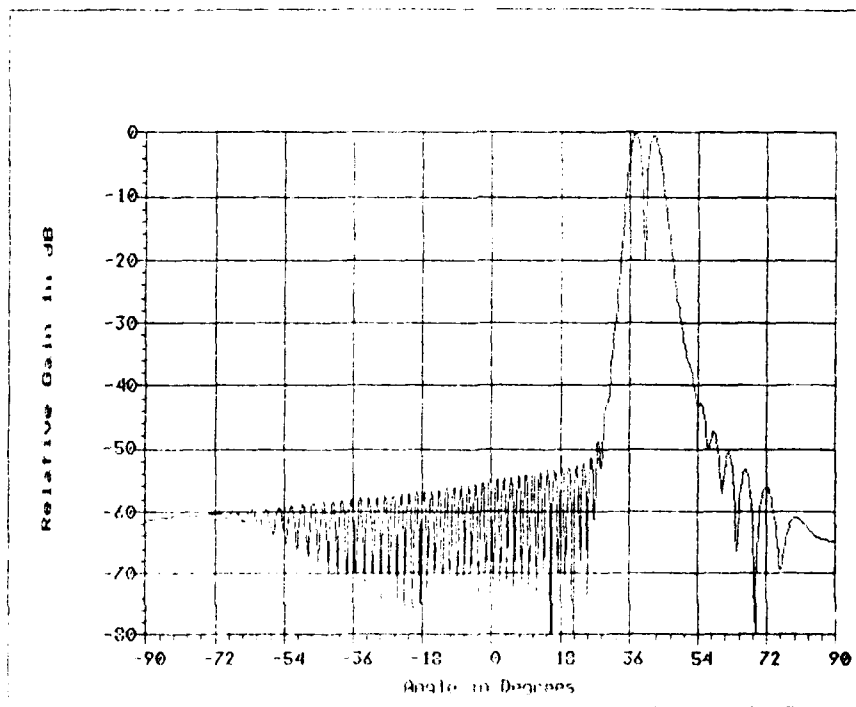


b) 40 degree scanned sum pattern

Figure 4. Sum pattern performance of a cylindrical array



a) Broadside difference pattern



b) 40 degree scanned difference pattern

Figure 5. Difference pattern performance of a cylindrical array

SUM TAPERS

DIFFERENCE TAPERS

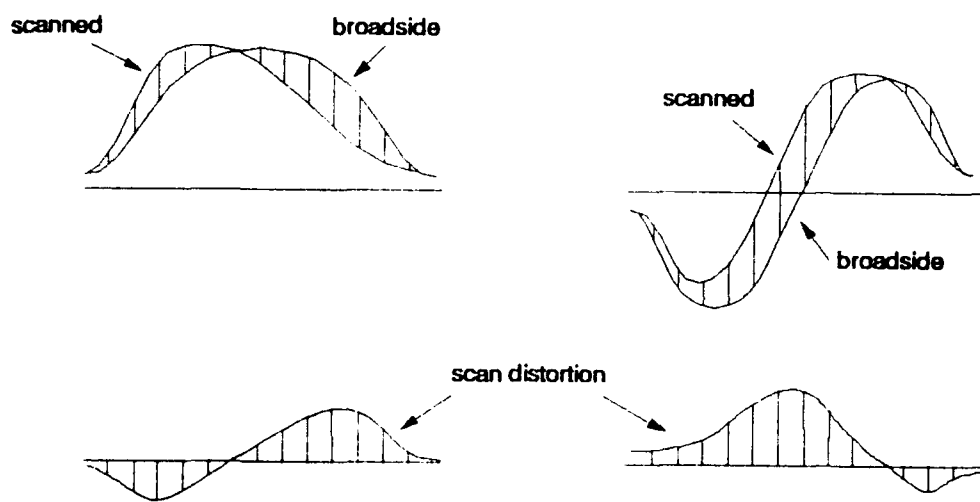


Figure 6. Distortion error due to scanning a cylindrical array

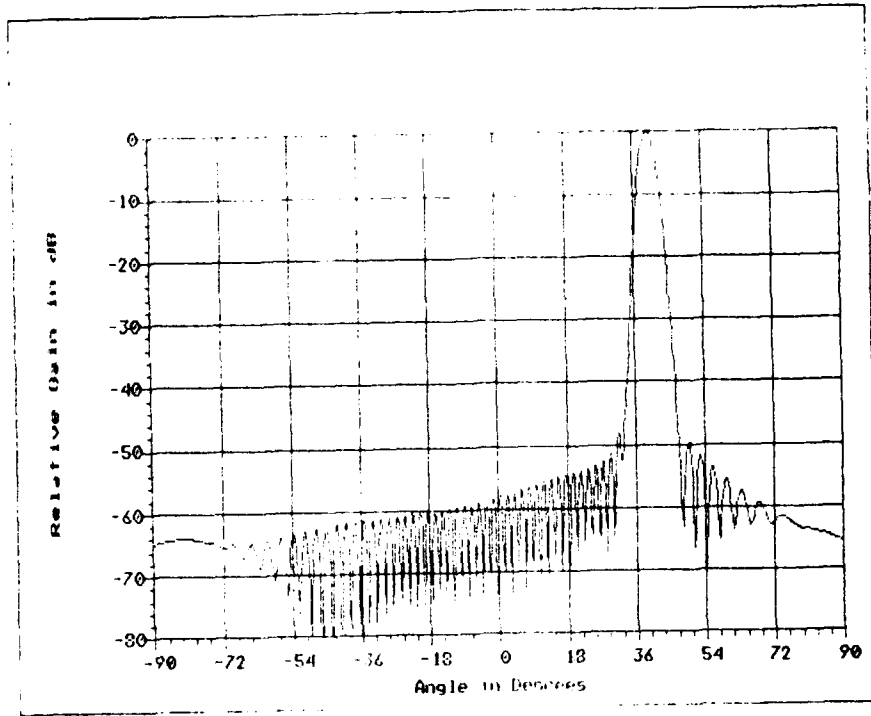
3.1 Scan Correction Optimization

The amount of signal being exchanged between the two distributions is determined by optimization guidelines. The previously mentioned paper discusses optimizing the sum taper. The idea is to minimizing the skewness of the projected sum distribution in the scanned direction to most resemble the projected broadside distribution. While this greatly improves the scanned sum pattern, the difference pattern does not show the same improvement.

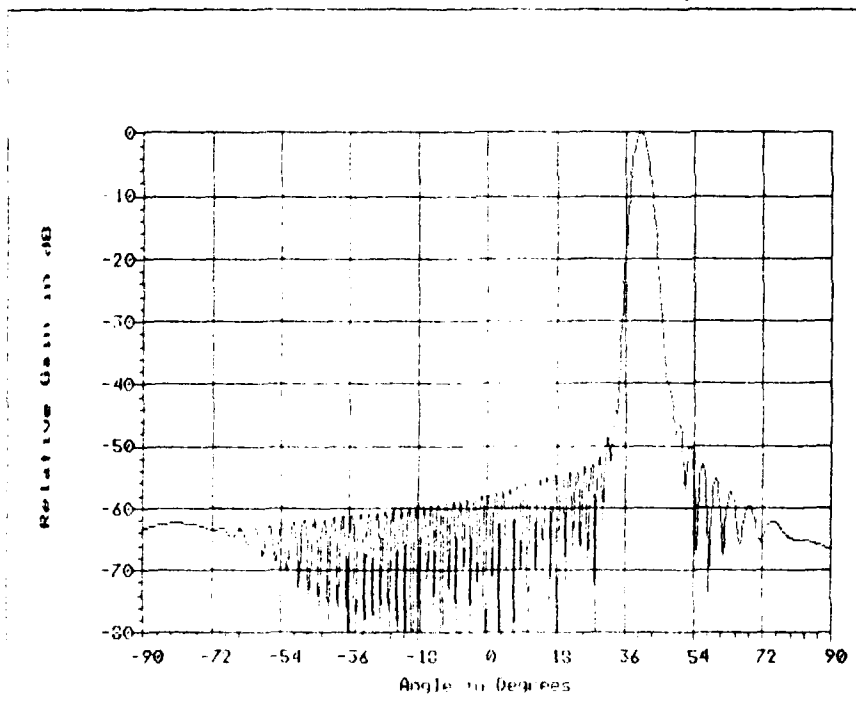
Instead, if the optimization guidelines are based on the null depth of the difference pattern, a more desirable overall performance can be achieved. This involves mixing the two illumination tapers by a percentage that minimizes the null depth. By doing so, it was found that both patterns perform more like the broadside case. Furthermore, the previous optimization tends to over-compensate the difference pattern to the extent of producing shallow null depth.

4.0 Results

As a demonstration, both optimization techniques have been applied to the scanned sum and difference patterns shown in Figures 4 and 5. The results are displayed in Figure 7 and 8 for the sum and difference patterns, respectively. Graph a) show the results of optimizing the sum taper whereas b) show the results of optimizing the difference null depth. Table 1 shows the percentage illumination taper mixing required for both techniques which are dependent upon the scan angle, element pattern, and the array configuration.

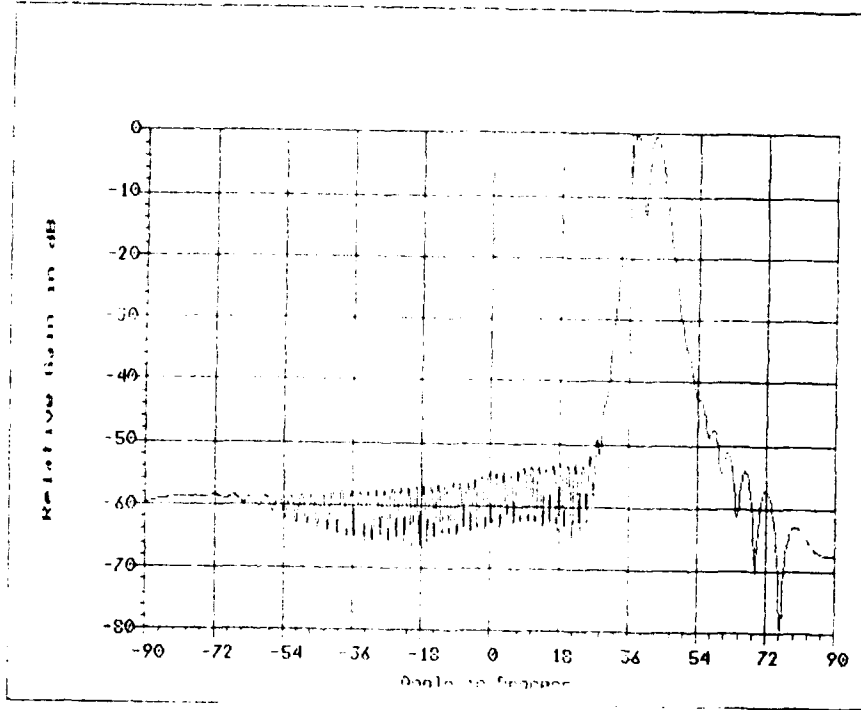


a) Sum taper optimization effect on sum pattern

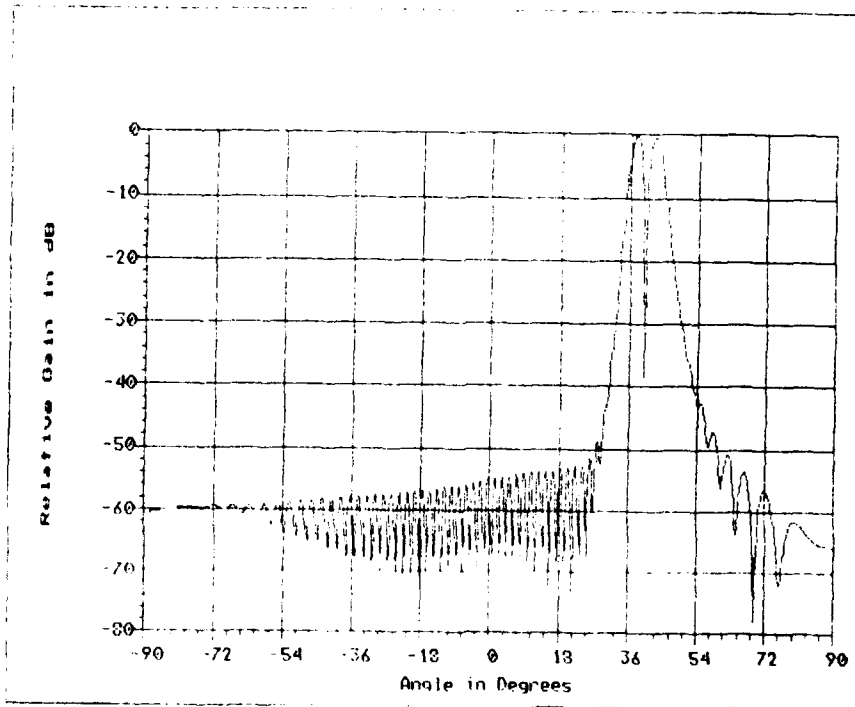


b) Difference null depth optimization effect on sum pattern

Figure 7. 40 degree scanned sum patterns using both optimizations



a) Sum taper optimization effect on difference pattern



b) Difference null depth optimization effect on difference pattern

Figure 8. 40 degree scanned difference patterns using both optimizations

Optimization	% Taper Mix at 40° scan
sum taper	6.3 %
difference null depth	1.0 %

Table 1. % taper mix required to correct for scan distortion

As seen in table 1, a major difference between the two optimizations is the amount of illumination taper being exchanged. By maintaining the symmetric quality of the projected sum taper, the tendency is to unbalance the the projected difference taper causing a shallow null depth. Furthermore, it is evident that the difference pattern null depth is much more sensitive to the illumination taper mixing than the base of the sum and difference beams and near-in sidelobes. This can be seen by comparing the effect both optimizations have on each pattern. Both sum patterns have very similar qualities whereas the difference patterns have significant changes in null depths. To optimize both simultaneously requires a slight nonorthogonality of sum and difference beams.

5.0 Conclusion

Cylindrical arrays exhibit skewed projected distributions when scanned in the curved plane. Previous work shows that the distortion of the projected sum distribution can effectively be compensated for by adding a small amount of difference taper. While this technique greatly improves the sum scanned pattern performance, the difference pattern null depth may become worse as a result of adding the same portion of sum taper to the difference. This can be solved without degrading the sum pattern by optimizing the difference null depth which was shown to be more sensitive to the illumination taper mixing.

- 1 The work described herein was supported by the United States Air Force, Rome Laboratory through contract No. F19628-88-C-0016 and under the direction of Mr. John Antonucci.

- 2 Antonucci, J.D., and Franchi, P.R., (1987) "A Novel Method To Correct Radiation Distortion Of Conformal Antennas", RADC-TR-87-139, ADA193675

HIGH RESOLUTION AURORAL CLUTTER MAPPING USING THE VERONA AVA LINEAR ARRAY RADAR

D. S. Choi, B. Weijers, R. J. Norris, and N. B. Myers

Electromagnetics and Reliability Directorate
Rome Laboratory, Hanscom AFB, MA

Abstract - The Verona Ava Linear Array Radar (VALAR) is a high resolution experimental HF backscatter data acquisition system designed to investigate the characteristics of high latitude auroral clutter. The transmit system located in Ava, New York, is capable of providing RF signals in the 2-30 MHz band with up to 300 kW average power. The receive system at Verona, New York, consists of a 72 element linear antenna array (extending 700 meters in length) and 36 identical HF receivers. Since the completion of system test and calibration at the end of 1989, data acquisition campaigns have been carried out on a near monthly basis. In this paper we provide a brief description of VALAR and present some examples of initial results from the preliminary analysis of HF auroral backscatter data acquired during 1990. These examples demonstrate the capability of VALAR as a high resolution HF backscatter data acquisition system.

1. INTRODUCTION

Over-the-horizon backscatter (OTH-B) radar systems operating at high latitudes are subject to periods of degradation in performance due to the presence of electron density irregularities in the auroral ionosphere. OTH-B radar systems utilize oblique reflection of HF waves from the ionosphere to propagate a signal to the ground beyond the line of sight of the transmitter. The backscattered signal from the ground is returned to the receive array, in general located near the transmitter, by a second oblique reflection from the ionosphere. The signal propagating in the auroral ionosphere can be backscattered directly to the receive array when the wave normal of the HF signal is perpendicular (or al-

most perpendicular) to the magnetic field-aligned irregularities¹. This unwanted backscattered radar signal is termed auroral clutter, and is one of the identified sources of residual clutter encountered by OTH-B radars operating at high latitudes. Residual clutter is characterized by an increase in the effective noise level above the external noise when the transmitter is turned on. It also tends to spread the Doppler frequency beyond the normal ground backscatter Doppler limits of +/- 1 Hz. Many important properties of auroral clutter remain unidentified and are poorly understood, requiring extensive analysis and characterization prior to the development and evaluation of clutter mitigating techniques.

The Verona Ava Linear Array Radar (VALAR) is a unique experimental HF backscatter radar system dedicated to investigating the characteristics of auroral backscatter. The system is currently operating in a data acquisition mode to collect HF propagation data. The elemental data collected are then processed and analyzed at Rome Laboratory, Hanscom AFB. In this paper we provide a brief description of VALAR and present some initial results from the analysis of data collected during 1990.

2. SYSTEM DESCRIPTION

VALAR was developed by Rome Laboratory to establish a dedicated experimental HF backscatter data acquisition system to resolve various residual clutter and clutter mitigating issues. Currently, the system is configured to acquire HF auroral backscatter data to investigate the characteristics of auroral clutter. The transmit system is located at the Rome Laboratory HF transmit site in Ava, New York, and the receive system is at the Verona Test Annex in Verona, New York, 30 km from the transmitter. The approximate geographical location of VALAR is 43° 24' North and 75° 23' West. From this location, geographic north is within 5° of geomagnetic north.

2.1. *Transmit system*

The transmit system at Ava features various transmitter and antenna configurations for both low and high power requirements. The facility is capable of supplying RF waves in the 2-30 MHz band with up to 300 kW average power. It has the capability to simultaneously transmit a wideband Swept-Frequency Continuous Wave (SFCW) and a narrowband linear Frequency-Modulated Continuous Wave (FMCW) signals. The wideband SFCW signal is required to operate the sounder located in Verona to obtain wideband oblique backscatter ionograms. During the data acquisition phase, a slanted rhombic antenna was used in conjunction with a Continental transmitter to support the high transmit power requirement of VALAR. At 10 MHz, the theoretical 3 dB elevation beamwidth is 14° centered at 10° elevation. The theoretical 3 dB azimuthal beamwidth is also 14° .

2.2. *Receive system*

2.2.1. *Antenna array*

The receive system at Verona Test Annex includes a 700 meter linear array. The configuration of the linear array is shown in figure 1. It consists of 36 sub-arrays, each with two active and two passive monopoles. The boresight of the array is 10° east of true north. The array was designed to optimize the performance over the frequency band of 6 to 12 MHz because auroral clutter is primarily a nighttime phenomena and the ionosphere does not support higher frequencies during these times. Antenna pattern measurements at 12 MHz have shown 2.5° 3 dB beamwidth, 23 dB array gain, and 30 dB RMS sidelobe levels². Measurements have also shown that an azimuthal coverage of -30° to $+30^\circ$ (with respect to the boresight of the array) is possible at 12 MHz. The coverage area of VALAR, superimposed on a map of North America, is shown in figure 2. Also depicted in figure 2 is the approximate position of the auroral oval at 21:00 EST during an average magnetic index of

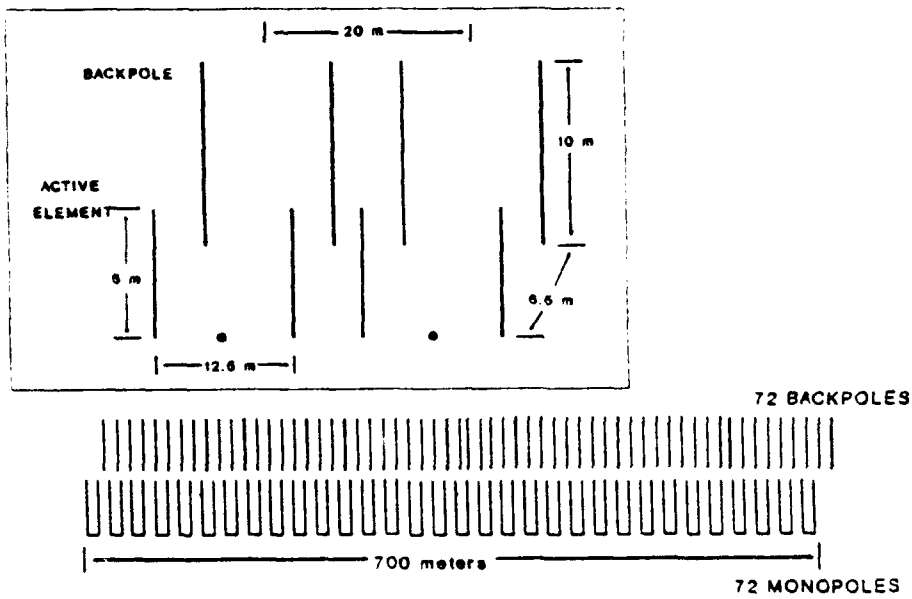


Figure 1. Configuration of VALAR receive antenna array showing the linear array and subarray geometry

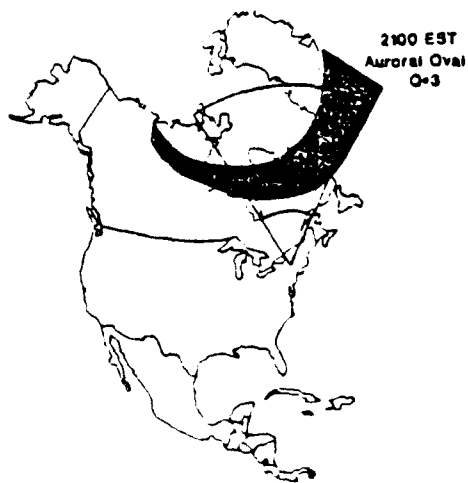


Figure 2. Coverage area of VALAR. Also shown is the approximate position of the auroral oval at 21:00 EST with magnetic index $Q=3$.

Q=3. Note that both equatorward and polarward boundary of the auroral oval is within the field of view of VALAR. Thus VALAR is ideal system to observe and characterize HF backscatter from the auroral ionosphere.

2.2.2. Receive electronics

The basic block diagram of the system is shown in figure 3. It consists of 36 identical subsystems, a MicroVaxII, and a Kennedy tape recording device. Each subsystem, in addition to the subarray discussed above, also includes a preamplifier and an HF receiver. The receiver converts the HF signal at the output of the preamplifier to complex digital baseband data. The digitized data are temporarily buffered in the RAM of each receiver, then serially transferred

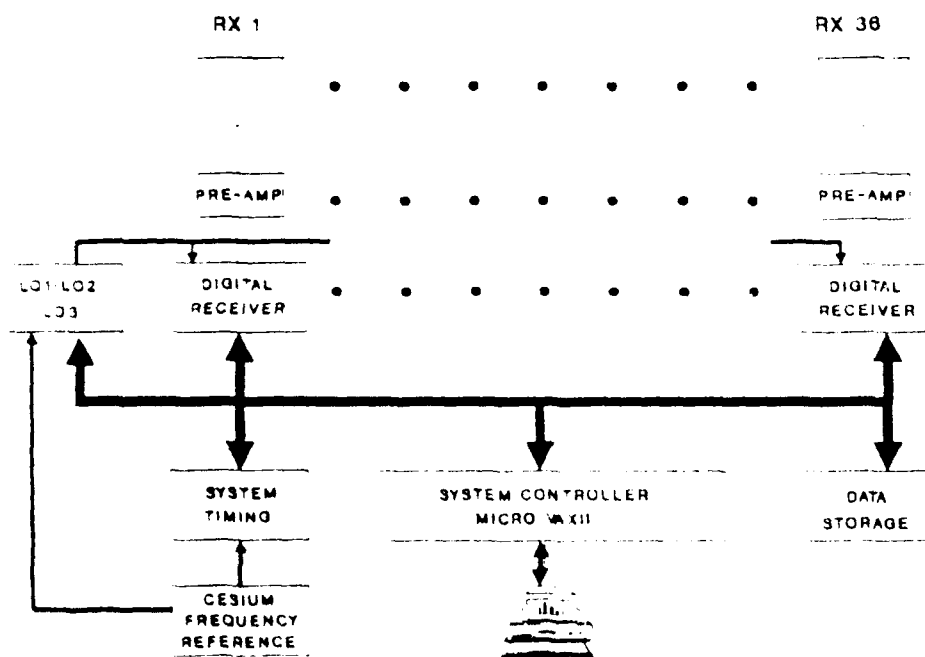


Figure 3. VALAR receive system block diagram

to the Kennedy tape drive and recorded on a tape. The MicroVaxII is the system controller for all data acquisition commands and transfers. The data acquisition software on the MicroVaxII allows the user to select various system parameters during the data acquisition phase. Typical values of system parameters are shown in table 1.

Transmit Power	100 kW (RMS)
Waveform	Linear FMCW
Sweep Rate	250 kHz/s
Waveform Repetition Frequency (WRF)	25 Hz
Sweep Bandwidth	10 kHz
Baseband Bandwidth	+/- 5 kHz
Sampling Rate	10 kHz
Coherent Integration Time (CIT)	3.2 seconds

Table 1. Typical system parameters used during data acquisition

2.2.3. Diagnostic software

In addition to the data acquisition software, a diagnostic software is also available on-site. This software enables a quick check of the system performance and the quality of the data being recorded. The operator can simultaneously display the amplitude, phase, and signal-to-noise ratio (SNR) of all 36 channels, examine the frequency spectrum of a single channel, and plot azimuth distribution of power incident on the aperture for a given range. Further data processing is accomplished at Rome Laboratory, Hanscom AFB, Massachusetts.

3. INITIAL RESULTS

On September 24 1990, HF propagation data were collected during the period of 20:00 to 23:00 eastern standard time (EST). A waveform repetition frequency (WRF) of 25 Hz was selected to eliminate possible range ambiguity. The average transmit power was 100 kW and the operating frequency was 10.58 MHz for the data presented in this section.

3.1. Oblique backscatter ionograms

The wideband oblique backscatter ionograms of figure 4 present a good comparison of ground backscatter echoes with the direct scatter echoes from field-aligned irregularities. Figure 4a, obtained at 20:30 EST, is typical ionogram showing 2F ground backscatter during undisturbed ionospheric conditions.

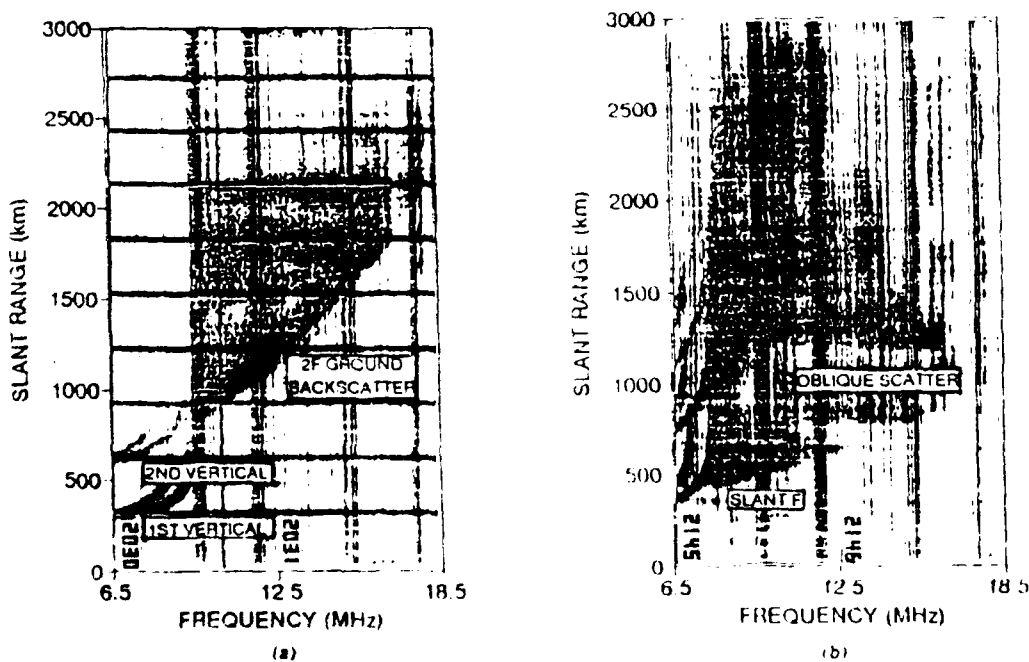


Figure 4. Oblique backscatter ionograms obtained during September 24 1990 at (a) 20:30 and (b) 21:40 EST

The '2F' indicates a signal that is obliquely reflected from the F-region ionosphere, backscattered from the ground, and obliquely reflected a second time to the receive array. As indicated on the ionogram, the main features are the first vertical incidence, the second vertical incidence, and the 2F ground backscatter. The first vertical incidence is a signal that propagates vertically, reflects from the ionosphere, and returns to the receiver. The second vertical incidence refers to a signal that travels the ray path of the first vertical incidence twice. Note that the 2F ground backscatter begins from the second vertical incidence and linearly increases in slant range with increasing frequency. This is because, in general, an obliquely transmitted signal requires two reflections from the ionosphere to return to the receiver. As the transmit frequency increases, the oblique angle of reflection increases, thereby increasing the slant range of the 2F ground backscatter region.

In comparison to figure 4a, the ionogram obtained at 21:40 EST (figure 4b) shows additional backscattered signals. These additional backscattered signals are identified as slant-F and oblique scatter. The slant-F and oblique scatter are two of the three identified types of HF auroral clutter at high latitudes³. Slant-F echoes are the direct backscattered signals from field-aligned irregularities in the F-region ionosphere. From the location of VALAR, it is normally associated with irregularities in the sub-auroral F layer. The oblique scatter is typically associated with echoes from auroral F region and may exhibit both long and short slant ranges. The long slant range is associated with high elevation angle while the short slant range implies low elevation angle⁴. The third type, echoes from auroral E-region, is not observed by VALAR, except under disturbed magnetic conditions.

3.2. Characteristics of 2F Ground Backscatter

Figure 5 shows the amplitude-range-azimuth (ARA) map of backscatter energy at 20:30 EST. The leading edge of the 2F ground backscatter occurs at 900 km, and this is in agreement with the oblique ionogram shown in figure 4a. The ground backscatter is observed at all azimuths, and is the dominant

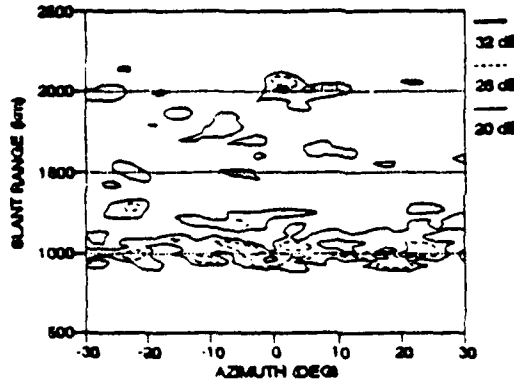


Figure 5. Amplitude-range-azimuth (ARA) map of the backscatter energy observed at 20:30 EST. Three contour levels of constant amplitudes are shown for slant range and azimuth.

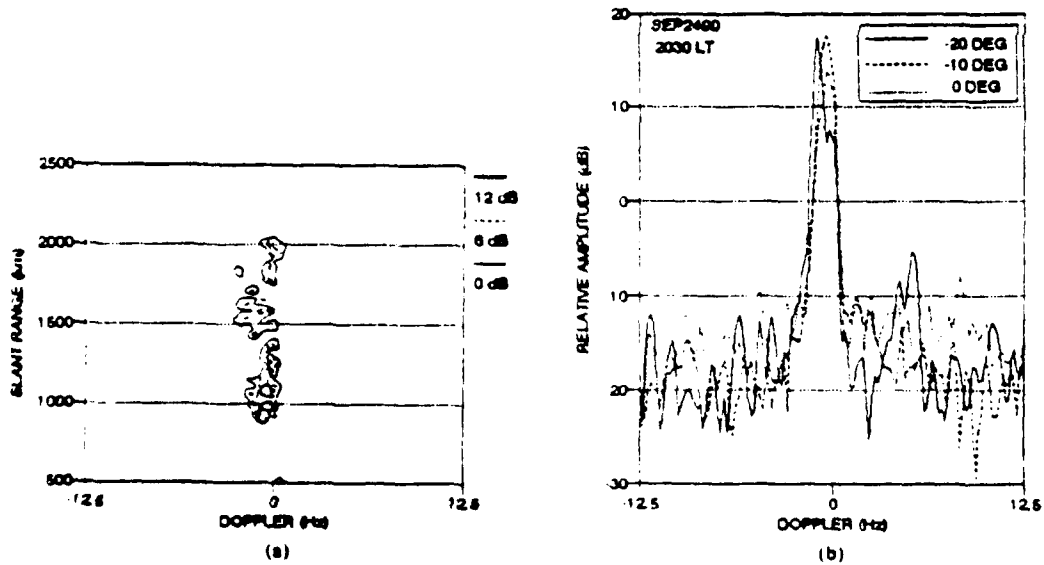


Figure 6. (a) Amplitude-range-Doppler (ARD) map of the backscatter signal at 20:30 EST for -10° (true north) beam, and (b) the mean Doppler spectrum of 2F ground backscatter for various azimuth beams.

backscatter in the figure. The Doppler characteristics of 2F ground backscatter can be examined for various azimuth angles. Figure 6a is the associated amplitude-range-Doppler (ARD) map with the beam steered at -10° (true north). The strongest signals are returned from a slant range of 900 to 1200 km. The spread in Doppler is very small, indicating a fairly undisturbed ionosphere. Figure 6b shows the mean Doppler spectrum (averaged over slant range from 900 km to 1000 km) for various azimuth beams. The 2F ground backscatter is shown to be about 30 dB above the mean clutter/noise level and the spread in Doppler is confined to ± 1 Hz about 0 Hz.

3.3. Characteristics of auroral clutter

3.3.1 Range-azimuth distribution of auroral backscatter

The ARA map of backscattered energy at 21:40 EST is shown in figure 7. There are three principle features: (1) the slant-F echoes at 550 km are confined in azimuth, (2) the oblique scatter at 800 km is relatively weak in amplitude, and (3) the oblique scatterers beyond 1200 km are of different scale sizes and locations. Upon initial observation, three independent echoes from auroral F-region are identifiable between 1200 and 1500 km (other irregularity patches of different sizes and locations were also observed at later times). The 2F ground backscatter, expected around 1400 km when examining the ionogram in figure 4b, is not identifiable because the auroral F-region echoes dominate at this slant range. The oblique scatter at 800 km corresponds to low elevation angle ray. Since the array elements are vertical monopoles with very poor low elevation coverage, the weak relative amplitude observed is expected.

3.3.2. Doppler characteristics of auroral backscatter

ARD maps for 21:40 EST are shown in figure 8. The azimuth beams were steered to -20° , -10° , and 0° , respectively. The main features of these figures are: (1) the slant-F echoes at 550 km exhibits shift in peak Doppler frequency as

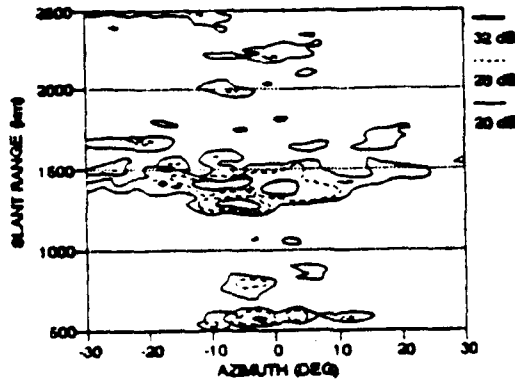
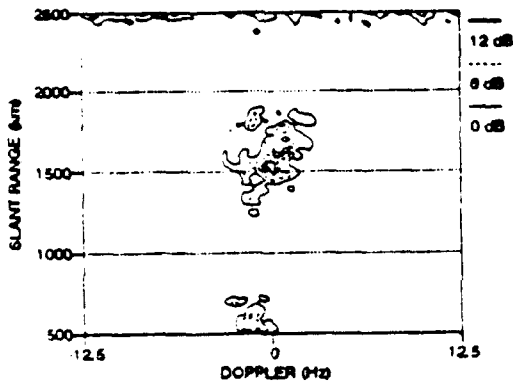
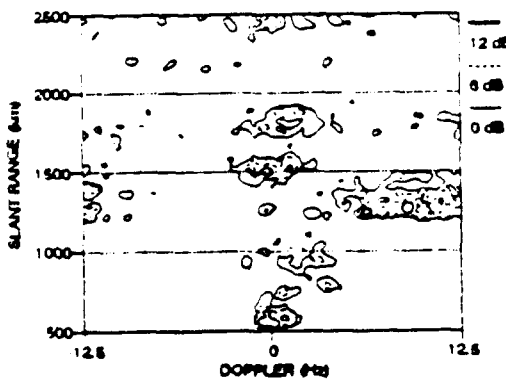


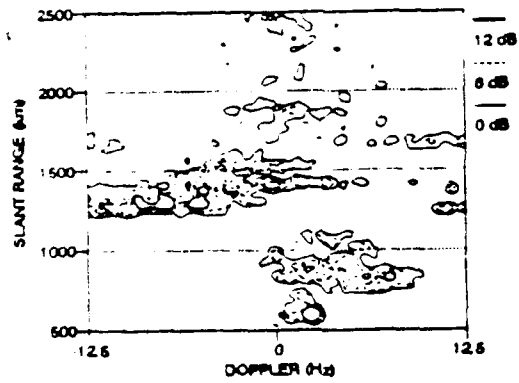
Figure 7. ARA map of the backscatter energy at 21:40 EST



(a)



(b)



(c)

Figure 8. ARD maps at 21:40 EST for various azimuth beams.
(a) -20° , (b) 10° , and (c) 0° .

a function of azimuth angle, (2) the strong echo at 1500 km (figure 8a) shows spread about 0 Hz, and (3) the direct backscatter from auroral F-region at 1200-1400 km (figure 8b and c) exhibits very large shift and spread in Doppler. Note the difference in Doppler characteristics of the auroral clutter at -10° in comparison to the beam at 0° . While the auroral clutter at -10° is characterized by positive Doppler, the Doppler at 0° is predominantly negative. Also identifiable in figure 8c is the low angle oblique scatter at 800 km.

Figure 9 shows the mean Doppler spectrum of slant-F echoes for these three different azimuth beams. The peak Doppler frequency shifts from negative to positive as the beam is steered from west to east of true north. This indicates that the electron density irregularities responsible for the slant-F echoes drift away from the radar at the -20° beam and towards the radar at 0° . The slant-F echoes are also characterized by relatively narrow Doppler spread of 5 Hz, independent of azimuth.

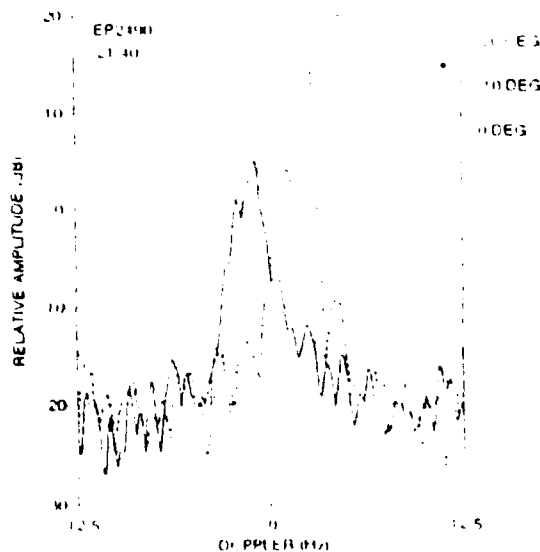


Figure 9. Mean Doppler spectrum of slant-F echoes for -20° (solid line), -10° (dotted line), and 0° (dashed line).

While the slant F echo shows shift in frequency, the strong echo at 1500 km (figure 8a) exhibits relatively small spread in Doppler about 0 Hz. At this angle of incidence (-10° west of true north) the direct backscatter from the auroral F-region should show a wide spread and shift in Doppler due to the motion of the irregularities. Since the general motion of the large-scale auroral irregularities is east to west and this beam is west of the other two, it is possible that the auroral clutter has not affected this azimuth beam as of 21:40 EST. Therefore, we conclude that the signal at 1500 km is the ground backscatter. This signal is also identifiable in figure 8b.

Figure 10 shows the mean Doppler spectrum of ground backscatter at 20:30 and 21:40 EST for the -10° beam. Also shown in figure 10 is the mean Doppler spectrum of external noise (transmitter off). The increase in effective noise level due to clutter is about 10 dB and the spread in Doppler is about ± 5 Hz. Since the origin of this echo is the ground, the source of clutter is most likely at the midpoint of the propagation path. This increase in effective noise

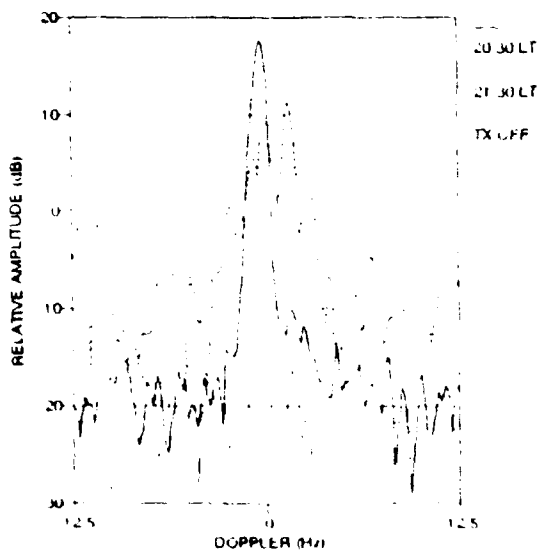


Figure 10. Mean Doppler spectrum of ground backscatter at 20:30 EST (solid line), 21:40 EST (dashed line), and external noise (dotted line) for -10° azimuth beam.

level and the spread in Doppler are probably due to the induced phase and amplitude distortion along the wavefront of the signal as the wave propagates in the ionosphere. This conclusion is true if there were no multi-path modes due to direct backscatter from the auroral F-region in the same range bin. We believe that this is the case since the spread in Doppler is relatively small and it is centered about 0 Hz.

The difference in Doppler characteristics of auroral clutter seen in figure 8b and c can be explained as follows. In order to eliminate range ambiguity, a WRF of 25 Hz was required. This selected value of WRF limits the Doppler bandwidth to -12.5 to 12.5 Hz, and consequently the maximum unambiguous Doppler velocity observable. The maximum unambiguous Doppler velocity for given operating frequency and WRF is 177 m/s. If the Doppler velocity is greater than 177 m/s, an ambiguity results due to Doppler aliasing. All positive Doppler velocity greater than 177 m/s will 'wrap-around' to the opposite band and appear as negative Doppler. Considering the approximate position of the auroral oval and the direction of the electrojet current relative to VALAR at 21:40 EST, the observed Doppler should be positive. Furthermore, the Doppler velocity along the radar look direction for the 0° beam will be greater than the -10° beam. Therefore, we can conclude that the negative Doppler observed for the 0° beam is equivalent to Doppler velocities greater than 177 m/s.

4. SUMMARY AND CONCLUSIONS

Initial results from the VALAR HF backscatter radar system have been presented in this paper. The capability of the VALAR system to observe auroral clutter makes it a useful tool for understanding and mitigating the problems associated with OTH-B radars operating at high latitudes. The development of auroral clutter in the evening has been shown. The slant-F echoes were identified as originating in the sub-auroral zone ionosphere exhibiting less Doppler spread than the oblique scatter echoes and were localized in azimuth. The oblique scatter echoes caused by ionospheric irregularities were shown to be dy-

ADAPTIVE NULLING AND SPATIAL SPECTRAL ESTIMATION USING AN ITERATED PRINCIPAL COMPONENTS DECOMPOSITION

Dean O. Carhoun

The MITRE Corporation, Bedford, MA 01730

ABSTRACT

An iterative algorithm is described for computing a reduced rank principal component least squares estimate of the adaptive weight vector to be used for spatially nulling interference received in the sidelobes of the formed beams of an array of antenna elements. Based on a power/deflation method for extracting estimates of the dominant eigenstructure components, the algorithm is used to approximate the subspace spanned by the sample covariance eigenvectors associated with the directions of arrival of spatially coherent interference. Side information is also produced that can aid the discrimination between interference and noise subspaces. Performance is illustrated by the results of processing actual signals recorded from the individual elements of a linear antenna array operating in the HF band.

1. INTRODUCTION

Adaptive nulling and high resolution direction-finding are important aspects of sensor array processing. Adaptive sidelobe cancellation methods are employed to suppress spatially coherent interference in the sidelobes of an antenna pattern. Composed of a primary element, or main beam, signal corrupted by interference and noise together with a set of auxiliary-array elements employed to sense the interference and noise fields, a weighted linear combination of the auxiliary-array element signals is used to suppress the corresponding interference components of the main beam. The optimal weight vector can be determined by a number of methods based on linear least squares estimation. Computations based on QR decomposition or modified Gram-Schmidt orthogonalization are known to be efficient and appropriate for real-time data domain implementation.

The number of coherent interfering sources is generally unknown and a practical system design must provide a sufficient number of auxiliary sensors to suppress the largest expected number of sources. When the number of auxiliaries exceeds the number of actual sources by a large margin, problems of reduced directivity of the adapted antenna pattern and increased noise level are encountered, particularly when the number of time samples available is relatively small. A robust solution is reduced rank principal component processing based on eigenanalysis of the auxiliary data [1,2]. A perceived computational penalty associated with a full eigenanalysis of the auxiliary array data makes this solution appear unattractive for real-time system implementation. Similarly, the eigenanalysis required for a variety of high-resolution spatial spectral estimation methods tends to inhibit their use.

This work was supported by the MITRE Sponsored Research program.

In these applications it is often unnecessary to obtain all of the eigenanalysis components; often a few dominant components will suffice to characterize the most troublesome sources. Reduced rank approximation of the array data matrix, only requires calculation of the p largest singular values and corresponding vectors [3]. Iterative methods are available for such computation [4]. Tufts and Melissinos have shown the efficiency of a power/deflation method to determine the dominant eigenvalues and eigenvectors of the sample covariance matrix in a frequency domain spectral estimation application [5]. We will show that this technique is equally effective for sensor array processing.

In our version of the power/deflation method, we operate on the array data matrix directly, alternately approximating the right and left singular vectors at each iteration. For rapid convergence at each power/deflation step we initially employ a retrodirective steering vector derived from a simple measurement of the complex coherence function of the array. Deflation is implemented as a simple orthogonal projection of the data matrix.

It is important in subspace estimation methods to be able to distinguish reliably between the signal (including interference) and noise subspaces. This is generally achieved by methods that rely on the spectral distribution of the eigenvalues [6]. From a spatial point of view, coherent sources and noise can be distinguished by their relative spatial coherence, information that is contained in the mutual coherence functions that we measure after each deflation.

An important attribute of the algorithm is its computational simplicity. Aside from the normalization required for each eigenvector estimate, the algorithm consists almost entirely of matrix/vector products and these are readily implemented in linear systolic arrays. We have found this simple algorithm to be remarkably effective for suppressing interference observed in actual signals recorded from the individual elements of HF antenna arrays. It provides an accurate estimate of the singular values, but is less accurate for approximating individual eigenvectors. Approximation of the left singular vectors is poor. The calculated eigenvector estimates, however, form an orthonormal set that spans a subspace that is close to the subspace spanned by the actual eigenvectors, as measured by the canonical angles between subspaces [7]. Since adaptive spatial processing only involves projection onto the orthogonal complement of the interference subspace, it is this measure that is important rather than the accuracy of estimating individual eigenvectors.

2. ADAPTIVE BEAMFORMING FUNDAMENTALS

Assume an array of N omnidirectional antenna elements whose outputs are coherently combined to form a narrow beam in a desired direction. Assume that T complex digital samples, representing an analytic signal, are recorded from each array element and let X denote a $T \times N$ matrix of elemental array data in which the j th column, x_j , consists of T samples recorded from the j th element. Let w_q be the $N \times 1$ steering vector used to form and point a beam in the desired direction. Assume that $M < N$ of the array elements are also employed as the auxiliary elements of an adaptive sidelobe canceller. Let A represent the auxiliary data matrix and let w be its adaptive weight vector. Denoting the main beam output as $y = Xw_q$, the sidelobe canceller output is expressed as $z = y - Aw$ where the least squares estimate of w can be obtained by minimizing $z^H z$ (superscript H denotes conjugate transpose). The adaptive weight vector is denoted as

$$w = (A^H A)^{-1} A y \quad (1)$$

The adapted output is expressed as

$$z = y - A(A^H A)^{-1} A^H y = P_A^\perp y \quad (2)$$

where $P_A^\perp = I - A(A^H A)^{-1} A^H$ is an operator that projects the main beam vector y onto the orthogonal complement of the vector subspace spanned by the columns of A .

Let $A = U S V^H$ be the singular value decomposition of A . After a reduced rank approximation, the adapted output may be expressed as

$$z_p = (I - U_p U_p^H) y \quad (3)$$

where U_p is a matrix consisting of the p left singular vectors corresponding to the p largest singular values of A .

Next, suppose that all of the array elements are sensed as auxiliary elements and that reduced rank principal component approximation is used to select the number of degrees of freedom for adaptive sidelobe cancellation, in effect choosing the auxiliary element outputs in the eigenspace rather than the element space. It follows directly from (1) and the SVD of X that the adapted auxiliary weight vector can be determined as the projection of the quiescent weight vector onto the vector subspace spanned by the columns of V_p , the reduced rank right singular vectors,

$$w_p = V_p V_p^H w_q \quad (4)$$

V_p consists of the columns of V , resulting from the SVD of X , which correspond to the p largest singular values. The adapted output can be expressed as

$$z_p = X(I - V_p V_p^H) w_q \quad (5)$$

We see from (5) that we may interpret the orthogonal projection operator, $(I - V_p V_p^H)$, either as an operator used to modify the quiescent steering vector or as a spatial filter applied to the array data matrix to remove the interference components from the elemental signals prior to beamforming.

In adaptive nulling applications and in a variety of eigenstructure-based direction-of-arrival algorithms, a key step is determination of the subspace projection operator $(I - V_p V_p^H)$. Iterative methods designed to extract only a few of the dominant components will often suffice. The algorithm we describe below is a data-domain version of a standard power/deflation method for extracting dominant eigenvectors [4].

3. ITERATED PRINCIPAL COMPONENTS ALGORITHM

Let X be the $T \times N$ data matrix to be analyzed and let its SVD be expressed as

$$X = \sum_{i=1}^N s_i u_i v_i^H \quad (6)$$

where the singular values are indexed by decreasing size, $s_i \geq s_{i+1}$. Choose any vector

$$\tilde{v}_1 = a_1 v_1 + \sum_{j=2}^N a_j v_j, \quad \sum_{j=1}^N |a_j|^2 = 1 \quad (7)$$

where $a_1 \neq 0$. Then

$$X \tilde{v}_1 = a_1 s_1 u_1 + \sum_{j=2}^N a_j s_j u_j \quad (8)$$

and

$$\mathbf{X}^H(\mathbf{X}\tilde{\mathbf{v}}_1) = a_1 s_1^2 (\mathbf{v}_1 + \sum_{j=2}^N \frac{a_j}{a_1} \frac{s_j^2}{s_1^2} \mathbf{v}_j). \quad (9)$$

After k iterations of successive multiplication by \mathbf{X} and \mathbf{X}^H we obtain the estimate

$$b_k \hat{\mathbf{v}}_1 = a_1 s_1^{2k} (\mathbf{v}_1 + \sum_{j=2}^N \frac{a_j}{a_1} (\frac{s_j}{s_1})^{2k} \mathbf{v}_j). \quad (10)$$

The error term declines rapidly with the number of iterations when $s_1 > s_j$ and it is also reduced by a starting vector that is already close to \mathbf{v}_1 .

After k iterations we can normalize, obtaining $\hat{\mathbf{v}}_1$, and deflate \mathbf{X} by the orthogonal projection

$$\mathbf{X}^{(2)} = \mathbf{X}(\mathbf{I} - \hat{\mathbf{v}}_1 \hat{\mathbf{v}}_1^H) \quad (11)$$

so that $\mathbf{X}^{(2)} \hat{\mathbf{v}}_1 = 0$. We then repeat the power iteration using the deflated data matrix to obtain an estimate $\hat{\mathbf{v}}_2$ of the second eigenvector. We then deflate $\mathbf{X}^{(2)}$, obtaining

$$\mathbf{X}^{(3)} = \mathbf{X}^{(2)}(\mathbf{I} - \hat{\mathbf{v}}_2 \hat{\mathbf{v}}_2^H) \quad (12)$$

which is orthogonal to both \mathbf{v}_1 and \mathbf{v}_2 , and repeat the process. At each power step we estimate the singular values as

$$s_i^2 = \hat{\mathbf{v}}_i^H \mathbf{X}^{(i)} \mathbf{X}^{(i)H} \hat{\mathbf{v}}_i \quad (13)$$

which we can monitor. Deflating by orthogonal projection guarantees that the estimates $\hat{\mathbf{v}}_1, \hat{\mathbf{v}}_2, \dots, \hat{\mathbf{v}}_p$ are mutually orthogonal.

The accuracy of approximation is aided by choosing an initialization vector $\tilde{\mathbf{v}}_1$ that is already close to the eigenvector being estimated. We have found it effective to start with a retrodirective steering vector calculated from a measurement of the complex mutual coherence across the array. Fundamental to all adaptive phased array processing is the phase distribution across the array resulting from one or more incident wavefronts. While this phase information is embedded in the eigenvectors, it can also be estimated directly from a computation of the complex coherence function [8]. Let one of the array elements be used as a reference and denote its analytic signal vector as $\mathbf{x}_r = \mathbf{a}_r e^{j\phi_r}$ where \mathbf{a}_r is a complex vector of T samples and $e^{j\phi_r}$ is a scalar, multiplying each of the components of \mathbf{a}_r , representing the stationary wavefront phase at the r th element. Similarly, let $\mathbf{x}_k = \mathbf{a}_k e^{j\phi_k}$ represent the analytic signal vector observed at the k th element. We form the zero-lag cross correlation between the reference signal and each of the other elemental signals to obtain the complex coherence function

$$\mathbf{x}_r^H \mathbf{x}_k = \mathbf{a}_r^H \mathbf{a}_k e^{j(\phi_k - \phi_r)}. \quad (14)$$

The real part of (14) measures the mutual coherence across the array and the complex exponential $e^{j(\phi_k - \phi_r)}$ describes the phase distribution. The phasor $e^{j(\phi_r - \phi_k)}$ can be used as a retrodirective steering vector that matches the phase of the impinging wavefronts. An improved estimate of the steering vector can be obtained by actually forming a retrodirective beam and using the beamformed output as a new reference in a second measurement of the complex coherence function. The process can be repeated if necessary.

In the iterated principal components algorithm we measure the complex coherence function after each deflation of the array data matrix. As we will see, the corresponding mutual coherence functions provide useful side information that can aid the discrimination between the coherent source and noncoherent noise subspaces. As the coherent source components are stripped away by deflation, the mutual coherence functions become more impulsive.

4. PERFORMANCE EXAMPLES

We will illustrate the iterated principal components algorithm with two examples. Our first example will illustrate adaptive nulling of atmospheric transient noise observed in the signals recorded from a narrow band 82-element linear HF antenna array. Figure 1 shows an 8.5 second duration (16384 samples) analytic signal envelope received from a single element (number 41) tuned to the 30-meter band. Transient noise occurring between 1 and 2 seconds and again between 6 and 7 seconds is plainly evident. We first analyzed a 64-sample record containing the large transient at 1.9 seconds. In applying the iterated principal components algorithm we used four power iterations after each deflation and employed a retrodirective steering vector for initialization that used one beamforming iteration in its estimation. Table 1 compares the singular values computed using a full SVD based on LINPACK with those estimated using the iterated algorithm. The rolloff of the singular values is in close agreement. Figure 2 shows the normalized mutual coherence using element 41 as a reference; the mutual coherence falls gradually across the array and the low spatial frequency suggests a small angle of incidence with respect to boresight. Figure 3 shows the normalized mutual coherence after the ninth deflation; the revealing feature is the impulsive character suggesting that after nine deflations the remaining energy is spatially noncoherent.

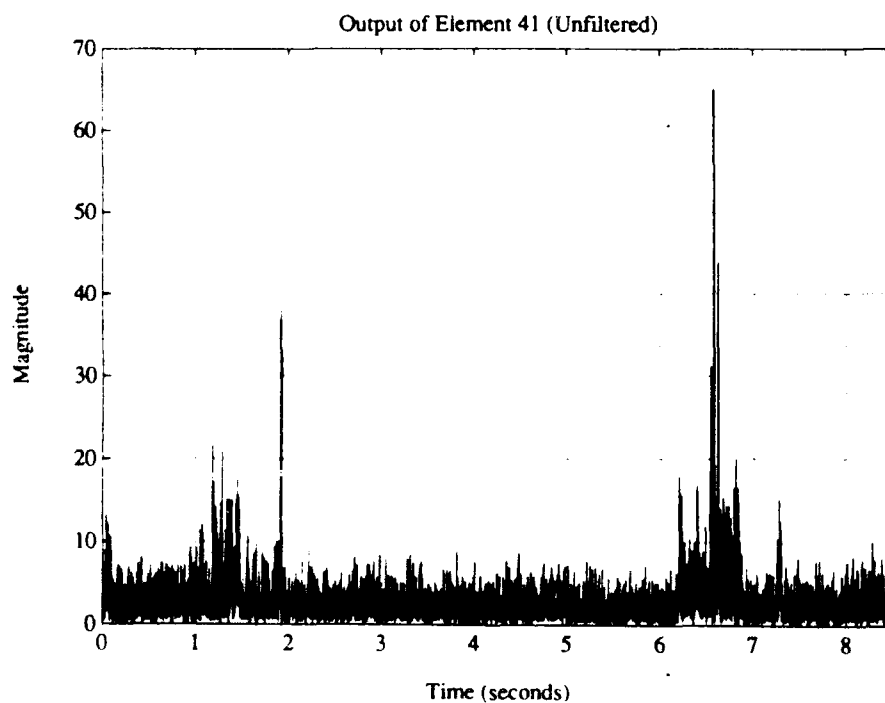


Figure 1. Narrowband HF array example. Envelope detected output of element 41.

Table 1. Narrowband HF Array (largest 16 singular values)

<u>LINPACK</u> <u>ZSVDC</u>	<u>ITERATED</u> <u>ALGORITHM</u>	<u>LINPACK</u> <u>ZSVDC</u>	<u>ITERATED</u> <u>ALGORITHM</u>
721.2977	721.2816	70.7203	72.3032
521.7135	521.7357	54.8268	54.4552
182.5159	179.1683	51.2389	51.2665
144.4880	148.3494	44.8159	44.9306
127.1940	122.7303	41.8515	40.0940
107.1745	112.5506	38.5397	38.3638
88.0332	87.2924	36.2363	37.0364
73.8818	73.2500	33.9341	33.8594

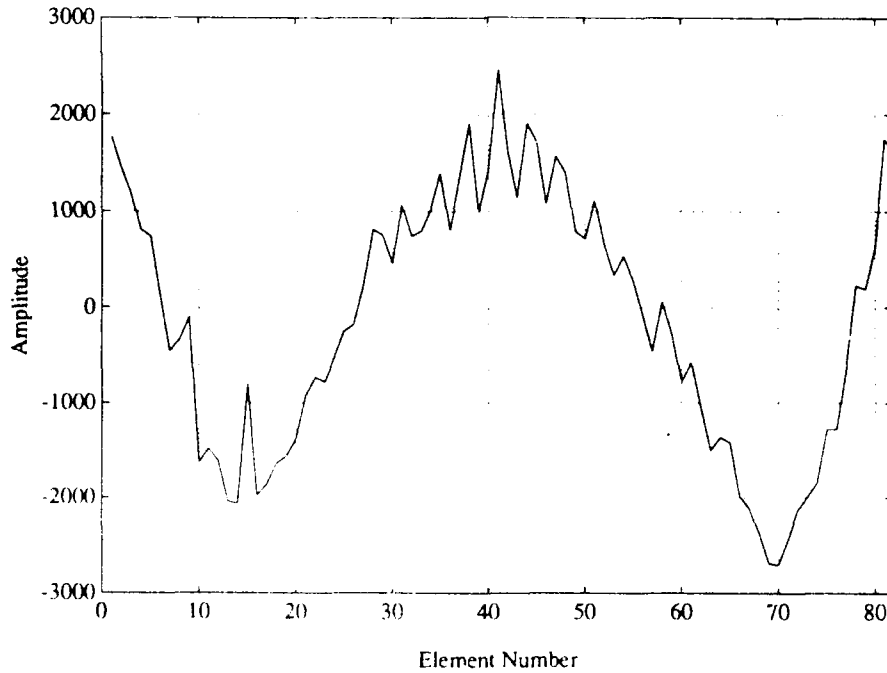


Figure 2. Narrowband HF array example. Mutual coherence using element 41 as a reference (solid line).

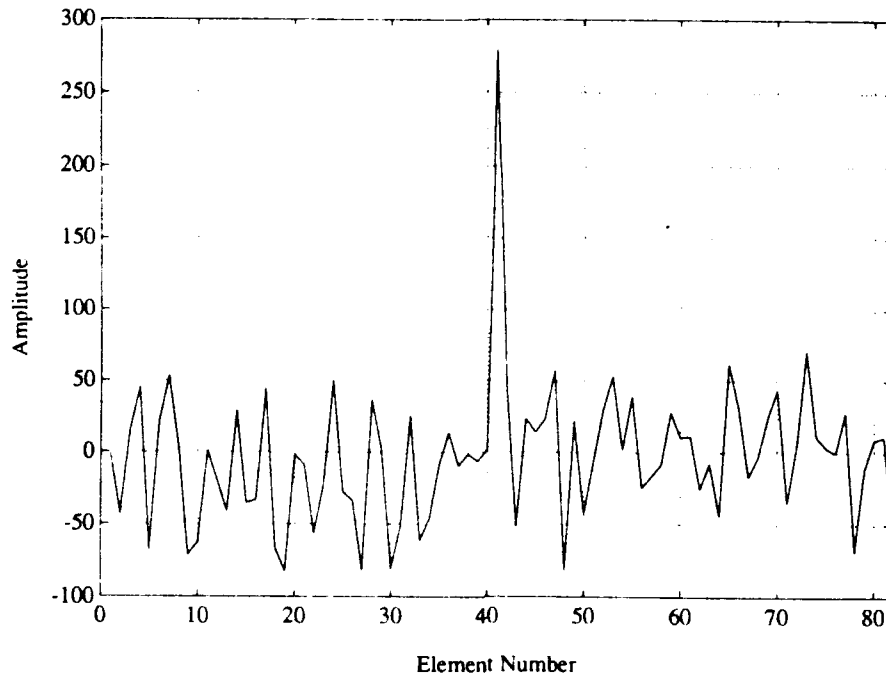


Figure 3. Mutual coherence after 9th deflation (dashed line).

The same analysis was applied to the large transient at 6.6 seconds. Similar behavior was observed in the mutual coherence estimates and the decay of the singular values. In each case we selected five principal components for the reduced rank approximation. A spatial filter was constructed as the product of the orthogonal projection operators obtained from each transient analysis and applied to the entire 16,384-sample data matrix. Figure 4 shows the filtered output of element 41. Comparison with figure 1 shows reduction of the transient noise. The suppression was nearly the same as when the spatial-filter was obtained using the full LINPACK SVD.

The second example is taken from a computer simulation of a 64-element narrow band linear array designed to test the algorithm when several of the singular values are nearly equal. Four sources at different incidence angles were simulated with the received powers adjusted to equalize three of the singular values. Table 2 compares the singular values resulting from analysis of a 256-sample array data record using the iterated algorithm with those obtained from a full SVD using LINPACK. The rolloff is similar, including the plateau where the values are nearly equal. Figure 5 shows the pre- and post-filter output spectra employing a spatial filter designed from the iterated algorithm with a rank-4 approximation. The suppression of the sources is equivalent to that obtained from the rank-4 filter designed using the LINPACK SVD.

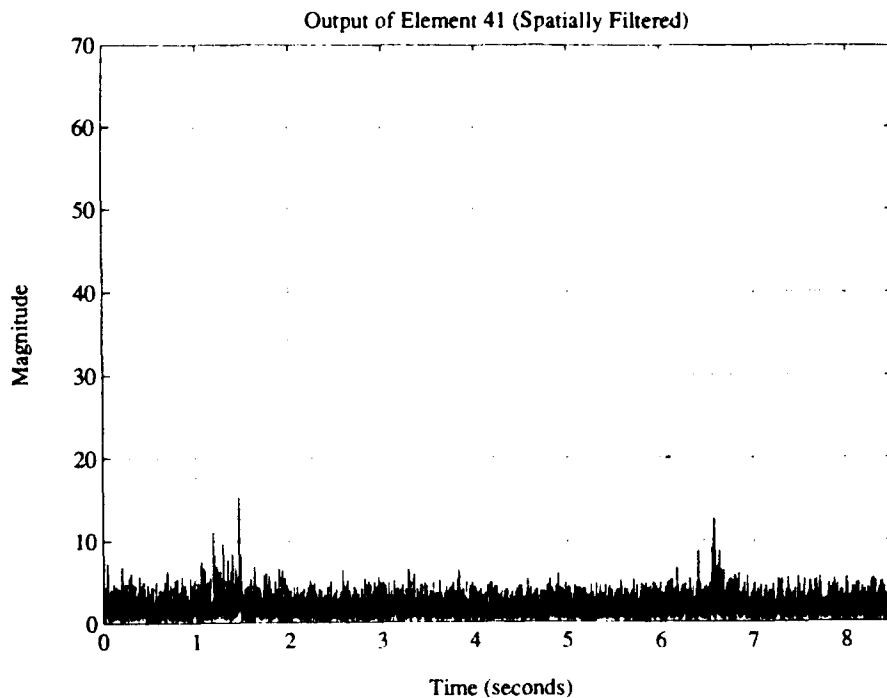


Figure 4. Narrowband HF array example. Spatially filtered output of element 41.

Table 2. Computer Simulated 64-element Array (largest 16 singular values)

<u>LINPACK</u> <u>ZSVDC</u>	<u>ITERATED</u> <u>ALGORITHM</u>	<u>LINPACK</u> <u>ZSVDC</u>	<u>ITERATED</u> <u>ALGORITHM</u>
340.8877	340.8877	0.5702	0.5677
109.9218	109.4461	0.5578	0.5507
107.9417	108.0722	0.5496	0.5424
105.2986	105.6597	0.5415	0.5293
0.7734	0.7592	0.5364	0.5346
0.6001	0.6011	0.5270	0.5370
0.5927	0.5592	0.5223	0.5167
0.5836	0.5582	0.5144	0.5111

These examples illustrate the ability of the iterated algorithm to approximate the singular values of the data matrices and to approximate the interference subspaces adequately enough for adaptive spatial filtering, and by implication, for direction finding using an eigenstructure method such as MUSIC. Approximation of the individual eigenvectors is relatively poor, but as we noted earlier, the important consideration is approximation of the signal subspace. For each example we calculated the canonical angles between subspaces by calculating the singular values of the matrix formed as the Hermitian outer product of the matrix of approximated eigenvectors with the matrix of eigenvectors calculated using the LINPACK routine. In both cases, the deviation from unity singular values, which would indicate very close approximation, was small.

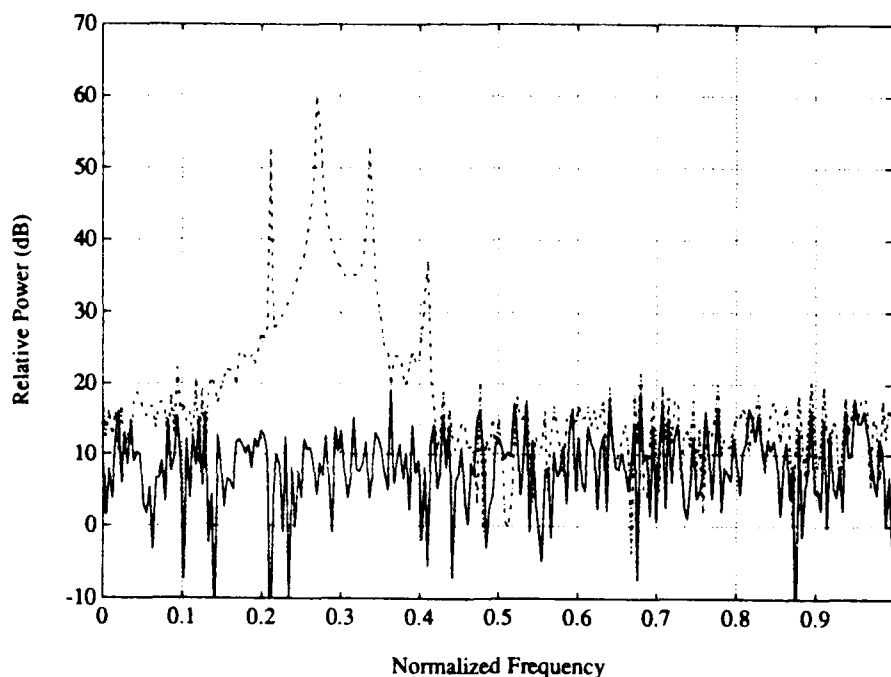


Figure 5. Computer simulated 64-element array example. Unadapted power spectrum (dashed line). Spatially filtered power spectrum (solid line).

5. COMPLEXITY OF IMPLEMENTATION

The computational complexity of the algorithm can be assessed by counting the number of required complex multiply-accumulate operations. We will assume two iterations to estimate the retrodirective steering vectors used for initialization followed by four power iterations and deflation. We will assume a $T \times N$ data array and p principal components to be estimated.

The complex coherence function requires TN operations, both for computing the function and forming a beam; since these computations are required for each principal component estimated, $3pTN$ are required, aside from normalization of the steering vector components. Four power iterations to estimate each eigenvector requires an additional $8pTN$ operations followed by pTN operations to estimate the eigenvalues. After normalization of the eigenvector estimates, $2pTN$ operations are required to deflate the data matrix. A small number, $2pN$, of operations are used to project the quiescent weight vector, followed by TN operations to produce the adapted output. The sum of these amounts to $(14p+1)TN+2pN$ complex multiply-accumulate operations. This compares favorably with $O(2TN^2+4N^3)$ operations required for a full SVD using the Golub-Reinsch method [9]. It is competitive with $O(T(N^2+N))$ operations required for modified Gram-Schmidt orthogonalization and it provides the additional benefits of a reduced-rank principal components estimate. The algorithm is structurally simple, allowing most of the operations to be carried out in linear systolic arrays.

6. CONCLUSION

In this paper we have endeavored to show that an iterated principal components method is practical for real-time adaptive array processing. Three main points were made. 1) The power/deflation method of principal components analysis is an effective and computationally simple means of signal subspace estimation that can be used in adaptive nulling and direction finding applications. 2) A retrodirective steering vector derived from a complex coherence measurement of each deflated data array matrix provides an appropriate initialization for each sequence of power iterations. 3) The mutual coherence functions obtained after each deflation provide useful side information to help in the discrimination between signal and noise subspaces.

REFERENCES

- [1] W. F. Gabriel, "Using Spectral Estimation Techniques in Adaptive Processing Antenna Systems," *IEEE Trans. Antennas and Propagation*, AP-34:291-300 (1986).
- [2] D. O. Carhoun, R. A. Games, R. T. Williams, "A Principal Components Sidelobe Cancellation Algorithm," *Proceedings 24th Asilomar Conference on Signals, Systems and Computers* (1990).
- [3] D. W. Tufts, R. Kumaresan, I. Kirsteins, "Data Adaptive Signal Estimation by Singular Value Decomposition of a Data Matrix," *Proc. IEEE*, Vol. 70 (June 1982).
- [4] J. H. Wilkinson, "The Algebraic Eigenvalue Problem," Clarendon Press, Oxford (1965).
- [5] D. W. Tufts and C. D. Melissinos, "Simple, Effective Computation of Principal Eigenvectors and their Eigenvalues and Application to High-Resolution Estimation of Frequencies," *IEEE Trans. Acoustics, Speech, and Signal Processing*, ASSP-34:1046-1053 (1986).
- [6] M. Wax and T. Kailath, "Detection of Signals by Information Theoretic Criteria," *IEEE Trans. Acoustics, Speech, and Signal Processing*, ASSP-33:387-392 (1985).
- [7] G. W. Stewart, "Perturbation Theory for the Singular Value Decomposition," *Second International Workshop on SVD and Signal Processing*, U. of Rhode Island (June 1990).
- [8] M. Born and E. Wolf, "Principles of Optics," Pergamon Press, London (1960).
- [9] G. H. Golub and C. F. VanLoan, "Matrix Computations," Johns Hopkins University Press, Baltimore (1983).

FOCAL ARC PATTERN MEASUREMENTS

Peter R. Franchi and Harvey Tobin

Rome Laboratory
Electromagnetics & Reliability Directorate
Hanscom Air Force Base, Massachusetts 01731

ABSTRACT:

Problems exist with the measurement of large aperture antennas due to the far field requirement. This paper discusses a new method to measure a phased array at about 1/10 the normal far field. The basic idea involves focusing the test array at probe antenna a distance R away from the aperture, and then measuring an antenna pattern by moving the probe antenna on a constant focal arc given by $R \cos(\theta)$. This arc minimizes phase aberrations due to defocusing error. To minimize the amplitude errors, the pattern of the probe antenna is carefully matched in order to compensate for the $1/R$ variation induced amplitude error. The application of this technique will enable arrays to be measured in anechoic chambers, allowing convenient classified testing, while avoiding the effects of weather, and will reduce the risks inherent in the high power testing on transmit. The results of a computer simulation is presented that characterizes the validity and limitations of the technique.

INTRODUCTION:

Traditional antenna measurements use $2D^2/\lambda$ as a criteria for measuring an antenna under test (AUT) in the far field, where R is the distance from the AUT to a point in space, D is the aperture size of the AUT, and λ is the operating wavelength. Problems arise when D becomes large, which increases the distance R , therefore more real estate is needed to measure the far field antenna pattern.

Development over the years has led to techniques to measure the far field pattern of the AUT on smaller ranges. Using a smaller range reduces outside interference, eliminates testing time due to poor weather conditions, and provides the option of doing classified testing. Many of the previous smaller range techniques eliminate or lessen these problems. There are however, other problems with these techniques. For example, transformation from near field probing to the far field requires many sample points, the large size and high surface tolerance requirements of a reflector restricts the use of a compact range.

This paper describes a technique to measure the far field antenna pattern over a 100° angular sector that is 1/10 the size of the conventional far field range, but with errors comparable to the errors one would expect from a far field range.

APPROACH:

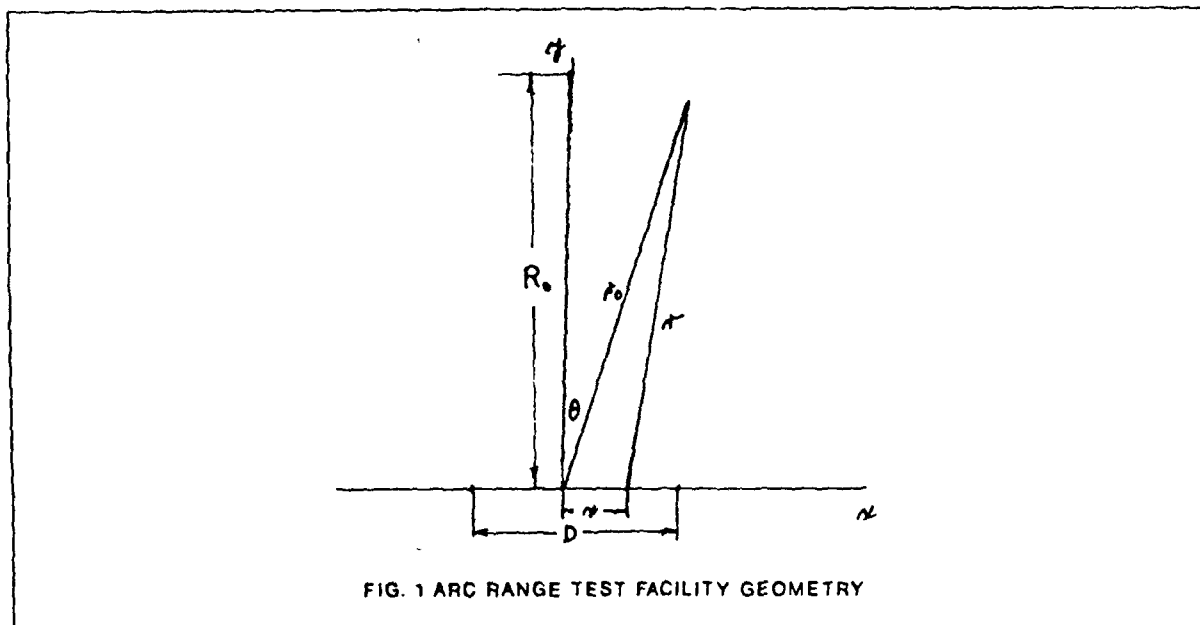
The accepted standard for an antenna to be measured in the far field is given by $2D^2/\lambda$. This criteria is an approximation, and there exists an inherent phase error of $\lambda/16$. This phase error is accepted since having no error would require the antenna being tested to be infinitely removed from the probe antenna.

In the expansion of the distance R given by

$$R = R_0 - r \cos(\theta) + \frac{r^2 \sin(\theta)}{2R_0} + \frac{r^3 \sin^2(\theta) \cos(\theta)}{2R_0^2} + \dots \quad (1)$$

when the quadratic term $\frac{x^2 \sin^2(\theta)}{2R_0}$ has an error of $\lambda/16$, then the error due to the cubic, fourth, and higher order terms are reduced by factors proportional to $\frac{D}{R}$, $\frac{D^2}{R^2}$, etc. If the quadratic term could be set to zero, the minimum range would now be set allowing the much smaller cubic term to grow to $\lambda/16$, and this would occur at a much smaller range. The effects of other type of errors such as amplitude error, fourth order error, elevation plane error etc., must be monitored to insure these errors do not exceed the cubic error term.

The method of eliminating the quadratic term involves focusing the AUT at some distance R , which is much less than the far field distance. An antenna pattern measured by scanning the array will be a duplicate of the far field pattern for only a small range of angles. To scan beyond this arbitrary angle the array must be repeatedly refocused, if the probe antenna remains a constant distance from the AUT. Reducing this distance as the test probe rotates yields no quadratic error. This basic point is the fundamental condition for this technique. This point can be more easily understood from the derivation of the phase from the test array to the probe antenna. The configuration is shown in Figure 1, where D is the length of the AUT, θ is the angle from broadside to the probe antenna, and R_0 the distance from the center of the array to the probe.



A general expression describing the field at the probe horn due to the array is given by,

$$E(\theta) = C \int f(x) G(x, \theta) e^{jkr(x, \theta)} dx \quad (2)$$

where C is a constant, $f(x)$ is the aperture distribution, $G(x, \theta)$ is the pattern of the probe antenna as a function of θ and $r(x, \theta)$ the distance from an arbitrary point on the test array to the probe antenna. Writing $r(x, \theta)$ in the usual series expansion form given by

$$\begin{aligned} r(x, \theta) &= (r_0^2 + x^2 + 2xr_0 \sin(\theta))^{1/2} \\ &= r_0 + \frac{(x^2 + 2xr_0 \sin(\theta))r_0}{2r_0^2} - \\ &\quad \frac{(x^2 + 2xr_0 \sin(\theta))^2 r_0}{8r_0^4} \\ &\quad - \frac{(x^2 + 2xr_0 \sin(\theta))^3 r_0}{16r_0^6} + \dots \end{aligned} \quad (3)$$

combining terms,

$$r(x, \theta) = r_0 + x \sin(\theta) + \frac{x^2(1 - \sin^2(\theta))}{2r_0} - \frac{x^3(\sin(\theta) - \sin^3(\theta))}{2r_0^2} + \dots \quad (4)$$

If r_0 is large enough compared to D the quadratic, cubic and higher order terms can be ignored (maximum edge error is $\frac{\lambda}{16}$ when $x = \frac{D}{2}$). So for the phase only the first two terms apply and the constant term R_0 has no effect. If also in equation (2) $G(x, \theta)$ is always aimed at the center of the array then (2) can be written as,

$$E(\theta) = cG(x, \theta) \int_{-D/2}^{D/2} f(x) e^{jkx \sin(\theta)} dx \quad (5)$$

This is the conventional far field expression and is a Fourier transform of the aperture distribution $f(x)$. If quadratic focusing at R_0 is added to equation (1) the result is

$$E(\theta) = C \int_{-D/2}^{D/2} f(x) G(x, \theta) e^{j\left(\frac{-x^2}{2R_0} + r(x, \theta)\right)} dx \quad (6)$$

Ignoring the terms higher than the cubic, the phase expression will now be

$$k \left(r(x, \theta) - \frac{x^2}{2R_0} \right) = k \left(r_0 + x \sin(\theta) + \frac{x^2 \cos^2(\theta)}{2r_0} - \frac{x^2}{2R_0} - \frac{x^3 \sin(\theta) \cos^2(\theta)}{2r_0^2} \right) \quad (7)$$

The quadratic term is,

$$\frac{x^2}{2} \left(\frac{\cos^2(\theta)}{r_0} - \frac{1}{R_0} \right) \quad (8)$$

If $r_0 = R_0 \cos^2(\theta)$, the quadratic term is zero, and the cubic term becomes the dominant error source. Since it is smaller than the quadratic term by $\frac{D}{2r_0}$, the range requirement can be reduced close to this ratio.

A comparison of the ranges indicates the potential for considerable reduction in range requirement. For the conventional far field $\frac{R}{\lambda} = 2\left(\frac{D}{\lambda}\right)^2$ and for this case $\frac{R}{\lambda} = \left(\frac{D}{\lambda}\right)^{\frac{3}{2}}$.

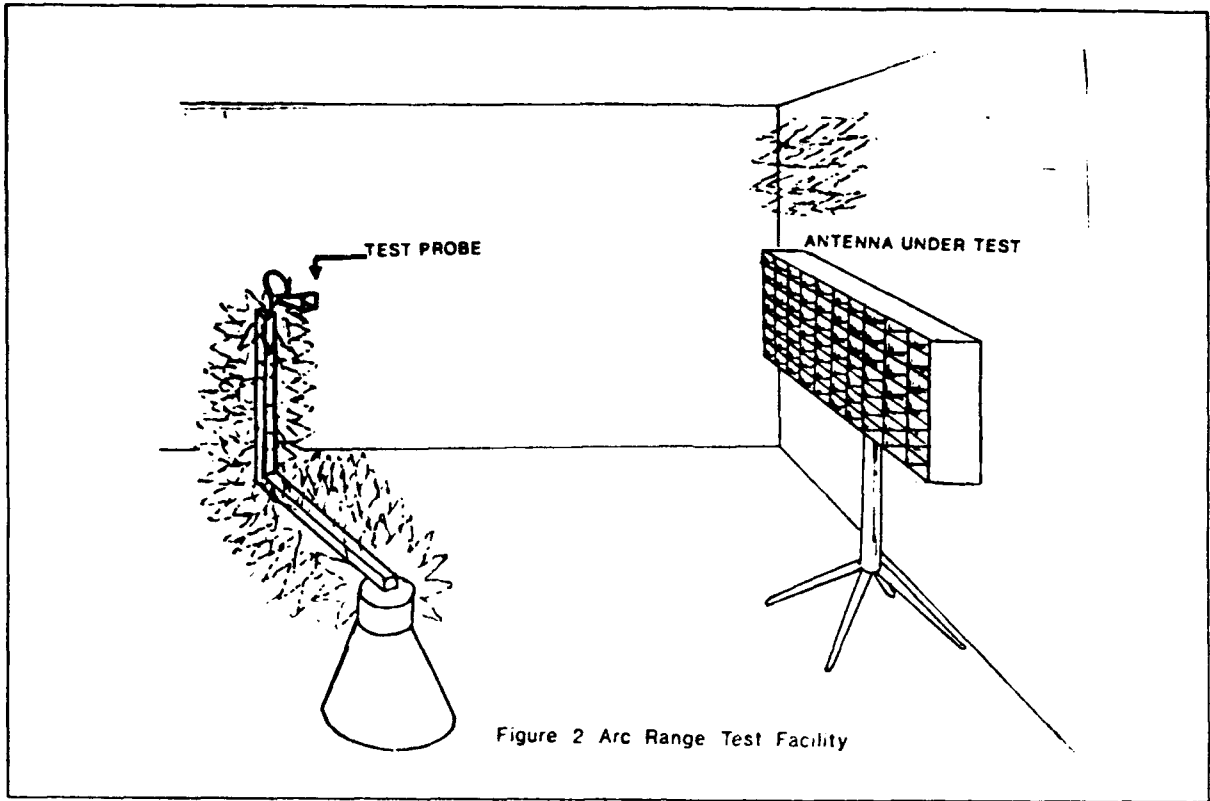
D/λ	R/λ	R/λ (reduced)	Reduction Ratio
20	800	89	90
40	3200	253	12.6
60	7200	465	15.5

Table 1:

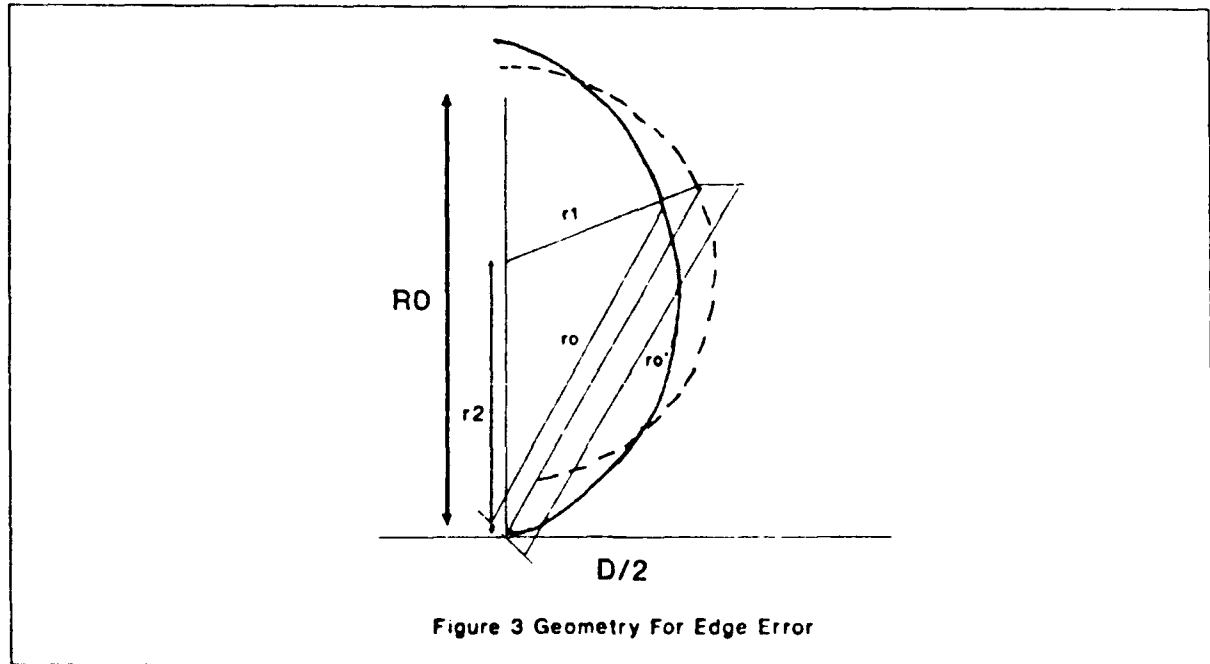
The significant range reduction indicated by TABLE 1 cannot be realized unless the amplitude variation in the denominator of equation (1) is compensated by the horn pattern $G(x, \theta)$ so that the ratio is constant.

The constant focus arc, defined by $R_0 \cos^2(\theta)$ is not on a circle as it would be for $R_0 \cos(\theta)$. Since it is very convenient to measure antenna patterns by either rotating the transmit antenna or the receive antenna, we choose to approximate the constant focus arc by a circular arc that will be a good match over a large angular range, about 100°. This practical convenience adds some small additional error, which is analyzed in the following section.

Figure 2, is a schematic drawing of the measurement arrangement. The transmit antenna shown here is a horn mounted away from and above the rotating mount. Absorber covers the vertical and horizontal supports to minimize any reflections from them.



In Figure 3, r_1 is the distance from the antenna being measured to the center of rotation of the mount, r_2 is the distance from the transmit antenna (phase center) to the mount, and r'_0 the distance from that phase center to the center of the antenna being tested.



Only the changes in path length to various points on the test array caused by using a circular arc instead of the actual constant focus arc will affect the antenna pattern, not the total array phase which will change as a function of θ . The maximum error will occur at the array edges.

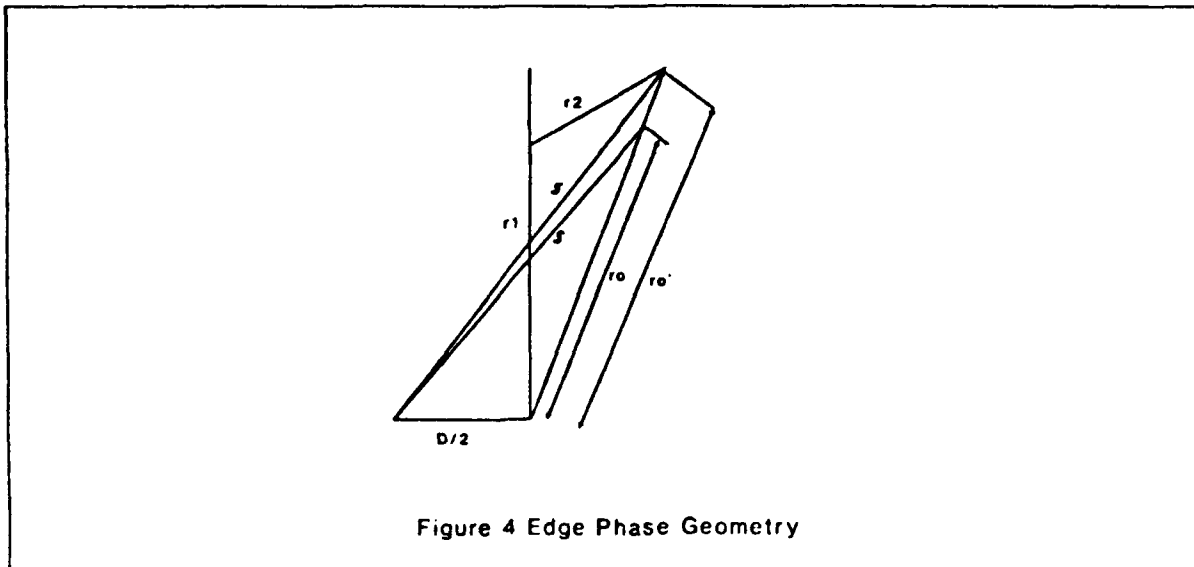


Figure 4 Edge Phase Geometry

In Figure 4, s is the distance from a point on the constant focus arc to one edge of the test antenna and s' the corresponding point (same angle) on the circular arc to the same edge. From the law of cosines,

$$s^2 = \left(\frac{D}{2}\right)^2 + r_0 + Dr_0 \sin(\theta) \quad (9)$$

and,

$$s'^2 = \left(\frac{D}{2}\right)^2 + r_0' + Dr_0' \sin(\theta) \quad (10)$$

The edge of the array, at $(x = \frac{D}{2})$, would have a phase, ψ , relative to that at the center of $\psi = \frac{kD^2}{8R_0}$. This phase shift focuses the array at R_0 where

$$\begin{aligned} \psi_0 &= \frac{2\pi}{\lambda}(s - R_0) \sin \theta = 0 \\ &= 2\pi \left(\left(\frac{D}{2}\right)^2 + R_0^2 \right)^{\frac{1}{2}} - R_0 \\ &= \frac{2\pi D^2}{8\lambda R_0} \end{aligned} \quad (11)$$

The phase error at the edge of the antenna due to the use of the circular arc is

$$\begin{aligned} \delta &= k(s' - r_0') - \psi_0 \\ &= k \left(\left(\frac{r_0'^2 + D^2}{4 + r_0' D \sin(\theta)} \right)^{\frac{1}{2}} - r_0' \right) - \frac{\pi D^2}{4\lambda R_0} \end{aligned} \quad (12)$$

Expanding for $r_0' \gg \frac{D}{2}$,

$$\begin{aligned} \delta &= k \left(r_0' + \frac{D \sin(\theta)}{2} + \frac{D^2}{8r_0'} - \frac{D^2 \sin^2(\theta)}{8r_0'^2} - r_0' \right) - \frac{\pi D^2}{4\lambda R_0} \\ &= \frac{2\pi}{\lambda} \left(\frac{D \sin(\theta)}{2} + \frac{D^2 \cos^2(\theta)}{8r_0'} \right) - \frac{\pi D^2}{4\lambda R_0} \end{aligned} \quad (13)$$

$$r_2^2 = r_1^2 + r_0'^2 - 2r_1r_0' \cos(\theta) \quad (14)$$

$$r_0' = r_1 \cos(\theta) + (r_2^2 - r_1^2 \sin^2(\theta))^{\frac{1}{2}} \quad (15)$$

$$\delta = \frac{2\pi D \sin(\theta)}{\lambda} + \frac{2\pi D^2 \cos^2(\theta)}{8\lambda r_0'} - \frac{\pi D^2}{4\lambda R_0} \quad (16)$$

Where $\frac{\pi D \sin(\theta)}{\lambda}$ is just the linear term. Now

$$\delta = \frac{\pi D^2}{4\lambda R_0} \left(\frac{R_0 \cos^2(\theta)}{r_0'} - 1 \right) \quad (17)$$

$$\delta = \frac{\pi D^2}{4\lambda R_0} \left[\frac{R_0 \cos^2(\theta)}{r_1 \cos(\theta) + (r_2^2 - r_1^2 \sin^2(\theta))^{\frac{1}{2}}} - 1 \right] \quad (18)$$

If $r_1 = .53R_0$ and $r_2 = .41R_0$ the maximum error is

$$\frac{\pi D^2 (.076)}{4\lambda R_0} \quad (19)$$

With the conventional definition of far field range $R = \frac{2D^2}{\lambda}$, δ can be calculated to be,

$$\delta = \frac{\pi (.076) R}{8R_0} = \frac{.03R}{R_0} \quad (20)$$

for $\frac{R}{R_0} = 10$ or a maximum phase deviation of about $\frac{\lambda}{20}$.

RESTRICTIONS ON THE MAXIMUM ARRAY HEIGHT:

If the height h , of the antenna being tested is held to the limit imposed by the far field condition for the minimum range of r_0 , the elevation plane phase variation as r_0 and θ vary will have little or negligible effect on the azimuth antenna pattern. This condition is

$$\frac{2h^2}{\lambda} \leq r_0(\min) = .41R_0 \quad (21)$$

If R_0 is set at 1/10 the far field distance given by

$$R_0 = \frac{2D^2}{\lambda} (1/10) \quad (22)$$

then

$$\frac{2h^2}{\lambda} \leq .41R_0 = \frac{2D^2}{10\lambda} (.41) \quad (23)$$

or

$$h \leq .2D \quad (24)$$

This restriction of the height (that it be less than 1/5 the width of the tested antenna) can be loosened by the application of some focusing in elevation. By applying elevation plane focusing at a middle range $.73R_0$, in between the maximum range R_0 at $\theta = 0^\circ$ and the minimum range $.41$ at $\theta = 50^\circ$, the height restriction increases to nearly 1/3 of D . The elevation edge phase is given by,

$$\begin{aligned} \psi_e &= k \left\{ [(0.73R_0)^2 + \left(\frac{h}{2}\right)^2]^{\frac{1}{2}} - .73R_0 \right\} \\ &\approx \frac{.73\pi h^2}{2\lambda R_0} \text{ for } R_0 \gg h \end{aligned} \quad (25)$$

Keeping the edge phase to $\frac{\lambda}{16}$ or less,

$$\left[(.41R_0)^2 + \left(\frac{h}{2}\right)^2 \right]^{\frac{1}{2}} - .41R_0 - \frac{\psi_e}{k} \ll \frac{\lambda}{16} \quad (26)$$

$$\frac{h^2}{.41(2.4)R_0} - \frac{.73h^2}{4R_0} \leq \frac{\lambda}{16} \quad (27)$$

$$\frac{h^2}{\lambda} \leq \frac{R_0}{1.96} \quad (28)$$

If again, $R_0 = \frac{2D^2}{\lambda} (\frac{1}{10})$

$$\frac{h^2}{\lambda} \leq \frac{D^2}{9.8\lambda} \quad (29)$$

or,

$$h \leq .32D \quad (30)$$

In short, if no elevation plane focusing is used, the height of the antenna being tested must be $\leq 1/5$ the width of that antenna. If elevation plane focusing is used, then the maximum height is just under $1/3$ the width. Finally, if the elevation plane had the same focus as the azimuth plane the height would be just over $1/4$ the width.

AMPLITUDE COMPENSATION:

In equation (2) the ratio $G(x, \theta)$ to $r(x, \theta)$ must approximate a constant or the measured field on the focal arc will not resemble the actual far field. For example if $G(x, \theta)$ represented the pattern of an isotropic radiator ($G(x, \theta) = k$), but $R(x, \theta)$ even for $R(x = 0)$ varies from R_0 to $.41R_0$. The far field pattern would, therefore, be too high for angles near $q50^\circ$. Let the test antenna or horn be directed at the center of the rotating mount and make an angle α with the center of the antenna being tested. The effects of amplitude errors inherent in the measurements are now considered. Since the distance from the center of the array being tested (r_0) varies as a function of scan angle θ , there must be a corresponding pattern variation from the test horn or the pattern of the array being tested will change incorrectly as θ varies. This is equivalent to keeping $\frac{G(x, \theta)}{r(x, \theta)}$ in equation (2) constant. It is relatively easy to match the $1/R_0$ variation with the choice of small feed array or horn, but the resulting variation across the array being tested is the unavoidable amplitude error. The test horn will always face the center of the mount and will make an angle α with the center of the array being tested. If the horn pattern is approximated by $a = b \cos(\theta)$ and by the law of sines, $\sin(\alpha) = \frac{r_2}{r_1} \sin(\theta)$. If $\frac{a+b \cos(\alpha)}{r_0'} = k$, and k is 1, then

$$a + b \cos(\alpha) \approx r_0' = r_1 \cos(\theta) + (r_2^2 - r_1^2 \sin^2(\theta))^{\frac{1}{2}} \quad (31)$$

so

$$a + b \cos(\alpha) \approx r_2 \cos(\alpha) + r_1 (1 - \frac{r_2}{r_1} \sin(\alpha))^{\frac{1}{2}} \quad (32)$$

for small angles,

$$\begin{aligned} a + b \cos(\alpha) &\cong r_2 (1 - (\frac{\alpha^2}{2})) + r_1 (1 - \frac{r_2^2}{r_1^2}) \\ &\cong r_1 + r_2 (1 - (\frac{\alpha^2}{2})) (1 + (\frac{r_2}{r_1})) \\ &\cong r_1 + r_2 \cos(\alpha) (1 + \frac{r_2}{r_1})^{1/2} \end{aligned} \quad (33)$$

so,

$$a \cong r_1 = .53 \quad (34)$$

$$b \cong r_2 = .41 \quad (35)$$

$$c \cong (1 + (r_2 + r_1))^{\frac{1}{2}} = 1.33 \quad (36)$$

Since these values are derived only for small angles, minor modifications are required to cover larger ranges of α . If $a = .56$, $b = .38$, and $c = 1.4$, then these values match r' to within 2% over the 100° range. A better match is possible with a different choice of constant horn pattern representation, but this choice is clearly close enough. The choice of the correct pattern of the test probe antenna will provide a very close match to the $1/r_0$ variation to the center of the array being tested, but because of the changing distances from the

edges of this array to the test probe, there will be an amplitude variation across the array aperture that will change as a function of scan angle θ , beginning with,

$$s' = \left(\left(\frac{d}{2} \right)^2 + (r')^2 + D r' \sin(\theta) \right)^{\frac{1}{2}} \quad (37)$$

as before,

$$r_0' = r_1 \cos(\theta) + (r_2^2 - r_1^2 \sin^2(\theta))^{\frac{1}{2}} \quad (38)$$

from the law of sines,

$$\Delta \alpha = \sin^{-1} \left(\frac{d \cos(\theta)}{2s'} \right) \quad (39)$$

The comparison between the test probe pattern at $\alpha + \delta \alpha$ and the $\frac{d}{r'}$ variation across the aperture can now be made, and is shown in Table II.

D/R_0	α°	0.0	13.0	26.2	40.3	56.2	82.0
	θ°	0.0	10.0	20.0	30.0	40.0	50.0
.125		.948	.909	.832	.718	.562	.313
		.934	.892	.814	.699	.544	.288
.075		.945	.912	.843	.737	.589	.344
		.936	.905	.836	.729	.583	.335
0		.940	.922	.866	.772	.634	.398
		.940	.921	.865	.770	.635	.401
.075		.943	.938	.894	.812	.685	.458
		.938	.932	.888	.804	.678	.453
.125		.948	.952	.916	.842	.781	.500
		.934	.936	.901	.824	.702	.482

Table 2:

The maximum error is at $\theta = 50^\circ$ at the closest edge of the array to the test probe and in the table is given by $(.288/.313)^2$ or $.7dB$. This effect is equivalent to a phase error of about $\frac{\lambda}{75}$. For an array aperture of $.5R_0$, this error is only equivalent to $\frac{\lambda}{22}$. By keeping the aperture to less than $\frac{R_0}{3}$ ($1dB$ amplitude error) along with other restrictions the total error effects should be kept to $\frac{\lambda}{16}$ or less. If the testing of a large physical array (but electrically small) were required the aperture requirement could be reduced to $\frac{R_0}{2}$ since the phase error contributions would then be negligible.

SUMMARY OF ERROR CONDITIONS:

The various error conditions for the previous section can be summarized. First the error limitations due to the cubic or coma error term is,

$$\frac{R_0}{\lambda} \geq 1.36 \left(\frac{D}{\lambda} \right)^{\frac{2}{3}} \text{ for scan angles of } \pm 50^\circ \quad (40)$$

second the error limitation due to the approximation of a circular arc instead of the actual focal arc is

$$\frac{R_0}{\lambda} \geq .152 \left(\frac{D}{\lambda} \right)^2 \quad (41)$$

The range limitations will be less than that caused by the cubic term for array sizes less than 80λ . In practical terms the cubic error range limitation will dominate. Third, the amplitude error distortions across the array will be

$$\frac{R_0}{\lambda} \geq \frac{2.5D}{\lambda} \quad (42)$$

Again for all arrays greater than 3 or 4 wavelengths, the range limitations is determined by the cubic error term or,

$$\frac{R_0}{\lambda} \geq 2.5 \frac{D}{\lambda} \text{ for } \frac{D}{\lambda} < 3.5 \quad (43)$$

$$\frac{R_0}{\lambda} \geq 1.36\left(\frac{D}{\lambda}\right)^{\frac{1}{2}} \text{ for } 3.5 < \frac{D}{\lambda} < 80 \quad (44)$$

$$\frac{R_0}{\lambda} \geq .152\left(\frac{D}{\lambda}\right)^2 \text{ for } \frac{D}{\lambda} > 80 \quad (45)$$

Finally, there is a height restriction on the array which is (with focusing in elevation) $h \leq .32D$. If a very low sidelobe range were required, for example $\frac{6D^2}{\lambda}$, the equivalent edge phase error would be $\frac{\lambda}{48}$. With this error condition the low sidelobe conditions give the following range and height restrictions,

$$\frac{R_0}{\lambda} \geq \frac{3.3h}{\lambda} \text{ for } \frac{D}{\lambda} < 2 \quad (46)$$

$$\frac{R_0}{\lambda} \geq 2.36\left(\frac{h}{\lambda}\right)^{\frac{1}{2}} \text{ for } 2 < \frac{D}{\lambda} < 27 \quad (47)$$

$$\frac{R_0}{\lambda} \geq .456\left(\frac{h}{\lambda}\right)^2 \text{ for } \frac{D}{\lambda} > 27 \quad (48)$$

So for large low sidelobe arrays the limitation is caused by the use of the circular arc. The height restriction remains basically unchanged since smaller edge phase allowance is offset by the greater range now required.

SIMULATION RESULTS:

The development of a computer simulation helped to determine the validity of the theoretical results. A 64 element array with $\frac{\lambda}{2}$ spacing is used as the antenna under test (AUT). Two different cases were simulated. The first placed the test probe at 19.2ft from the AUT. The distance corresponds to 1/8 the actual far field distance for a 64 element array operating at X-band. Figure 5 represents the far field of the AUT. To bring about real testing conditions a 30dB Taylor amplitude distribution with .4 random amplitude errors was applied to the array elements. Figure 5 also contains the pattern measured in the near field, with the probe antenna rotated on the constant focal arc given by $R_0 \cos(\theta)$, with $R_0 = 19.2\text{ft}$, $R_1 = 10.0\text{ft}$ and $R_2 = 8.0\text{ft}$, and the pattern measured with the probe antenna rotated on a constant radial arc with $R_0 = 19.2\text{ft}$, $R_0 = 0\text{ft}$, and $R_0 = 19.2\text{ft}$. The results show there is good agreement at all angles for the focal arc patterns and fairly good agreement for the constant radius patterns.

Since those results showed good agreement, it was decided to reduce the range to 1/16 of the far field difference. Figure 6 represents the corresponding patterns with the focal arc having $R_0 = 9.6\text{ft}$, $R_1 = 5.0\text{ft}$, and $R_2 = 4.0\text{ft}$. Larger deviations are more visible. Beyond 20° or 25°, the constant radius patterns are not close to the actual far field patterns.

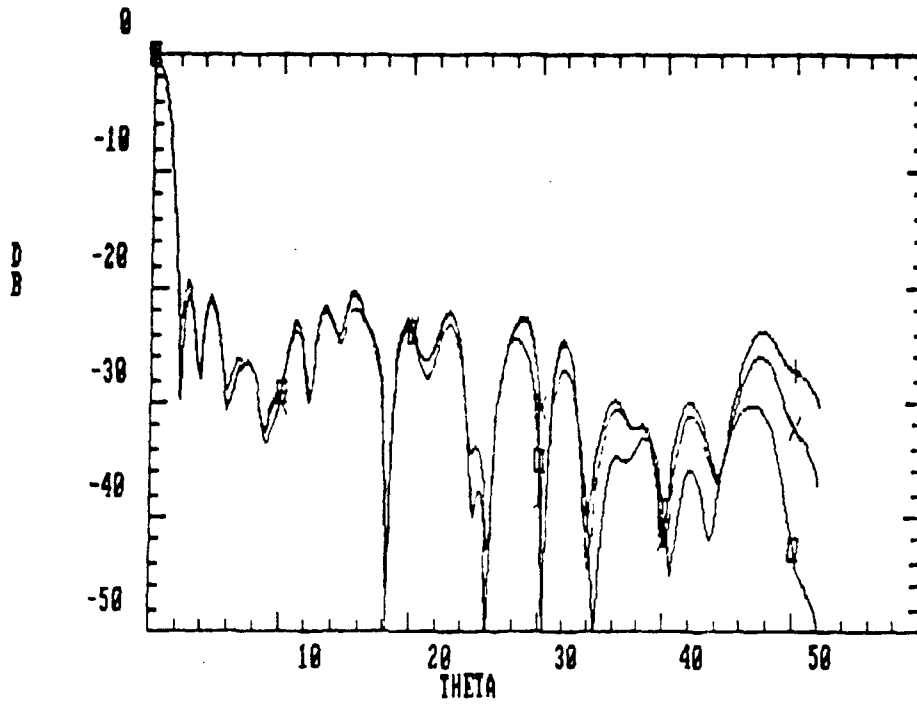


Figure 5 Comparison Plots, +FF, xF.Arc,oR.Arc
30dB Random Taylor R = 19.2'

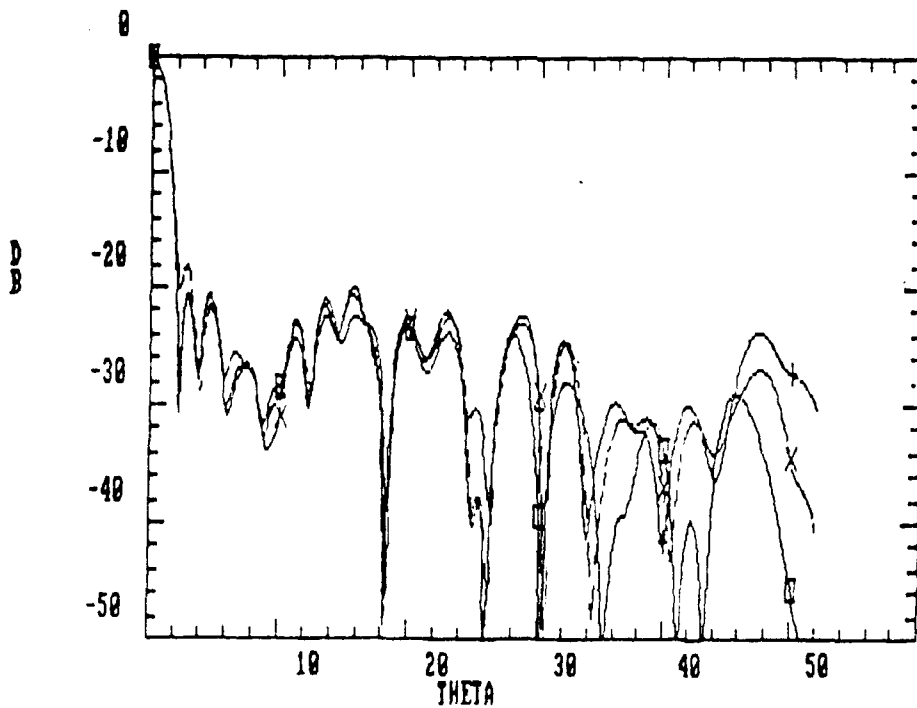


Figure 6 Comparison Plots, +FF, xF.Arc,oR.Arc
30dB Random Taylor R = 9.6'

CONCLUSION:

It is possible to reduce the distance required to measure the far field pattern of an array by close to an order of magnitude. This reduction results from swinging the probe antenna on an arc that approximates the perfect focal arc defined by $r = R_0 \cos(\theta)$. A probe on this arc will give no quadratic or defocusing error. The dominant error term now becomes the cubic error term or coma. For scan ranges of $\pm 50^\circ$ the reduction in far field distance is given by this error term, and R_0 the short range requirement is the conventional far field range R_{FF} reduced by $\frac{2}{3}(\frac{\lambda}{D})^{\frac{1}{2}}$ or,

$$R \leq R_{FF} \frac{2}{3} \left(\frac{\lambda}{D} \right)^{\frac{1}{2}} \quad (49)$$

A 45λ array would, for example, require 1/10 the conventional far field distance. The use of this type of range imposes some restrictions. These include the array to be focused at R_0 , the height be less than 1/3 the width and the probe antenna pattern match the $1/r$ distance variation. With these restrictions very good results were obtained by computer simulations.

REFERENCES:

1. P.R. Franchi, H.Tobin, "Technique to Measure Large Arrays" Proc.1988 Antennas and Applications Symposium, RADC TR-89 - 121 Vol II. ADA213815
2. P.R. Franchi, H.Tobin, "Technique to Measures Large Antenna Arrays that Contain Random Amplitude Errors" Proc. 89 Antennas and Applications Symposium, RADC TR-90 - 42 Vol II. ADA226022
3. A.J. Fenn. "A Near Field Technique for Phased Array Antenna Adaptive Nulling Performance Verification". MIT Lincoln Laboratory, Project Report SRT - 24, 13 November 1987.

ENGINEERING ANALYSES ASSOCIATED WITH THE DEVELOPMENT
OF AN AIRBORNE PHASED ARRAY RADAR ANTENNA

C. H. Tang
The MITRE Corporation
Bedford, MA 01730

This is an interim report to discuss a number of engineering problems aroused during the development of the Joint STARS radar antenna. These problems can be grouped in three engineering areas: design, test, and maintenance. The design consideration includes two major concerns of a large airborne radar antenna - thermal/vibration problems and airframe effects. The test consideration is represented by the problem of measurement accuracy of a short ground range and a plan for accurate in-flight pattern measurements. To facilitate the maintenance of the Joint STARS antenna, a number of operational problems that require some quantitative engineering guidelines are currently being studied.

Paper to be Presented at
The 1991 Antenna Applications Symposium
Allerton Park, Monticello, IL
25-27 September, 1991

1.0 INTRODUCTION

The Joint (U.S. Air Force and U.S. Army) Surveillance and Target Attack Radar System (Joint STARS) employs a multifunction radar which includes a multimode pulse doppler MTI and a Synthetic Aperture Radar (SAR). The side-looking radar antenna, which is housed in the belly of an E-8 aircraft (a converted Boeing 707), scans electronically in azimuth and rotates mechanically in elevation.

In order to meet the specified performance requirements, several unique hardware features are developed for the low sidelobe, precision beam-pointing and high phase coherency radar antenna system. The development and implementation of these radar antenna features necessitated an antenna risk reduction program and occupied a major portion of the full scale development program. During the full scale development, more engineering attentions are paid toward the integration of the radar antenna with the designated airframe. Two major areas of concern are the antenna thermal and vibration problems and the airframe effects. A fair amount of engineering effort was also spent on the antenna tests and the associated range quality questions. Since a true, high quality, far-field range was not available, various problems associated with the use of a short ground range were investigated together with the consideration of verifying test data through the use of a compact range. In addition, to meet the requirement for airborne pattern verification, a plan for accurate in-flight pattern measurement was proposed. The operational consideration of the Joint STARS radar antenna also motivated the study/analysis of a number of engineering problems. *These include the antenna built-in test/calibration, the antenna failure/repair criteria, and the depot-level antenna range requirements.* They are considered germane to the maintenance of Joint STARS.

In Section 2, various functions of the Joint STARS radar system and novel features of its antenna system will be briefly summarized. Specific design considerations of the radar antenna are discussed in Section 3. Three levels of design considerations are distinguished: the antenna architecture, its hardware implementation, and the integration of the antenna with the airframe. The first two

levels of the Joint STARS radar antenna design have been disclosed by Shnitkin^{1,2}. Here, the integration problem of the Joint STARS radar antenna system are discussed, after a few general comments on the different levels of design considerations.

Two examples of the test considerations are reviewed in Section 4. The problem of the short range antenna measurement accuracy is summarized in 4.1 and a plan for accurate airborne pattern measurements mentioned in 4.2.

2.0 JOINT STARS AND ITS RADAR ANTENNA

Joint STARS is designed to look deep into enemy territory, detecting and tracking moving and/or stationary targets such as tanks or personnel carriers, while flying in friendly air space. Major radar functions include a multimode pulse doppler MTI and a spot-light SAR.

To achieve the MTI performance and target locations accuracy requirements, a three-port antenna architecture was selected. Pairwise DPCA (Displaced Phase Center Antenna) cancellation of mainlobe clutter between adjacent subarrays leaves two clutter-free residue channel containing moving target information. These channels then form a virtual interferometer, the baseline of which is equal to that of the original subarray spacing, and whose output provides a high accuracy measurement of target position. The information for FTI (Fixed Target Indicator) is provided by the spot-light SAR processing operations.

The Joint STARS radar antenna (24 x 2 ft) is a horizontally polarized, rectilinear lattice slot array. Each array element (called stick) is formed by a vertical column of in-line, vertical, broadwall slots in a custom designed, single-ridged waveguide cavity. The phase of each stick is controlled by a variable, non-reciprocal, latching ferrite phase shifter, in order to provide $\pm 60^\circ$ of azimuth beam scan, among other functions. The array face is formed by 12 lengthwise-contiguous subarray panels, which are attached to an aluminum trestle to form a rigid structure. A cross-section

of this box structure with all RF components within it is shown in Figure 1. This box structure is closed with end plates which transition to bearings, drives and trunion. The trunions are attached to the hardback. For each subarray, there is a dual-mode combiner, also custom designed, that provides two independent amplitude tapers for the corresponding elements. The front port of each of these combiners is attached to a symmetrical, 12-way, waveguide manifold that forms the full-aperture, sum illumination mode. The rear ports of each of these sets of four contiguous subarray combiners are attached to three, 4-way, corporate manifolds, respectively, which form the three nonoverlapping, subaperture, sum illuminations.

The full-aperture sum manifold is always used for transmission, while either the full-aperture or subaperture manifolds can be used for reception. As mentioned above, the received signals from the three subarray ports are used for the MTI processing, while the SAR processing operates on the signal from the full-aperture.

A more detailed description of the Joint STARS radar antenna can be found in Reference 1, in which the following five novel antenna features were discussed.

- Collinear slotted array aperture
- Switchable dual-mode aperture
- Multifunction electronic phasing
- Automated phase alignment
- Triple temperature compensation

3.0 DESIGN CONSIDERATIONS - ANTENNA SYSTEM INTEGRATION

3.1 General Comments

From the perspective of a full-scale-development program, it is of interest to identify an hierarchy of antenna design activities that facilitates the monitoring of progress of a system product. Based on the experience with the development of the Joint STARS radar antenna, three levels of antenna design activities are

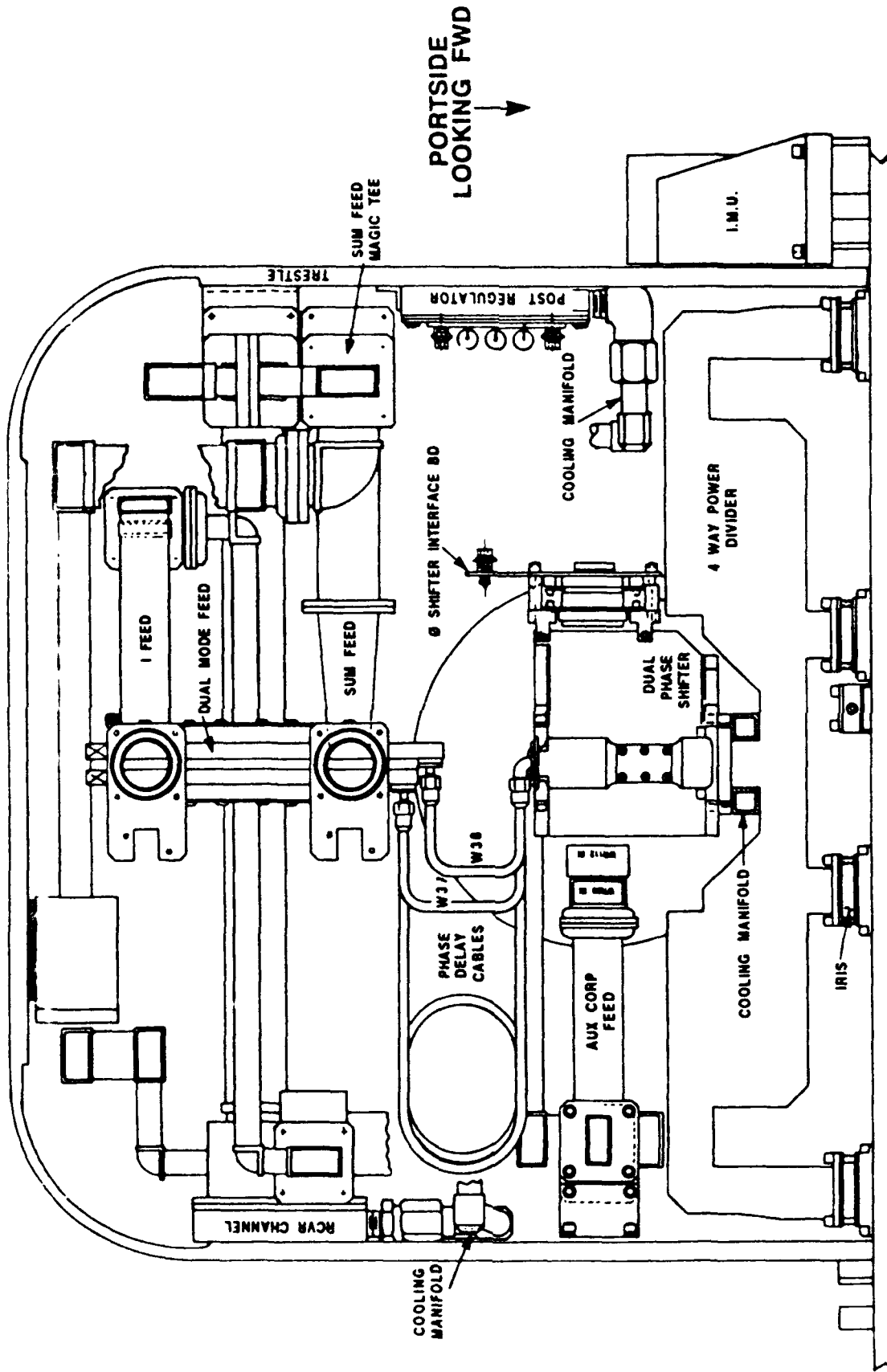


Figure 1. A Cross-Sectional Drawing of Joint STARS Radar Antenna

distinguished: (A) Antenna architecture, (B) Hardware implementation, and (C) Antenna system integration. With reference to the Joint STARS program, a few general comments are given for each of these design levels.

Antenna architecture is a realization of the antenna design concept which consolidates all the antenna-related system requirements in a self-consistent manner. The system performance requirements are then translated into a set of antenna specifications. For the Joint STARS radar, important antenna performance specifications include gain (MTI and SAR ranges), sidelobe level (MTI clutter cancellation, EMC, and ECCM), beamwidth (angle measurement for MTI and beam spoiling for SAR), and radar bandwidth. In addition, two other requirements, the on-aircraft antenna alignment and motion compensations required for the proper operations of MTI and SAR, are of significant importance. Thus, this level of antenna design effort plays a decisive role in the total antenna development cycle. Also, it should be emphasized that the design concept is not complete without the feature of an effective antenna built-in test, a required feature of most modern radar antennas.

For high performance radar systems, the selection of a realizable antenna architecture often requires the development of a prototype antenna system or a risk reduction program on the hardware implementation of critical antenna components. Even then, the final antenna design may still be a result of a number of design iterations.

For the Joint STARS radar antenna, critical components include the radiating stick, the dual-mode combiner, and the BIT-CAL system which consist of a travelling wave waveguide feed coupled to the back of each stick for RF signal injection and a processing procedure, converting the phase shifter settings to the array pattern information (for details see reference 2).

Hardware implementation is the process of converting the antenna architecture into a detailed antenna design. The effort is usually divided into two tasks --

electrical design and mechanical design. Typically, the electrical considerations include: the antenna error and loss budgets, the evaluation of the array mutual couplings, and the antenna bandwidth limitation (which may cause signal distortion for large bandwidth signals or beam-pointing errors for small bandwidth signals). The mechanical design considerations include the detailed design of the antenna structure that is consistent with the requirements of the electrical performance and the various environmental factors, including size and weight constraints.

In the case of the Joint STARS radar, the antenna system integration involves three major concerns -- the radome effect, the airframe effect, and the antenna thermal and vibration problems arising from integrating the antenna and the radome with the E-8 fuselage. Specific considerations are highlighted in the following.

3.2 ANTENNA THERMAL AND VIBRATION PROBLEMS

Due to more severe environmental and varied operational conditions, airborne radar antennas need to meet more stringent mechanical specifications. A number of structural/thermal deformation problems typically associated with a large airborne array antenna will be discussed.

In order for the antenna to properly perform its function, tight phase tolerances are placed on all its components. As a result of these requirements, the antenna face is manufactured to be flat within 0.020-inch over its 24-foot length, the slot-to-slot spacing is tightly controlled and the corporate feed line lengths are equalized. These conditions are disturbed when the antenna is operated under power. Heat generated by RF losses, control circuitry, and supplied by the Liquid Cooling System (LCS) cause differential expansion. Each corporate feed path lengthens in direct proportion to the temperature of each line. Each line now has a new length and a different phasing. The antenna face expands -- more in the center where high heat load exists than the ends. This causes a slot-to-slot variation. The antenna face is hotter than the trestle back rails and causes the entire structure to bend with the center of the antenna face moving out up to 0.3-inch relative to the ends in a

worst-case calculation. Attachment of the feed line from the rotary joint and the attachment of the corporate feed to the trestle at specific points initially caused twist of the antenna face, but these effects were eliminated by the use of thermal isolation shims at the attachment points.

Since the radome enclosing the radar antenna is not hermetically sealed and there is no ambient thermal control provision, the antenna thermal condition is thus also affected by the ambient temperature, which is characterized by the weather of the day of operation and the aircraft altitude.

The NASTRAN finite element (FE) model was utilized by Grumman (the Joint STARS prime contractor) and Norden (the radar subcontractor) to study various antenna structural aspects. These include bowing due to gravity loading, torsional vibratory motion due to drive motor excitations, and lateral, vertical and torsional vibratory motion due to boundary layer induced random vibration excitations.

Summarized in Table 1 are a list of structural and thermal effects and the corresponding compensation technique considered.

Using a linear array model, pattern calculations were performed to evaluate effects of various array structural deformations on the antenna pattern characteristics. The most noticeable effect on the patterns due to the array bowing is the broadening of the main beam. Within the deflection range expected, the bowing distortion has negligible effect on the antenna sidelobe level.

3.3 AIRFRAME EFFECTS

The effect of airframe scattering on the antenna performance is a general concern that must be taken into account in any airborne radar system design. This is particularly true for high performance radar systems requiring very low sidelobes and high precision beam pointing. A framework for the study of airframe effects is suggested in Table 2. Listed are four different electromagnetic effects and the

**Table 1.
Antenna Deformation Compensation Techniques**

Structure & Thermal	Deformation Effects	Compensation Considered
G Load Deflections	Array face bowing, slot misalignments	Bowing correction (Measure deflection and correct)
Vibration	Array face bowing, slot misalignments	Structure design No dynamic compensation considered
Temperature Gradients	RF and ambient Array face bowing Slot misalignment	Cooling design Bowing correction (Measure temperature & correct)
Trestle-Array Temperature Difference	Array bowing & twisting (also due to unbalanced motor torque)	Thermal structure design Bowing correction
In-plane Expansion	Stick-to-stick distance variations	Phase correction (Measure temperature & correct)
Feed Expansion	Sum feed phase errors	BIT injection (FFT and correct)
BIT W/G Expansion	BIT performance BIT accuracy	BIT correction (Measure temperature, compute BIT feed phase and calibrate)

Table 2
Airframe Effects on
Radar/Antenna Performance

EM Effects	Aircraft Structure	Radar/Antenna Performance	Method of Evaluation
Blockage	Wings and engine nacelles, transmission blockage, reception shadowing	Gain, beam width, beam pointing, sidelobe level, ECCM, EMC	Geometrical optics (GO), radar field of view, blockage equations
Reflection	Wing surface reflection, other multipath propagations	Reflection lobes, multipath interference, ECCM, EMC	Geometrical optics (GO), reflection equations
Refraction	Layered radome refraction	Beam shift, insertion phase, transmission loss & reflection	Radome spec-insertion phase, transmission & reflection, radome measurement, radome antenna measurements
Diffraction	Edge diffraction - wing and engine nacelles, creeping wave - fuselage and engines	Sidelobe level ECCM, EMC	Geometrical theory of diffraction (GTD) NEC - BSC flight measurements

corresponding airframe structures that cause the effect. For each effect, major antenna performance impacts are identified together with the method to be used for evaluating these impacts.

The primary airframe effect of concern is the airframe obstruction of the radar's field of view. The blockage-incurred amplitude error is systematic in nature. Its effect tends to overwhelm the underlying random phase errors and it results in higher close-in side lobes, in comparison with the pattern corresponding to the unobstructed aperture. Usually, the antenna gain reduction can be directly related to the percentage increase of blockage. However, the increase of peak sidelobes can not be so predicted, it depends on the antenna scan and aircraft pitch angles in addition to the percentage of blockage.

Major concern on the reflection effect may be expected to come from the wing surface. For the Joint STARS configuration, significant reflection lobes from the wing may occur in relatively large negative angles, which fall in the degradation allowance region allotted by the system specification. The concern for the diffraction effect is expected to be from various edges (hardback, wings, and engine nacelles) and curved surfaces (fuselage, wings, and engine nacelles). Major impact of these effects can be expected to be on the peak and average sidelobe levels.

The analyses of these various scattering mechanisms can provide valuable engineering information for a more effective radar system. For the Joint STARS radar development, airframe effects were studied to address a number of specific engineering problems.

- a. Relative radar antenna performances with respect to different airframes -- E-8 (Converted Boeing 707) vs. OV-10 (twin-propeller aircraft)

- b. Relative radar antenna performances with respect to different engines -- E-6 (CFM56) vs. E-8 (JT3D), the former has a larger diameter while the latter is longer in length.
- c. The effect of antenna location adjustment on the antenna performance.

Geometrical optics ray tracing procedures and geometrical theory of diffraction calculations were performed to provide quantitative results for these engineering problems.

3.3.1 BLOCKAGE BY ENGINE NACELLES AND WINGS

Using the geometrical optics theory, equations were derived for determining the blockage of antenna field-of view. Two different optical pictures were analyzed: (i) the receive picture - a plane wave incidence is assumed to project profiles the wing and engine nacelles on the antenna array plane for each look angle, and, (ii) the transmit picture -- the antenna phase center is used as the origin of transmit rays to determine the profiles of the wing and engine nacelles viewed by the antenna. These blockage pictures can be used to provide a definition of the degradation allowance region.

Based on the results of the ray trace analysis, array pattern calculations were performed for various look angles that incur blockage. In addition to the antenna gain and peak sidelobe level, the effect of aperture blockage in the Joint STARS interferometric angle measurement accuracy was studied.

It is found that blockage-induced interferometer errors are not proportional to the magnitude of blockage, but, rather are dependent upon the shadow geometry. If, for example, the shadow of the engine nacelle falls predominantly on the center subaperture, large interferometer errors are predicted. On the other hand, if the shadow produces equal blockage for subapertures, the error is small.

3.3.2 EVALUATION OF DIFFRACTION EFFECTS

To assess the effect upon the Joint STARS radar antenna patterns of the scattering from engines and wings, the OSU Basic Scattering Code was slightly modified and a complementary pattern synthesis code was written to allow the calculation of the scattering from structures in the near-field of a large array. The wing and two engines were modelled as a flat plate with two solid cylinders just below. Dimensions were obtained from available data.

To study the scattering mechanisms involved, GTD pattern calculations were performed for different sticks and subarrays. The calculated stick patterns show dips due to blockage by the engines (because of creeping wave diffraction around the bottoms of the engines, blockage is not total), and certain amount of forward scattering due to diffraction off the rims of the cylinders modelling the engines (plus some specular scattering off the flat ends of these cylinders). The angular locations of the dip and forward scattering vary as the stick position changes.

The OSU code allows computation of patterns for selected components of the problem (either structures or electromagnetic field components). Thus, the diffraction and reflection components can be calculated separately for comparison.

The array azimuth patterns were also calculated for various scan angles. The calculated scanned azimuth patterns show that as long as the antenna is not optically blocked by the aircraft structure, the airframe effect tends to increase the sidelobe relatively mildly (5 to 10 dB). When the antenna is directly blocked by the engine, the forward scattering lobe becomes larger than the mainbeam.

With a proper modelling of the aircraft structure, the GTD calculations can provide useful information on the increased levels of sidelobes and their locations for the assessment of ECCM and EMC problems.

4.0 EXAMPLE OF TEST CONSIDERATIONS

There have been many antenna test issues aroused during the Joint STARS radar system development. Two of these test consideration are mentioned here.

4.1 ASSESSMENT OF SHORT RANGE ANTENNA MEASUREMENTS

Since a good quality far-field range was not available to the contractor, a short (950') range at Norden was used for the Joint STARS antenna pattern measurements. The required quadratic phase correction of the range error is done through the radar antenna phase shifters.

To evaluate the feasibility, a number of analyses were performed to study various sources of measurement errors. These included (i) the effectiveness of the quadratic phase correction to compensate for field curvature, and (ii) the effect of the terrain reflection level of the range on the measurement accuracy. Using a simulation model, the two-dimensional array patterns were calculated to compare the far-field and compensated short range antenna array characteristics. These simulations included cases for different levels of array amplitude and phase errors and for various different antenna scan angles. For the range reflection problem, an analytical expression was derived for generating parametric curves showing the sidelobe level measurable for different measurement accuracies.

Based on these analyses, it was concluded that sidelobe levels can, in principle, be measured within an accuracy of ± 1 dB if the range can be made sufficiently clean. This requires a better than -58 dB effective reflectivity which is defined to represent the combined effect of interfering signal reductions due to the range reflectivity and the transmitting antenna sidelobe level. The measured range reflectivity is such that a very low sidelobe transmitting antenna was necessary.

The use of a very low sidelobe transmitting antenna introduced another problem. The range geometry and the required sidelobe level was such that an

amplitude taper of 1 dB across the aperture of the antenna-under-test was produced. Further simulations were performed to show that this causes an error of 3.6 dB in the first sidelobe. Other sidelobes are not significantly impacted.

Based on these assessments, a quality verification of the short range was recommended.

4.2 IN-FLIGHT PATTERN MEASUREMENT PLAN

The need to accurately measure in-flight airborne antenna patterns has become more urgent for modern high performance airborne radar systems. The measurement of airborne patterns is required in the Joint STARS system specification. To meet this requirement, a study was performed to address various requirements for such a measurement.³ An in-flight test plan is currently being developed and specified.

5.0 SUMMARY

This interim report summarized a number of antenna related engineering problems studied during the development of the Joint STARS radar system which is currently undergoing system tests. Three levels of antenna design considerations: antenna architecture, antenna hardware, and antenna system integration, were briefly discussed. Specific discussion focussed on the engineering problems of the Joint STARS radar antenna system integration. The emphasis was on determining the limitations of the antenna performance imposed by the antenna environmental effects.

ACKNOWLEDGEMENT

This work is supported by Electronic Systems Division (AFSC), Hanscom AFB, MA. The author also acknowledges contributions made by P. Hayes, G. A. Robertshaw, B. N. Suresh Babu and members of the MITRE Task Force Team on Joint STARS Radar Antenna Thermal and Vibration Designs, as documented in various MITRE reports.

LIST OF REFERENCES

1. Shnitkin, H. (1991), "A Unique Joint STARS Phased-Array Antenna" *Microwave Journal*, January, 1991, pp. 131-141.
2. Shnitkin, H. (1985), "Rapid In-flight Phase Alignment of an Electronically Phased-Scanned Antenna Array." *Phased Array 1985 - Symposium Proceedings*, pp. 293-302.
3. Tang, C. H. (1989), "Requirements for Accurate In-flight Pattern Testing." *11th Annual AMTA Symposium*, October 9-13, 1989, Monterey, CA.

**AN EFFICIENT, LOW COST METHOD OF MODIFYING THE E-3A ANTENNA
ELEVATION BEAM OFFSET ANGLE**

**D. P. Parrish
P. S. Hacker
R. K. Vogelsang
J. R. Stepanek
K. G. Ramsey**

September 25-27, 1991

**Prepared for
1991 Antenna Applications Symposium
Allerton Park
Monticello, Illinois**

**By
Westinghouse Electronic Systems Group
Design Engineering and Manufacturing Operations Divisions
Baltimore, MD 21203**

ABSTRACT

The E-3A antenna system employs electronic scanning in elevation in order to accomplish its mission. As part of a recent radar system performance upgrade effort, it was deemed necessary to change the elevation plane offset angle between the transmit and receive beams.

The electronic elevation scanning function for the antenna is effected on both transmit and receive by a set of very accurate ferrite rotary field phase shifters and associated analog and digital control circuitry. The transmit/receive elevation beam offset function is effected by a set of non-linear ferrite phase shifters which are located in a part of the antenna R. F. signal combining network which is dedicated to the receive function.

Since virtually all the E-3A antennas are now installed in aircraft with an accompanying radome, it was necessary to derive a modified elevation beam offset scheme since the normal factory procedure does not work satisfactorily in the presence of a radome, and the cost of removing an antenna from each aircraft in the USAF inventory and sending it back to an antenna range for the beam offset angle modification was prohibitive.

To this end, a new procedure for adjusting the antenna elevation offset angle, when mounted on the E-3A aircraft, was invented.

The new procedure, described in this paper, employs the very accurate performance of the transmit/receive rotary field phase shifters to calibrate the non-linear beam offset phase shifters in order to preserve antenna elevation plane sidelobe performance after the elevation beam offset angle change has been effected. This procedure is done in such a way that it also calibrates out radome errors, and aircraft and miscellaneous antenna range multipath error sources.

1. INTRODUCTION

The E-3A antenna has an elevation scan mode in which the receive beam lags the transmit beam in elevation as shown in figure 1.

Recently an operating mode was added to the E-3A system which required a change to the antenna transmit/receive elevation beam offset angle Θ_1 (of figure 1). This change, in theory, is a trivial one. It requires only that the antenna be taken back to the antenna range and the receive beam retuned, in the transmit/receive offset ("Squint") configuration.

The antenna has two primary operating configurations: "Squint" and "No Squint." The "Squint" configuration is employed when the antenna is rapidly scanned in elevation to reduce target return loss. The "No Squint" configuration is employed when the antenna main beam is "Stationary".

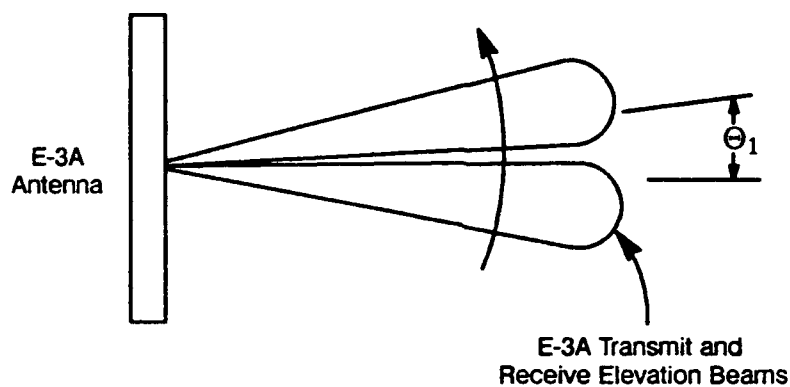


Figure 1. E-3A Antenna Elevation Scan Mode

The normal receive beam Squint configuration tuning operation, as performed on a far field antenna range, is effected by modulating the beam steering phase shifters and adjusting the beam offset phase shifters until a tuned radiator indication is received.

Figure 2 shows a block diagram of the E-3A antenna system.

The beam steering phase shifter, which is common to the transmit and receive paths, serves to scan the antenna beam (or transmit/receive beam pair, in the Squint configuration) in elevation while maintaining extremely tight phase accuracy in the elevation plane feed network of the antenna. This, in conjunction with tight feed network amplitude control achieved by the use of processor aided waveguide coupler manufacturing techniques, provides ultra low elevation plane sidelobes over the required elevation plane angular search/track volume.

The beam offset phase shifters are used as 1 bit devices which provide either a zero or desired non-zero value of Θ_1 (see figure 1). The beam offset phase shifters are receive-only devices and have a non-linear phase versus drive current characteristic.

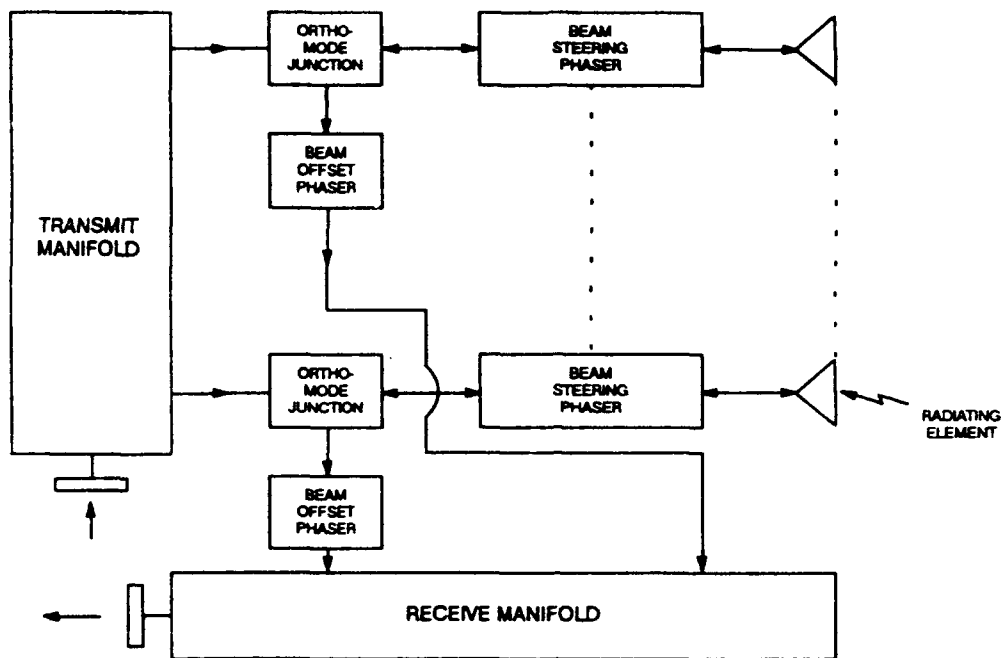


Figure 2. E-3A Antenna Block Diagram

Figures 3 and 4 show the phase versus drive characteristics for both the beam steering and the beam offset phase shifters. The beam steering phase shifter is very linear and can be used as a secondary standard for many phase calibration applications.

The beam steering phase shifter is a rotary field type which operates in magnetic saturation and derives its phase shift via the rotation of a quadripole magnetic field within the ferrite half wave plate shown in figure 5.

On transmit, the signals entering the beam steering (rotary field) phase shifters are vertically polarized. They are converted to right hand circular polarization in the non-reciprocal quarter wave plate. The circularly polarized signal is then phase shifted by varying the sine and cosine coils in a systematic fashion in the ferrite half wave plate. From there it enters the reciprocal quarter wave plate where it is converted from right hand circular polarization to vertical polarization and sent to the radiating aperture.

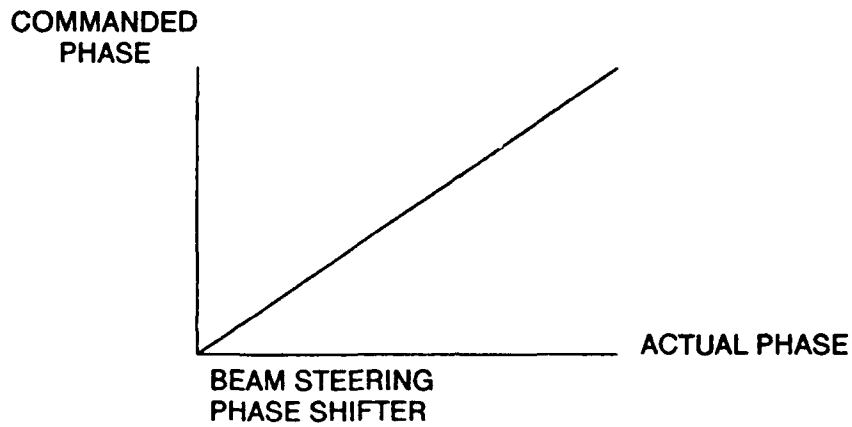


Figure 3. Beam Steering Phase Shifter Characteristics

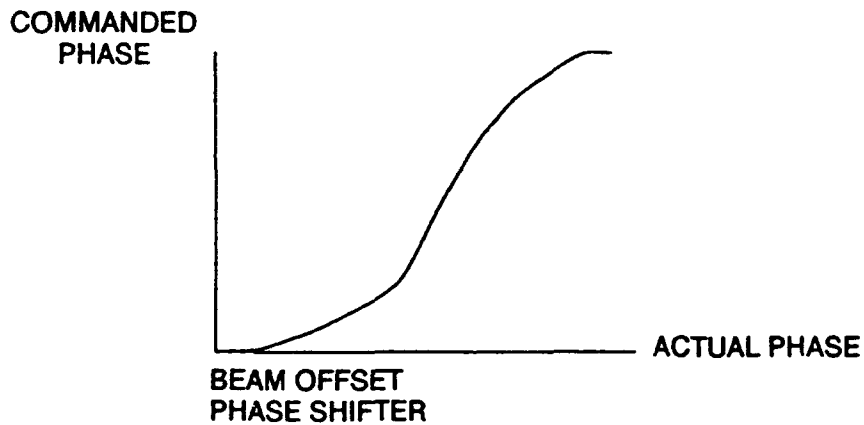


Figure 4. Beam Offset Phase Shifter Characteristics

On receive, just the opposite happens except that the non-reciprocal ferrite quarter wave plate converts the right hand circular polarizations from the ferrite half wave plate to horizontal polarization where the orthomode junctions delivers it to the beam offset phase shifters and the receive manifold.

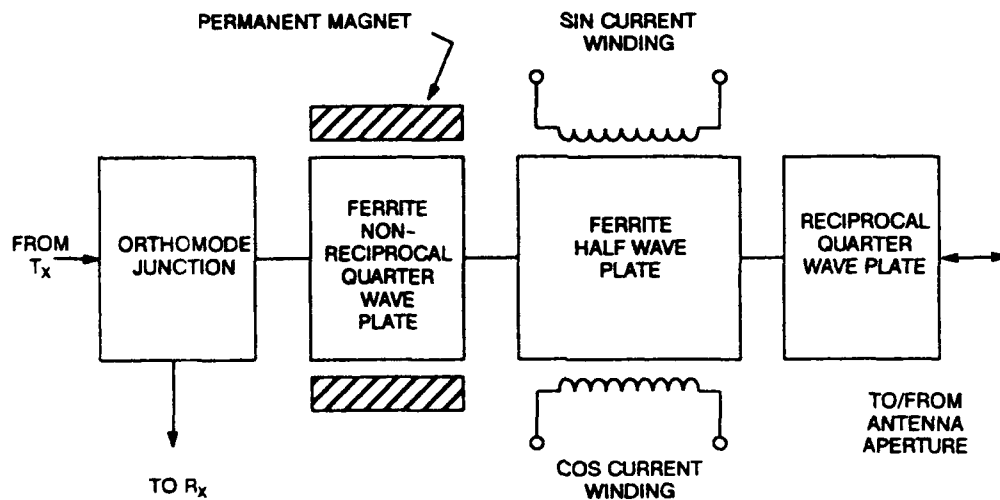


Figure 5. Beam Steering Phase Shifter Block Diagram

2. TECHNICAL DISCUSSION

From the foregoing discussion it is clear that far field pattern adjustment of the E-3A antenna transmit /receive beam elevation offset angle is a straight forward task with minimum complexity.

For a recent major program modification, however, it became necessary to develop a retrofit plan for a large number of existing aircraft based antennas.

The brute force method of modifying the elevation beam offset angle was to remove each of the antennas and their support equipment from its platform aircraft and take it to a "nearby" far field antenna range and simply retune the receive "Squint" Elevation Pattern. When this task was quoted for all aircraft in the USAF inventory, the cost was prohibitive.

It became obvious that a new method of tuning the receive "Squint" pattern needed to be invented. Furthermore, since antennas had to remain on the aircraft, the new tuning method would have to be done through a highly curved radome, and in the pres-

ence of significant multipath sources (not the least of which being the platform aircraft itself).

Since the radome and the extreme multipath conditions provide significant phase errors, the new tuning method had to be such that it was not sensitive to these sources of phase error.

Amplitude errors from the multipath sources mentioned above would only be a problem if the sum of the direct wave and the spuriously scattered multipath sources created a null or "near null" at one of the array elements being tuned; fortunately, this was not found to be a problem in developing the new tuning procedure.

Figure 6 shows a layout of the range geometry used in developing the new tuning procedure. The transmitting source was located, as shown, operating in a ground level range mode, looking over a flat runway surface toward the rotodome mounted antenna. The ground location of the transmitting source helped reduce otherwise strong elevation multipath, which was a potential source of elevation plane aperture illumination nulls at the E-3A antenna being tuned. Such nulls create very low signal to noise ratios when they occur and do not allow the radiator at a null location in elevation to be tuned (see figure 2).

Each radiator shown in figure 2 is a horizontally running slotted waveguide radiator connected to transmit and receive elevation feed networks. The radiators are spaced approximately a half wavelength apart in elevation.

Figure 7 shows the test equipment setup used in tuning the antenna. It is a processor managed setup which is very efficient in the tuning of each radiator phases automatically and in the storage and retrieval of all tune data. The word tune is used here in the context of a set of radiator phase alignments to produce a desired elevation antenna pattern.

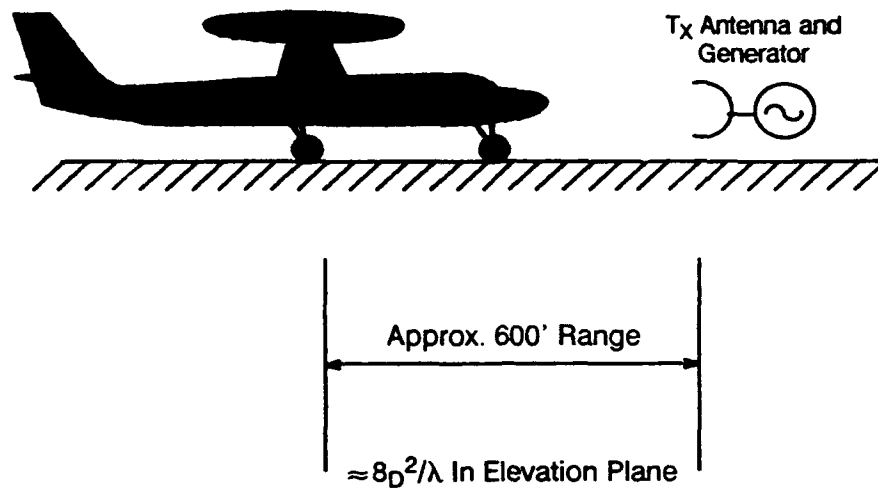


Figure 6. Range Geometry For Improved Tuning Procedure

The antenna is phase aligned in elevation by selecting a radiator to be tuned and modulating it in 90° steps as shown in figure 8. An untuned phase shifter will have an amplitude imbalance between the 90° and 270° states (which represent respectively the vector sum of the quantities $\bar{A} + A_{90}$ and $\bar{A} + A_{270}$; where $\bar{A} = \sum_{K=1}^{N-1} A_K$, as shown in figure 8(A), and A_{90} and A_{270} are the 90° and 270° modulation position vectors of the phase shifter being modulated and tuned.).

When a phase shifter is aligned with all its aperture voltage distribution counterparts, i.e., the components of the voltage sum $\sum_{K=1}^{N-1} A_K$, the 90° and 270° levels are balanced, as shown in figure 8(B) and the phase shifter is considered to be tuned.

The "tuned" antenna indications of figure 8(B) are easily obtained on a clean far field antenna range and are positive indications that the elevation aperture distribution is well tuned and has a very good pattern in the plane of scan.

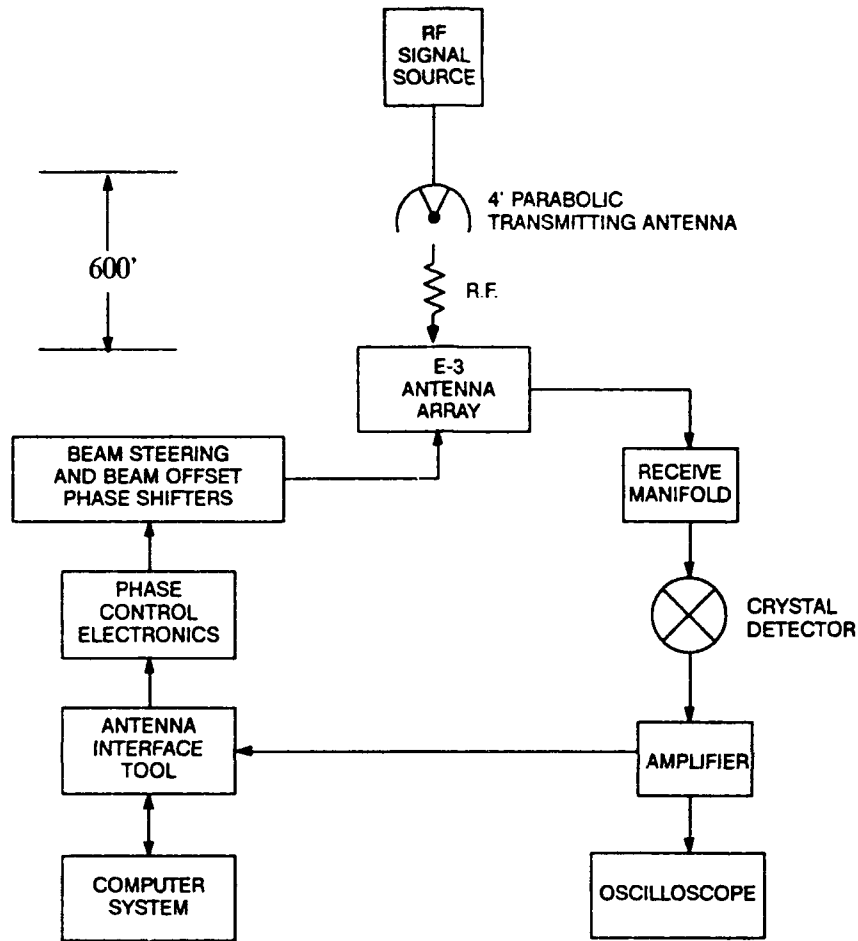


Figure 7. E-3A Antenna Phase Tuning Instrumentation Arrangement

The problem which needed solving, however, was the problem of modifying the E-3A antenna elevation offset angle with the antenna on the aircraft, with the radome in place and in the presence of significant antenna alignment site multipath, such that elevation pattern performance was maintained and the desired elevation beam offset angle change effected within the desired tolerance range.

The presence of the radome and sources of multipath on a less than ideal far field antenna range causes the signal from the transmitting source of figures 6 and 7 to have a "non-flat" phase distribution in the elevation plane upon arrival at the antenna aper-

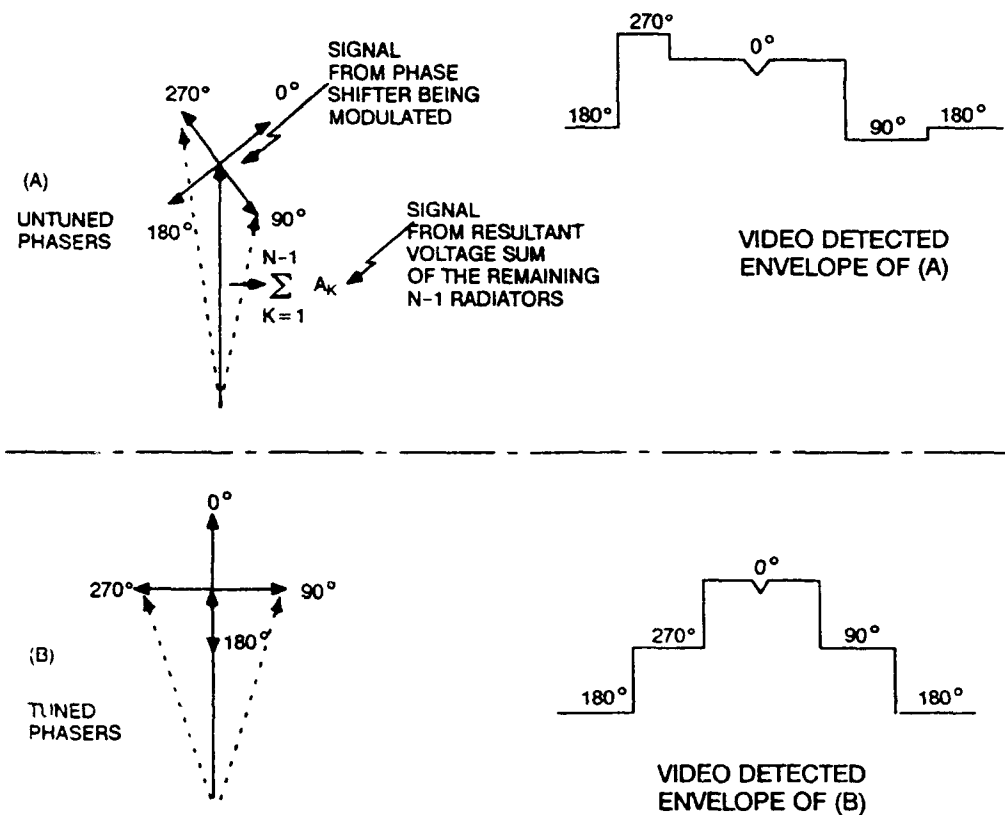


Figure 8. Antenna Phase Tuning Relationships

ture. This makes the antenna appear to be detuned where the relative phases of the individual radiators are being examined with the tuning setup of figure 7 and precludes the use of the balanced $90^\circ/270^\circ$ states (see figure 8) as a positive indication that the antenna is tuned in the plane of scan. This, coupled with the fact that the beam offset phase shifters are too non-linear to tilt a phase front and maintain the phase slope and phase front flatness required to obtain the desired values of the modified elevation beam offset angle and scan plane pattern sidelobe performance necessitates the development of a new approach to the E-3A receive pattern tuning problem.

The approach which was developed was one in which the “secondary phase standard” characteristics of the beam steering phase shifters were used to calibrate the phase changes required of the beam offset phase shifters in order to arrive at the phase front which produce the desired “new” elevation beam offset angle and associated pattern sidelobe performance.

Instead of relying on a balanced modulation pattern during the elevation plane beam offset angle adjustment, the new procedure employs a processor managed operation which measures the A/B ratio (see figure 9) for each radiator and stores it in memory for tuning use a a later time.

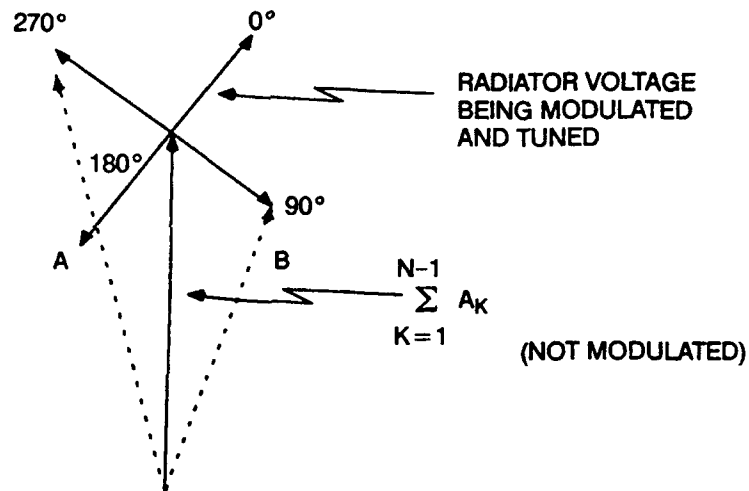


Figure 9. Phase Shifter “Tuning” Diagram

Because of the radome and sources of multipath, a tuned antenna will have radiators with tuning modulation patterns as shown in figure 9. These modulation patterns have non-unity A/B ratios (in general). The control software for the test equipment set-up of figure 7 was modified to accurately measure the A/B ratios for a tuned antenna with phase error sources (radome and multipath) between it and the antenna range R.F. source.

From simple antenna theory it is easily shown that:

$$\frac{2\pi s}{\lambda} (\sin\Theta_1 - \sin\Theta) = \Delta\phi \quad (1)$$

λ = freespace wavelength

$\Delta\phi$ = interelement phase differential

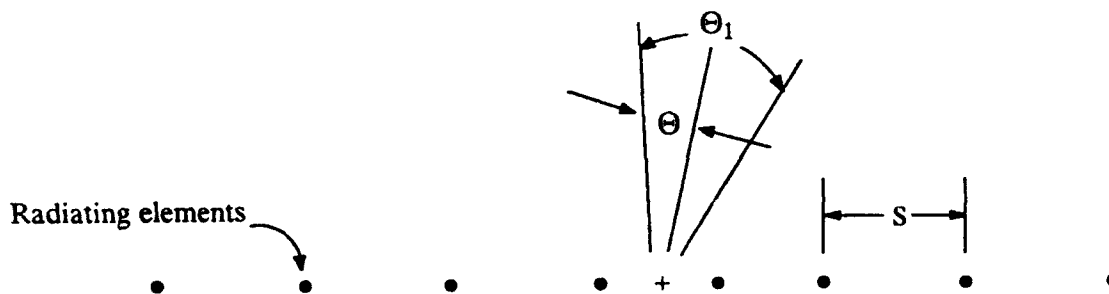


Figure 10. Linear Array

Where the parameters of equation (1) are defined in figure 10 above.

Thus equation (1) gives the adjacent radiator phase differential for a beam motion, in the plane of scan, of $\Theta_1 - \Theta$.

For an N element linear array, the phase of each element can be written:

$$\Phi_k = \frac{2\pi s}{\lambda} (\sin\Theta_1 - \sin\Theta) (K - N/2 - .5) \quad K = 1, 2, \dots, N \quad (2)$$

3. PROCEDURE IMPLEMENTATION

The method used for calibrating the beam offset phase shifters such that the desired squint angle is achieved begins with the antenna in the no squint mode, where the transmit and receive beams point in the same direction. Because the transmit and receive beams are aligned Θ is zero and equation 2 becomes:

$$\Phi_k = \frac{2\pi s}{\lambda} (\sin\Theta_1) (K-N/2-.5) \quad K = 1,2,\dots,N \quad (3)$$

with Φ_k being the phase for any radiator R_K which will rotate the phase front about the phase center of the radiating array by the desired amount.

The beam steering phase shifter of the K th radiating element can be very accurately steered to the value given in equation (3) thus giving us a very precise way of calibrating the motion of a beam offset phase shifter (the units whose phase must be changed to effect a new elevation beam offset angle).

The E-3A antenna array is now illuminated with a "plane wave" from the ground level range transmitter. The video detected envelope in figure 8 is monitored by an oscilloscope. While monitoring the display, the no squint receive beam is electronically scanned until maximum amplitude is achieved. This ensures proper alignment of the receive beam with the transmitted beam down range thus providing the best signal-to-noise ratio. At this point the computer stores the A/B ratio for a selected radiating element (stick). The beam steering phase shifter is now adjusted for the stick being tuned by the amount designated in equation (3). The beam steering phase shifters are steered in the opposite direction from the desired squint angle change, so that the beam offset phase shifters are tuned in the proper direction (opposite and equal to that of the beam steering phaser units).

Using the beam offset phase shifter for the stick being tuned the phase change Φ_K is negated and the original A/B ratio re-obtained. The beam offset phaser setting that was commanded to achieve the original A/B ratio is the desired tune value for the new squint angle. The computer now records this value for later use. At this time the beam steering and beam offset phase shifters for the stick being tuned, are returned to their original no squint tune values and the process is repeated until the new beam offset tune values have been recorded for all radiating sticks. Figures 11 and 12 show the effective receive beam phase front after adjusting the beam steering and beam offset phase shifters during the elevation beam offset modification.

These figures show the phase front movement if all beam steering phase shifters were adjusted and then the beam offset phase shifters re-adjusted to return the beam to broadside. As stated previously, it is necessary to perform this calibration one stick at a time. The problem with adjusting all of the beam steering phase shifters to the appropriate phase settings involves the measurement of the A/B ratio. The A/B ratio is based on a vector summation of all the complex aperture voltages of the sticks in the array; and by changing more than one beam steering phase shifter at a time, the solution for the new beam offset tune values is not unique.

Therefore by negating the phase shift of the beam steering phase shifter with the beam offset phase shifter for an individual stick, the signal from the resultant voltage sum of the remaining N-1 radiators is constant and allows a direct calibration of the non-linear beam offset phaser shifter by the "secondary standard" beam steering phase shifter.

The new beam offset tune values can be used to produce the desired squint angle. Figure 13 shows the phase front of the receive beam formed by using the new beam offset tune values.

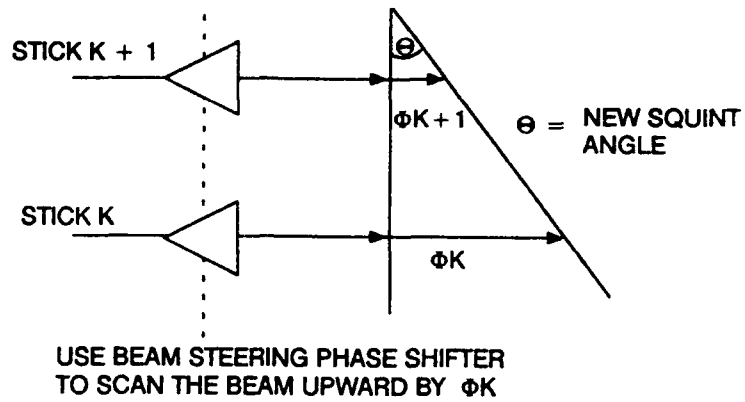


Figure 11. Effective Representation of Beam Steering Adjustments

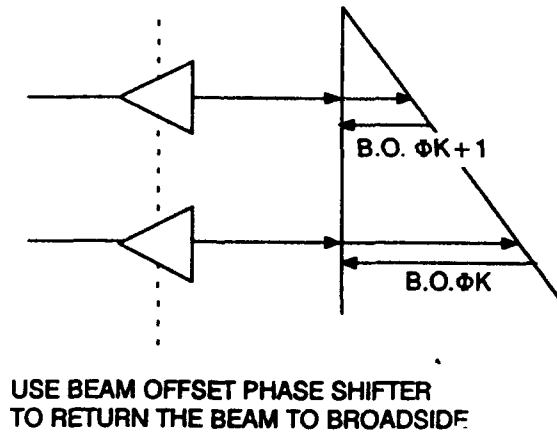


Figure 12. Effective Representation of Beam Offset Adjustments

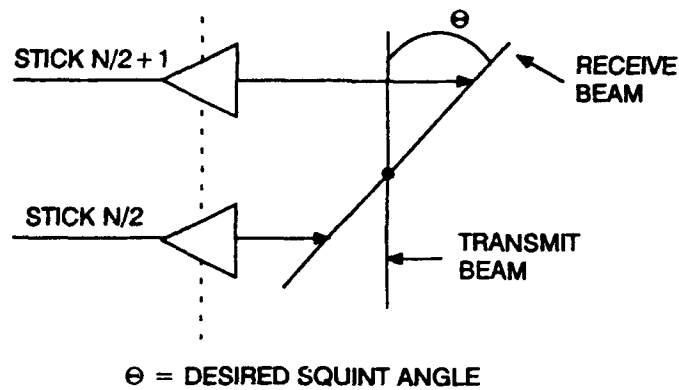


Figure 13. Phase Front of Squinted Receive Beam

Figures 11 through 13 are shown without the phase errors introduced due to the phase distorting radome and multipath effects. The presence of these phase errors do not have an effect on the accuracy of this calibration procedure because they are accounted for in the measurement of the A/B ratio.

4. SUMMARY

The procedure described herein provides a method of retuning the E-3A receive/transmit squint angle in the presence of large phase error sources while avoiding the removal of the antenna from the aircraft. It accomplishes this task on a far from ideal antenna range (lots of multipath and a phase distorting radome) by calibrating the phase errors out of the R.F. measurements which are the basis for the elevation beam adjustment procedure. This calibration or subtraction of the phase errors from the measurement was made possible by the use of secondary phase standard rotary field phase shifters.

CIRCULAR PHASED ARRAY DEVELOPMENT FOR ELECTRONIC
SCANNING OF AN ENDFIRE BEAM

Gary G. Sanford

Patrick Westfeldt, Jr.

Ball Communication Systems Division

Broomfield, Colorado 80038

ABSTRACT

Full azimuth scanning of a high gain horizon beam has often been accomplished by mechanical rotation of a large aperture. From an airborne platform point-of-view, doing the same job with a single electronically steered aperture would be desirable. This paper presents the results of an experimental development at Ball Communications Systems Division (BCSD), where an arrangement of active and parasitic elements in a large circular array resulted in a high gain beam near the horizon. It is shown that electronic control and reconfigurability of the active and parasitic elements allows full 360-degree azimuth steering, along with a limited scan capability in elevation.

In one configuration, measurements of a 1306-element, 15-wavelength circular aperture, resulted

in aperture gain of 23.5 dBil at 10 degrees elevation, with 3.0 dB aperture efficiency.

1.0 INTRODUCTION

This paper describes an experimental effort to achieve high gain on or near the horizon from the aperture shown in Figure 1. The aperture is a planar array of 1306 elements arranged in 20 concentric rings with a center element. Ring spacing is 0.358λ and azimuthal spacing between elements is nominally 0.358λ , yielding a circular aperture with diameter 14.68λ at 4.8GHz. Although the elements appear as printed circuit patches, they are actually electrically small top-loaded monopoles. For all measurements, the aperture was mounted on a ground plane 7.5 feet (about 37λ) in diameter, so that the low angle peak of any vertically polarized beam occurred at about 10° above the horizon.

The motivation for this effort was the desire for a low profile, high gain, electronically steered antenna, to be used conformal to a substantially flat airborne platform. Full 360-degree scanning in azimuth was specified, and additional issues such as elevation scanning, low sidelobes, bandwidth, thickness and power handling were also considered. The key technical issue

was clearly the achievement of an electronically steerable high gain beam in a substantially endfire mode. It is recognized that this issue might have been more easily investigated in an aperture of wire monopoles with a normal periodic lattice.

The following sections describe the identification of a concept and the development of hardware to evaluate the concept. The hardware development evolved almost entirely from an experimental procedure, because the analysis software available during the study was not applicable to this problem. In view of the limitations of this process, the results were most gratifying.

2.0 CONCEPT IDENTIFICATION

Broadside directivity for an aperture of this size is 33.25 dB, and using a half-space isotropic element pattern, the computed directivity at 10° elevation is approximately 27.0 dB. However, it is well known that this low angle value is not physically realizable by normal phased array techniques. A qualitative explanation for this problem is that any interior element in the aperture of Figure 1 must radiate across a surface of matched elements in order to contribute to an endfire beam. The power lost in this process

severely degrades the gain by a factor proportional to the planar aperture size.

In a study of monopole arrays by the MIT Lincoln Laboratory¹ in 1983, the computations showed that a central element in an array of this size suffers about 15 dB gain degradation from its isolated value. This behavior was confirmed during the circular array development, as shown in Figures 2 and 3. Figure 2 is the pattern for an isolated element on a 7.5 foot ground plane, yielding a normal measured gain of 5.15 dBil at the low angle peak. Figure 3 shows the corresponding gain of -11.1 dBil for the same element in the center of 1306 identical terminated elements (scale is not the same on the two patterns).

The solution concept pursued in this study is illustrated in Figure 4, where almost half of the elements are switched into a parasitic condition. The idea is that these elements comprise a semi-corrugated structure capable of supporting a surface wave mode. The surface wave is launched by an active band of elements steered close to endfire, in a rectangular geometry across the entire diameter of the circle. Elements behind the active band are not used in this version of the concept, except perhaps as attenuation for backlobes. The antenna may also be thought of as a

planar Yagi antenna (or array of parallel Yagis), where the active launch is provided by a phased array instead of an element/reflector combination. Using the summation of aperture gain from appropriately spaced parallel Yagis, and using a linear gain factor of $7.5L/\lambda$, predicted gain for the arrangement in Figure 4 is approximately 26.0 dBil. Some precedent was found for this approach in a 1976 study at RADC², where low angle gain was enhanced by shorting out all the active waveguide elements in a 64-element array and exciting a surface wave on this structure with an external launch.

Electronic azimuthal scanning is provided for in this concept by allowing all elements to be reconfigurable as either active or parasitic elements. Thus both the active and parasitic band delineation is changed, as well as the phasing of the active elements, to steer the beam to a given angle. A conceptual schematic of how this reconfiguration could be accomplished in the transmit case is shown in Figure 5. Provision is made for the parasitic reactance on the element to be variable, to allow for bandwidth, lattice and launch efficiency issues, as well as the possibility of elevation scanning configurations.

3.0 EXPERIMENTAL HARDWARE DEVELOPMENT

Although it is clear that appropriate software must be developed to achieve a reliable design, the attempt was made in this study to prove the basic low angle gain concept by experimental means. The first step in this procedure was to test the effect of parasitic elements on a 62-element subset of the full array, as shown in Figure 6. Central embedded element patterns were measured, first with all elements terminated, and then with 12 parasitic elements as shown. Furthermore, the parasitic reactances on all 12 elements were varied until optimum "director" and "reflector" effects were observed. The optimum director effect is shown in Figures 7 and 8, where a 3.0 dB improvement in low-angle gain was observed. Figure 7 is the central element pattern with all other elements terminated, and Figure 8 is the same pattern with 12 parasitic elements trimmed to the optimum length. Reflector effects of similar magnitude were observed for different values of the reactances.

Although there was no guarantee that the parasitic value observed above was correct for the full array, this reactance was in fact installed on 513 of the elements, as shown in Figure 9. Individual element patterns were measured for various interior elements,

with a typical result shown in Figures 10 and 11. Figure 10 is the pattern of one of the central elements, showing a gain at 10° elevation of -9.6 dBil. In Figure 11, with 513 elements parasitic, the corresponding gain of the same element was -0.3 dBil. Although there was significant variation among the elements tested, enhancement due to the parasitic surface ranged from 7.5 dB to 10.5 dB for all elements.

An active band of 256 elements was selected along with an organization of two-way power dividers, as shown in Figure 12. Fixed beam endfire phasing was applied, and far-field amplitude and phase patterns were taken for all 128 two-element arrays, with a view towards establishing the best phasing relationships for the active band. The amplitude data proved to be equally significant, as it was found that elements close to the parasitic surface had much higher gains in the steering direction than those further back. The variation from front to back was as much as 11.0 dB, with more severe degradation in the center than at the edges. In view of this data, the size of the active band was reduced, and feed systems were built to determine the effects of both 64-element and 128-element active bands.

4.0 FULL ARRAY RESULTS

Figure 13 is the feed side of the active element band, showing a partition of the 256 elements into subsets of 64 and 128 elements. Pattern, gain and directivity data was taken for the array excited with each of these active bands in turn.

Figure 14 is the azimuth conical pattern at 10° elevation for the 64-element active band case (the azimuth pattern for 128 active elements was almost identical, with slightly lower peak gain). Measured peak gain was 21.1 dBil, which includes feed system loss of 2.4 dB. The beam was well formed, and at this level the sidelobes were well behaved.

Figures 15 and 16 are the elevation patterns for the 64-element and 128-element cases, respectively. Both patterns exhibit substantial direct radiation from the active band, representing power not coupled into the surface wave mode. The more directive launch of the 128-element active band results in less direct radiation and narrower beamwidth, but the aperture gains for the two cases are identical (with feed system losses removed). Evidently, mutual coupling losses in the 128-element case offset the improved directivity. Table 1 is a summary of the peak of beam performance for both cases. The directivity improvement (and

coincidentally identical aperture efficiency degradation) for the 128-element case was 0.7 dB.

TABLE 1. Circular Phased Array Peak of Beam Results

	<u>64 Active</u>	<u>128 Active</u>
GAIN	21.1 dBil	20.8 dBil
FEED LOSS	2.4 dB	2.7 dB
APERTURE GAIN	23.5 dBil	23.5 dBil
DIRECTIVITY	26.4 dBil	27.1 dBil
APERTURE EFFICIENCY	3.0 dB	3.7 dB

5.0 CONCLUSION

The low angle gain values and aperture efficiency achieved in this effort allow a reasonable expectation of success for an antenna system of this type. However, many issues must be addressed before proof of concept can be claimed. Although an experimental process produced good results in this case, reliable modeling will play a significant role in the success of future development efforts.

REFERENCES

1. Fenn, A. J. (1985) Theoretical and Experimental Study of Monopole Phased Array Antennas, IEEE Trans. Antenna Propagat., Vol. AP-33, No. 10, pp.1118-1126
2. Mavroides, W. G. and Mailloux, R. J. (1976) An Array Technique for Zenith to Horizon Coverage. RADC-TR-76-360, ADA035503

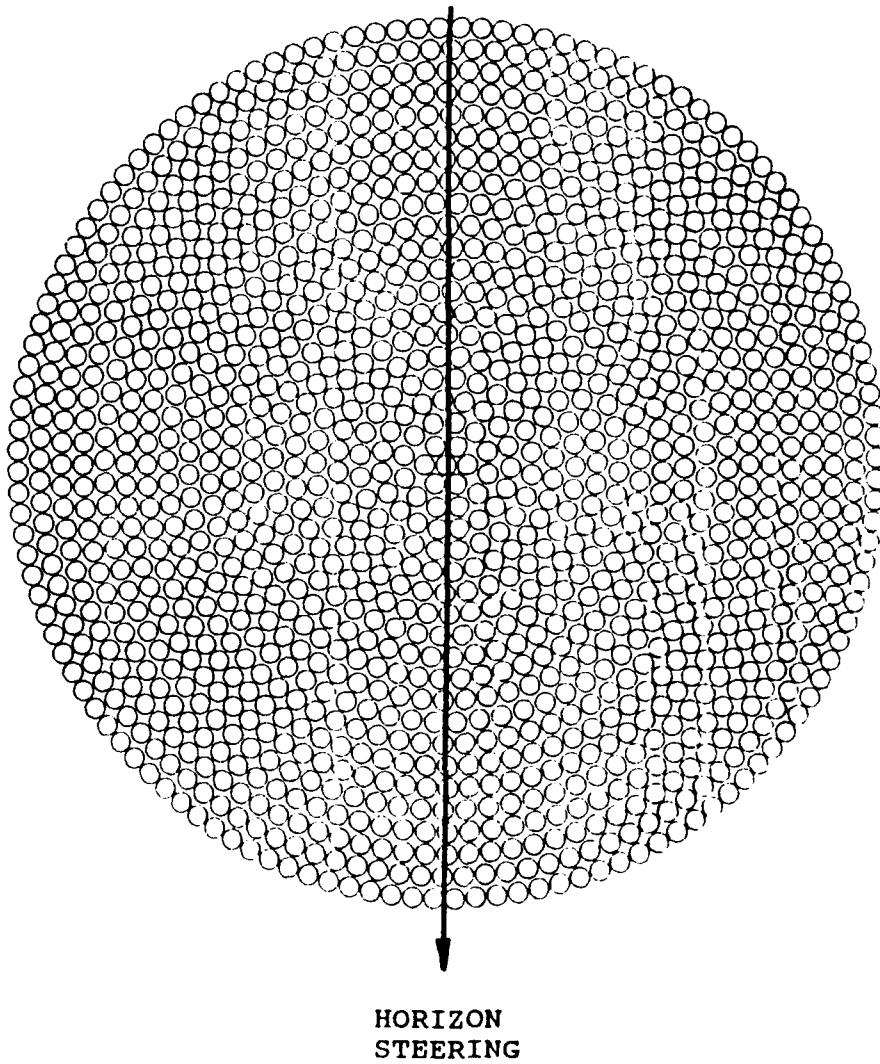


Figure 1. Circular Phased Array Aperture

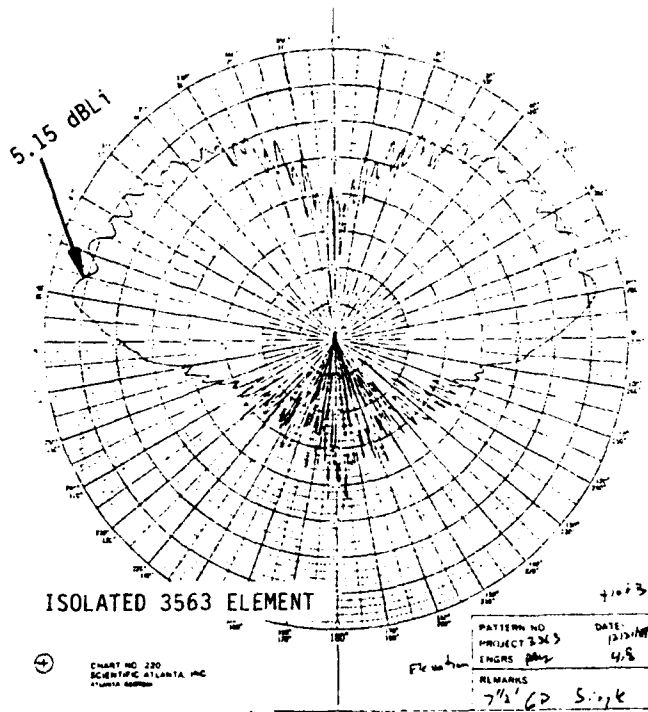


Figure 2. Isolated Element Pattern for Top Loaded Monopole

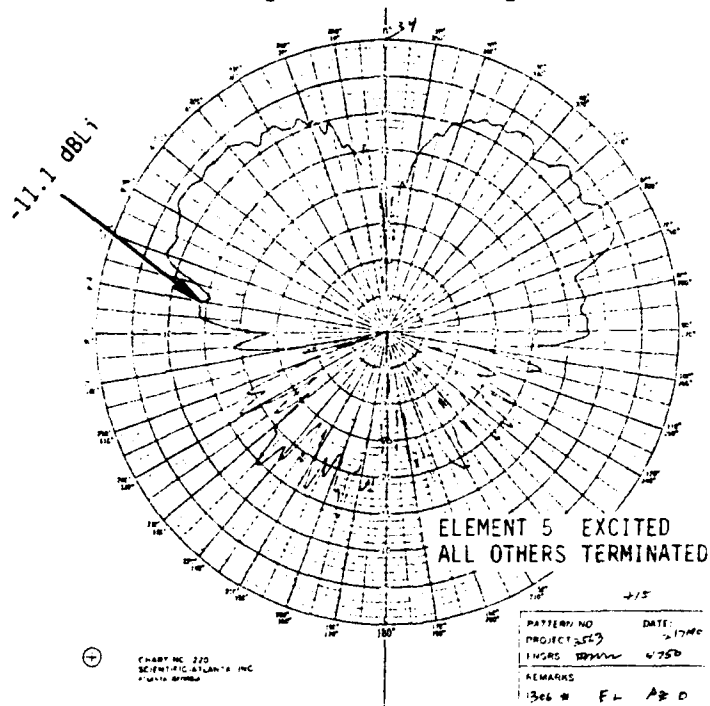


Figure 3. Embedded Element Pattern for Top Loaded Monopole

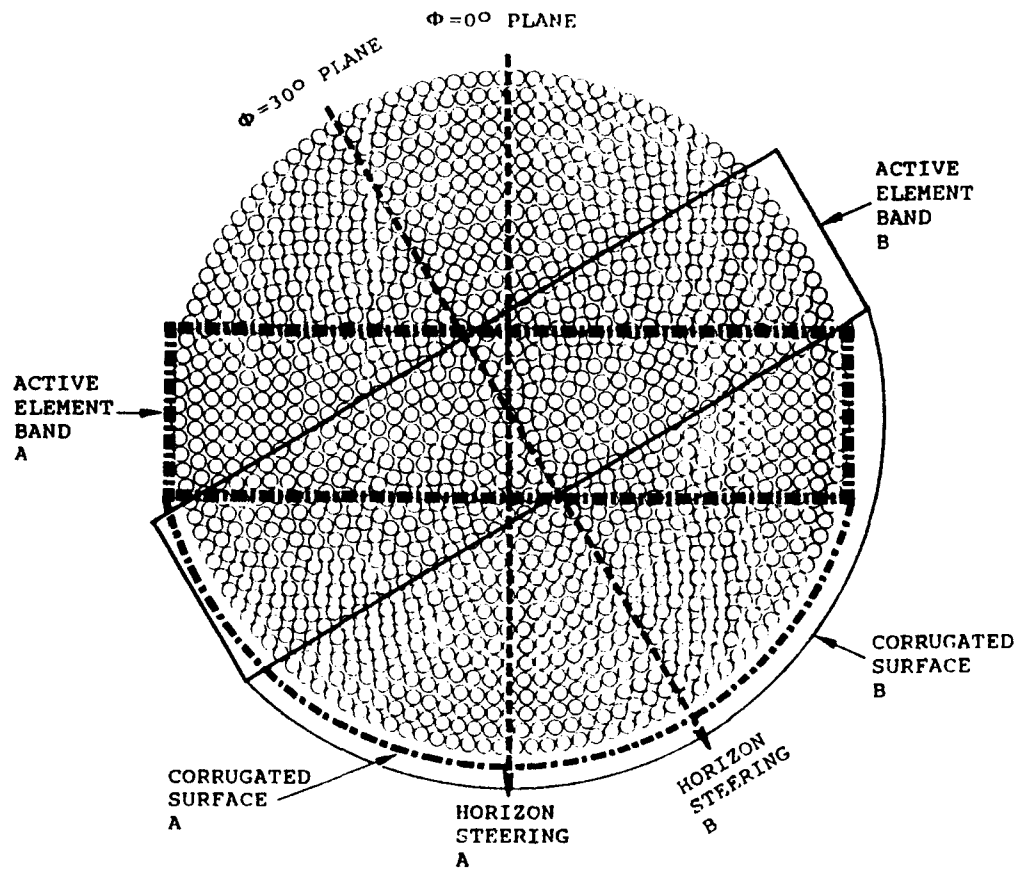


Figure 4. Circular Phased Array Steering Concept

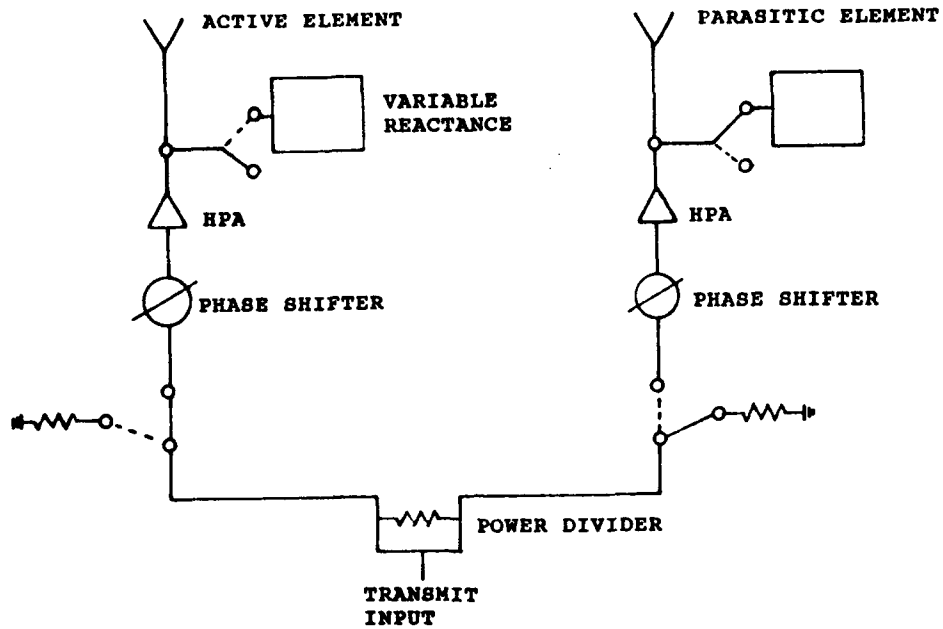


Figure 5. Switching Between Active and Parasitic Elements

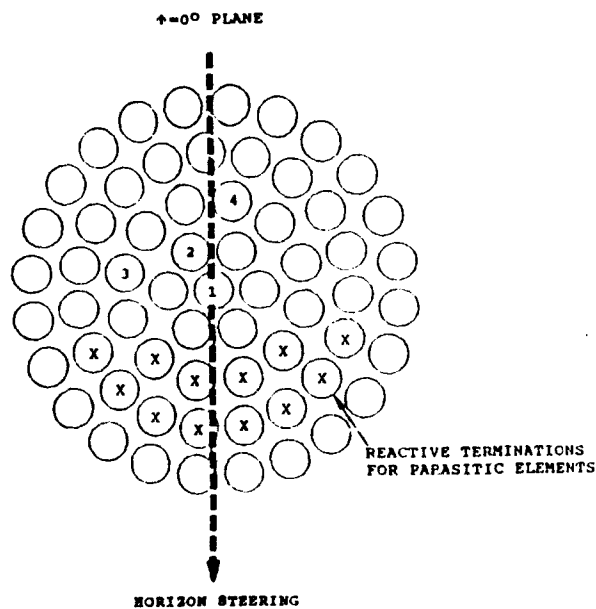


Figure 6. Array Subset Experiment

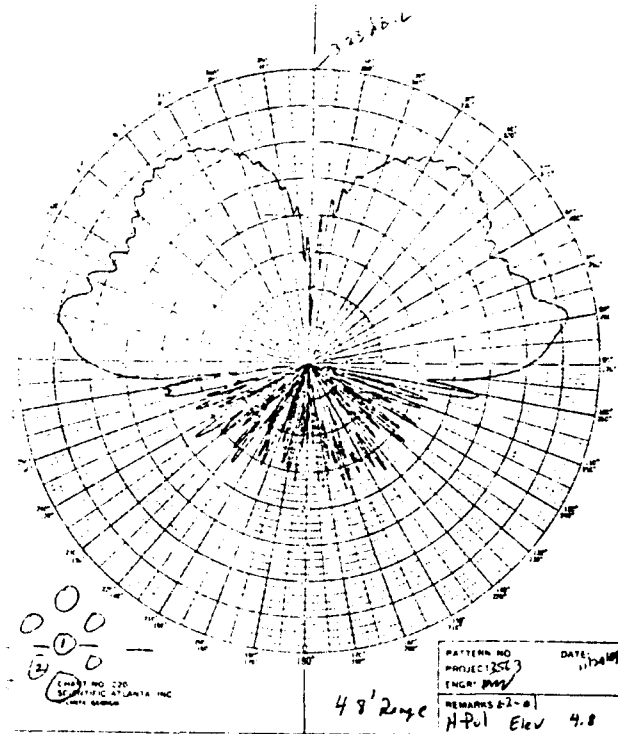


Figure 7. Embedded Element Pattern with All Others Terminated

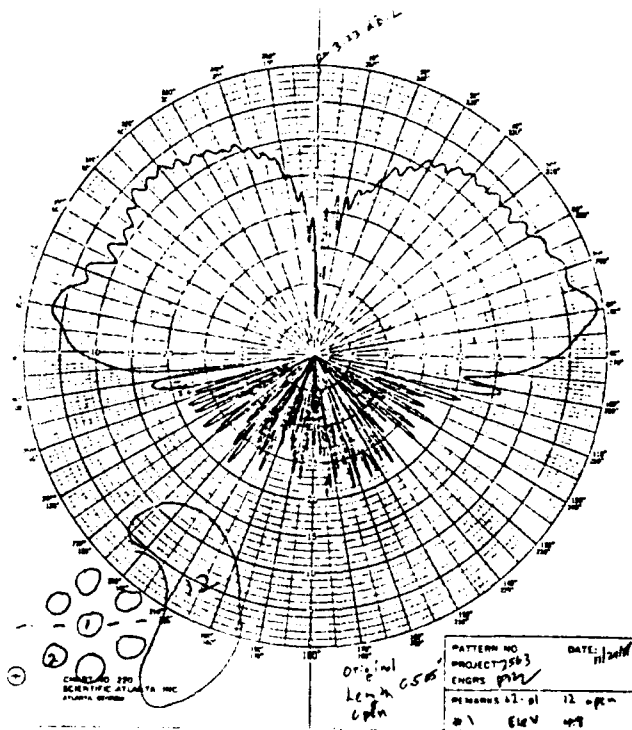


Figure 8. Embedded Element Pattern with Parasitic Director Effect

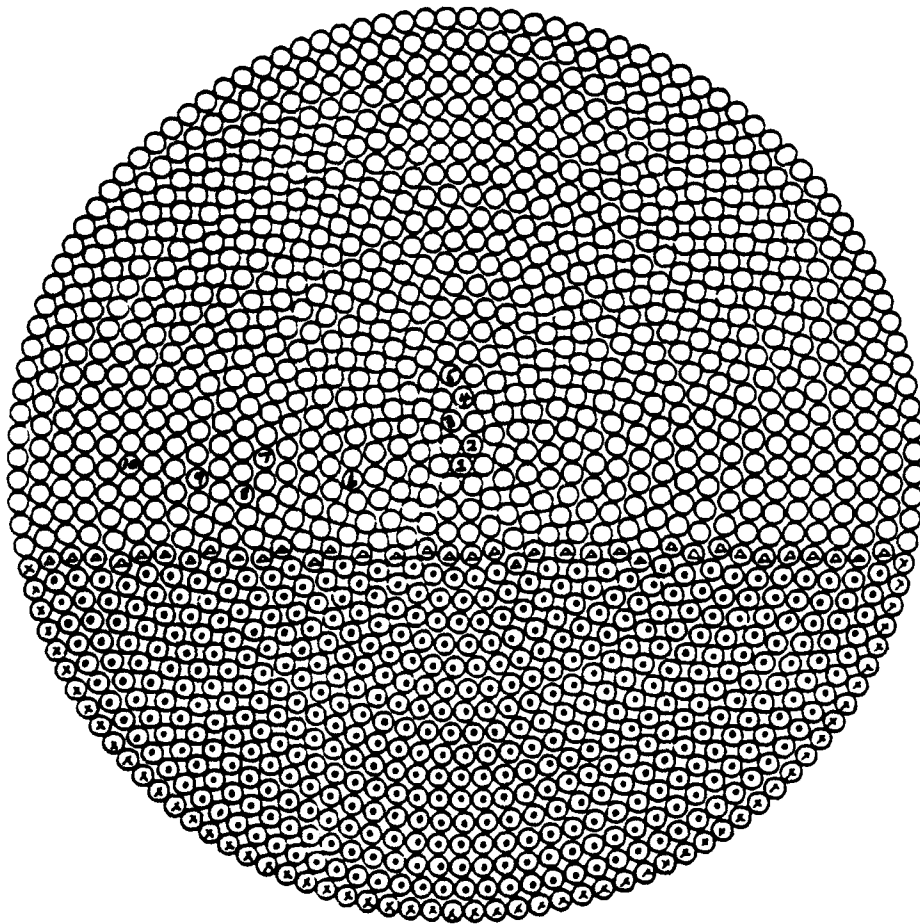


Figure 9. Circular Phased Array with 513 Parasitic Elements

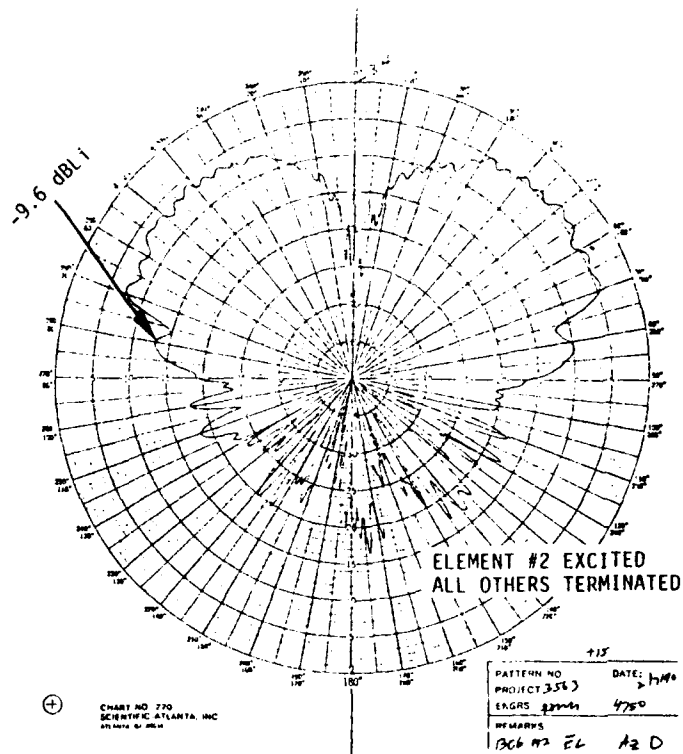


Figure 10. Embedded Element Pattern with All Others Terminated

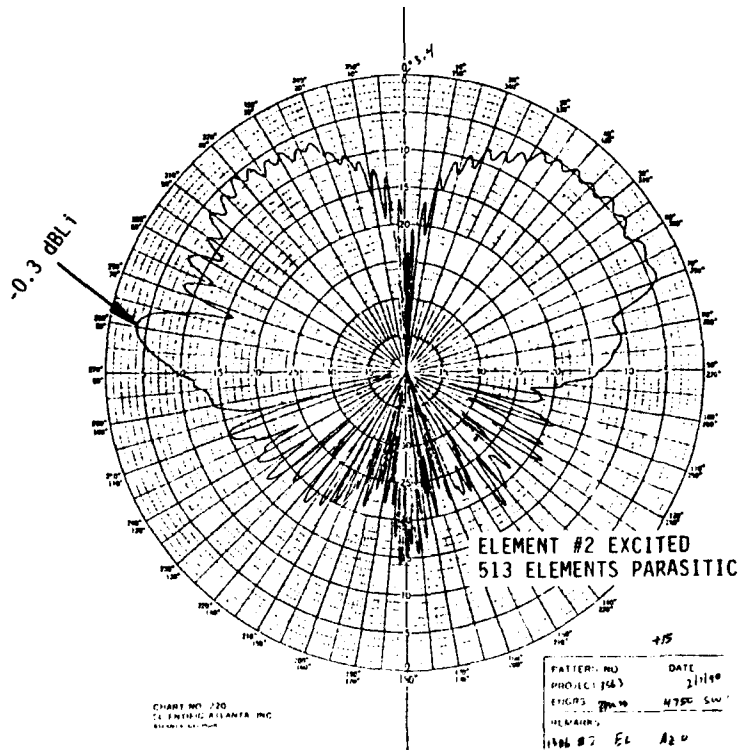


Figure 11. Embedded Element Pattern with 513 Elements Parasitic

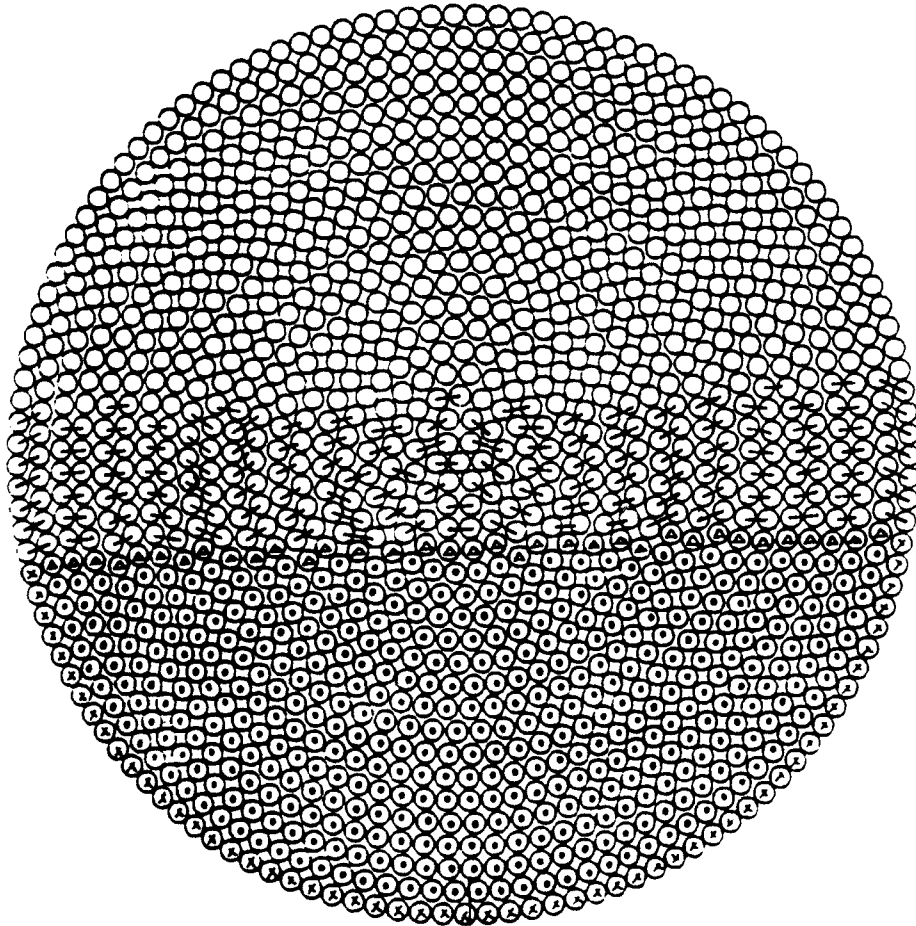


Figure 12. Active Band with Two-Way Power Divider Organization

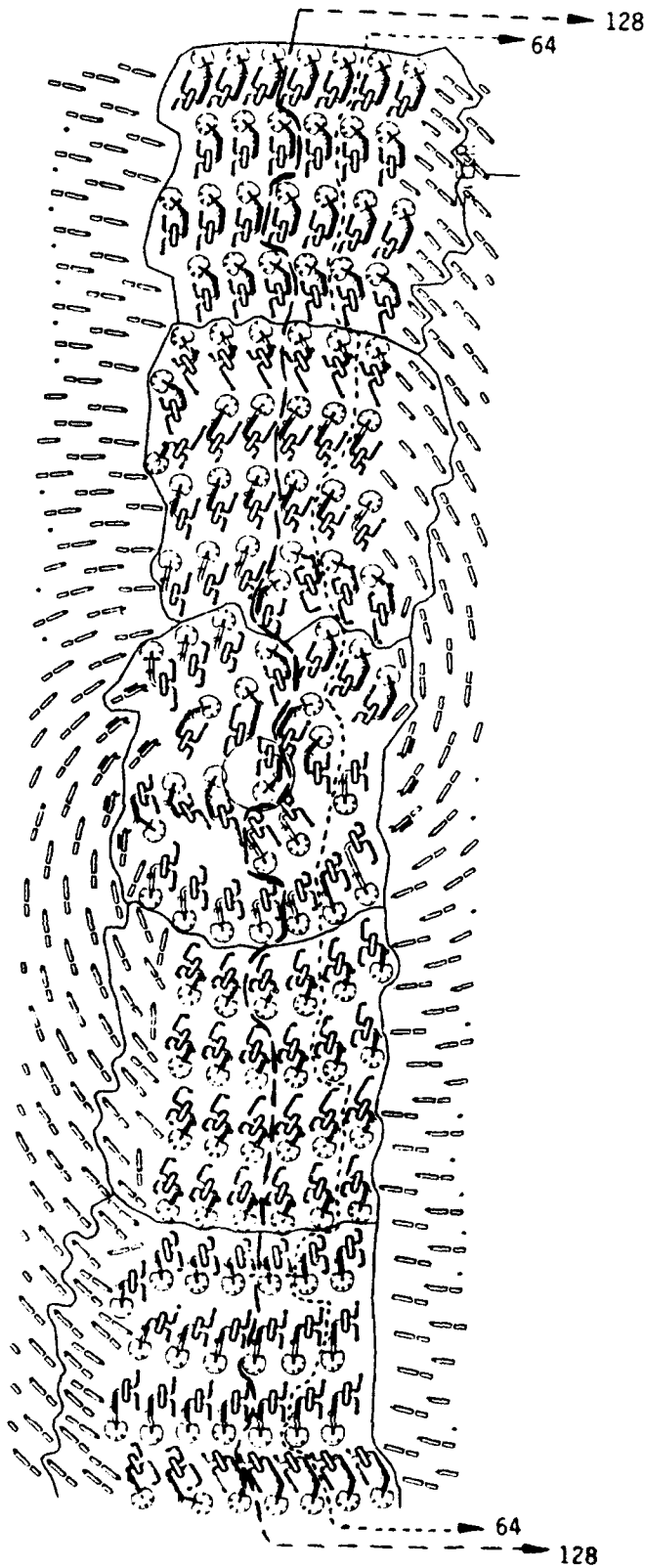


Figure 13. Arrangement of Eight-Way Power Dividers

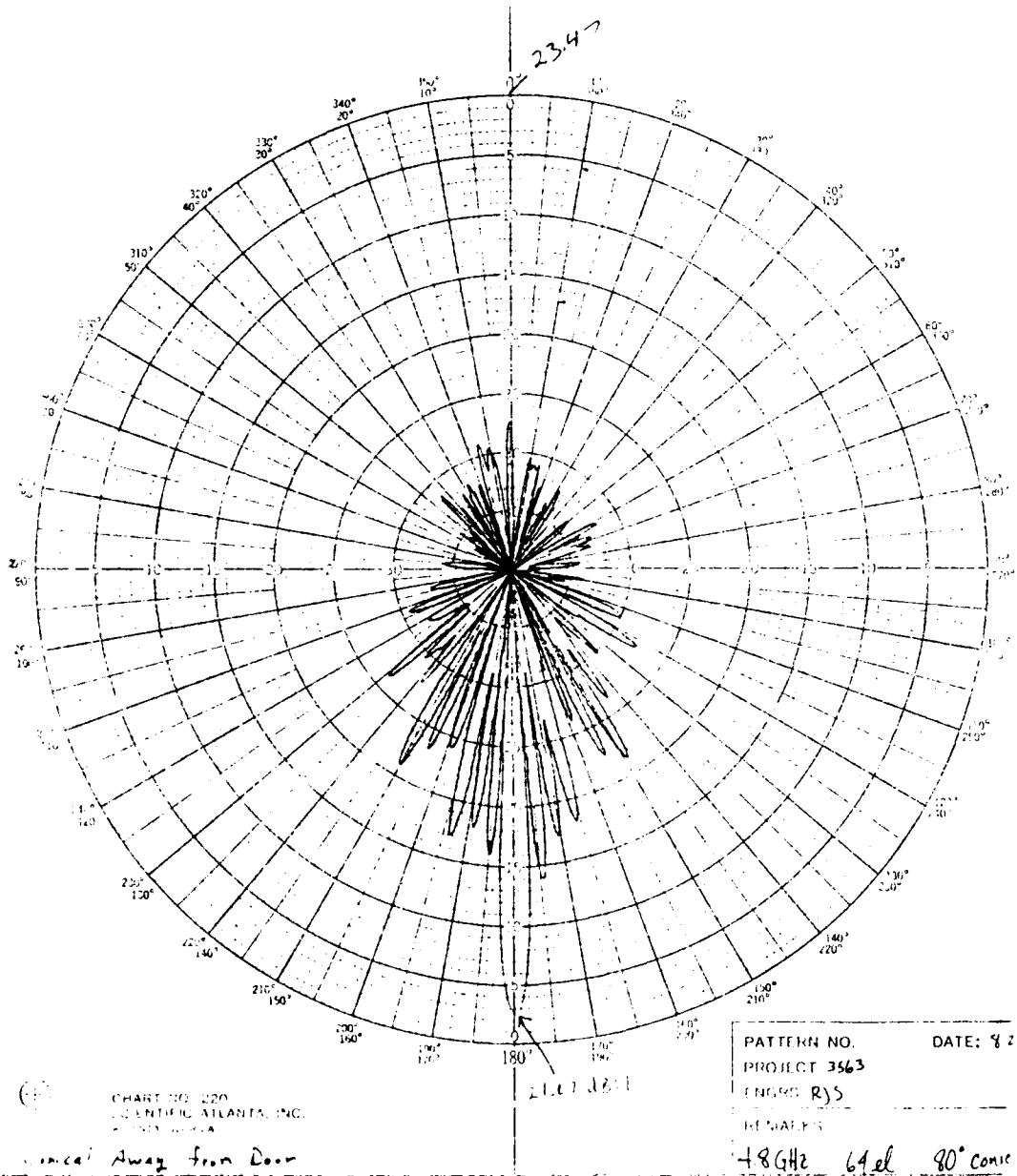


Figure 14. Conical at 10° Elevation with 64 Active Elements

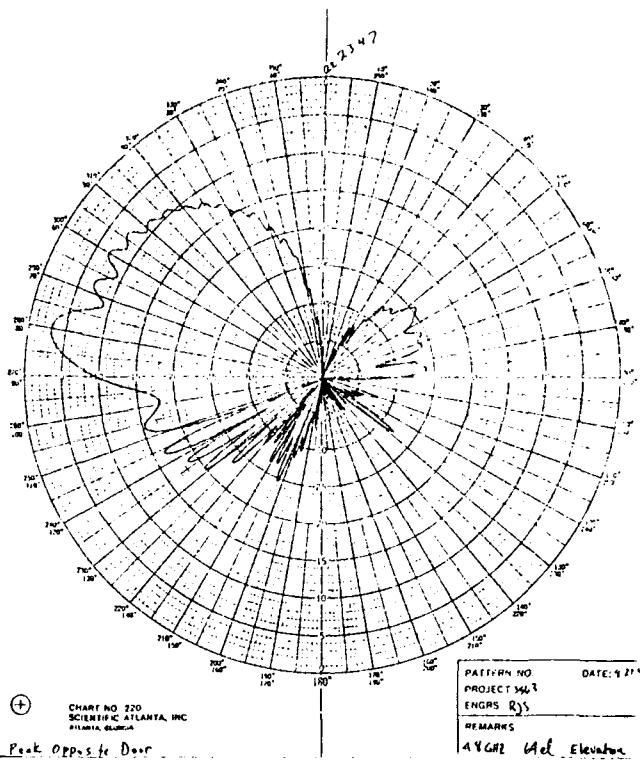


Figure 15. Elevation Pattern with 64 Active Elements

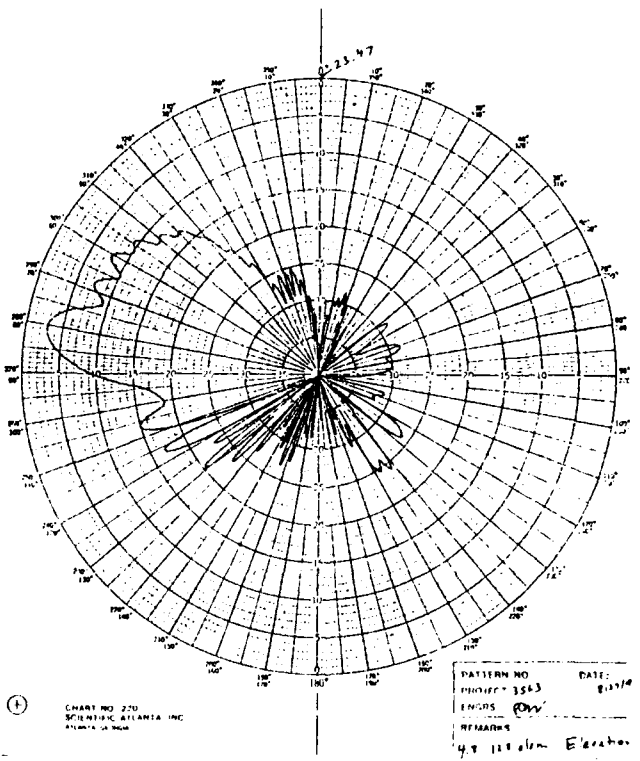


Figure 16. Elevation Pattern with 128 Active Elements

SLOT-COUPLED PATCH ARRAYS

C. Harry Chen, Paul G. Ingerson and William C. Wong

Antenna Systems Laboratory

TRW Space and Defense

Redondo Beach, CA 90278

Abstract

This paper addresses two slot-coupled patch arrays: a dual-polarized and a circularly polarized. Breadboard models were built and tested. Excellent performance was obtained.

1. Introduction

Microstrip patch antennas are becoming increasingly attractive in phased array design. The light weight and conformability make them ideal for aircraft, missile and many satellite applications. With the maturing of monolithic hybrid microwave circuit and monolithic microwave integrated circuit technologies, it is possible to produce active devices and circuit components as an integral part of a microstrip phased array, lowering the per-element cost and achieving the long-awaited goal of an economical phased array system.

Traditionally, the microstrip patch are excited by either microstrips on the same substrate (edge-fed) or coaxial probes through a ground plane (probe-fed)¹. Slot-coupling^{2,3} is an attractive alternative excitation method because it eliminates the need for feed-throughs in a multiple layer configuration. Feed-through assembling is labor-intensive, posing a long-term reliability problem in large phased arrays.

This paper describes the design of two slot-coupled patch arrays: a dual-polarized and a circularly polarized. Dual-polarized antennas are useful in communication and polarimetric radar applications. Circular polarization is commonly used in space communications. Experimental models consists of two co-phasally fed arrays. They can be used as an independent antenna or as the subarray building block in a large phased array antenna.

2. Array Description and Test Results

2.1 The Dual-Polarized Array

Feedline crowding, cross-coupling, bandwidth and pattern control are the main limitations in the existing dual-polarized patch array design^{4,5,6}. In one design approach, microstrip patches are connected in series using two orthogonal sets of feedlines^{4,5}. This series-fed patch array is restricted to narrow-band application because: (i) The equal phase condition

is only maintained at the center frequency, resulting in beam squint at other frequencies; and (ii) Mismatch and multiple reflection at every junction accumulate, resulting in degraded array return loss. In addition, controlling radiation patterns of a dual-polarization series-fed patch array is difficult. In a single polarization series patch array, amplitude taper is achieved by varying the patch width. This is not possible in a dual-polarization design since the patches must be square for the two orthogonal polarizations to operate at the same resonant frequency.

Corporate feed network will overcome the above problems. But the existing single-layer design⁶ requires long and close-spaced feedlines and thus thin substrate and high impedance to minimize the line-to-line and line-to-patch coupling. All of these again lead to narrow bandwidth and low efficiency.

Figure 1 illustrates our approach to the dual-polarization microstrip patch array: the edge-fed patches excite one sense of polarization and the slot-coupled patches excites the orthogonal sense of polarization. The two sets of microstrip feedlines are isolated by the common ground plane. Since the bandwidth of a corporate feed network is inherently wide, this configuration can be modified for broadband application by replacing regular patches with broadband stacked patches^{7,8,9}. Dual circular polarization can be achieved by covering the array with meander-line polarizer.

An experimental model 4 x 4 array (Figure 2) was constructed at C-band on two Arlon CuClad 250 substrates ($\epsilon_r = 2.45$): one substrate contains edge-fed microstrip patches while the other contains microstrip feedlines. The two substrate are separated by a slotted ground planes. The spacing between patches is $0.7 \lambda_0$. Figures 3 shows the measured and the calculated principle plane radiation patterns. Figure 4 shows the measured cross-pol pattern. The deep null in the boresight direction indicates low cross-coupling between two polarizations even though the patches are square. Figure 5 shows the measured efficiency: -1.11 dB (78%) for the edge-fed and -1.35 dB (73%) for the slot-fed. Since the radiation patterns are almost identical, the difference in efficiency can be attributed to slot-coupling loss, i.e. -0.24 dB (95% coupling efficiency). The bandwidth of the slot-fed patches (2.6% for -0.5 dB gain loss) is comparable to the edge-fed (2.1% for -0.5 dB gain loss). The array bandwidth (-0.5 dB gain loss) is about same as that of a single patch (2:1 VSWR), indicating the feed network bandwidth is wider than that of a single patch.

2.2 The Circularly Polarized Array

Circular polarization can be achieved by a single slot¹⁰ or by two orthogonal slots excited in phase quadrature. In the latter case, the two slots either intersect at the patch center^{9,11} or separated and offset from the center¹². The single slot approach has extremely narrow axial ratio (AR)

bandwidth. In the double slot approach, high polarization purity requires the slots to be fed in a balanced manner^{9,11}. A balanced feed network may require more space than available because additional real estate is needed for hybrids. Moreover, some balanced feed networks require feedline crossovers (or air-bridges) that increase fabrication complexity, cost and loss. Our approach is to excite the two slots with simple circuit in phase quadrature and average out the polarization impurity using the sequential rotation technique^{7,13}.

Figure 6 illustrates the circuit layout of a 2 x 2 CP subarray. Our experimental model consists of four such subarrays combined in parallel (Figure 7). For every patch, a reactive T-junction gives equal amplitude with the required 90° phase shift provided by the path length difference. The physical orientation of the feed circuit and the associated slots to every patch in the 2 x 2 subarray are then sequentially rotated by 90°. The rotation is accompanied by adjusting the feedline length so that the excitation to every CP element also has 90° progressive shift. Figure 6 shows the resultant phase relationship among the eight slots. Our experimental model was constructed at C-band on two Arlon Cu-Clad 250 substrate: one substrate contains 4 x 4 patches and the other has the slotted ground plane on one side and the microstrip feedlines on the opposite side. The two plates were then bolted together. The patch element size and spacing are identical to those of the dual-polarized array of Figure 2. Before the array were fabricated and assembled, the single double-slot CP element with the T-

junction feed network was fabricated and tested. While the VSWR was as good as the that of the LP element (better than -27 dB return loss), the axial ratio (AR) is only 4.0 dB. The poor single element AR is expected in view of the asymmetry introduced by the two off-center slots. The single element AR can be optimized by adjusting the line length difference and/or slot length/position. However, this was not done in our work since the sequential rotation technique will eventually average out the element polarization impurity in the array environment.

Figure 8 shows the measured AR of the completed 4 x 4 CP array. Both AR in the boresight direction and its range of variation within +/- 6° field of view are plotted. At the designed frequency, the AR is 0.3 dB at boresight and less than 0.5 dB within the +/-6° field of view. The bandwidth of 1.0 dB and 2 dB boresight AR are 2.2% and 3.5 %, respectively. The measured rotating linear radiation patterns at the designed frequency are shown in Figure 9. The CP gain was measured to be 18.9 dBi, corresponding to 78% (or -1.06 dB) efficiency. The feedline loss was estimated to be -0.5 dB. The -0.5 dB gain bandwidth is approximately 2.3 %, about same as the 1.0 dB AR bandwidth.

3. Conclusions

We have successfully constructed two slot-coupled patch arrays and demonstrated their performances. We found the slot-coupling is a very

efficient means of exciting microstrip patch antenna and the use of slot-coupling substantially simplifies the array fabrication. In addition, the dual polarization of high isolation and circular polarization of good polarization purity can be obtained. A CP slot-coupled patch array performs as efficient as its LP counterpart.

Acknowledgments

This work was performed under TRW IR&D project. Special thanks are due to Dr. S. J. Hamada, Antenna Systems Laboratory Manager, for his interest and support. The authors would like to thank Professor Y.T. Lo for many helpful discussions.

References

1. Lo, Y.T., Wright, S.M., and Davidovitz, M. (1989) "Microstrip Antennas", Chapter 13, *Handbook of Microwave and Optical Components*, K. Chang, Ed., John Wiley, New York.

2. Yang, R., Lo, Y.T., Aksun, M.I., and Chuang, S.L. (1991) "Simple and Efficient Analysis for A Slot-Coupled Patch Antenna with a Microstrip Line Feed", to be published in *IEEE Trans. Antennas and Propagation*.
3. Sullivan, P.L. and Schaubert, D.H. (1986) "Analysis of an Aperture coupled Microstrip Antenna", *IEEE Trans. Antennas and Propagation*, Vol. AP-34, 8:997-984.
4. Derneryd, A.G. (1976) "Microstrip Array Antenna", *6th European Microwave Conference*, 339-343.
5. Haddad, H., Fithian, M., and Coombs, D. (1986) "Heading for space: C-band Phased Array", *Microwaves & RF*, pp103-108, April 1986.
6. Lalezari, F. and Massey, C.D. (1987) "mm-Wave Microstrip Antennas", *Microwave Journal*, pp87-96, April 1987.
7. Chen, C.H., Tulintseff, A., and Sorbello, R.M. (1984) "Broadband Two-layer Microstrip Antenna", *1984 IEEE Antennas and Propagation Symposium Digest*, pp 251-254.
8. Hall, P.S., Wood, C., and Garrett, C. (1979) "Wide Bandwidth Microstrip Antenna for Circuit Integration", *Electronics Letters*, Vol. 15, pp 458-459.
9. Tsao, C.H., Hwang, Y.M., Killburg, F., and Dietrich, F. (1988) "Aperture-coupled Patch Antennas with Wide-bandwidth and Dual

Polarization Capabilities", 1988 IEEE Antennas and Propagation Symposium Digest, pp 936-939.

10. Aksun, M.I., Chung, S.L., and Lo, Y.T. (1990) "On Slot-coupled Microstrip Antennas and Their Applications to CP Operation-Theory and Experiment", IEEE Trans. Antenna Propagation, Vol. AP-38, pp 1224-1230.
11. Pozar, D.M., Targonski, S.D. (1991) "A Novel Wideband Circularly Polarized Aperture Coupled Microstrip Antenna", 1991 IEEE Antennas and Propagation Symposium Digest, pp 1098-1101.
12. Adrian, A. and Schaubert, D.H., (1987) "Dual Aperture-Coupled Microstrip Antenna for Dual or Circular Polarization", Electronics Letters, Vol. 23, pp 1226-1228, November 1987.
13. Hall, P.S., Dahele, J.S., and James, J.R. (1989) "Design principles of Sequentially Fed , Wide Bandwidth, Circularly Polarized Microstrip Antennas", IEE Proceedings, Vol. 136, Pt.H, No.5, pp381-388, Oct 1989.

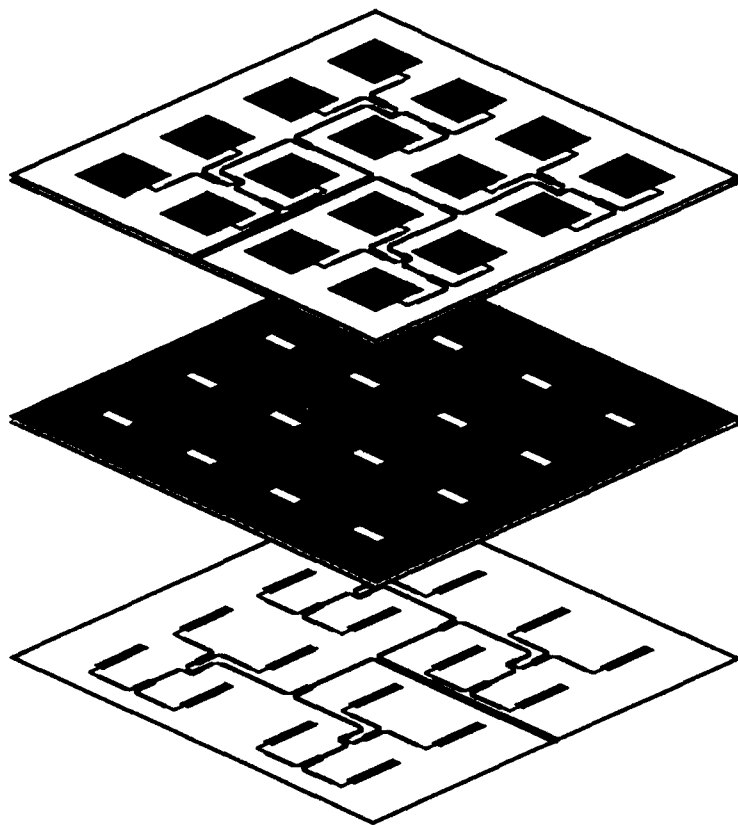


Figure 1. A Dual-Polarization Microstrip Patch Array with Wideband Corporate Feed Network

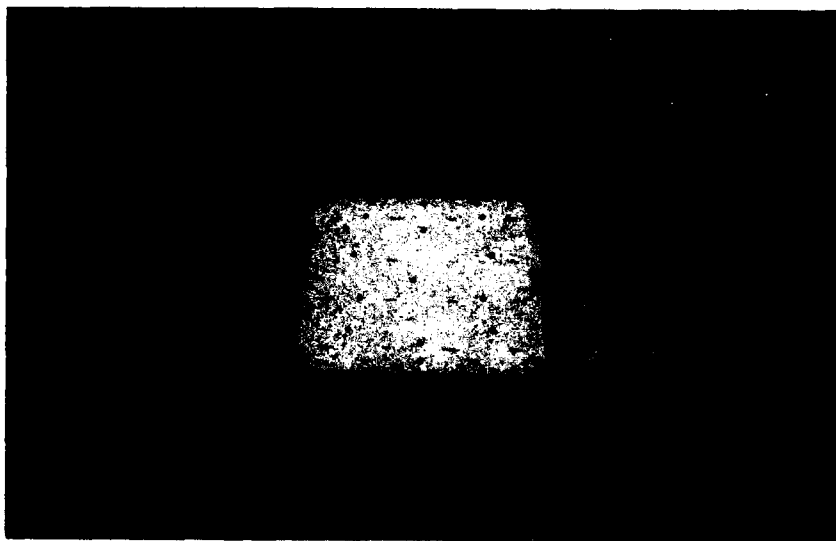


Figure 2. The Experimental Model of Figure 1.

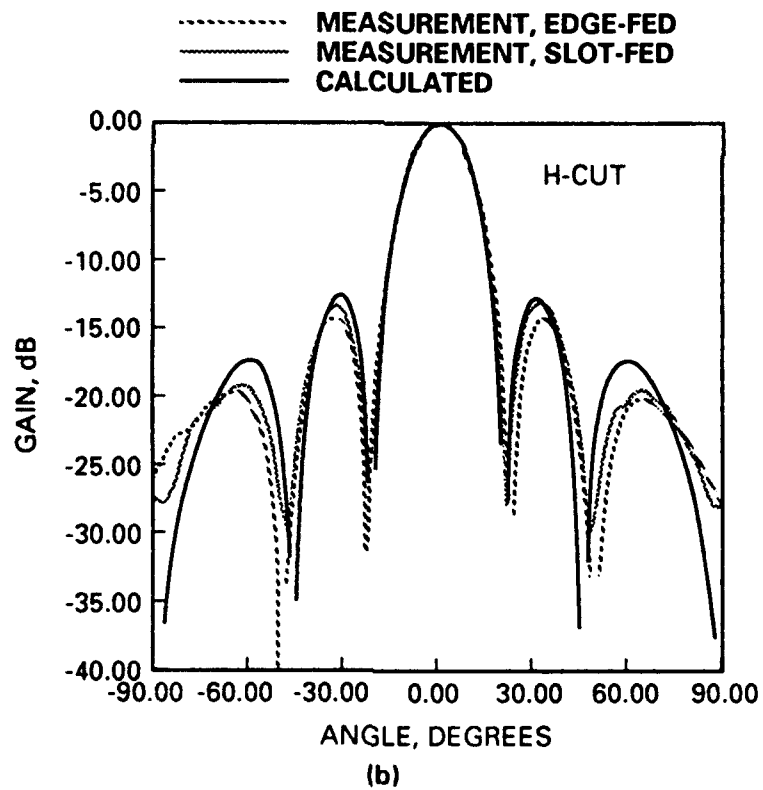
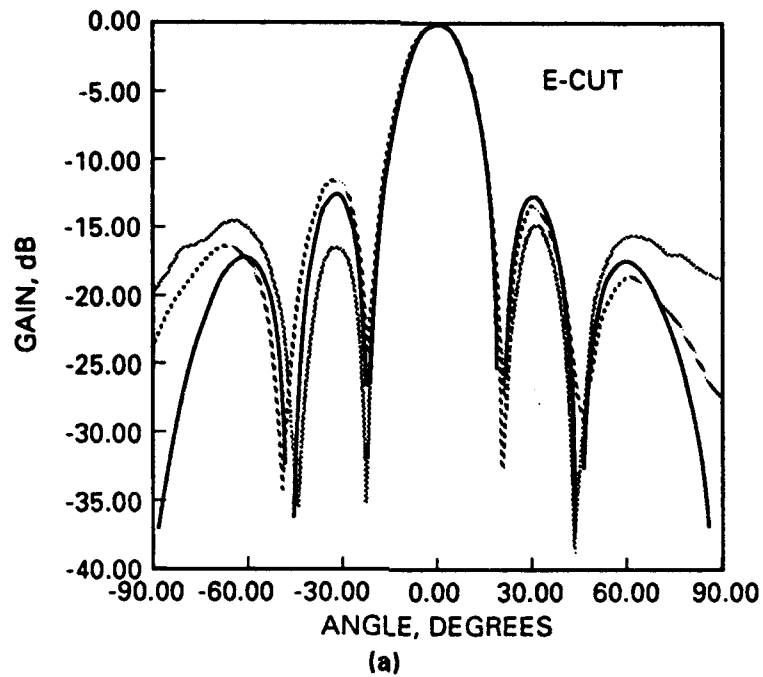


Figure 3. The Measured vs. the Calculated Patterns of the Dual-Polarized Patch Array of Figure 2. (a) E-Cut (b) H-Cut

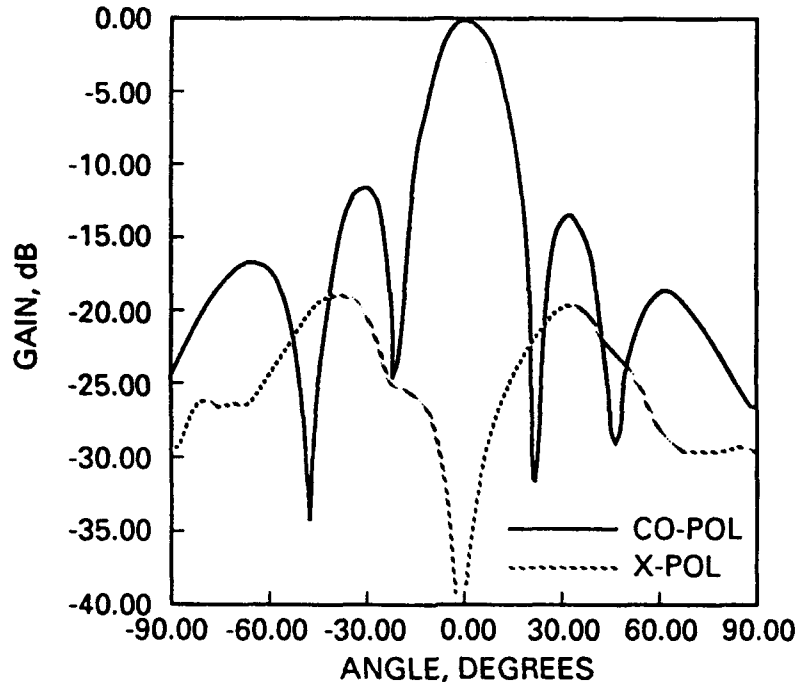


Figure 4. CO-Pol and X-Pol Patterns of the Dual-Polarized Patch Array of Figure 2.

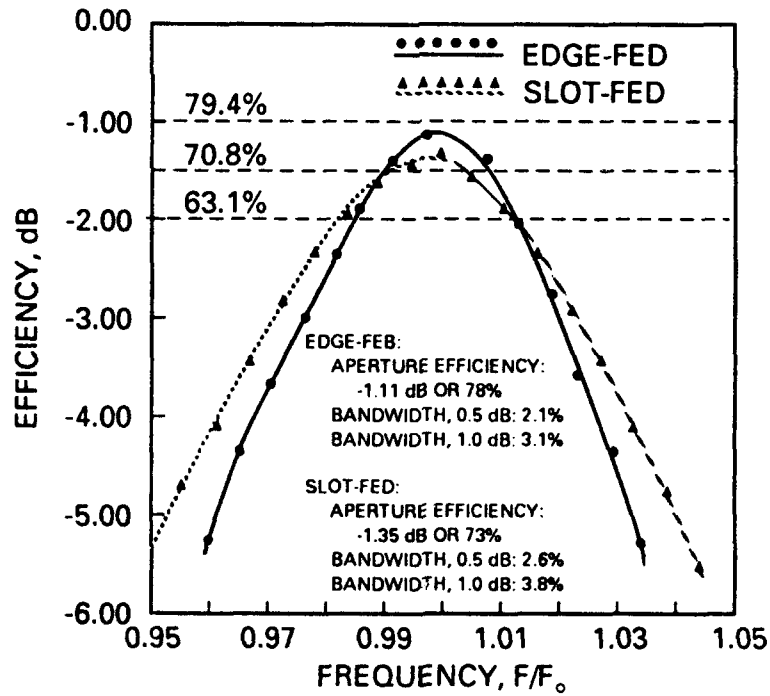


Figure 5. The Measured Efficiency of the Dual-Polarized Patch Array of Figure 2.

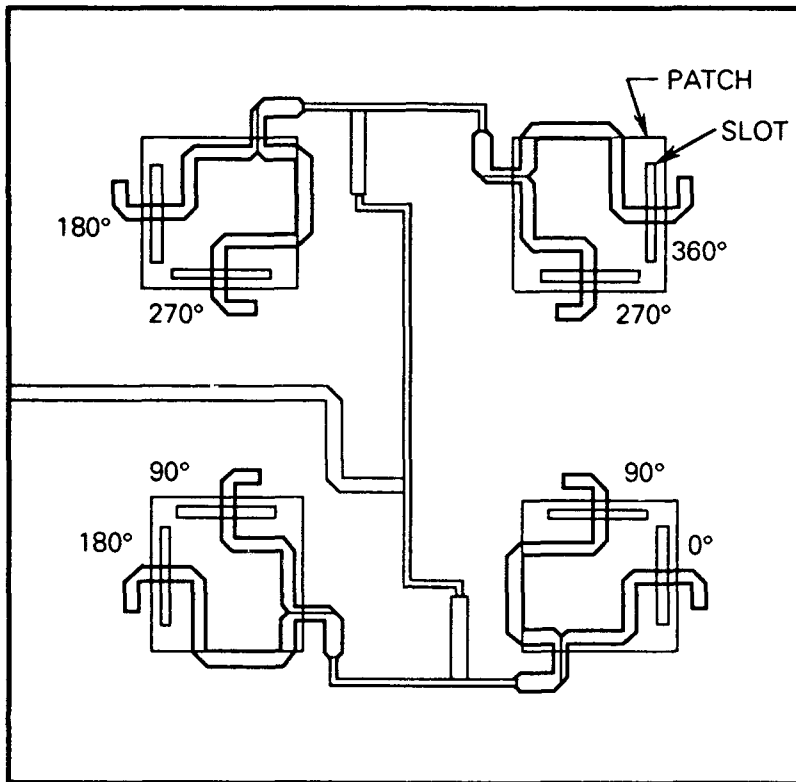


Figure 6. Subarray Circuit Layout for a Circularly Polarized Slot-Coupled Patch Array



Figure 7. The Experimental model of a CP Slot-Coupled Patch Array (Slots not Shown)

250872-91

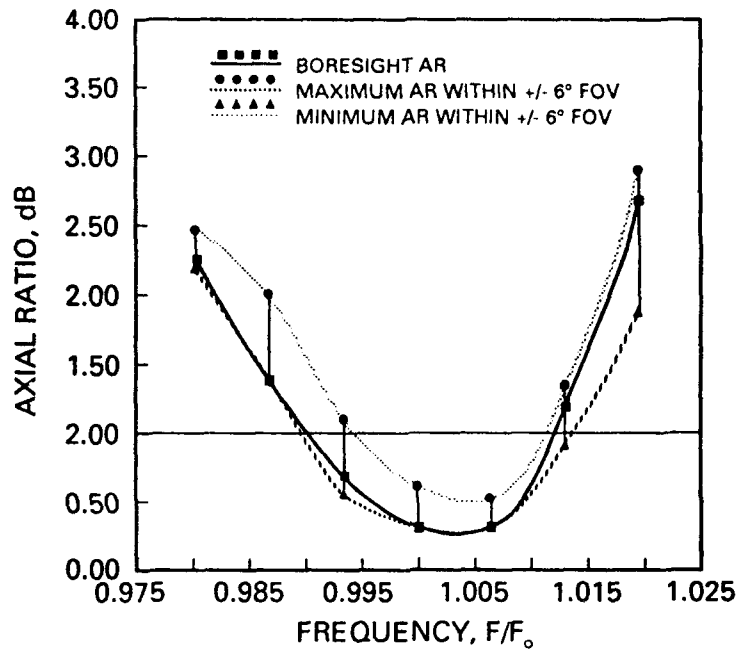


Figure 8. The Measured AR of the CP Slot-Coupled Patch Array of Figure 7.

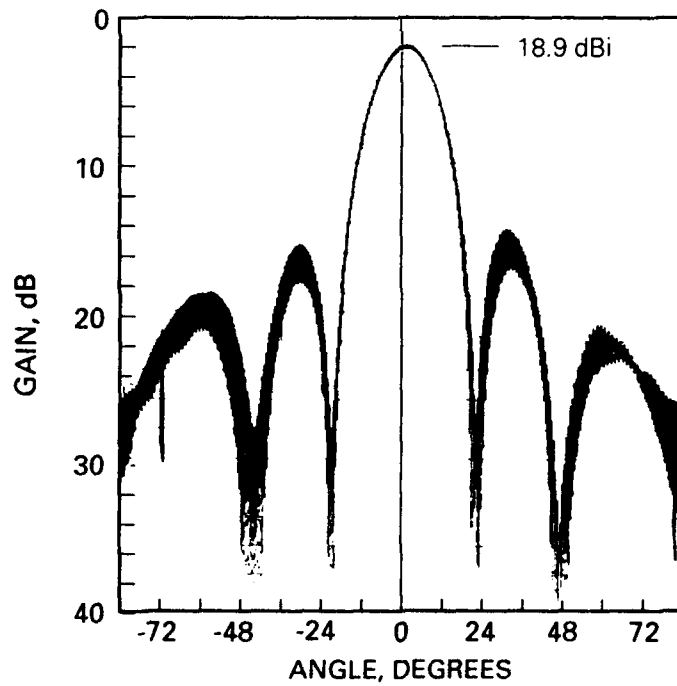


Figure 9. The Measured Spinning-Linear Pattern of the CP Slot-Coupled Patch Array of Figure 7.

ARRAY MUTUAL RESISTANCE CALCULATION
FROM FAR-FIELD RADIATION PATTERNS

David D. de Schweinitz

General Dynamics
Fort Worth Division

ABSTRACT

A method is described for calculating array mutual resistance from far-field radiation patterns. The relationship of mutual resistance to element gain and array gain is described and exploited. This calculation is often less difficult than near-field mutual impedance computations. Since only far-field performance is considered, results may be applied to broad classes of arrays without detailed analysis of specific element types. The mutual resistance value thus obtained is useful in determining the minimum achievable mutual coupling for a given array geometry. The general procedure is described in detail. It is illustrated for a Hertzian Dipole array, and results are shown to be mathematically equivalent to those obtained from traditional near-field analysis.

1. Introduction

If there were no mutual coupling in a given array, then its array gain would be equal to the vector sum of the individual element gains. If all embedded element patterns in the array were identical, and there were no mutual coupling, then the array gain would be equal to the element gain times the number of elements. This would be true for any scan condition where the signals from all elements add coherently in one direction. For this ideal array, the scanned array gain would exactly follow the envelope of the embedded element beam shape. There would be no array impedance change with scan angle (active VSWR). These properties hold regardless of array spacing, as long as there is no mutual coupling in the array.

The converse is also true: if the gain of an array over that of a single element is not equal to the number of elements, then there must be mutual coupling. Just as radiation resistance of an element may be determined from far-field radiation patterns, so may mutual resistance of array elements be determined from far-field array patterns.

This paper describes a "Resistance Method" of mutual coupling prediction. This procedure requires much less information about the element design than the standard method involving near-field computations. Since only far-field performance is considered, analysis of an array geometry may be performed independent of element type. Such analyses can be valuable in understanding inherent array performance aspects independent of the antenna element design.

A simple formula is presented that relates mutual resistance to array gain. It is assumed throughout this analysis that all elements are lossless. The only loss mechanism considered is the power transfer to terminated neighboring elements.

The coupling parameter that is of most interest to array designers and users is total mutual coupling. This includes the effects of both mutual resistance and mutual reactance. The Directivity Method allows for calculation of only the mutual resistance component. A minimum level of total mutual coupling is then predicted assuming no mutual reactance. The mutual resistance can be thought of as being set by the array geometry, while the mutual reactance is

determined by the element design. The Directivity Method, then, can be used to define a minimum achievable mutual coupling level obtainable for a given array geometry.

The Directivity Method is first described and illustrated for two Hertzian Dipole elements. The mutual resistance is calculated by the Directivity Method and compared with the values obtained using the dipole near-fields in the Reaction-Integral Equation. The equations obtained by the two methods are shown to be mathematically equivalent. The minimum mutual coupling parameter described above is then computed and compared with the exact value.

The method is then described in general terms. Structural-mode and antenna-mode mutual coupling are discussed as they apply to the various acceptable definitions of embedded element radiation patterns that may be used in the model. The majority of this paper deals with two-element arrays. Extension of the methods to larger arrays is discussed. From the relationships developed, a fundamental limitation on the mutual coupling performance of closely-spaced arrays is suggested.

2. Two-Element E-Plane Array of Hertzian Dipoles

Referring to Figure 1, the distant E-field from a single element is defined by:

$$E_{11} = \frac{I_{11} \eta L \sin \theta}{2 r} \quad (1)$$

\vec{E}_{11} (far field)

\vec{E}_E

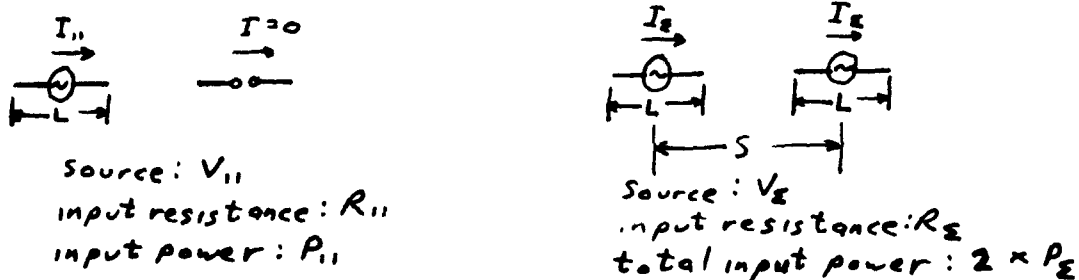


Figure 1 Hertzian Dipole Array Geometry

Note that for this Hertzian Dipole example problem, the element pattern used in these calculations is equivalent to the isolated element pattern. This is not the case for the analysis of general arrays. Embedded- element pattern considerations are discussed in the following section.

The single-element directivity is calculated by

integrating the radiation pattern. Spherical coordinates are used, with Theta defined as zero along the axis of the elements.

$$\begin{aligned}
 D &= \frac{U}{U_0} ; U = E^2 \left(\theta = \frac{\pi}{2} \right), U_0 = \frac{1}{4\pi} \int_0^{2\pi} \int_0^{\pi} E^2 \sin(\theta) d\theta d\phi \\
 U &= \frac{I_0^2 \eta^2 L^2}{4r^2} \\
 U_0 &= \frac{2 \cdot I_0^2 \eta^2 L^2}{3 \cdot 4r^2} \\
 D &= 1.5 \approx 1.8 \text{ dBi}
 \end{aligned} \tag{2}$$

The distant E-field from the broad-side-scanned array is given by:

$$\begin{aligned}
 E_{\Sigma} &= \left| e^{j0} + e^{jkscos\theta} \right| \left(\frac{I_0 \eta L \sin \theta}{2r} \right) \\
 &= \sqrt{2 + 2 \cos(kscos\theta)} \left(\frac{I_0 \eta L \sin \theta}{2r} \right)
 \end{aligned} \tag{3}$$

Note here that the broad-side far-field from the array with equal element currents is dependent only on the current magnitudes. Array spacing is not a factor in this equation. If the impedance of an array element were the same as that of a single element, then the array gain can be seen to be 3 dB greater than that of a single element, independent of spacing. Yet we know that spacing is an important factor in array gain. We

can conclude, therefore, that the impedance of an array element must be dependent on array spacing. The mechanism for that dependency is mutual coupling. This argument is the basis for the Directivity Method of mutual resistance calculation.

Continuing with the example, array directivity is then calculated by integrating its far-field radiation pattern:

$$D = \frac{U}{U_0}; U = E^2 \left(\theta = \frac{\pi}{2}\right), U_0 = \frac{1}{4\pi} \int_0^{2\pi} \int_0^\pi E^2 \sin\theta \, d\theta \, d\phi$$

$$U = 4 \frac{I_\Sigma^2 \eta^2 L^2}{4\pi r^2}$$

$$U_0 = \left[\int_0^\pi (1 + \cos(kS \cos\theta)) \sin^3\theta \, d\theta \right] \frac{I_\Sigma^2 \eta^2 L^2}{4\pi r^2} \quad (4)$$

$$D = \frac{U}{U_0} = \frac{4}{\int_0^\pi (1 + \cos(kS \cos\theta)) \sin^3\theta \, d\theta}$$

This expression for directivity can be used as is,

employing numerical integration to generate directivity values for specific spacings. This is the method that is used in the analysis of general arrays. It is interesting for our purposes, however, to solve the expression in closed form. The process is tedious but straight-forward (involving several steps of integration by parts). and yields:

$$\int (1 + \cos(ks \cos \theta)) \sin^3 \theta \, d\theta \quad (5)$$

$$= \frac{4}{3} - \frac{4 \cos(ks)}{(ks)^2} - \frac{4 \sin(ks)}{(ks)^3}$$

The expression for the array directivity then reduces to:

$$D = \left[\frac{1}{3} - \frac{\cos(ks)}{(ks)^2} - \frac{\sin(ks)}{(ks)^3} \right]^{-1} \quad (6)$$

The directivity equation (6) defines the far-field signal level that would result from a given input power to the array, as a function of spacing.

The field equations (1) and (3) define the far-field signal level as a function of element currents.

Relative array vs. element currents may therefore be calculated by equating these relationships:

$$\frac{D(\text{array})}{D(\text{element})} = \frac{E^2(\text{array})}{E^2(\text{element})} = \frac{4\left(\frac{I_{\Sigma}^2 \eta^2 L^2}{4r^2}\right)}{\left(\frac{I_{11}^2 \eta^2 L^2}{4r^2}\right)} = 4 \frac{I_{\Sigma}^2}{I_{11}^2} \quad (7)$$

$$\Rightarrow \frac{I_{11}^2}{I_{\Sigma}^2} = 4 \frac{D(\text{element})}{D(\text{array})}$$

The relationship between the radiation resistances of the array and the single element may then be determined by equating the input powers and using Equation 7:

$$P(\text{element}) = P(\text{array})$$

$$I_{11}^2 R_{11} = 2 I_{\Sigma}^2 R_{\Sigma} \Rightarrow \frac{R_{\Sigma}}{R_{11}} = \frac{I_{11}^2}{2 I_{\Sigma}^2} = 2 \frac{D(\text{element})}{D(\text{array})} \quad (8)$$

This leads to a general expression for the relative radiation resistances of two-element arrays with identical element patterns:

$$\frac{R_{\Sigma}}{R_{11}} = 2 \frac{D(\text{element})}{D(\text{array})} \quad (9)$$

Mutual resistance is then calculated to be:

$$R_{\Sigma} = R_{11} + \frac{I_2}{I_1} R_{12} = R_{11} + R_{12} \Rightarrow R_{12} = R_{\Sigma} - R_{11}$$

$$R_{12} = R_{11} \left(\frac{R_{\Sigma}}{R_{11}} - 1 \right) = R_{11} \left(2 \frac{D_{(element)}}{D_{(array)}} - 1 \right) \quad (10)$$

It can be seen from Equation 10 that for close spacings where the array gain is low, the mutual resistance is positive. For the spacing where the array provides 3 dB of increased gain over that of the element (one half-wavelength for omni-directional radiators, approximately 0.7 wavelength for Hertzian Dipoles), the mutual resistance is zero. For the spacings where the array exhibits greater than 3 dB of gain improvement, the mutual resistance is negative. For very wide spacings, the resulting interference-type array pattern yields 3 dB of array gain over that of a single element, and mutual resistance is zero, as expected.

For the Hertzian Dipole array:

$$\frac{D_{(element)}}{D_{(array)}} = \frac{1}{2} - \frac{3 \cos(ks)}{2 (ks)^2} - \frac{3 \sin(ks)}{(ks)^3} \quad (11)$$

yielding for the mutual resistance:

$$R_{12} = R_{11} \left(\frac{-3 \cos(kS)}{(kS)^2} - \frac{3 \sin(kS)}{(kS)^3} \right) \quad (12)$$

The relationship between array directivity and mutual resistance is illustrated in Figure 2, where these quantities are plotted as a function of element spacing.

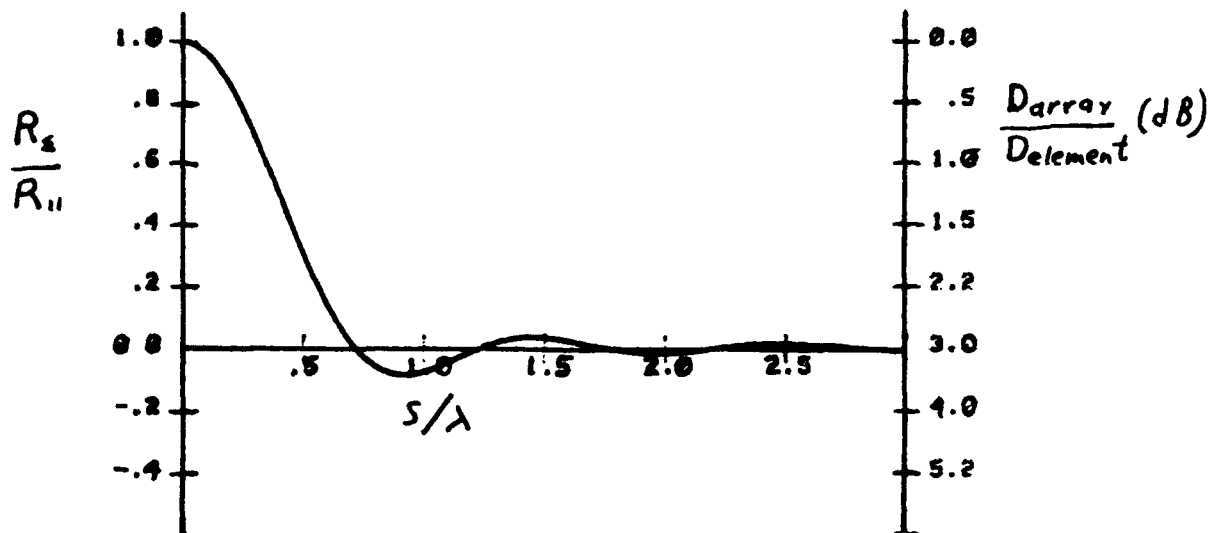


Figure 2. Relative Directivity and Mutual Resistance of two Co-Linear Hertzian Dipoles

Mutual coupling may then be estimated from the ratio of mutual- to self-resistance. The absolute mutual resistance is calculated here for comparison purposes. The radiation resistance of a single Hertzian Dipole element, obtained from its far-field radiation pattern, is well documented to be:

$$R_{11} = \frac{P_{rad}}{I_{11}^2} = \frac{1}{I_{11}^2} \int_0^{2\pi} \int_0^{\pi} \frac{E_{11}^2}{\eta} \sin\theta d\theta d\phi = \frac{2\eta\pi}{3} \left(\frac{L}{\lambda}\right)^2 \quad (13)$$

leading to:

$$R_{12} = -2\eta\pi \left(\frac{L}{\lambda}\right)^2 \left(\frac{\cos(ks)}{(ks)^2} + \frac{\sin(ks)}{(ks)^3} \right) \quad (14)$$

by Directivity Method

To summarize, the near-field mutual resistance has been calculated for a Hertzian Dipole array using only knowledge of the far-field radiation patterns. No limiting assumptions have been made, therefore the results should be identical to those obtained using the Reaction-Integral Equation and the near-fields. This is verified below:

$$Z_{12} = \frac{-1}{I_1} \int_0^L E_{12} dz = \frac{-L E_{12}}{I_1}, \text{ where}$$

$$E_{12} = \frac{-\eta k L I_1}{\lambda} e^{-jkr} \cos \theta \left[\left(\frac{1}{jkr} \right)^2 + \left(\frac{1}{jkr} \right)^3 \right] \hat{r} \\ - \frac{\eta k L I_1}{2\lambda} e^{-jkr} \sin \theta \left[\frac{1}{jkr} + \left(\frac{1}{jkr} \right)^2 + \left(\frac{1}{jkr} \right)^3 \right] \hat{\theta} \quad (15)$$

For end-to-end Hertzian Dipoles, the impressed field from one to its neighbor is equal to the radial field component with Theta set to zero:

$$Z_{12} = \frac{-L}{I_1} E_{12} = \frac{\eta k L^2}{\lambda} e^{-jks} \left[\left(\frac{1}{jks} \right)^2 + \left(\frac{1}{jks} \right)^3 \right] \\ = \frac{2\pi \eta L^2}{\lambda^2} e^{-jks} \left[\frac{-1}{(ks)^2} + \frac{j}{(ks)^3} \right] \quad (16)$$

The radiation resistance is the real part of this quantity:

$$R_{12} = \text{Re} \{ Z_{12} \} \\ = 2\pi \eta \left(\frac{L}{\lambda} \right)^2 \left[\frac{-\cos(ks)}{(ks)^2} - \frac{\sin(ks)}{(ks)^3} \right] \quad (17)$$

leading to,

$$R_{12} = -2\pi \eta \left(\frac{L}{\lambda}\right)^2 \left[\frac{\cos(kS)}{(kS)^2} - \frac{\sin(kS)}{(kS)^3} \right]$$

by Reaction Integral Method

(18)

which can be seen to be equivalent to Equation 14. The Directivity Method of mutual resistance calculation is therefore shown to yield an exact solution for the case of two end-to-end Hertzian Dipoles.

This analysis was provided to illustrate the Directivity Method and to demonstrate its validity. One could observe at this point that while the Directivity Method does yield an exact solution for a Hertzian Dipole array, it only provides half of the information that the Reaction-Integral Method provides, and requires at least as much computation. The value in the Directivity Method is obviously not the ability to determine mutual resistance of simple antennas that may be analyzed in closed form. Its value is the ability to predict a minimum achievable value for mutual coupling of general arrays. This procedure is described below.

The mutual coupling and passive input impedance of a linear, symmetric two-port network may be found from the Z-parameters by using the following equations:

$$S_{12} = \frac{2 Z_0 Z_{12}}{(Z_{11} + Z_0)^2 \cdot Z_{12}^2}, \quad Z_{in} = Z_{11} - \frac{Z_{12}^2}{Z_{11} + Z_L} \quad (19)$$

It is useful to calculate the mutual coupling with the input impedance of each port conjugate-matched to the load on the other port. The required conditions are described in Equation 20, with Z_{11}' representing the self-impedance of the reactively-tuned element.

$$Z_{in} = Z_L^* \Rightarrow Z_L = R_L + jX_L; R_L = \sqrt{R_{11}^2 + X_{12}^2 - R_{12}^2 - \left(\frac{R_{12}X_{12}}{X_{11}}\right)^2} \quad (20)$$

$$X_L = \frac{R_{12}X_{12}}{R_{11}} - X_{11}; \text{ let } Z_0 = R_L, Z_{11}' = Z_{11} + jX_L, Z_{12}' = Z_{12}$$

If the input impedance is real or the reactive impedances are not known, the relationship reduces to:

$$S_{12} \geq \frac{2 \frac{R_{12}}{R_{11}} \sqrt{1 - \left(\frac{R_{12}}{R_{11}}\right)^2}}{\left(1 + \sqrt{1 - \left(\frac{R_{12}}{R_{11}}\right)^2}\right)^2 - \left(\frac{R_{12}}{R_{11}}\right)^2} \quad (21)$$

The imaginary impedance components are not available from Directivity Method. This is equivalent to saying that these components are not dictated by the radiation

pattern shapes and the array geometry. These unknowns represent the available freedom in the array mutual coupling design that is independent of far-field performance. For this mutual coupling analysis, then, the reactive parts of the impedances are set to zero. The coupling value thus obtained represents the minimum achievable for an array with the far-field characteristics used in the analysis.

Minimum mutual coupling values for elements with the far-field performance of Hertzian Dipoles are plotted in Figure 3. Exact mutual coupling values, using the complex impedances obtained from the Reaction-Integral Equation, are also plotted.

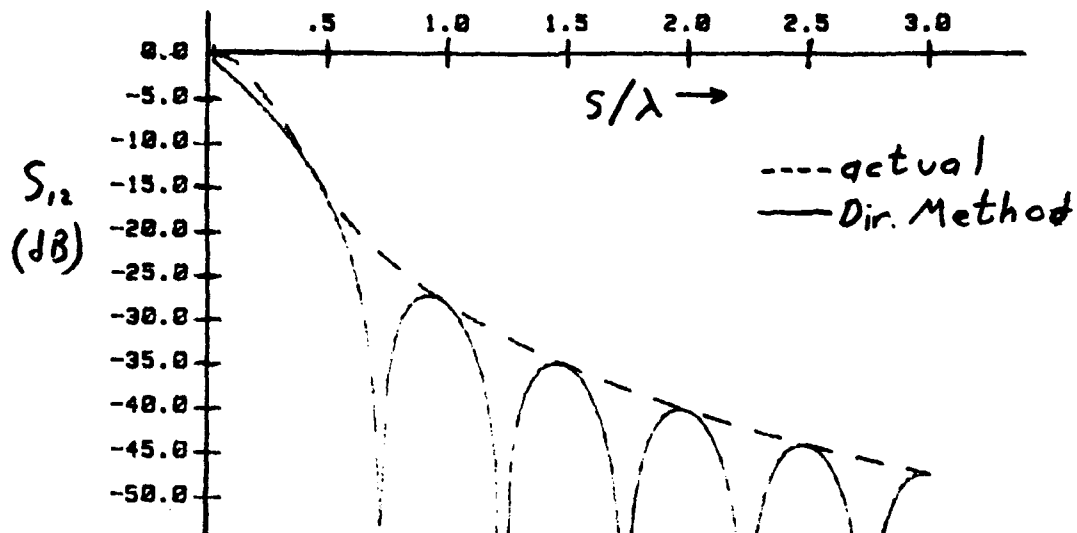


Figure 3. Theoretical Minimum vs. Actual Mutual Coupling for Co-linear Hertzian Dipoles

3. General Array Analysis: Alternate Definitions of Embedded-Element Radiation Patterns

The general equations for mutual resistance and mutual coupling given in Equation 19 are valid for any two-element array configuration with identical embedded-element radiation patterns. There are several definitions of embedded-element radiation pattern which may be used for this analysis, and one common definition which may not. These are described below.

In the discussion of the Hertzian Dipole array, the definition of the embedded-element pattern presented no problem. The radiation pattern of one element was considered to be the result of radiation from current flowing on that element only. This presented no problem because : (1) the assumed current distribution was very simple (uniform), and identical to that of an isolated element, (2) due to the small element size, the radiation patterns could be assumed to be identical, and (3) The array geometry was such that the individual current elements were distinct and separate. All current is properly accounted for by this method, and the results are exact.

This approach can be used in the definition of embedded-element radiation patterns if the elements are: (1) short, resonant elements that only support one major current mode, or (2) closely-spaced elements of any type, since radiation pattern predicted from each element will be broad and relatively independent of the exact current distribution. For spacings much less than one-half wavelength, in fact, it is reasonable to simply assume that the element pattern is omni-directional.

This approach to embedded-element pattern definition can be considered a pure application of array theory, since the computed array field is calculated simply by vector addition of the contribution of all of the current elements, and each current element is only counted once.

Problems could occur, however, when using this approach in the analysis of arrays with parasitic structure or elements. To use this approach, each current source must be completely assigned to one element or another, where in reality the border between adjacent elements may be blurred. Also, the actual current distribution across an array with parasitic elements, and therefore the effective element pattern, may be difficult to

predict. The embedded element pattern is often quite different from that of an isolated element of the same geometry.

A second valid embedded-element radiation pattern definition is based on a Z-parameter model of arrays. Each element pattern is calculated with the other element(s) open-circuited at the feed-point. For short, resonant elements, this is nearly equivalent to the above definition, since little current will flow in the open-circuited neighboring element(s). For larger, broad-band elements, however, the "structural-mode" coupled currents can be significant and lead to pattern distortion. This in turn invalidates the analysis because the element patterns could not be assumed to be equal.

A third definition of embedded-element radiation pattern is based on S-parameters, and is favored by antenna users. This is the common definition where the element is measured with the other element(s) terminated in Z_0 . This definition is not suitable for this analysis. It does, however, approach the Z-parameter-based definition described above as the mutual-coupling is reduced.

In summary: (1) closely-spaced arrays can be modeled assuming omni-directional element patterns. The minimum achievable mutual coupling will be fairly high and can be predicted quite easily using the Directivity Method. (2) Arrays with spacings of one half-wavelength or more can be made to achieve low mutual coupling. The embedded-element pattern that corresponds to the minimum mutual resistance can be readily predicted, and used as a tool in specifying and designing the array. As the coupling is reduced, the load impedances have a diminished effect on the embedded element pattern, and the analysis becomes more accurate.

4. General Two-Element Array

Calculated mutual impedance and minimum achievable mutual coupling of several different two-element arrays are plotted in Figure 4. The effect of embedded-element pattern beam width on mutual coupling is illustrated. One note should be made here regarding the mutual resistance values predicted by the Directivity Method. For the case of the Hertzian Dipole array, the value obtained through this analysis was the exact mutual resistance. For the general

case, the impedance phase may be rotated by feed network and other effects. Strictly speaking, these effects could be corrected out with knowledge of the far-field radiation phase, but this is neither practical or necessary. Mutual resistance is not a particularly useful quantity in itself. What is of interest is the minimum achievable mutual coupling. The mutual resistance value obtained through this analysis is valid for that purpose.

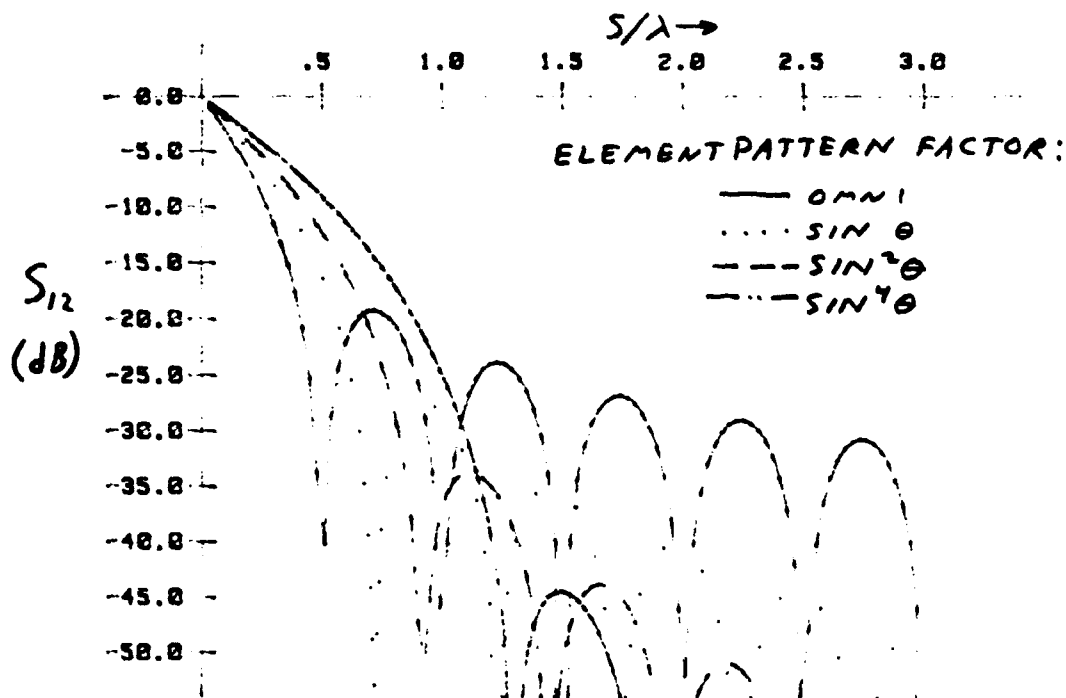


Figure 4. Minimum Achievable Mutual Coupling for Various Embedded-Element Radiation Characteristics

Several general comments may be made at this point for arrays which meet the conditions described above: (1) arrays of narrow-beam elements have more inherent coupling than arrays of wide-beam elements. (2) Mutual coupling may be eliminated only for arrays with spacings of one half-wavelength or greater. (3) One strategy for reducing mutual coupling in an array design is to try to shape the element pattern such that the ratio of array- to element-gain is equal to the number of elements.

5. Total Coupled Energy in Large Arrays

An indication of the extent of mutual coupling in a large array can be found from the relative radiation resistance of the array compared with that of an element. If the array is sufficiently long, the current magnitude in all elements may be assumed to be equal. For spacings of almost one full wavelength or closer, the directivity is approximately:

$$D \approx \frac{2L}{\lambda} = 2N \frac{s}{\lambda}, \quad s \leq \lambda \quad (22)$$

The relative radiation resistance of the array can then be determined by generalizing Equation 9:

$$R_{\Sigma} = R_{11} + (R_{12} + R_{13} + \dots) = R_{11} \left(N \frac{D(\text{element})}{D(\text{array})} \right) \quad (23)$$

6. Conclusions

This analysis gives an indication of the level of mutual coupling that must be present in arrays based solely on far-field performance and geometry. For arrays of omni-directional elements, total mutual coupling can only be minimized with half-wavelength (or a multiple of a half-wavelength) spacing. For arrays of directive elements, increased spacing must be used if mutual coupling is to be minimized. This suggests that if half-wavelength spacing and low mutual coupling are both desired, the embedded-element radiation pattern must be broad in any plane that the array has directivity.

Reference

Balanis, C. A. (1982) *Antenna Theory*, Harper and Row

NESTED COMPLEMENTARY PAIR ARRAYS FOR VEHICULAR APPLICATIONS

Dr. Klaus G. Schroeder
RESEARCH & DEVELOPMENT LABORATORIES
5800 Uplander Way
Culver City, California 90230-6608

ABSTRACT

An array system is described which covers an 8:1 frequency range in two subbands at VHF. Four beams are formed at right angles in each subband, which are selected by switching, and are independently selectable in each subband. The low-frequency subband uses wire-outline endfire complementary pairs and the high-frequency band uses endfire monopole pairs around a common central reflector. The system will fit on small vehicles, such as troop carriers, tanks, and helicopters. Patterns, input impedances and band-to-band isolation are presented for a full-scale mock-up.

1. EXTERNAL (ENDFIRE) COMPLEMENTARITY

The basic principles governing hybrid-fed complementary pairs were already evaluated previously,^{1,2,3} and a radiator concept described which circumvents the shortcomings of many self-complementary systems. This is the externally complementarized endfire pair of identical elements. Because the same structure is used for both elements, the impedance variation with frequency is identical. Figure 1 shows a typical endfire pair of conical monopoles, where the

impedance of the "front" element A (in the direction of propagation) has been complementarized with respect to "rear" element B by the insertion of time delay ΔT such that $\Delta T = S/V_p$, where V_p = velocity of propagation in the delay line. If S is chosen to be a quarter wavelength at midband, the complementarization is perfect at the center frequency. The amount of rotation the delay line produces around the Smith chart is then 180 deg at midband (perfect complementarity); $\lambda/8$ or 90 deg at half the center frequency; and 270 deg at 1.5 times the frequency for a total impedance bandwidth of 3:1. In practice, up to 4:1 is achieved, because the impedance locus of the conical monopole tends to shrink with increasing frequency. In addition to impedance matching, the radiation resistances can be additive, improving the efficiency of electrically small pairs.⁴ A beneficial by-product of external complementarization is the complete or partial compensation of mutual impedances by the complementarization network. This is described in Figures 2 and 3. In Figure 2, the single endfire pair is analyzed for self- and mutual-impedances. Because of symmetry, the two inputs to the hybrids see the same set of impedances, except that the set at input A has gone through the complementarization network. As long as the amount of complementarization is sufficient to yield acceptable impedance averaging,⁴ the mutual impedances are averaged together with the self-impedances. This is also true for a pair in the presence of one (Figure 3) or more other pairs. The amount of matching power dissipated in the hybrid difference port now depends on the combined self- and

mutual-impedances averaged by the hybrid. The tighter the locus (with frequency) of the self-impedance around the Smith chart centerpoint, the higher the efficiency.

2. THE WIRE OUTLINE RADIATOR

Unfortunately, an efficient endfire complementary pair using these monopoles requires the monopole diameter to be about one third of the height (so that the impedance locus is tight, and the matching loss is no worse than that of say, a 4:1 VSWR), which is not attractive for vehicle installation. Even if the fat monopoles are built in wire cage construction (Figure 4) the resulting structure is mechanically not attractive. The solution to this mechanical problem⁵ is shown in Figures 5 and 6. Figure 5 describes the equivalency theorem, which states that a flat sheet radiator of a width equal to twice the conical monopole diameter has roughly the same impedance locus as the conical monopole provided the gap capacitance is kept approximately constant. The latter condition generally requires the angle, β , to be very small. The resulting flat sheet radiator is still not an attractive vehicular antenna, but it can be replaced with two vertical whips following the outline of the sheet, and interconnected by a feed line emanating from the central feed point (Figure 6). In order to obtain an acceptable impedance locus, a practical vehicular radiator is shaped as shown in Figure 7. The central feed connects to a horizontal feed bar (i.e., $\gamma = 0$) through a short vertical feed stub. The diameter of the horizontal bar and the height of the bar above the

ground plane (i.e., vehicle surface) are adjusted together for optimum impedance locus. Generally, the higher the feedbar has to be (e.g., to clear obstructions) the larger the diameter so as to produce the same Schelkunoff gap capacitance. The width of the feedbar, for optimum use in an endfire pair with four beam directions needs to be approximately a quarter wavelength, i.e., the same as the endfire spacing requirement. If only a single pair is to be implemented, the width can be chosen to be what the optimum conical monopole tends to indicate. Since the height of the optimum monopole is three times the diameter, the optimum equivalent width would be $2 \times h/3$, or (for a \sim quarter wave monopole) $\sim \lambda/6$. This is somewhat narrower, but yields a better impedance match in situations where only left/right or front/back beam directions are required.

3. VEHICULAR ARRAYS OF WIRE OUTLINE RADIATORS

Figure 8 shows an arrangement of two wire-outline monopoles on an armored vehicle (M-113 or similar) with the feedbars arranged so that the beam is pointing to the side (see Figure 9). Depending on which monopole has the delay line in its feed circuit, the beam is pointing either left or right. A simple beam reversal switch arrangement is shown in Figure 10. The feed bars A and B correspond to the bars in Figure 8. The delay line is shorted out for beam reversal, the two feed lines being chosen so that the differential delay either appears in the left (A) or right(B) line; resulting in beam positions I or II.

If four directions are desired (for 360 degree azimuth coverage), the

installation on the vehicle surface requires two additional feed bars. These are indicated in Figure 11 as dashed lines C and D, with associated vertical feed stubs providing additional feed points. Beam positions III and IV are then available from this arrangement, provided the feed circuit of Figure 12 is implemented.⁶ In order to avoid shorting out of the elements by the feed bars, feed line selector switches have to be placed at each element. The circuit of Figure 12 then allows selection of four beam positions at right angles. A top view of the switch layout is shown in Figure 13.

4. NESTED VEHICULAR ARRAYS OF COMPLEMENTARY PAIRS

The lowest frequency which can efficiently be covered depends on the maximum dimension across the vehicle on which the wire outline radiators can be mounted. For vehicles down to the size of an M-113 or similar (e.g., DRAGOON), 17 to 18 MHz is a practical lower pattern and gain limit for four-beam operation. The upper frequency end is then about 3 to 4 times that frequency. This can readily be extended higher by "nesting" a set of "standard" endfire monopole pairs inside the low-frequency array of wire outline radiators. The layout of this array is shown in Figure 14. The feed circuit for the standard endfire monopole is shown in Figure 15. Four endfire pairs are selected (again through switching), rotating the beam around the central reflector element, which is somewhat longer than the active element. The total nested array configuration is shown in Figure 16. Final sizing will depend on lowest frequency and highest

frequency desired; impedance match obtainable at the extreme frequencies; convenient crossover frequency and gain at the lowest frequency. The shown configuration, with some relaxation of one or the other parameters, can cover 18 to 160 MHz. The measured performances are described next.

5. PERFORMANCE MEASUREMENTS OF NESTED COMPLEMENTARY PAIR ARRAYS

The input impedance of a full-size 18 to 60 MHz "Low-band" array of wire outline endfire complementary pairs installed on an M-113 mock-up was measured in the presence of all switching hardware, feed hybrids, cables etc. with both low-band and high-band elements connected. The unused ports were terminated in 50 ohms, and measurements were made for beampointing to the front, the sides, and the rear. The worst case impedance locus (Figure 17) was observed for beampointing to the side for the low-band array while the high-band beams showed insignificant difference between beam positions (Figure 18). As was shown in previous measurement on reflector arrays,^{3,7} the presence of the (central) reflector helps the overall impedance match, because of imperfect complementarity at the high and low ends and beneficial addition of image element reactance.

The patterns for the low-band array are shown in Figure 19. Because the impedance match and gain/were optimized for the low frequency end, the front-to-back ratio above ~55 MHz tended to suffer. However, up to the selected crossover, the pattern performance is as good as can be expected for a limited-size

vehicle. At the low frequency end front-to-back ratio is about 5 dB. The high-band patterns (Figure 20) show 10 dB or better front-to-back ratio, because of the reflector.

A major consideration of the nested-array concept is the option to either combine both inputs through a crossover network, or feed each input from a separate transmitter. The latter option allows simultaneous operation of two different frequencies located in two different subbands, using separate transmitters, with the two beams pointing in arbitrary directions. This concept was tested by measuring the beam-to-beam coupling attenuation. The results showed that the coupling attenuation exceeds 20 dB everywhere except the high end of the low-band frequency range (~ 57 MHz), and for orthogonal beams. Even there, only 1.7% of the power incident on one beamport will be channeled to the other beamport, much less than what is reflected into the associated transmitter by virtue of the residual VSWR.

6. SUMMARY

The complementary pair matching technique was described, with emphasis on endfire complementary pairs, and it was shown how the spatial advantages of the wire outline vehicular radiator approach can be used to form nested arrays of radiators within radiators. The matching system effectively decouples the two radiating systems even when the spacing between individual high- and low-band elements is as low as 0.061 wavelengths, at the low frequency end of a $\sim 8:1$

frequency range dual-band system. Because of perfect or partial complementarity of mutual impedances, beam isolation is very good, and simultaneous operation of two transmitters is possible with the beams pointing at any of four switched positions. Because the system has completely instantaneous bandwidth and no tuning is required, very narrow pulses (as short as 10 nsec) can be transmitted for a 18 to 160 MHz system, and the power level is only limited by coaxial relays or broadband hybrids, which can be built for many kilowatts of average power, unless microsecond beam switching is required in which case the element switches will be the limiting component.

7. ACKNOWLEDGEMENTS

The author wishes to acknowledge the contributions of facilities by Collins Radio, Dallas, Texas, and the Voice of America under whose sponsorship the first complementary pair arrays were constructed. Credit is also due American Electronic Laboratories, Lansdale, PA; on whose test range some of the measurements were performed. Further thanks are due Mr. Preston Law, now of Radio Free Europe, and Mr. Paris Coleman, formerly of the Naval Research Laboratories, for their support and valuable technical comments over the years.

8. REFERENCES

- 1) Schroeder, K. G. (1964) The Complementary Pair—A Broadband Element Group for Phased Arrays, 1964 PTGAP International Symposium Digest, pp 128-133.

- 2) _____, (1965) A New Class of Broadband Antennas Using Complementary Pair Element Groups, 1965 IEEE National Convention, New York, N.Y., Mar 22-26.
- 3) _____, (1965) Linear Broadside Arrays of Complementary Pair Element Groups, URSI Fall Meeting, Dartmouth College, Hanover, N.H., Oct 3-6.
- 4) _____, (1965) On the Averaging of Reflection Coefficients in 180-Degree Hybrid Tees, Proceedings of the IEEE Jun, pp 626-627.
- 5) _____, (1988) Ultra-Broadband Antenna Impedance Matching Using Electrically Small Self-complementary Structures and Endfire Complementary Pairs of Thin-Wire Elements, Proceedings of the TTCP/STP-8 Workshop on Mobile Platform Antennas, Vol. III, Ottawa, Canada, Feb 8-12.
- 6) _____, (1988) U. S. Patent No. 4, 750,000.
- 7) _____, (1977) Electrically Small Complementary Pair (ESCP) with Interelement Coupling, (Co-Author: K. M. Soo Hoo); IEEE Trans. on Antennas and Propagation, Vol. AP-24, No. 4, Sept, pp 411-418.

FIGURE 1 : END-FIRE COMPLEMENTARY PAIR OF CONICAL MONOPOLES (APPROXIMATELY 4:1 BANDWIDTH)

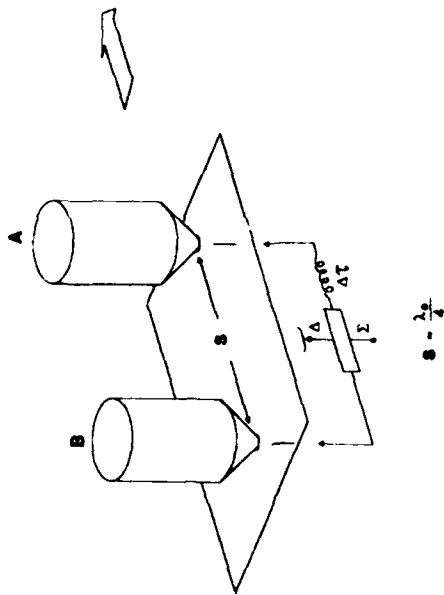


FIGURE 2: MUTUAL IMPEDANCE RELATIONS IN END-FIRE COMPLEMENTARY PAIR

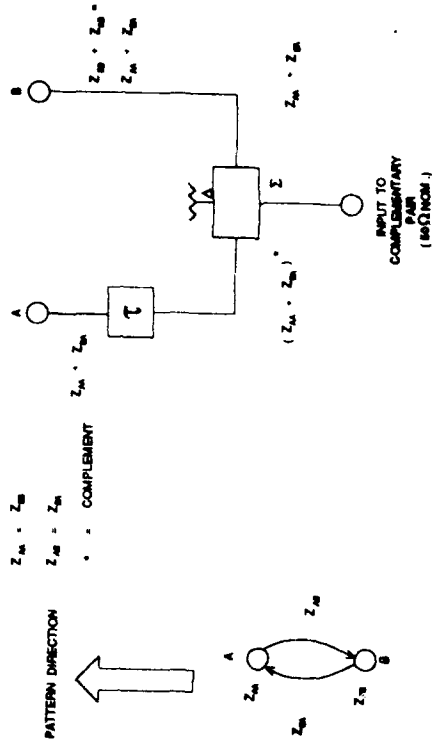


FIGURE 3 : AVERAGING OF MUTUAL IMPEDANCES FOR COUPLED COMPLEMENTARY PAIRS

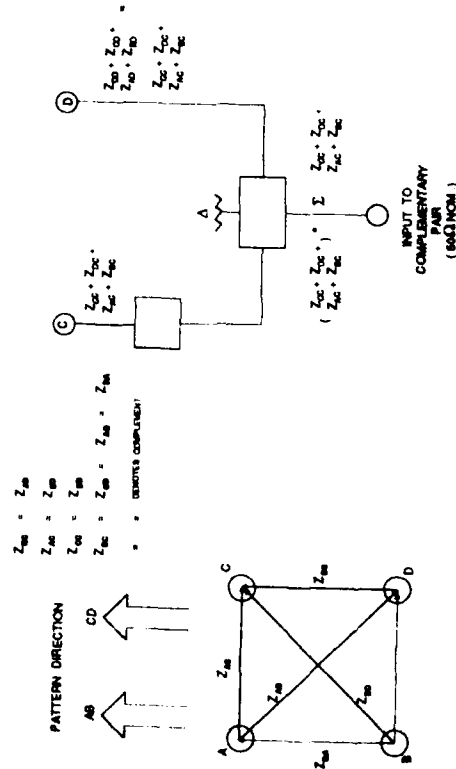


FIGURE 4 : END-FIRE COMPLEMENTARY PAIR OF CONICAL MONOPOLES IN WIRE-CAGE CONSTRUCTION (SUPPORT NOT SHOWN)

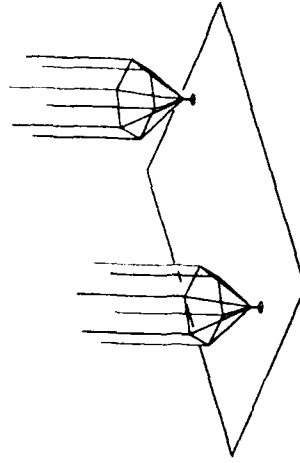
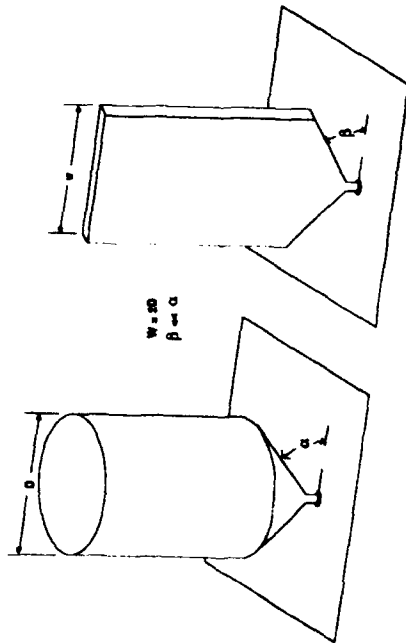


FIGURE 5. EQUIVALENCY BETWEEN CYLINDRICAL AND FLAT MONOPOLES



$W = 2D$
 $h = a$

$a = 66$ DEGREES (RADICAL)

FIGURE 6. EQUIVALENCY BETWEEN FLAT-SHEET AND WIRE OUTLINE MONOPOLES

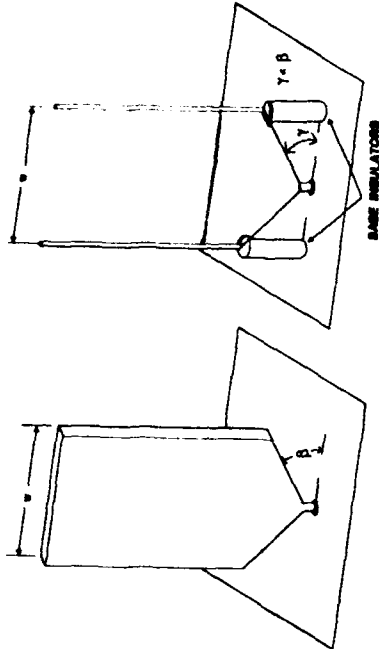
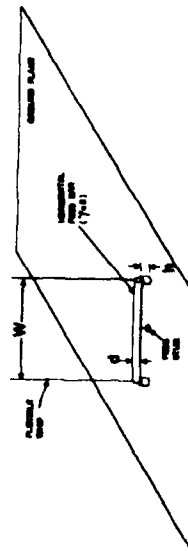


FIGURE 7. PRACTICAL WIRE-OUTLINE MONOPOLE FOR ENDFIRE COMPLEMENTARY PAIR



- $W = \frac{\lambda}{4}$
- $d =$ FEED BAR DIAMETER
- $h =$ HEIGHT OF FEED BAR
- $d, h =$ SELECTED EXPERIMENTALLY TO COMPENSATE AS FOR CONICAL MONOPOLE
- $T = 0$

FIGURE 8. LOW-BAND ENDFIRE COMPLEMENTARY PAIR ON M-113 VEHICLE (LEFT / RIGHT BEAMS)

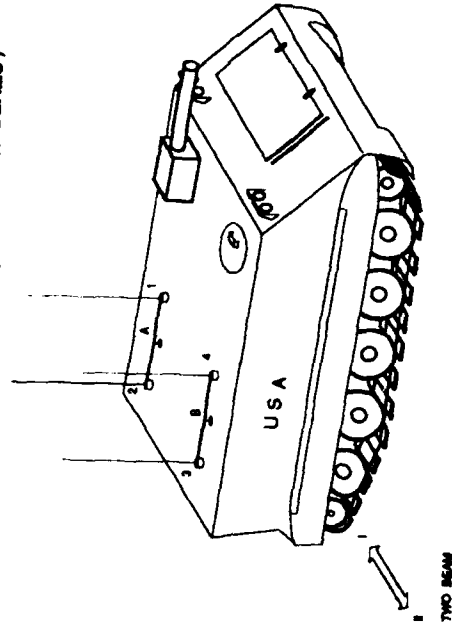


FIGURE 9 : LOW-BAND FEED CONFIGURATION :
END-FIRE COMPLEMENTARY PAIR OF
" WIRE OUTLINE " RADIATORS

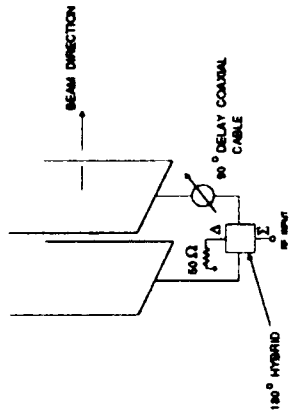
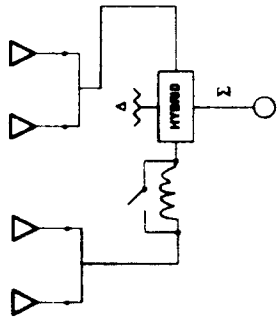


FIGURE 10 : SIMPLIFIED FEED SYSTEM FOR LEFT / RIGHT BEAM
COVERAGE ONLY FOR LOW-BAND WIRE OUTLINE
END-FIRE COMPLEMENTARY PAIR ARRAY



(BEAM POSITION 1)

FIGURE 11 : LOW-BAND END-FIRE COMPLEMENTARY PAIR
ON M-113 VEHICLE (FOUR BEAMS)

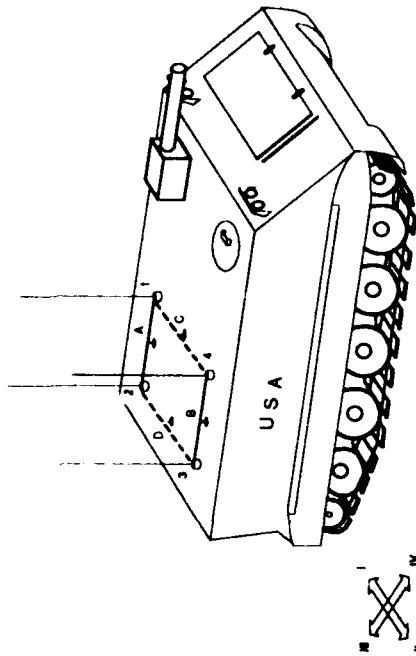


FIGURE 12 : COMPLETE FEED SYSTEM FOR FRONT / AFT-LEFT / RIGHT
FOUR-BEAM WIRE OUTLINE COMPLEMENTARY PAIR ARRAY

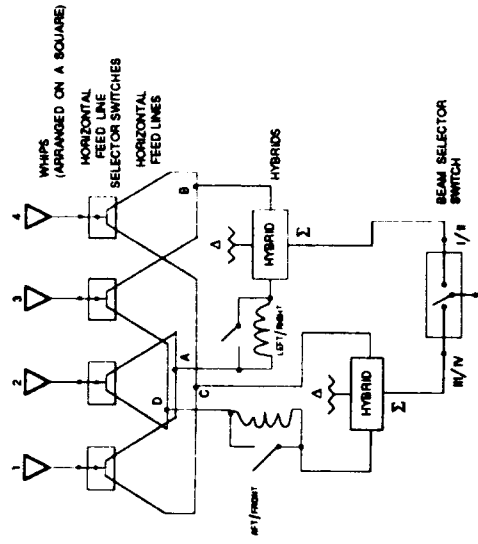


FIGURE 13 : FOUR-BEAM, LOW-BAND ARRAY CONFIGURATION (TOP VIEW)

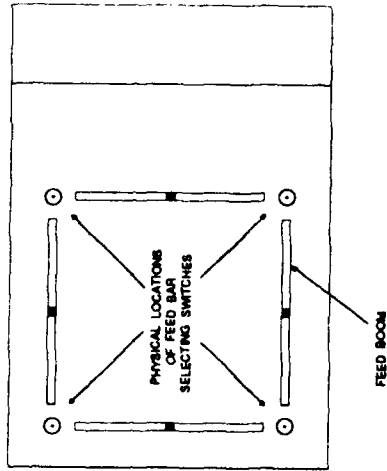


FIGURE 14 : TOP VIEW OF FOUR-BEAM HIGH-BAND ARRAY CONFIGURATION

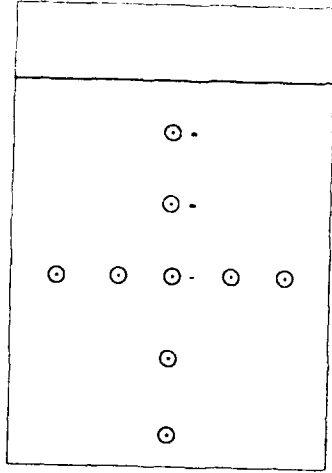


FIGURE 15 : HIGH-BAND FEED CONFIGURATION :
END-FIRE COMPLEMENTARY PAIR OF
MONOPOLES WITH PASSIVE
REFLECTOR

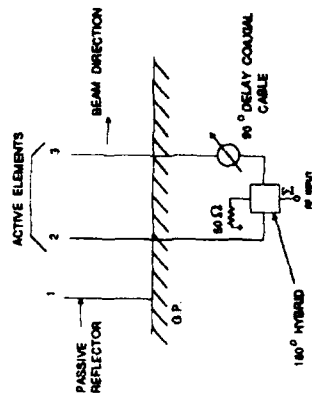


FIGURE 16 : LOW-BAND AND HIGH-BAND NESTED COMPLEMENTARY
PAIR ARRAYS ON M-113

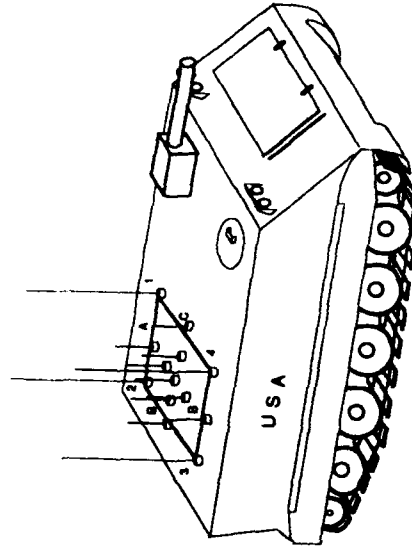


FIGURE 17: FOUR-BEAM FULL SCALE LOW-BAND ARRAY SUM-PORT IMPEDANCE ON VEHICLE MOCK-UP

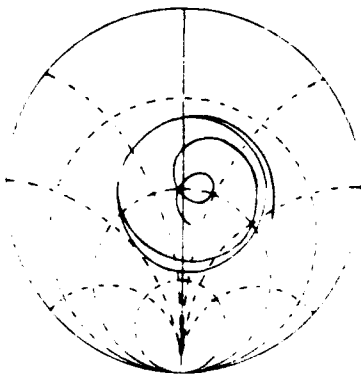
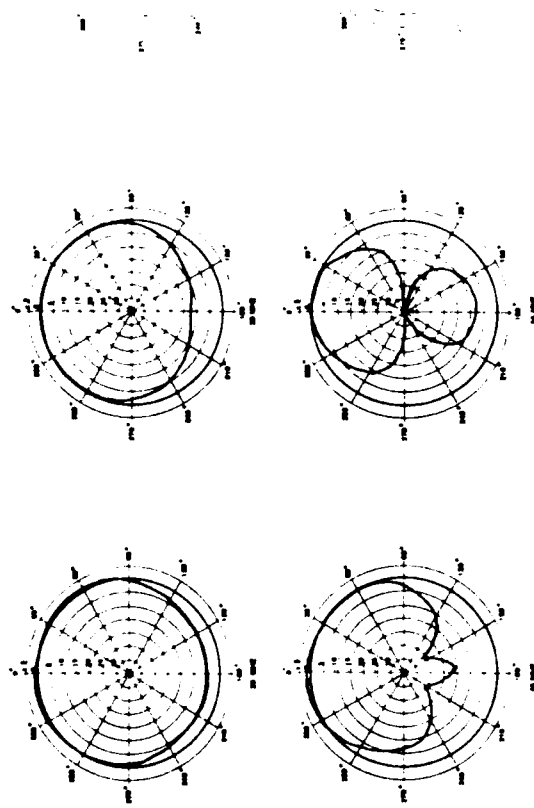


FIGURE 19: LOW-BAND AZIMUTH PATTERNS (BEAM POINTING TO SIDE OF VEHICLE)



FIGURE

TRANSIENT EFFECTS IN REFLECTOR ANTENNAS

R. C. Hansen
Consulting Engineer
P.O. Box 570215
Tarzana, CA 91357
818-345-0770

Abstract

Reflector antenna transient times are investigated. The current build-up transient time, $D^2/16fc$, is important off-axis, and is related to the pattern build-up transient time which varies with pattern angle. Both transient times vary with f/D , and increase directly with D/λ . The pattern transient time, during which the sidelobe structure is established, while zero on-axis, may be larger for large angles than the current transient time. These transient times must be considered in the design of wideband systems as they may affect signal fidelity at the edges of the main beam, and noise, clutter, and signal in the sidelobe region.

1.0 INTRODUCTION

An ideal paraboloidal reflector (no blockage, no surface errors) will simply radiate on-axis, a replica of the feed radiated waveform.^{1,2,3} This is due to the quasi-optical nature of the reflector, and its property of equal path lengths on-axis. Off-axis the path lengths differ, and transient effects occur. These are of two different, but close related types. First is the transient current and transient time on the reflector surface. Second is the pattern build-up (and decay). This build-up also has an associated transient time, as a function of pattern angle. Transmitting antennas are considered here although the results apply equally well to receiving antennas.

Every antenna has at least one transient time related to the build-up, or decay of currents on the antenna. In some complex antennas there may be more than one transient time, or the values may be diffuse. But for most antennas there is a well defined time. For dipoles, for example, it is simply the time for the wave to travel from the feed point

to the dipole ends.⁴ For a reflector antenna it is the time for the current to fill the reflector surface.⁵ Similarly every waveform has a critical time. This may be the pulse width for an impulse or pulsed radar system, or may be the bit time in a phase modulation system. It is now well known that the transient performance of all antennas is critically determined by the ratio of the antenna transient time to the waveform time. If this ratio is small, the antenna acts essentially as a linear transducer. When the ratio is large, the antenna produces a pseudo-differentiation for some angles. A crude way of understanding this is to consider an impulse excitation of a dipole. The impulse radiates at each discontinuity, that is at the ends and at the feed. Due to a reversal of field at the ends the input waveform is reversed (differentiated). Since the three radiation components combine with different phases at different angles, the waveform distortion is a function of angle. When the ratio is neither large nor small, the antenna will produce a build-up transient period and a corresponding decay transient period that are close together or even overlapping,

so that these cases are generally complicated. For a reflector antenna, the transient time ratio of major importance on-axis is that of the feed. Once the importance of this time ratio is understood, it is not necessary to dwell further on this topic.

This paper is, in general, concerned with the transient pattern build-up and decay, and the relevant transient times.

2.0 TRANSIENT EFFECTS DUE TO CURRENT BUILD-UP

Since the parabolic reflector is an equal path length antenna, the radiation from an expanding circle of current on the reflector surface reaches the far-field point on-axis simultaneously. Off-axis there is a transient effect which manifests itself when the signal is modulated with critical period comparable to or smaller than the transient time. To understand this, take the case of a pulse applied to an ideal feed in a parabolic reflector. Consider a focus-fed paraboloidal reflector antenna of diameter D , with a wideband (ideal) feed. The path length from the feed to any point on the reflector surface,

and then on to a virtual aperture plane normal to the axis, is of course constant. However, the path length to the reflector surface alone is $f \sec^2(\psi/2)$ where ψ is measured from the feed, and f is the focal length, see Fig. 1.

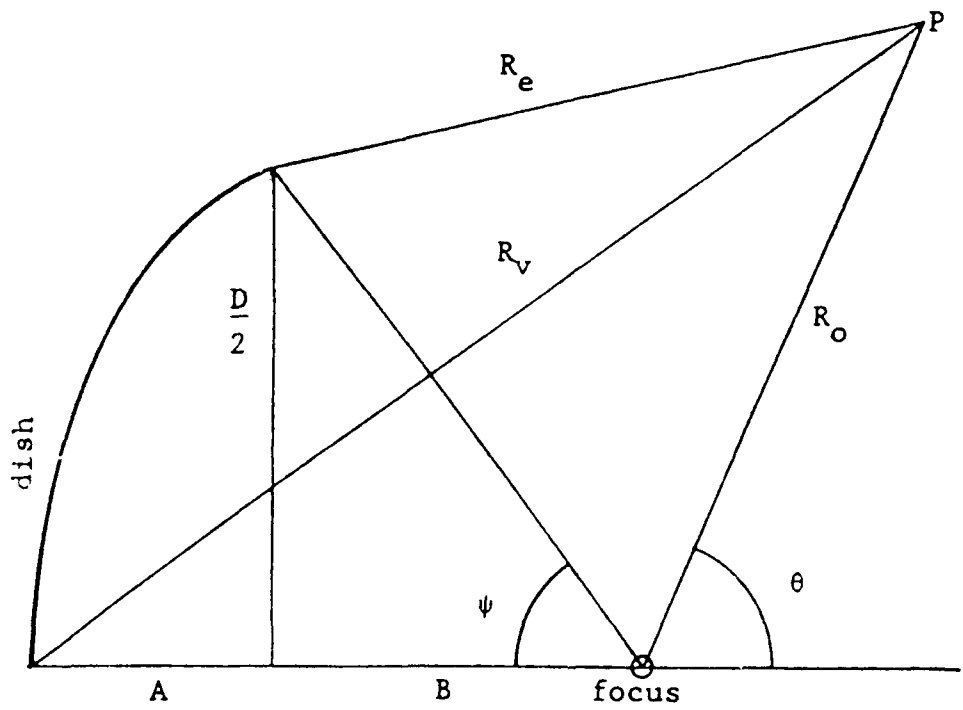


Fig. 1

Ray Geometry

If a pulse is initiated at the feed, the wave reaches the reflector apex at time f/c where c is the velocity of light. As time goes on, the illuminated

spot at the apex expands, so that at any time after f/c the reflector is illuminated inside a circle, and not illuminated outside this circle, as sketched in Fig. 2.

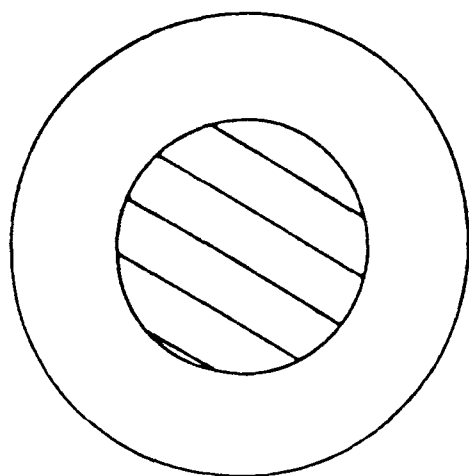


Fig. 2

Build-up Excited Disk

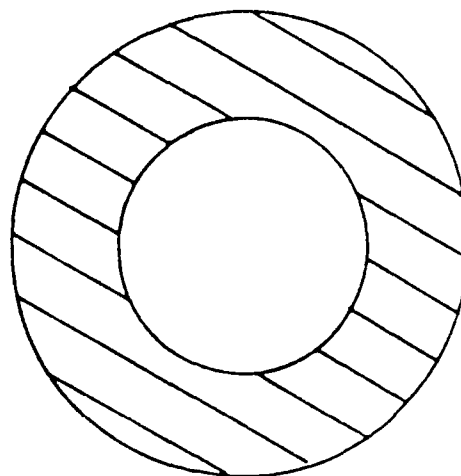


Fig. 3

Decay Excited Annulus

At a time after apex illumination equal to $\tau = D^2/16fc$, the full reflector is illuminated; this time is called the reflector transient time.

Consider now the decay phenomenon. Now there is an un-illuminated circle on the surface; the illuminated area is an annulus, whose inner diameter

increases with time until the pulse trailing edge appears at the reflector edge; see Fig. 3.

During the expansion of the disk of current, the time of expansion plus the travel time to a far-field point on-axis is constant. However off-axis, due to the path length differences that are explicated in Section 3, there is a creep of time as the disk expands. This distorts the waveform, with the distortion increasing with pattern angle.

Consider a carrier modulated with bi-phase PCM. At any time in a bit, the entire reflector surface produces the field on-axis. Off-axis the time creep will allow, if the reflector transient time is less than the bit time, the transition to the next bit to occur at a circle on the surface. The first bit is enjoying the directivity and pattern of the annulus of current, while the second bit is tied to the disk of current. As the diameter of the transition circle increases with time, the directivity and pattern (sidelobes) also change with time.

To quantify these effects approximately, the excitation of plane virtual aperture at the reflector edge is used. A circular one-parameter distribution

is used, with a steady-state -25 db sidelobe level⁶; this represents many front-fed dish antennas. For the build-up transient period, the directivity is simply that of a circular one-parameter distribution with smaller diameter and less edge taper, from which directivity is easily found. The annular region of the decay transient period is less simple, although the annular distribution is just the full distribution minus the inside distribution. If the ratio of inside to outside radius of the annulus is γ , the field is

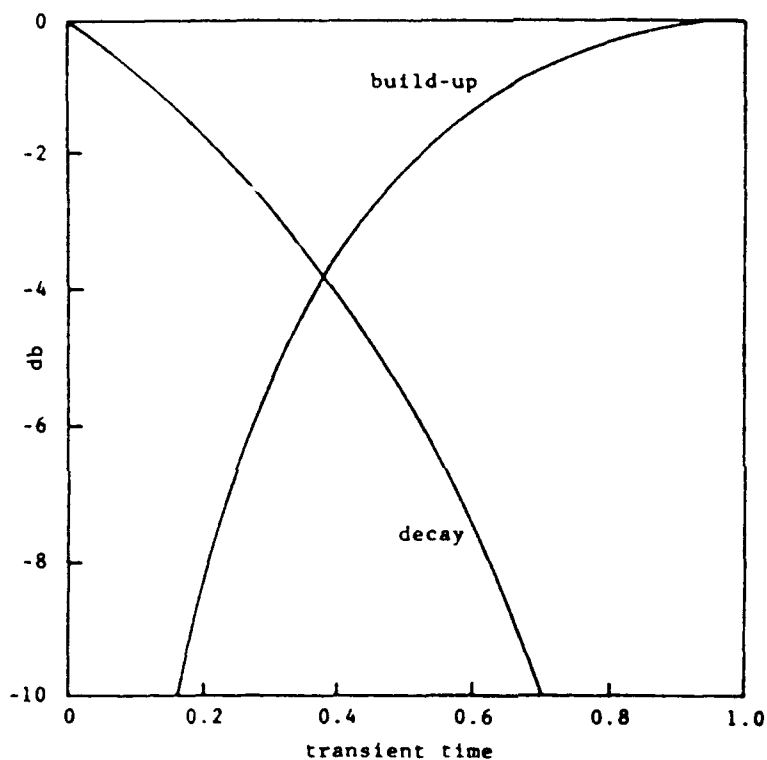
$$E = \frac{2J_1(\pi\sqrt{u^2 - H^2})}{\pi\sqrt{u^2 - H^2}} - \frac{2J_1(\pi\sqrt{\gamma^2u^2 - H^2})}{\pi\sqrt{\gamma^2u^2 - H^2}} \quad (1)$$

Relative directivity is obtained by changing the limits in the one-parameter formula⁶, with the result:

$$\eta = \frac{4\{I_1(\pi H) - \gamma I_1(\pi\gamma H)\}^2}{\pi^2 H^2 \{I_0^2(\pi H) - I_1^2(\pi H) - \gamma^2 \{I_0^2(\pi\gamma H) - I_1^2(\pi\gamma H)\}\}} \quad (2)$$

Calculations have been made⁵ of the directivity during the disk and annulus transient periods for a

25 db pattern. Fig. 4 gives directivity build-up (disk) and decay (annulus) relative to steady-state directivity; it may be noticed that the build-up is slow, while the decay is gradual.



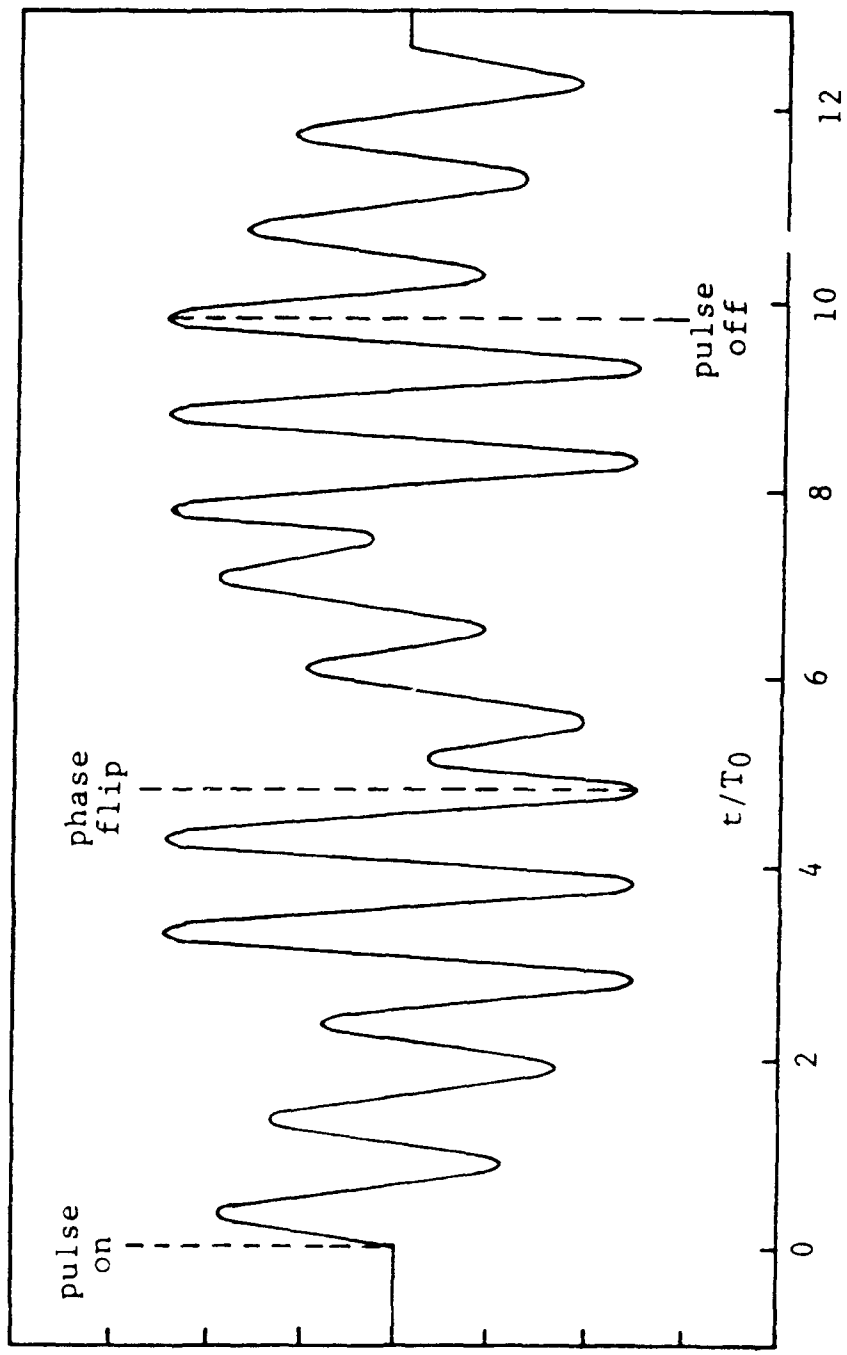
Transient directivity relative to steady-state directivity

Fig. 4

This analysis is of course only approximate; it is a transient aperture approach. An analysis including diffraction effects should remove the discontinuities

in Fig. 4 where the build-up directivity has slope discontinuities. One might expect more accurate curves to contain oscillations in the transient periods, and at steady-state times near the transient periods.

Returning to the PCM waveform, as a bit transition approaches, the directivity of the bit decreases (ala Fig. 4), and the annular current sidelobes are significantly higher. The directivity for the next bit is increasing (ala Fig. 4) and the sidelobes are again higher (with respect to the partial directivity), but less high than those of the annulus. These smeared out transitions can produce increased noise or clutter through the sidelobes, and lower signal through the diminished directivity; both increase the bit error rate. Fig. 5 shows the computed on-axis waveform as the bit transition moves over the reflector surface.⁷ It can be noted that four cycles are affected. The data of Fig. 5 are for an angle in the first sidelobe. Signal degradation will be worse at larger angles, but may be acceptable on the edges of the main beam. Precise calculations are needed to assure a satisfactory signal when the



Far-field of Reflector Antenna with Bi-phase Modulation
 (Courtesy SUN, 1991)

Fig. 5

time ratio is not large.

Thus again, the ratio of reflector transient time to waveform time is the critical factor. Similar distortions occur with other types of modulation when the reflector transient time to waveform time ratio is not large.

The preceding discussion was concerned with degradation in both signal and noise during current transitions on the reflector surface; next pattern transients will be discussed.

3.0 TRANSIENT PATTERN EFFECTS

The transient effects in pattern build-up and decay are caused by the fact that path lengths are equal only on the axis. Referring to Fig. 1, the distances from vertex and edge to P are R_v and R_e :

$$R_v = \sqrt{R_0^2 + 2R_0f \cos \theta + f^2} \approx R_0 + f \cos \theta \quad (3)$$

$$R_e = \sqrt{R_0^2 + 2R_0B \cos \theta \pm R_0D \sin \theta + B^2 + D^2/4} \quad (4)$$

$$\approx R_0 + (f - D^2/16f) \cos \theta \pm \frac{D}{2} \sin \theta \quad (5)$$

where the approximate values are for large R_0 , and the \pm refers to the lower (not shown) and upper edges respectively. The relative times are of course represented by distances; a time line as sketched in Fig. 6 will aid in following the sequence. Let the time origin start when the pulse leading edge appears at the reflector vertex. Since the entire pattern must be formed to produce the desired directivity, the ray contributions will be observed both at pattern angle θ , and on-axis. Even though the current first appears at the vertex, the first ray to reach any part of the pattern comes from the close edge, a total feed-to-point distance of

$$R_0 + f(1 + \cos \theta) + (D^2/16f)(1 - \cos \theta) - (D/2) \sin \theta \quad (6)$$

This includes the time for the edge current to appear, $D^2/16f$. Thus the pattern first forms at $\theta = \pi/2$, (only forward hemisphere radiation is considered); since the reflector and pattern are symmetric, a conical pattern first appears. As time increases, the edge currents form the pattern for angles less than $\pi/2$, and currents inside the edge

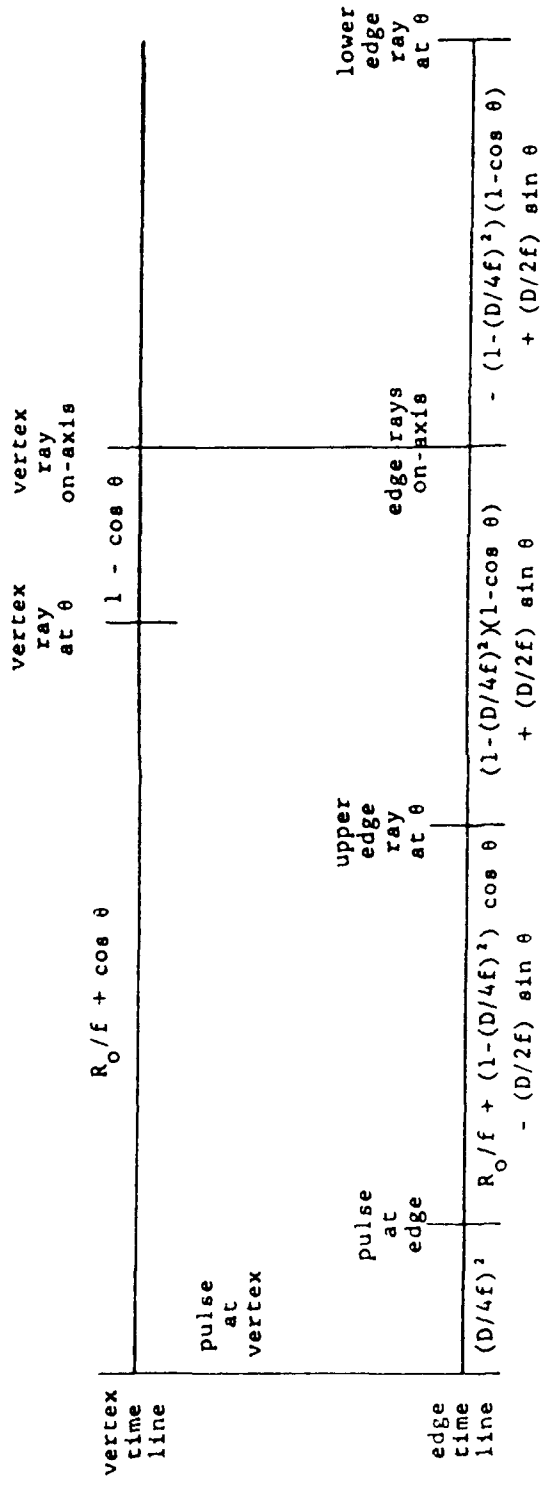


Fig. 6
Vertex and Edge Ray Time (Distance) Lines

add to the pattern at $\theta = \pi/2$.

This process of forming the sidelobes continues until the vertex ray appears at $\theta = \pi/2$, after a time (distance) of $R_0 + f \cos \theta$. At a time $f(1 - \cos \theta)$ later, the vertex ray appears on-axis, with a total feed-to-point distance of $R_0 + 2f$. At the same time the edge rays (and all rays) arrive on-axis. This is the equal path length property. Now all of the reflector currents are forming the pattern on-axis. However the lower edge ray has not yet appeared at angle θ . After an additional delay, as shown in Fig. 6, all of the currents are contributing to the entire pattern; steady state has been reached. The current transient time, as shown before, is $D^2/16fc$.

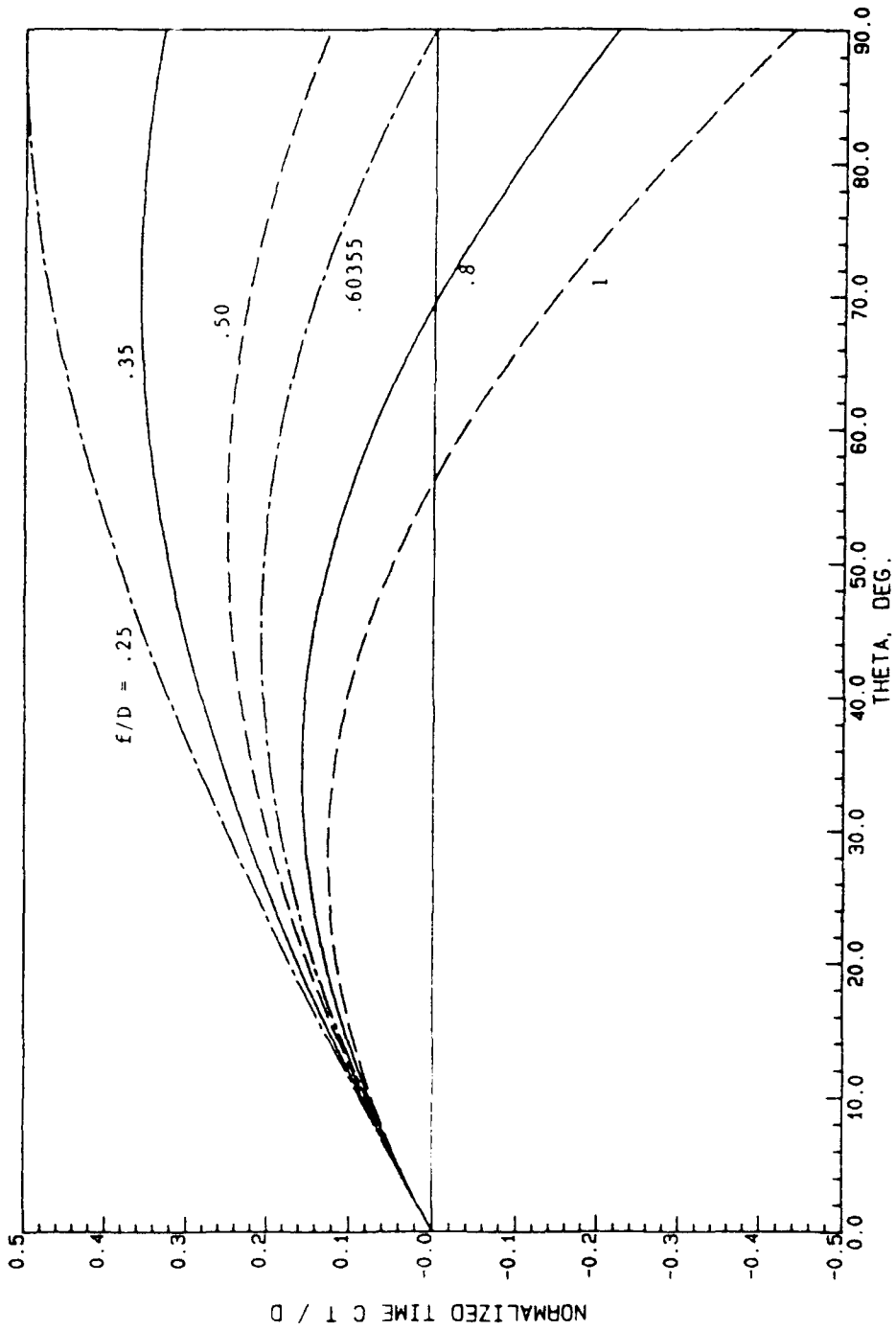
When the pulse trailing edge appears at the vertex, a reverse process is initiated. First the edge ray contributions disappear at $\theta = \pi/2$, followed by the disappearance of contributions from inside the edge, etc.

The longest pattern transient time occurs with the ray from the far edge of the reflector. The transient time is:

$$\tau = \frac{D}{c} \cdot \frac{(1-16f^2/D^2)(1 - \cos \theta) + 8f/D \sin \theta}{16f/D} \quad (7)$$

It is convenient to normalize this transient time by multiplying by the velocity of light and dividing by dish diameter. The results for several f/D are shown in Fig. 7. The pattern transient times are larger for most angles, although they are zero on-axis. The peak pattern transient time, excluding the values for angles near 90 deg., occurs when the angle equals the edge angle of the dish, and is twice the current transient time. For angles near 90 deg., and large f/D , the pattern transient time approaches $-f/D$; this large magnitude for pattern transient time is a result of using the focus as phase center for determination of far-field distance. Since the sidelobe structure is completely established only after this pattern transient time, system noise and clutter will be affected during the transient period.

To give an example of these times, a 10 m diameter reflector with $f/D = .4$ has a current transient time of 5.21 nanosec, and a maximum pattern transient time of 10.43 nanosec (at $\theta = 64$ deg.).



REFLECTOR ANTENNA PATTERN TRANSIENT TIME

Fig. 7

The $\theta = 90$ deg. time is 8.54 nanosec.

4.0 SUMMARY

The reflector current transient time of $D^2/16fc$ is important for modulated waveforms when the ratio of transient time to waveform time is not small. The pattern build-up and decay transient time may be larger than the current transient time. All transient times increase directly with D/λ . These transient times are important, and must be considered in some modern systems designs.

5.0 REFERENCES

1. Susman, L. and Lamensdorf, D. (1971) Picosecond pulse antenna techniques, RADC-TR-71-64, Report, Sperry Rand Res. Center, Sudbury, MA, AD-884-646
2. Martins, V. C. et al, (1973) Picosecond pulse reflector antenna investigation, RADC-TR-73-215, Report, BDM, Vienna, VA, AD-771-132

3. Maddocks, H. C. (1974) Time domain aperture antenna study, vol. 2, RADC-TR-254-2, Report, Vermont Univ., Burlington, VT, AD-A002 144
4. Sengupta, D. L. and Tai C. T. (1976) Radiation and Reception of Transients by Linear Antennas, in Transient Electromagnetic Fields, L. B. Felsen, Ed., Springer
5. Hansen, R. C. (1987) Short-pulse excitation of reflector antennas, Proc. IEE 134, Pt H:557-559
6. Hansen, R. C. (1976) A one-parameter circular aperture distribution with narrow beamwidth with low sidelobes, Trans. IEEE AP-24:477-480
7. Sun, E. Y. (1991) Time-domain analysis of reflector antennas and its applications, PhD Thesis, USC

BEAMSPACE LOW SIDELOBE PATTERN SYNTHESIS

Daniel J. Lawrence

W. Timothy Carey

Joseph A. Smolko

Raytheon Company

Missile Systems Division

Tewksbury, MA 01876-0901

ABSTRACT

Modern antenna applications typically require simultaneous low sidelobe receive sum and difference patterns. One method of achieving low sidelobes is presented and involves the optimal combination of full-aperture beams. This method consists of calculating weights that optimize power over a simultaneously formed set of full gain beams (basis beams) in a selected far-field region. A single low sidelobe composite pattern is formed from the basis beams by this optimally weighted beam combination. When these weights are applied digitally, simultaneous receive sum and difference composite beams can be formed to provide monopulse functions. The most interesting result is the formation of low sidelobe level difference patterns. Simulated results show that under -50 dB rms sidelobe level sum and difference patterns (relative to the peak of the beams) can typically be realized by a five beam cluster of uniformly illuminated beams. Simulations are also provided that show response over frequency.

1. Introduction

Low sidelobe antenna applications generally require the design of precision RF power distribution networks. These networks must often provide efficient low sidelobe level receive sum and difference illumination tapers with wide scan angle capabilities, wide instantaneous bandwidth and a wide operating bandwidth. Multiple simultaneous beam networks in the form of constrained feeds and semi-constrained feeds are the preferred networks to meet such requirements. In constrained feeds, a precise calculation of power dividers or coupler values is usually employed for amplitude control at the element level. In the case of semi-constrained feeds, for example a Rotman lens, an approximately uniform illumination pattern is inherent in the lens and the low sidelobe taper must be applied with attenuators at the array ports to yield the desired pattern. Both of these methods specify a low sidelobe level taper along the array and require stringent tolerances in the weights at the element level.

An alternative set of methods that provide desirable sidelobe performance involves beamspace combination. In these methods, the resultant weighted linear combination of beams from multiple beam networks furnish the desired pattern. These methods can be applied to both multiple beam constrained feeds (Butler Matrix) and semi-constrained feeds (Rotman lens). Many methods of beamspace combination are available and offer the potential for overall simpler network designs. One such method is investigated in this paper. An optimization method based on maximizing (or minimizing) power over given regions of space is utilized to achieve the desired low sidelobe level design. Presented herein is a review of the supporting theory and simulated results of this method.

2. Multiple Beam Forming Network

The initial concept is to utilize the output of a multiple simultaneous beam network (as shown in Figure 1) to form the required low sidelobe pattern.

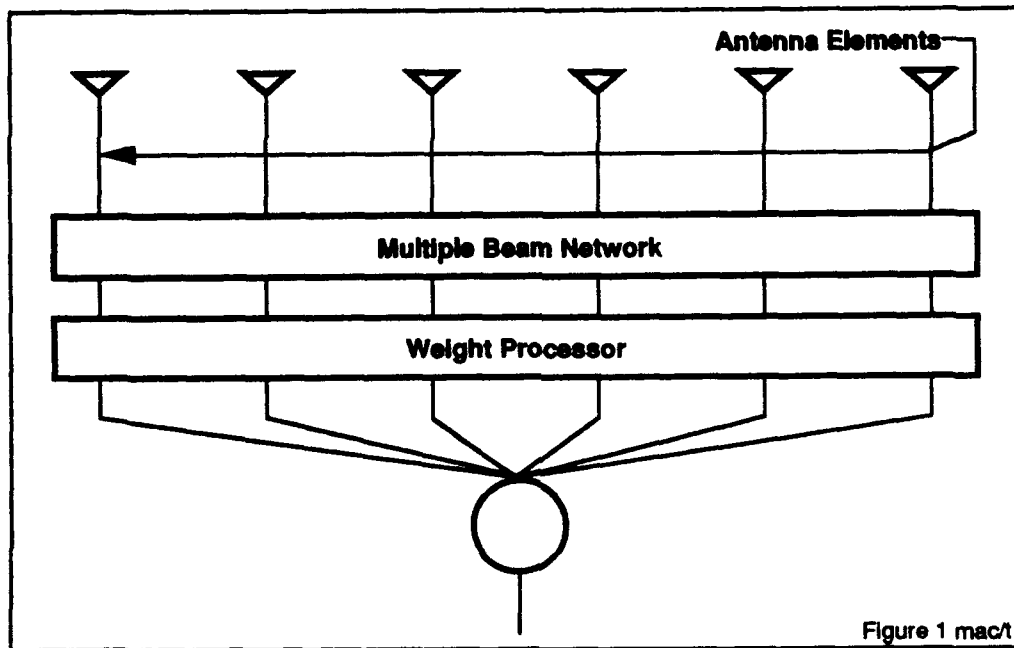


Figure 1. Multiple Beam Feed Network

Such an architecture can utilize either a Butler matrix, a Rotman lens or any suitable multiple beam feed. A large number of simultaneously beams are provided from which a small cluster of beams can be selected. The selected beams are fed through a weighted summing network (weight processor) to form an acceptable composite beam. The task then becomes to calculate weights that provide the desired pattern.

A simple power optimization method is shown to provide weights that form desirable composite patterns. For all simulations, these weights are calculated assuming the beam network forms full gain $(\sin(x)/x)$ beams. Based on this

assumption, weights can be calculated that provide a selection of patterns with varying sidelobe levels.

Array steering can be accomplished with the composite beam by control of the phase at each element. Another method for array steering is to select a different group of beams centered in the direction of the desired steering angle to form a steered composite beam. Or finally beam steering can be provided by a combination of both of these techniques. The latter two methods support wide scan-angle wide instantaneous bandwidth performance.

3. Low Sidelobe Optimization

The fundamental concept of low sidelobe beamforming from basis beams involves optimizing the combined power of a selected set of full gain beams; however the optimization is performed on only a portion of the total far-field space. To determine the total power, the far-field complex voltage of each beam is first integrated over the desired region of optimization. Mathematical representation of these complex voltages is shown in Equation 1.

$$\begin{matrix} \text{Mainbeam} \\ \text{Region} \end{matrix} \quad V_{i(\text{total})} = \int \int f_i(u,v) \delta u \delta v \quad \forall (i|i=1,2,3,\dots,N) \quad (1a)$$

or

$$\begin{matrix} \text{Sidelobe} \\ \text{Region} \end{matrix} \quad V_{i(\text{total})} = \int \int f_i(u,v) \delta u \delta v \quad \forall (i|i=1,2,3,\dots,N) \quad (1b)$$

Where $f_i(u,v)$ is the i th far-field complex basis beam voltage. The integration is performed either over the main beam region or the sidelobe region. The exact limits of integration depend on the sidelobe level desired. In general, however, the main beam region is defined as that region which encompasses the main beams from the selected cluster as shown in Figure 2.

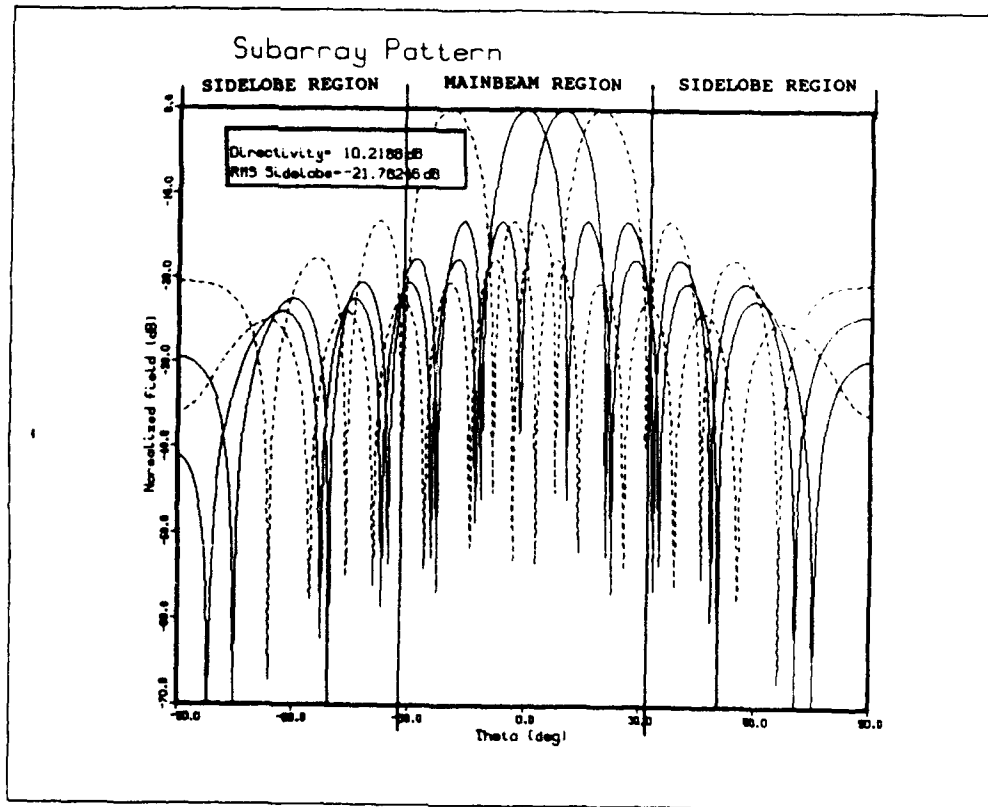


Figure 2. Selected Far-Field Regions of Basis Beams

The total voltage for each one of the constituent beams (v_i) is calculated over the same far-field space region and is used to form an N dimensional basis set. The basis is formed by calculating the outer product of the voltages in (2).

$$\begin{pmatrix} V_1(t) \\ V_2(t) \\ V_3(t) \\ \vdots \\ V_N(t) \end{pmatrix} (V_1^*(t), V_2^*(t), V_3^*(t), \dots, V_N^*(t)) = \quad (2)$$

$$\begin{pmatrix} V_1(t)V_1^*(t) & V_1(t)V_2^*(t) & V_1(t)V_3^*(t) & \dots & V_1(t)V_N^*(t) \\ V_2(t)V_1^*(t) & V_2(t)V_2^*(t) & V_2(t)V_3^*(t) & \dots & V_2(t)V_N^*(t) \\ V_3(t)V_1^*(t) & V_3(t)V_2^*(t) & V_3(t)V_3^*(t) & \dots & V_3(t)V_N^*(t) \\ \vdots & \vdots & \vdots & \ddots & \vdots \\ V_N(t)V_1^*(t) & V_N(t)V_2^*(t) & V_N(t)V_3^*(t) & \dots & V_N(t)V_N^*(t) \end{pmatrix} = \Phi$$

Φ can be considered to consist of integrated cross correlations of the desired beamspace region to be optimized. The combined power can be expressed as a quadratic equation:

$$Power \ out = W^* \Phi W \quad (3)$$

where w is the vector of unknown weights. A minimax optimization problem of the total output power is established and is maximized for mainbeam integration regions and conversely minimized for sidelobe integration regions. The optimum power in this region is determined by finding the weight vector (W) that provides the maximum/minimum over the N dimensional paraboloid as shown in (4).

$$\min_{W \in \mathbb{C}} W^* \Phi W \quad \forall (w | w = 1, 2, 3, \dots, N) \quad (4)$$

One technique that can be employed to supply the proper weights is the Rayleigh Quotient:

$$\frac{W^* \Phi W}{W^* W} = \lambda \quad (5)$$

In the Rayleigh Quotient the maximum to the normalized quadratic equation of (5) is simply the largest eigenvalue of the matrix (λ_{\max}). The set of weights which provide this maximum is the eigenvector associated with the maximum eigenvalue. Similarly the eigenvector associated with the smallest eigenvalue (λ_{\min}) provides the minimum. So the optimization is solved based on minimizing sidelobes or maximizing main beam directivity.

Once the weights are found, the resultant voltage pattern can be computed by forming the weighted linear combination.

$$F(u, v)_{\text{total}} = \sum_{i=1}^N W_i V_i(u, v), \quad (6)$$

where each u,v position is a point in the far-field. Since every beam in the multiple cluster is defined for every u,v the resultant linear combined pattern is likewise defined.

The total far-field power pattern is:

$$P_{\text{out}} = F(u, v) * F(u, v)^* \quad (7)$$

4. Selection of Optimization Region and Basis Beams

The selection of the region for optimization and the far-field spacing of the multiple basis beams are the two critical parameters for forming the final combined pattern.

The boundary of the optimization region can be selected by applying energy conservation principles. The total normalized power available is determined by integrating across the far-field region of the array, extending through both the sidelobe and mainbeam regions. Allotment of energy is made by only including a portion of the total far-field region into the optimization. This portion becomes actively maximized while the remaining portion becomes passively minimized. Although no closed form solution is presented, a common sense approach is used. As larger regions are selected, more of the total array power will occur in the main beam region required by energy conservation. When the correct equilibrium of maximized to minimized power occurs, a directive mainbeam results with low sidelobes. However, the optimization occurs at the expense of increased loss, corresponding directly to the taper efficiency. Scaling of the optimization area can be used to determine the proper region for different frequencies.

A region is selected that is symmetrical about the desired pointing direction. As this region is increased, the width of optimization about the main beam increases and the sidelobe region decreases. Lower sidelobe levels result, however, at the expense of wider, less efficient main beam. As the area of optimization increases further, a break point is found and the optimization splits the single mainbeam into two beams. This beam is a desirable difference pattern having low sidelobes. As the

optimization area is further increased, the center region loses its directivity and multiple beams within the maximized region begin to form.

As this method behaves according to the principle of energy conservation and ultimately relies on the total energy available, care must be taken in the placement of the basis beams. If basis beams are formed with their directivity placed at random angles the total energy for combination becomes diffuse and a power equilibrium occurs as the energy maximized in one region is not much greater than the power minimized in the other region. A nondirective beam occurs and may yield poor results.

5. Simulated Results

A 47-element linear array with a spacing of $\lambda/2$ at 18 GHz is simulated to demonstrate typical performance. Figure 3 illustrates the combined pattern performance presented in terms of the directivity and rms sidelobe level as a function of the selected optimization region at 18 GHz. As shown, the optimization area is varied between 2 and 16 degrees integrated symmetrically about boresight. At an area of 10.2 degrees, the rms sidelobe level of the sum beam decreases to a low of -63.6 dB relative to the peak of the main beam (RPMB). As this area is further increased past 10.2 degrees, difference patterns are formed. A -57.3 dB rms sidelobe level difference pattern relative to the peak of the difference beams (RPDB) is shown to be at a minimum value of 12 degrees. As the area is further increased the low sidelobe level difference pattern becomes distorted as more than two symmetric beams begin to form. The combined low sidelobe level patterns of

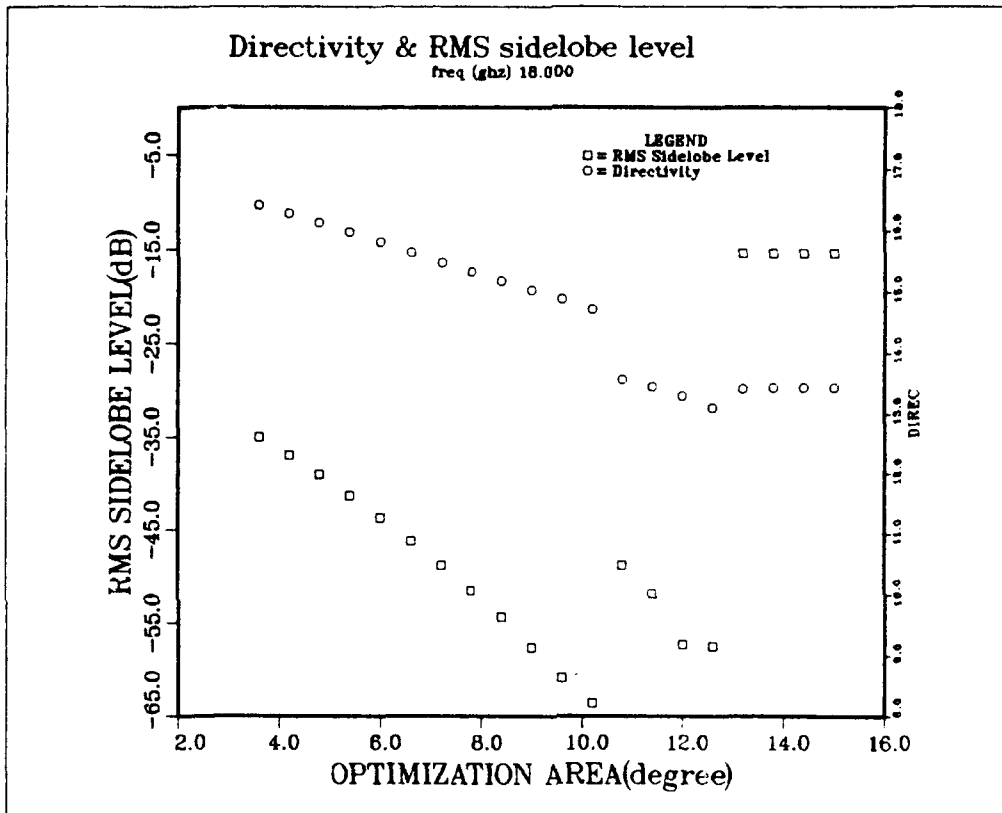


Figure 3. Composite Pattern Performance for Selected Optimization Region

the 10.2 and 12 degree case are shown in Figures 4 and 5, respectively. Examination of the sidelobe structure of both the sum and difference pattern reveals that higher sidelobes occur toward the main beam and fall off quickly which is typical for optimized patterns.

The combination consists of five uniformly illuminated weighted basis beams selected almost orthogonal with beams pointing in the far-field at spacings of -4.8, -2.4, 0.0, 2.4 and 4.8 degrees. These beams are shown in Figure 6 (the center and two outside beams are shown for clarity purposes). Calculated weights for the sum beam are 0.054, 0.55, 1.0, 0.55, and 0.054 while difference pattern weights are 0.424, 1.0, 0 -1.0 and -0.418.

To investigate the performance of this method over a wide operating bandwidth, two more cases at the lower frequencies of 12 and 6 GHz were examined. Results of the 12 GHz case for a chosen optimization region between 6 and 18 degrees are shown in Figure 7. A low sum pattern rms sidelobe level of -59.6 dB RPMB occurs at an optimization area of 14.4 degrees; likewise the difference pattern has a minimum rms sidelobe level of -54.9 dB RPDB at an optimization area of 17.4 degrees. The basis patterns are spaced at -7.0, -3.5, 0, 3.5 and 7.0 degrees.

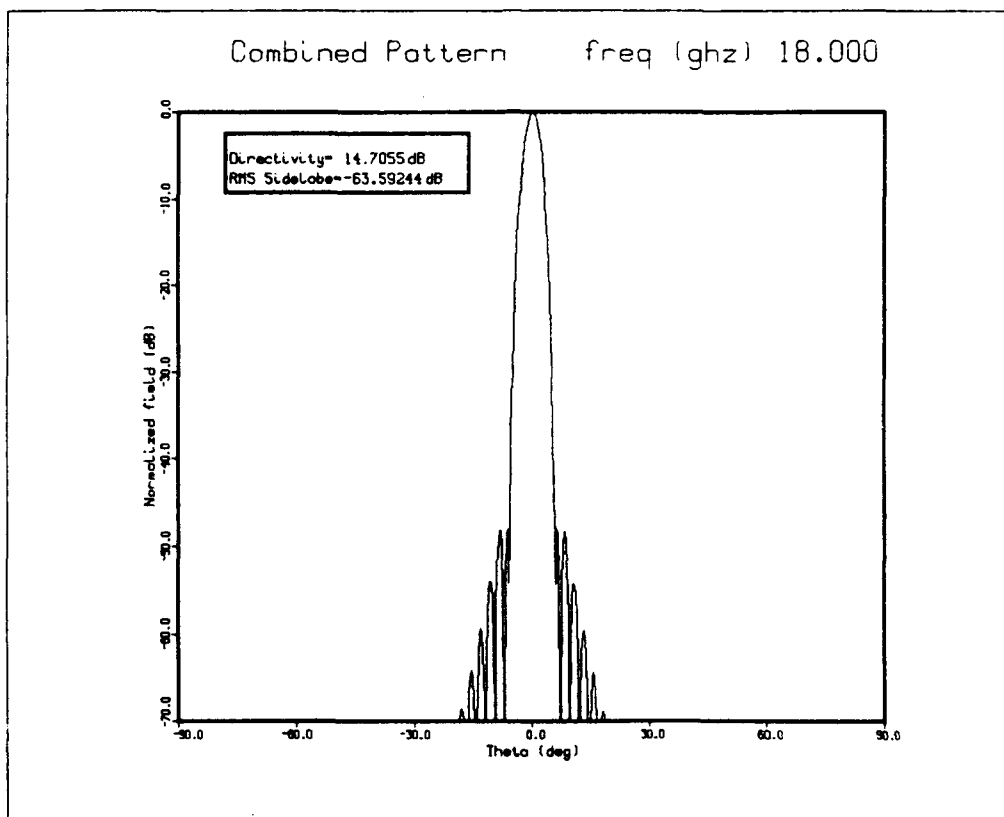


Figure 4. Composite Sum Pattern

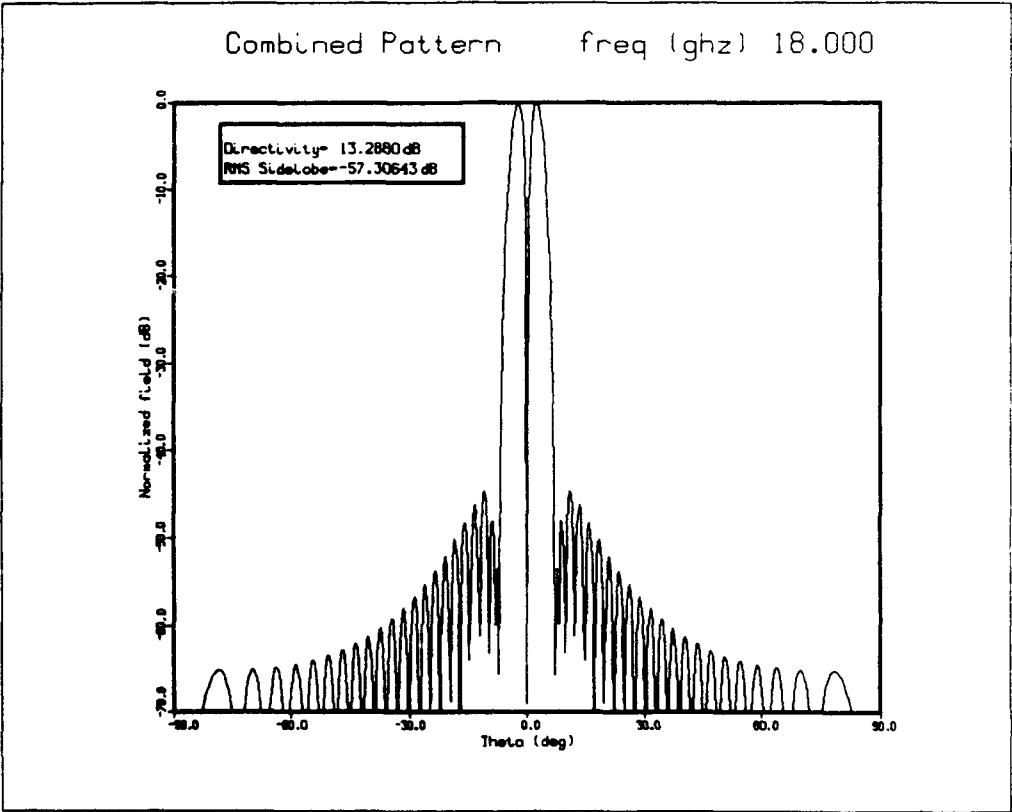


Figure 5. Composite Difference Pattern

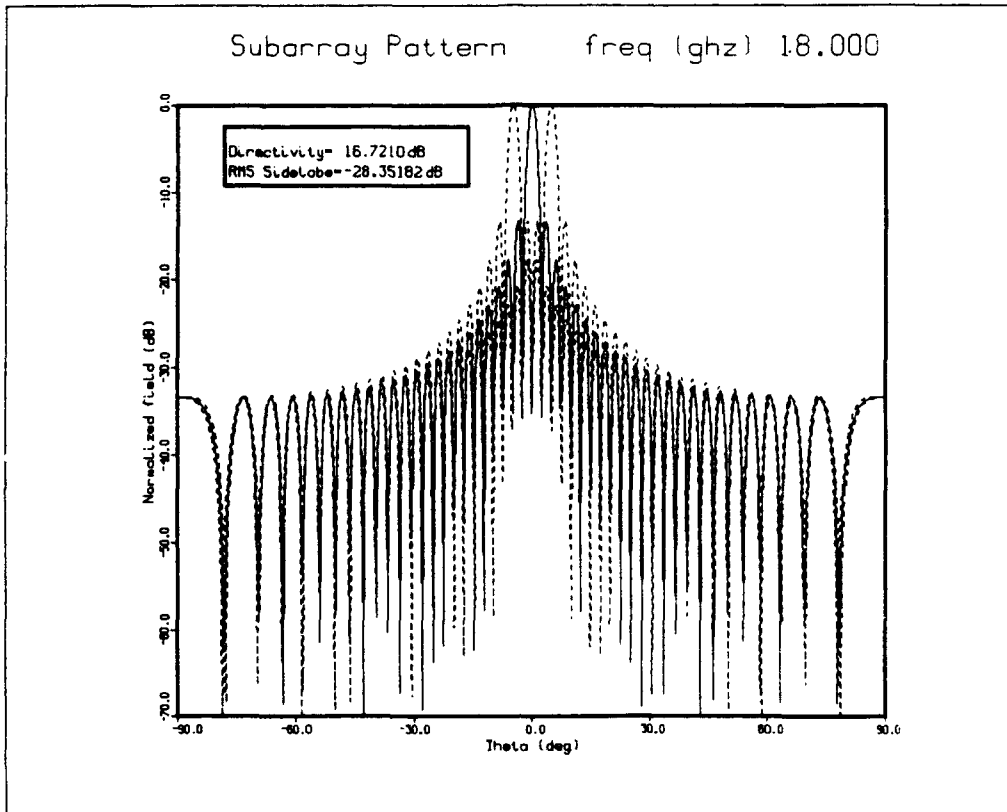


Figure 6. Basis Beams

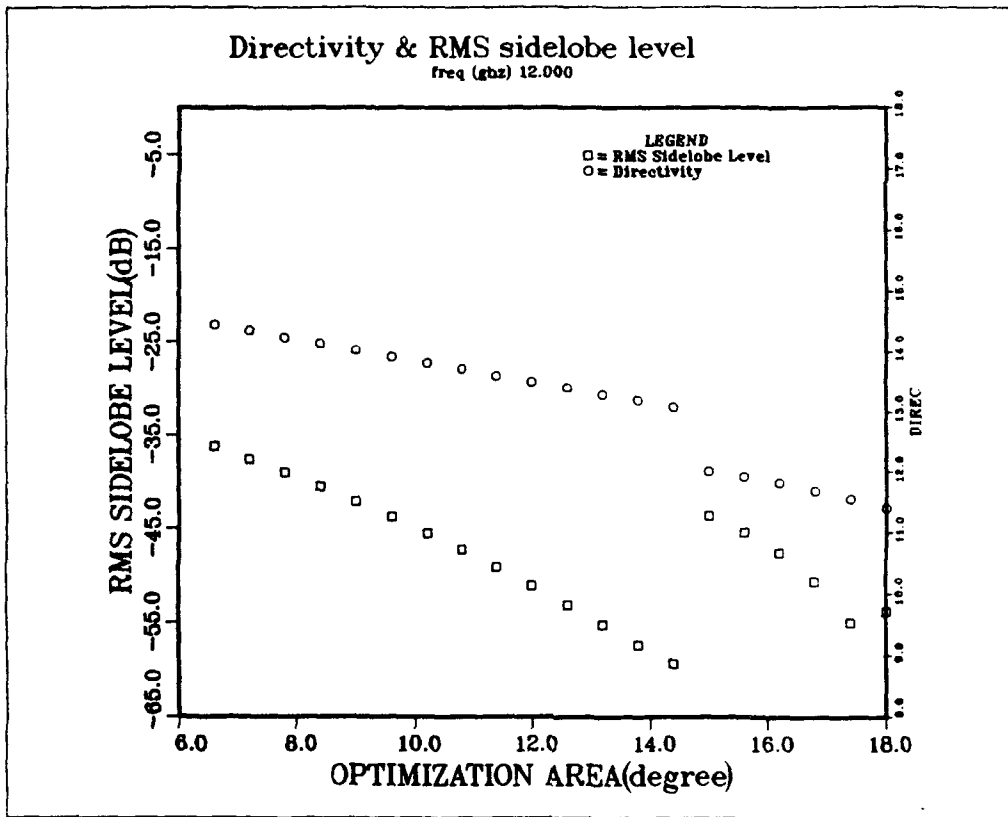


Figure 7. Composite Pattern Performance for Selected Optimization Region

A 6 GHz optimization is shown in Figure 8, which results in minimum sum beam rms sidelobe levels of -51.8 dB RPMB and difference beam sidelobe levels of -49.6 dB RPDB. Basis beams are located at angles of -13.6, -6.8, 0.0, 6.8 and 13.6 degrees.

6. Bandwidth Considerations

The performance of the combined beam pattern over frequency is evaluated. One of the problems that exists at frequencies other than the center frequency is the relative movement of the basis beams. As the frequency increases, the antenna becomes electrically larger and the basis beams become more directive. The spacing of the beams in the far-field also increases. Analogous results occur for frequencies below the center frequency and combinations other than frequencies close to the center frequency show unacceptable results for low sidelobe level designs.

Calculations of the weights yield the best results when the beams are orthogonal (or nearly orthogonal). It was also subsequently discovered that calculating new weights for each new frequency with the same beam spacing did not necessarily yield optimal results. Rather, weights are calculated at the center frequency for orthogonal basis beams and "frozen" for combination of basis beams at frequencies across the band. These results are shown in Figures 9 and 10. As the frequency is further increased or decreased, other beams can be selected to provide for the proper spacing. This technique can be adopted to increase the operating bandwidth of the system. The optimized weights are calculated at a frequency corresponding to a distance of $\lambda/2$. The combined pattern uses the basis beams realized at different frequencies.

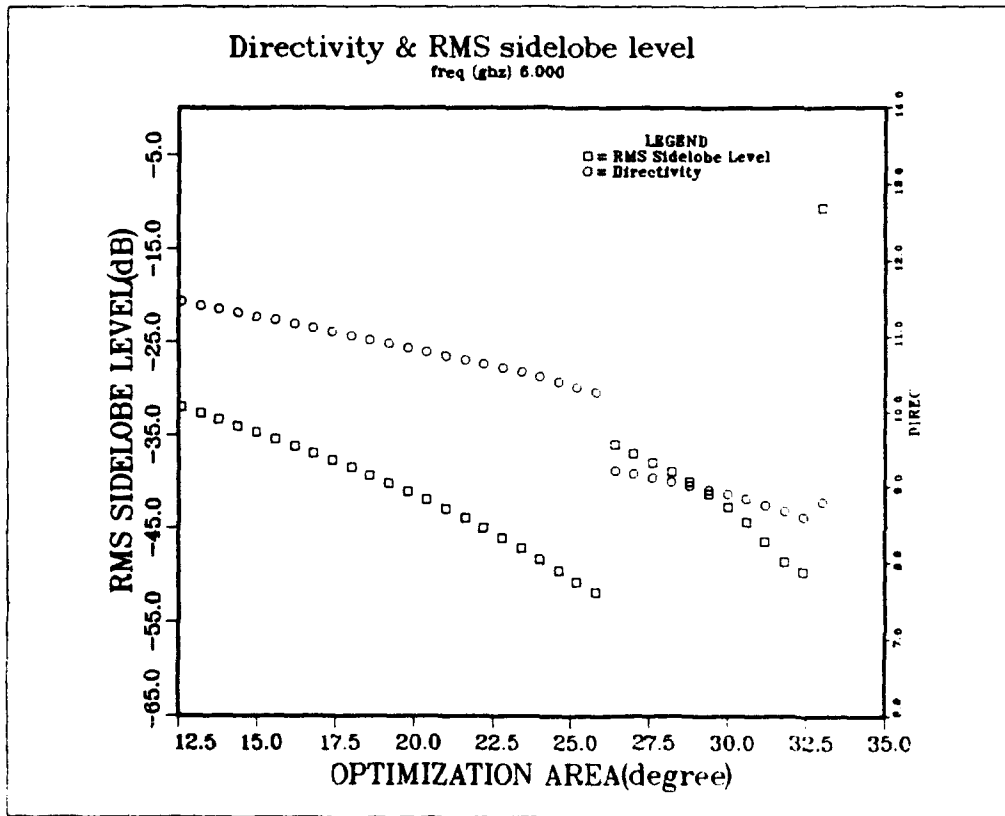


Figure 8. Composite Pattern Performance for Selected Optimization Region

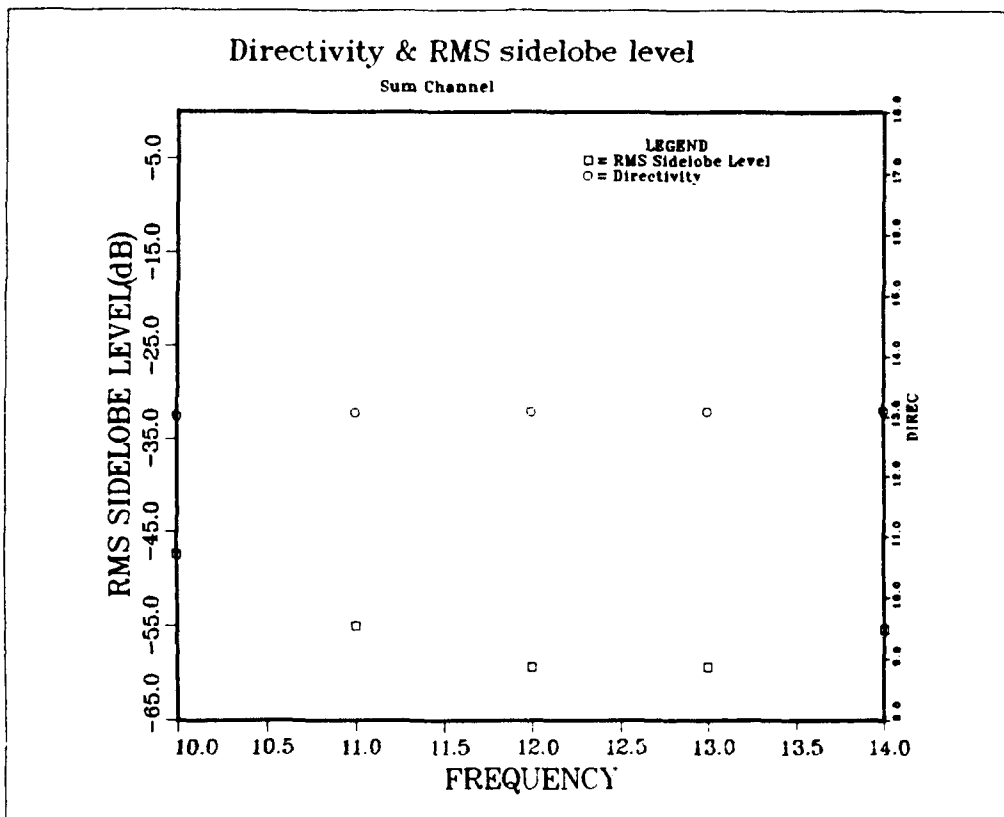


Figure 9. Composite Pattern Performance Over Frequency

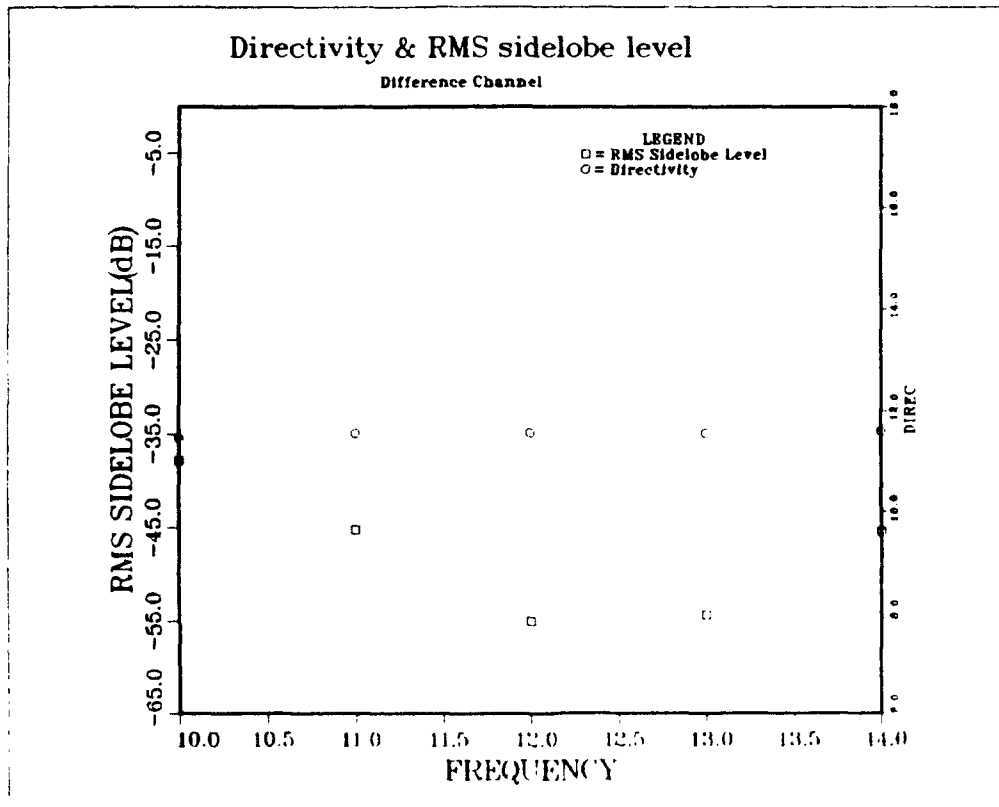


Figure 10. Composite Pattern Performance Over Frequency

7. Conclusions

An optimization technique is investigated that maximizes or equivalently minimizes power in far-field regions to provide low sidelobe receive sum and difference patterns. This technique uses energy conservation as the fundamental principle for the pattern synthesis. Results indicate that this method can be used for modern radar systems that require broad instantaneous bandwidth and a wide operating range.

This method shows promise in that it may provide for a simpler feed network design. Attenuators of the semi-constrained lens designs can be replaced by weighted summing networks that can be digitally implemented, taking full advantage of the simultaneously formed beams. Once weights are found, weight modification can be made, for example, to provide adaptive nulling of hostile jammers.

VALIDATION OF INTEGRAL EQUATION MODEL WITH HIGH-DIELECTRIC MICROSTRIP ROTMAN LENS MEASUREMENTS

*A. F. Peterson and E. O. Rausch
Georgia Institute of Technology
Atlanta, Georgia*

ABSTRACT: To reduce the physical size of a Rotman lens, a reduction in the overall electrical size of the lens can be combined with a microstrip fabrication using substrate materials with large relative permittivities such as TiO_2 . An integral equation formulation for predicting the scattering matrix (S-matrix) associated with a Rotman lens has been developed to aid in the design of a compact, low-sidelobe, high-performance lens. The model incorporates the tapered transitions used to transform from 50Ω transmission lines to the larger lens apertures, and in principle is limited only by the assumption that the device behaves as a planar circuit. S-parameter measurements obtained from a lens having dielectric constant of 100 will be compared with theoretical predictions in order to validate this model.

1. INTRODUCTION

Rotman lenses are frequently employed in electronic counter measure (ECM) systems to drive high power sources or in electronic support measure (ESM) systems to determine the angle-of-arrival of microwave signals. Two advantages of these lenses are their broadband performance and frequency-invariant beam directions. Disadvantages include their large physical size when operated at low frequencies and the relatively high sidelobe levels within the lens cavity across the output ports. Lens size may be reduced by fabricating the microstrip lens on a high-dielectric substrate [1]. Sidelobes may be minimized by proper lens design.

A typical lens design effort is based on Rotman's [2] or Gagnon's [3] formulation. But these equations yield only the beam and array port contours, and do not specify the sidewall design. In practice, the sidewalls are usually established by closing the beam and array port contours in an arbitrary manner. Chan developed a theoretical model that showed the importance of the sidewall configuration in controlling the ripple level across the lens contours. [4] These ripples, in turn, define the minimum attainable sidelobe level. Chan's model incorporates an integral equation describing the electric field distribution in the port apertures around the lens cavity. This formulation takes into account the mutual coupling between all fundamental and higher-order modes excited at the taper-lens interface of each aperture throughout the lens. By utilizing the reflection coefficients of the higher-order modes entering the tapered transitions, the multimode S-matrix produced by the integral equation can be reduced to a dominant mode S-matrix. In principle, the formulation is limited only by the assumption that the device behaves as a planar circuit [5-6]. (The planar circuit assumption is equivalent to neglecting the fringing fields at the open sides of the microstrip lines.) For Rotman lenses constructed with low-permittivity substrate materials, good agreement was reported between measured and theoretical results.

In this paper Chan's formalism is modified and extended to include lenses with high dielectric substrates made of TiO_2 ($\epsilon_r \cong 100$). The theoretical model is described and numerical results are presented for comparison with measured S-parameters. The S-matrices are plotted in a phasor format for comparison.

2. MICROSTRIP WAVEGUIDE UNDER PLANAR CIRCUIT ASSUMPTIONS

Consider a Cartesian coordinate system with the planar lens geometry parallel to the x-y plane. The primary assumption associated with planar circuits is that the fields do not vary with z, or equivalently that there are no fringing fields at edges of the conducting strips or plates. These constraints dictate that the electric

field in the lens has only a z-component, while the magnetic field has only a transverse component (parallel to the x-y plane).

Under the planar circuit hypothesis [5-6], a microstrip waveguide can be modeled as a homogeneous dielectric region (with permittivity and permeability given by ϵ and μ , respectively) surrounded by perfect electric walls on the top and bottom and perfect magnetic walls on the sides. (The perfect magnetic walls are symbolic in nature and provide the no-fringing effect.) The transverse-electric (TE) electromagnetic fields that can exist in this structure and propagate with y-dependence $e^{-j\beta y}$ have the form of discrete waveguide modes

$$E_z(x,y,z) = E_0 \cos\left(\frac{m\pi x}{a}\right) e^{-j\beta_m y} \quad (1)$$

$$H_x(x,y,z) = \frac{E_0 \beta_m}{\omega\mu} \cos\left(\frac{m\pi x}{a}\right) e^{-j\beta_m y} \quad (2)$$

$$H_y(x,y,z) = \frac{j E_0}{\omega\mu} \frac{m\pi}{a} \sin\left(\frac{m\pi x}{a}\right) e^{-j\beta_m y} \quad (3)$$

where "a" denotes the width of the guide, "b" denotes the height, "m" is an integer ranging from 0 to ∞ , and

$$\beta_m = \begin{cases} \sqrt{\omega^2 \mu \epsilon - \left(\frac{m\pi}{a}\right)^2} & \omega^2 \mu \epsilon > \left(\frac{m\pi}{a}\right)^2 \\ -j \sqrt{\left(\frac{m\pi}{a}\right)^2 - \omega^2 \mu \epsilon} & \left(\frac{m\pi}{a}\right)^2 > \omega^2 \mu \epsilon \end{cases} \quad (4)$$

Some of the modes represent propagating solutions (real-valued β) and some represent fields having evanescent decay along the y direction (imaginary β). There are at most a finite number of propagating modes associated with the smallest

values of m . The mode having the lowest index ($m=0$) is actually a transverse electromagnetic (TEM) mode.

For the TEM mode, the characteristic impedance of the "planar circuit" microstrip transmission line is defined as the ratio of the equivalent voltage and current, and is given by

$$Z_0 = \frac{b}{a} \sqrt{\frac{\mu}{\epsilon}} \quad (5)$$

The characteristic impedance of a higher-order mode in a microstrip transmission line can be defined as

$$Z_m = \frac{\omega \sqrt{\mu \epsilon}}{\beta_m} Z_0 \quad (6)$$

The impedance of an actual microstrip line will differ from Equation (5) due to the effects of fringing fields. Scaling can be used to compensate for these effects.

3. COMPENSATION FOR FRINGING FIELDS

Microstrip transmission lines having substrate material ϵ different from that of the exterior medium (ϵ_0) do not support a true TEM mode of propagation at microwave frequencies. However, the observed behavior of microstrip is closely approximated by a quasi-TEM solution that appears to propagate in a medium having an effective relative permittivity [7]

$$\epsilon_{\text{eff}} = \frac{\epsilon_r + 1}{2} + \frac{\epsilon_r - 1}{2} \frac{1}{\sqrt{1 + 12 b/a}} \quad (7)$$

where ϵ_r is the relative permittivity of the substrate material. The effective relative permittivity represents a weighted average of the permittivity of the substrate and the exterior medium, and provides the proper wavelength, propagation constant, and phase speed for the quasi-TEM mode.

Empirical expressions for the characteristic impedance of the quasi-TEM mode in microstrip have been developed, and correlate well with laboratory measurements over a wide range of parameters. These are given by ^[7]

$$Z_0 = \frac{1}{2\pi} \sqrt{\frac{\mu}{\epsilon_0 \epsilon_{\text{eff}}}} \ln\left(\frac{8b}{a} + \frac{a}{4b}\right) \quad a < b \quad (8)$$

$$Z_0 = \sqrt{\frac{\mu}{\epsilon_0 \epsilon_{\text{eff}}}} \frac{1}{[a/b + 1.393 + 0.667 \ln(a/b + 1.444)]} \quad a > b \quad (9)$$

According to these formulas, the actual characteristic impedance is always smaller than that predicted by Equation (5). This difference is a consequence of the additional capacitance associated with the fringing fields.

A simple way of incorporating fringing fields into the planar circuit model is to employ the effective relative permittivity in place of ϵ_r , while simultaneously increasing the electrical width "a" of the transmission line in order that Equation (5) produce the same impedance as Equation (8) or (9). For illustration, Table 1 provides numerical values calculated for a substrate of relative permittivity $\epsilon_r=100$. It should be possible to scale the electrical size of the entire lens (including the tapered transmission lines at the input and output ports) to compensate for fringing effects, in order to use the planar circuit description for the theoretical modeling.

The empirical formulas presented in Equations (7)-(9) were developed for the quasi-TEM mode of propagation, and may not accurately describe higher-order modes on microstrip. For lack of a better model, however, we will use these empirical formulas in conjunction with Equation (6) to describe the behavior of

higher-order modes in the tapered transmission lines connected to the aperture ports.

Table 1

Difference between Equation (5) obtained from the "planar circuit" assumptions and the more accurate formulas from Equations (7)-(9); also illustrates the effective a/b obtained by scaling the width in order to make Equation (5) equivalent to the more accurate expressions from (8) and (9).

actual a/b	Z_0 (Eq. 5)	Z_0 (Eq. 8-9)	ϵ_{eff} (Eq. 7)	effective a/b
0.033	1130	45.1	53.1	0.8
0.1	377	35.4	55.0	1.1
0.33	113	24.9	58.6	1.5
1	37.7	15.8	64.2	2.4
3	12.6	8.2	72.6	4.6
10	3.77	3.2	83.9	11.9
30	1.26	1.2	92.3	32.5

4. GENERALIZED S-MATRIX DESCRIPTION

In the vicinity of a lens aperture, consider the local coordinate system (n,t,z) where n represents the variable along the normal vector pointing into the lens, and t is a variable directed along the tangent vector to the aperture so that $\hat{n} \times \hat{t} = \hat{z}$. We assume that in each lens aperture, the transverse electromagnetic fields can be expressed in terms of a superposition of waveguide modes according to

$$E_z(t,n) = \sum_{m=0}^{M-1} \{a_m e^{-j\beta_m n} + b_m e^{j\beta_m n}\} \frac{\sqrt{Z_m}}{b} \sqrt{\epsilon_m} \cos\left(\frac{m\pi t}{a}\right) \quad (10)$$

and

$$H_t(t,n) = \sum_{m=0}^{M-1} \{-a_m e^{-j\beta_m n} + b_m e^{j\beta_m n}\} \frac{\beta_m \sqrt{Z_m}}{\omega \mu b} \sqrt{\epsilon_m} \cos\left(\frac{m\pi t}{a}\right) \quad (11)$$

where

$$\epsilon_m = \begin{cases} 1 & m=0 \\ 2 & m>0 \end{cases} \quad (12)$$

and, as indicated previously, the electrical height of the guide is "b" and the width of the guide (including compensation for fringing fields) is "a." The characteristic impedance associated with mode m is denoted Z_m . The complex-valued coefficients $\{a_m\}$ and $\{b_m\}$ represent the incident and reflected modes immediately exterior to the lens. The coefficients $\{a_m\}$ and $\{b_m\}$ are normalized so that the power carried by the m-th incident mode is given by

$$\begin{aligned} \int_{z=0}^b \int_{t=0}^a \frac{1}{2} \operatorname{Re}\{\bar{\mathbf{E}} \times \bar{\mathbf{H}}^*\} dt &= \hat{n} \frac{|a_m|^2}{2} \frac{1}{a} \int_{t=0}^a \epsilon_m \cos^2\left(\frac{m\pi t}{a}\right) dt \\ &= \hat{n} \frac{|a_m|^2}{2} \end{aligned} \quad (13)$$

We seek a description of the lens in terms of the incident and reflected modes, and define a generalized S-matrix according to

$$\begin{bmatrix} b_1 \\ b_2 \\ \cdot \\ \cdot \\ \cdot \\ b_{NM} \end{bmatrix} = \begin{bmatrix} S_{11} & S_{12} & \cdot & \cdot & \cdot & S_{1,NM} \\ S_{21} & S_{22} & & & & \\ \cdot & & & & & \\ \cdot & & & & & \\ \cdot & & & & & \\ S_{NM,1} & & \cdot & \cdot & \cdot & S_{NM,NM} \end{bmatrix} \begin{bmatrix} a_1 \\ a_2 \\ \cdot \\ \cdot \\ \cdot \\ a_{NM} \end{bmatrix} \quad (14)$$

where we have assumed that there are N apertures around the lens periphery, each containing M modes. Theoretical properties of the S -matrix dictate that (1) the matrix is symmetric across the main diagonal, and (2) if the lens materials are lossless, the S -matrix is unitary. These properties can be used as a check on the accuracy obtained by the numerical model.

5. INTEGRAL EQUATION FORMULATION

The electromagnetic fields within the lens interior must satisfy Maxwell's equations or a suitable integral equation derived from them. One such equation is the electric-field integral equation (EFIE)

$$0 = E_z(\tau) + j\omega\mu \int_S H_t(\tau') \frac{1}{4j} H_0^{(2)}(kR) d\tau' + \hat{z} \cdot \nabla \times \int_S \hat{t}(\tau') E_z(\tau') \frac{1}{4j} H_0^{(2)}(kR) d\tau' \quad (15)$$

where the surface S is the periphery of the lens, τ denotes a parametric variable along S , and E_z and H_t are the tangential components of the electric and magnetic fields along the lens periphery. $H_0^{(2)}$ is the zero-order Hankel function of the second kind, and the argument R is the distance from the primed location (τ') to the unprimed location (τ) on the lens periphery. Equation (15) holds an infinitesimal distance inside the lens periphery. Equations (10) and (11) can be used to express Equation (15) directly in terms of the normalized mode coefficients. By weighing each side of the resulting equation with a testing function

$$\cos\left(\frac{p\pi t}{w}\right) \quad (16)$$

defined over aperture n, we obtain

$$0 = \sum_{m=0}^{M-1} \left\{ P(n,m,p) \sqrt{Z_m^n} \sqrt{\epsilon_m^n} (a_m + b_m) \right. \\ \left. - \sum_{q=1}^N \left[Q(n,p,m,q) \frac{\beta_m \sqrt{Z_m^q}}{\omega\mu} \sqrt{\epsilon_m^q} (a_m - b_m) \right. \right. \\ \left. \left. - R(n,p,m,q) \sqrt{Z_m^q} \sqrt{\epsilon_m^q} (a_m + b_m) \right] \right\} \quad (17)$$

where superscripts are used to denote the aperture index, subscripts are used for the mode index,

$$P(n,m,p) = \int_{\text{aperture } n} \cos\left(\frac{p\pi t}{a^n}\right) \cos\left(\frac{m\pi t}{a^n}\right) dt \quad (18)$$

$$Q(n,p,m,q) = \int_{\text{aperture } n} dt \cos\left(\frac{p\pi t}{a^n}\right) \int_{\text{aperture } q} dt' \cos\left(\frac{m\pi t'}{a^q}\right) \frac{\omega\mu}{4} H_0^{(2)}(kR) \quad (19)$$

$$R(n,p,m,q)$$

$$= \int_{\text{aperture } n} dt \cos\left(\frac{p\pi t}{a^n}\right) \hat{z} \cdot \nabla \times \int_{\text{aperture } q} dt' \hat{t}(t') \cos\left(\frac{m\pi t'}{a^q}\right) \frac{1}{4j} H_0^{(2)}(kR) \quad (20)$$

and where R in the argument of the Hankel functions is given by

$$R = \sqrt{[x(t)-x(t')]^2 + [y(t)-y(t')]^2} \quad (21)$$

If enforced in a similar manner over each of the N apertures, Equation (17) can be generalized to matrix form as

$$\mathbf{U} \mathbf{b} = \mathbf{T} \mathbf{a} \quad (22)$$

where \mathbf{U} and \mathbf{T} are $NM \times NM$ matrices. The entry of the \mathbf{U} -matrix representing the interaction of the p -th mode in the n -th aperture with the m -th mode in the q -th aperture is given by

$$\begin{aligned} u_{ij} = & -P(n,m,p) \sqrt{Z_m^n} \sqrt{\epsilon_m^n} \delta_m^p \\ & + Q(n,p,m,q) \frac{\beta_m \sqrt{Z_m^q}}{\omega\mu} \sqrt{\epsilon_m^q} \\ & + R(n,p,m,q) \sqrt{Z_m^q} \sqrt{\epsilon_m^q} \end{aligned} \quad (23)$$

where δ_m^p is the Kronecker delta function. The analogous entry of the \mathbf{T} -matrix is given by

$$\begin{aligned} t_{ij} = & P(n,m,p) \sqrt{Z_m^n} \sqrt{\epsilon_m^n} \delta_m^p \\ & + Q(n,p,m,q) \frac{\beta_m \sqrt{Z_m^q}}{\omega\mu} \sqrt{\epsilon_m^q} \\ & - R(n,p,m,q) \sqrt{Z_m^q} \sqrt{\epsilon_m^q} \end{aligned} \quad (24)$$

Once the \mathbf{U} and \mathbf{T} matrices are constructed, the generalized scattering matrix can be obtained in the form

$$\mathbf{b} = \mathbf{U}^{-1} \mathbf{T} \mathbf{a} = \mathbf{S} \mathbf{a} \quad (25)$$

6. REDUCTION OF THE GENERALIZED S-MATRIX TO THE ORDINARY S-MATRIX

In a practical lens configuration, the higher-order modes in the apertures of the various ports do not propagate beyond the tapered transition to a single-mode line. Thus, these modes carry no net energy away from the lens, and can be eliminated from the generalized S-matrix. In the process, the generalized S-matrix of order NM is reduced to an ordinary N-th order S-matrix.

The elimination procedure requires the complex-valued reflection coefficient Γ associated with each higher-order mode as seen looking into the tapered transition, which provides an auxiliary relationship

$$a_i = \Gamma b_i \quad (26)$$

The reflection coefficient can be determined from the theory of tapered transmission lines [8]. Once Γ is determined, Equation (26) provides a constraint that can be used to eliminate one row and column of the generalized S-matrix.

Suppose that the index i represents the very last entry in the generalized S-matrix. In other words, Equation (14) can be rewritten as

$$\begin{bmatrix} b_1 \\ b_2 \\ \cdot \\ \cdot \\ \cdot \\ b_i \end{bmatrix} = \begin{bmatrix} S_{11} & S_{12} & \cdot & \cdot & \cdot & S_{1i} \\ S_{21} & S_{22} & & & & \\ \cdot & & & & & \\ \cdot & & & & & \\ \cdot & & & & & \\ S_{i1} & & \cdot & \cdot & \cdot & S_{ii} \end{bmatrix} \begin{bmatrix} a_1 \\ a_2 \\ \cdot \\ \cdot \\ \cdot \\ a_i \end{bmatrix} \quad (27)$$

After substituting Equation (26) into Equation (27), the S-matrix has the form

$$\begin{bmatrix} b_1 \\ b_2 \\ \cdot \\ \cdot \\ \cdot \\ b_i \end{bmatrix} = \begin{bmatrix} S_{11} & S_{12} & \cdot & \cdot & \cdot & S_{1,i-1} \\ S_{21} & S_{22} & & & & \\ \cdot & & & & & \\ \cdot & & & & & \\ \cdot & & & & & \\ S_{i1} & & \cdot & \cdot & \cdot & S_{i,i-1} \end{bmatrix} \begin{bmatrix} a_1 \\ a_2 \\ \cdot \\ \cdot \\ \cdot \\ a_{i-1} \end{bmatrix} + \begin{bmatrix} S_{1i} b_i \Gamma \\ S_{2i} b_i \Gamma \\ \cdot \\ \cdot \\ \cdot \\ S_{ii} b_i \Gamma \end{bmatrix} \quad (28)$$

The i -th equation can be solved for b_i to produce

$$b_i = \frac{S_{i1} a_1 + S_{i2} a_2 + \dots + S_{i,i-1} a_{i-1}}{1 - S_{ii} \Gamma} \quad (29)$$

Substituting this result back into Equation (28) produces a matrix relationship

$$\mathbf{b} = \mathbf{S}' \mathbf{a} \quad (30)$$

where the entries of the new order- $(N-1)$ scattering matrix are given by

$$s'_{mn} = S_{mn} + \frac{S_{mi} S_{in} \Gamma}{1 - S_{ii} \Gamma} \quad (31)$$

This procedure is repeated, eliminating higher-order modes from the scattering matrix, until an $N \times N$ S-matrix is obtained that relates only the dominant TEM mode interactions.

7. ADDITIONAL PROCESSING

The S-matrix constructed in the preceding sections has reference planes located in the lens apertures. Because the S-parameters are defined in terms of the square root of power, the reference planes may be shifted down the tapered sections of transmission line toward the connectors via the simple addition of the appropriate phase length. In other words, the new S-matrix has the form [7]

$$\begin{bmatrix} e^{-j\theta_1} & 0 & \dots & 0 \\ 0 & e^{-j\theta_2} & & \\ \cdot & & & \\ \cdot & & & \\ 0 & & \dots & e^{-j\theta_N} \end{bmatrix} \begin{bmatrix} S_{11} & S_{12} & \dots & S_{1,N} \\ S_{21} & S_{22} & & \\ \cdot & & & \\ \cdot & & & \\ S_{N,1} & \dots & S_{N,N} \end{bmatrix} \begin{bmatrix} e^{-j\theta_1} & 0 & \dots & 0 \\ 0 & e^{-j\theta_2} & & \\ \cdot & & & \\ \cdot & & & \\ 0 & & \dots & e^{-j\theta_N} \end{bmatrix} \quad (32)$$

Additional phase length associated with connectors, etc. may be incorporated in a similar fashion.

8. NUMERICAL RESULTS

A computer program was developed in FORTRAN to produce the S-matrix for a general lens geometry. Although in principle the only approximation associated with the theoretical formulation is the planar circuit assumption, in practice the finite computational resources may limit the number of modes retained in each lens aperture. To demonstrate the convergence of the procedure as a function of the number of aperture modes, the program was applied to the 10-port Rotman lens shown in Figure 1. This lens configuration is lossless, and therefore should produce a unitary S-matrix. Table 2 presents the total power obtained as a function of the number of aperture modes. Observe that once three modes are employed, almost 99% of the power is accounted for. For this lens geometry, the dominant and one higher-order mode ($m=1$) propagate at the input to the tapered line, the other modes are evanescent in each of the apertures.

Figure 2 shows the lens geometry used to fabricate the high dielectric Rotman lens. The substrate material was TiO_2 . The real and imaginary dielectric constant were measured to be 93.2 ± 1 and ≤ 0.1 , respectively, between 2 and 4 GHz. Both sides of the substrate were metallized, first with $0.3 \mu\text{m}$ of titanium-

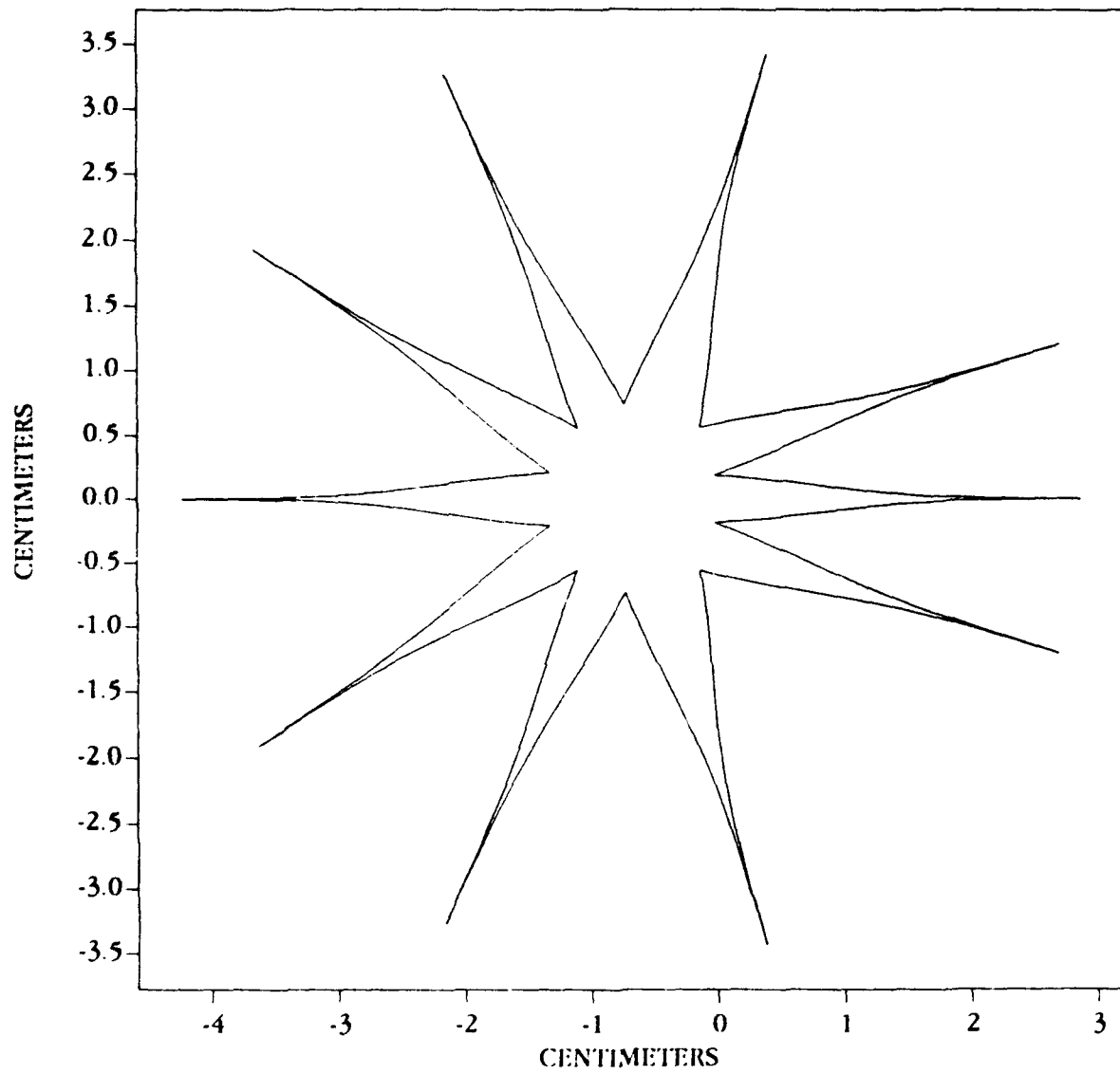


Figure 1. Ten-port Rotman lens

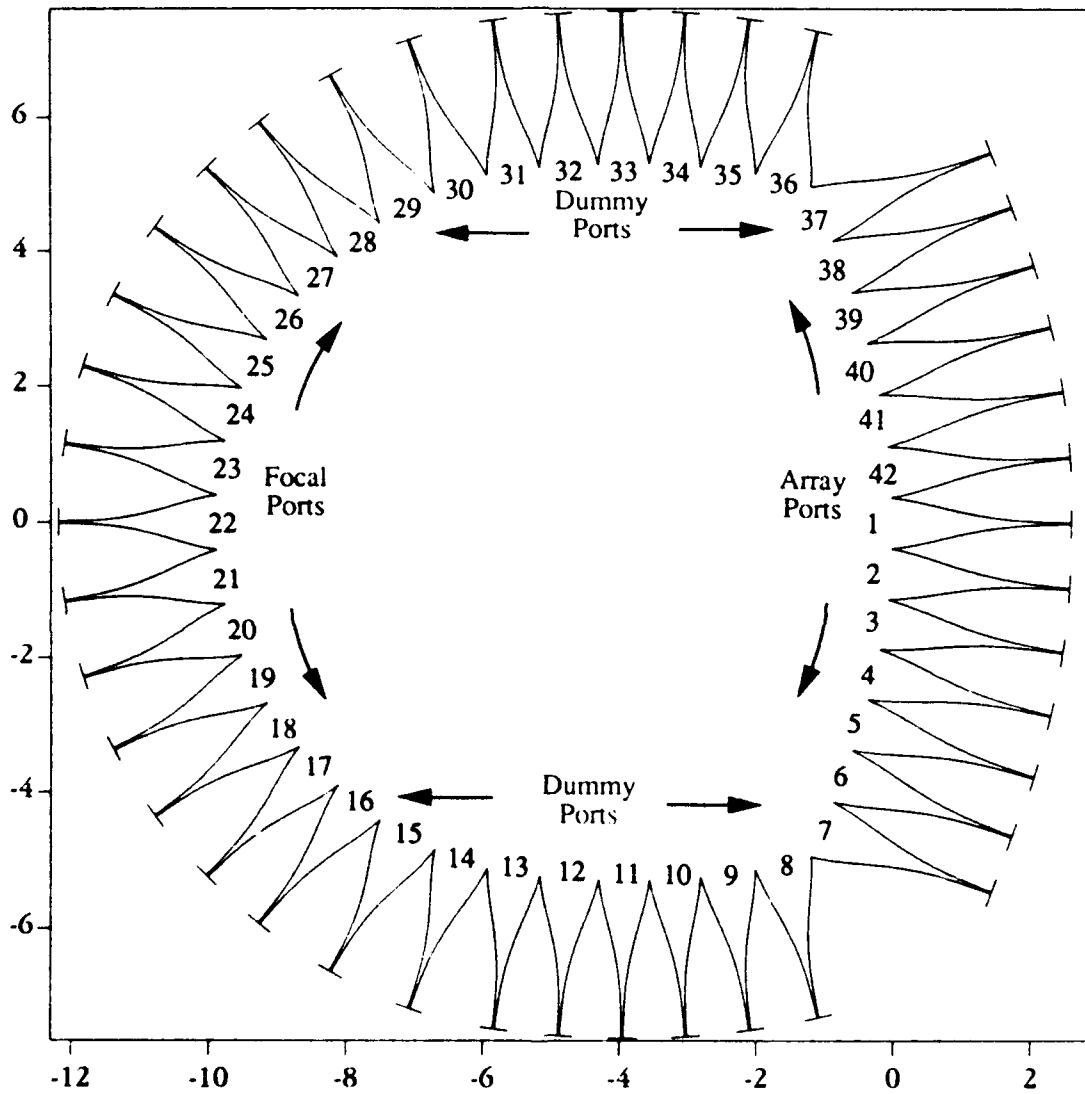


Figure 2. 42-port Rotman lens used for measurements. Ports 37 through 7 are the array ports. Ports 16 through 28 are the focal ports that give the direction of incoming signals. All other ports are 50 ohm dummy loaded to minimize the reflections from the sidewalls

Table 2

Percentage of the total power accounted for in each row of the S-matrix as a function of the number of waveguide modes employed in each aperture, for the 10-port lens geometry shown in Figure 1. The largest aperture has width 0.824 wavelengths; the smallest measured 0.496 wavelengths.

1 mode	2 modes	3 modes	4 modes	5 modes
72.5	96.9	99.0	99.1	99.0
66.8	93.4	98.5	98.8	99.0
79.4	93.8	98.8	98.7	99.0
70.2	87.8	97.3	98.1	98.5
68.7	87.9	99.1	98.8	99.2
69.4	93.5	99.1	98.8	99.1
68.7	87.9	99.1	98.8	99.2
70.2	87.8	97.3	98.1	98.5
79.4	93.8	98.8	98.7	99.0
66.8	93.4	98.5	98.8	99.0

tungsten to ensure film adherence, and secondly with 5 μm of gold. One side serves as a ground plane; the other was etched to imprint the lens pattern. The fragile ceramic substrate (1 mm thick) was protected with an aluminum housing that also incorporated 50 Ω SMA connectors for each port. S-parameter measurements at 2GHz were made by connecting the lens to a Hewlett-Packard system that consisted of an HP 8510B network analyzer, an HP 8350B sweep oscillator, an HP 8515A S-parameter test set, and a display/processor unit. The S_{ij} components of the matrix were measured by connecting port 2 and port 1 of the HP 8515A test set to the i-th and j-th ports of the lens, respectively. All other ports were

terminated with a 50Ω load. During the measurement process the input power was constant at 0 dBm. The resultant data were entered into a personal computer, and plotted as phasors in matrix format as shown in Figure 3. The scale of each phasor was 20 dB per 0.125 inch with a maximum data point of -7.55 dBm and a minimum data point of -30 dBm.

Figure 3 facilitates a quick assessment of the lens performance. For example, the S_{ii} components along the main diagonal represent the reflection coefficient from each port. These coefficients are determined primarily by (1) the impedance mismatch between the coaxial connector and the end of the microstrip taper, and (2) the length of the coaxial connector. The S_{ii} are nearly uniform in magnitude and phase, because both the impedance and connector lengths are nearly uniform from port to port. The S_{ii} magnitude is also large, because, in practice, each taper width could be reduced only to 0.2 millimeters which corresponds to a characteristic microstrip impedance of 30Ω for this configuration. The mismatch between the 30Ω microstrip and the 50Ω coaxial connector provided S_{ii} values of about -10 dBm ($VSWR \cong 1.6$). Components near the main diagonal, as well as in the upper right and lower left hand corners, have much smaller amplitudes, because these represent the small amounts of energy coupled between adjacent ports.

A similar pattern, generated from the theoretical predictions, is shown in Figure 4. The accuracy of these predictions may be assessed by subtracting the theoretical S-parameters from the measured data. The amplitude of the phasor difference pattern is shown in Figure 5. Relatively small differences (of approximately ± 4 dB or less) were obtained for the lens transmission paths between the input array ports and the focal ports (see Figure 2). These ports are numbered with j ranging from 1 to 7 or 37 to 42 and i ranging from 16 to 28.

From an inspection of Figure 5, it is apparent that large errors are observed primarily in those S-matrix components located parallel to the main diagonal, but shifted by 10 to 15 locations. These S-parameters represent the coupling between ports that are relatively widely spaced, typically one active port and one dummy

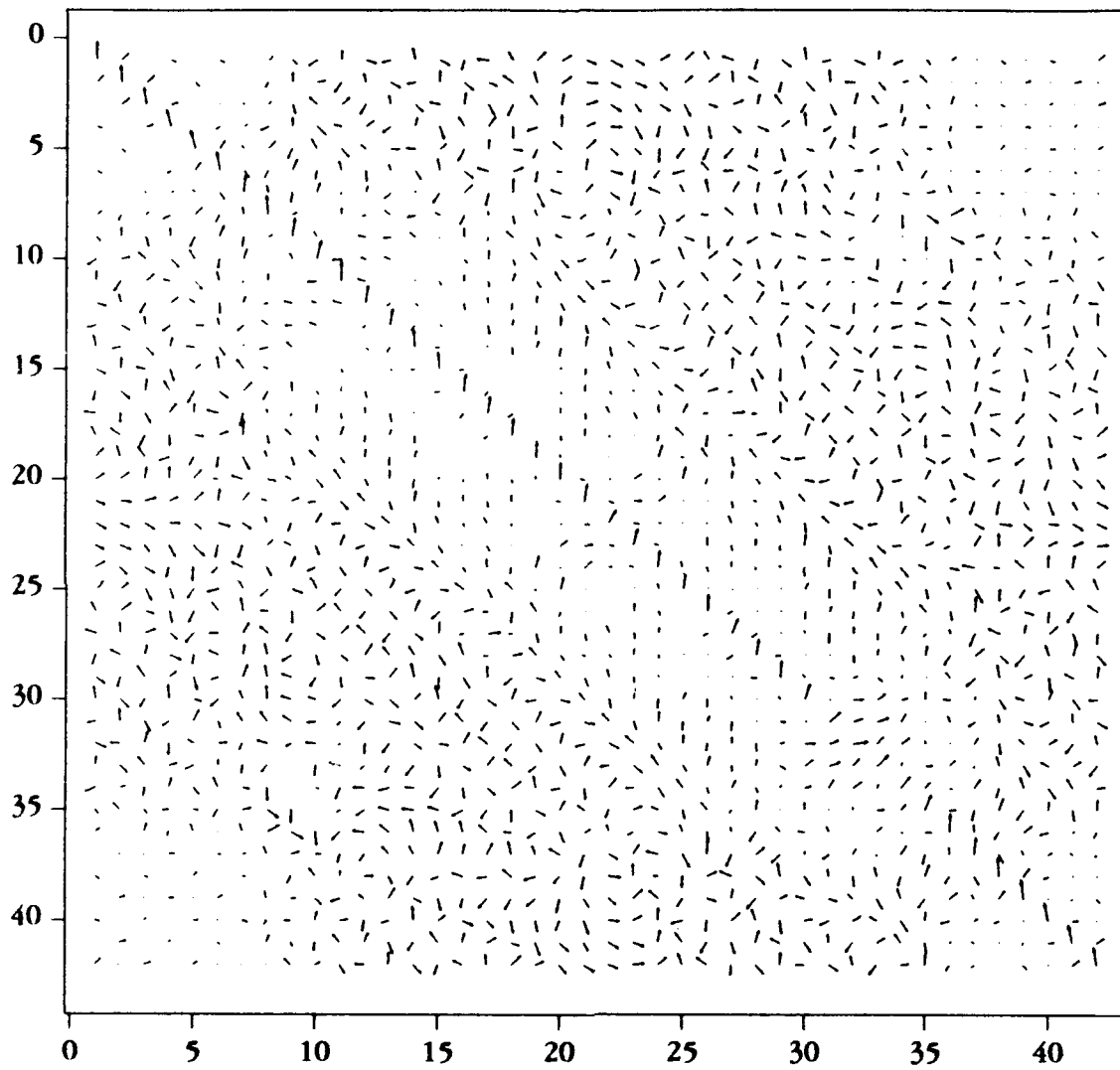


Figure 3. Phasor representation of measured S-matrix

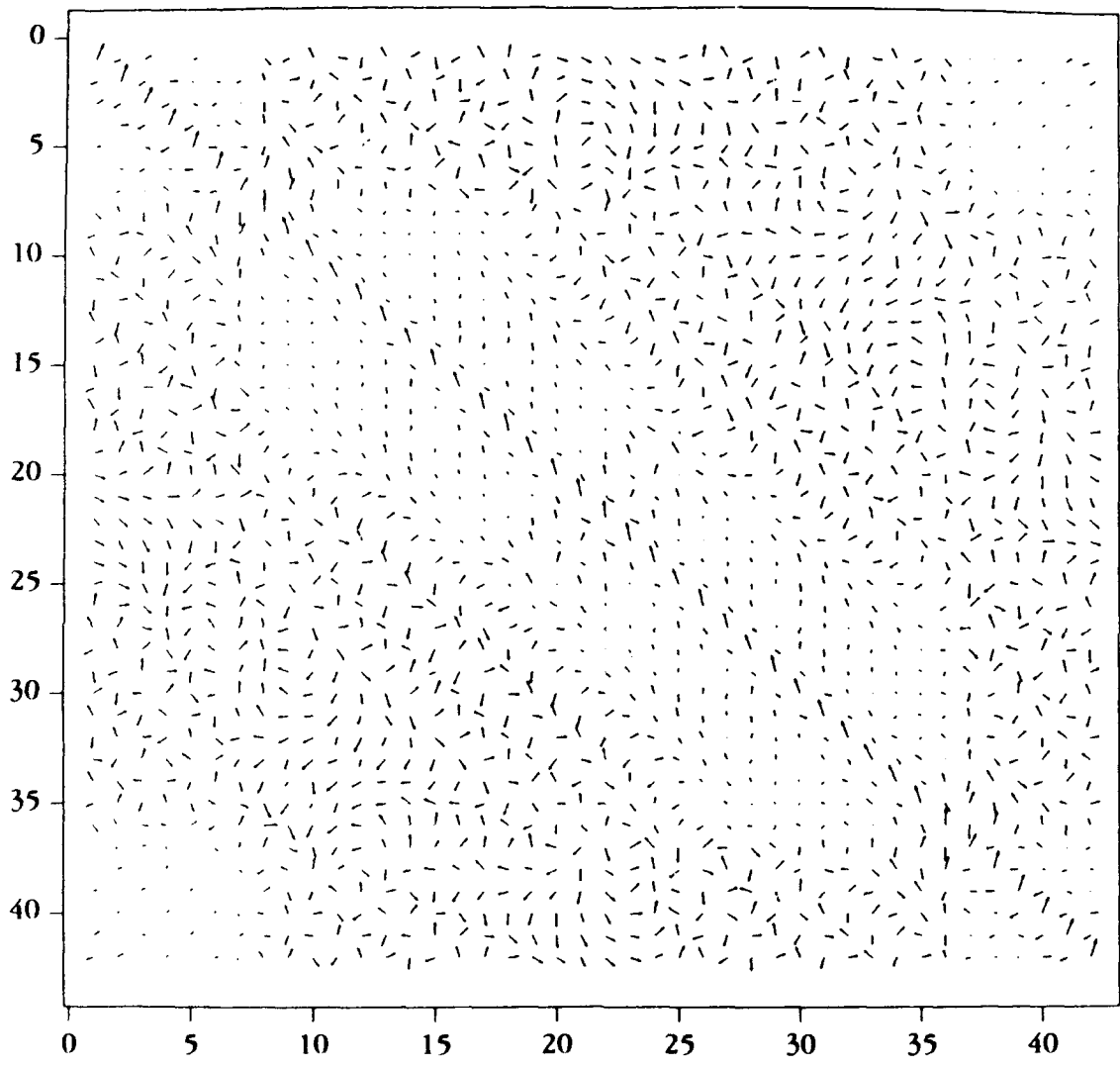


Figure 4. Phasor representation of computed S-matrix

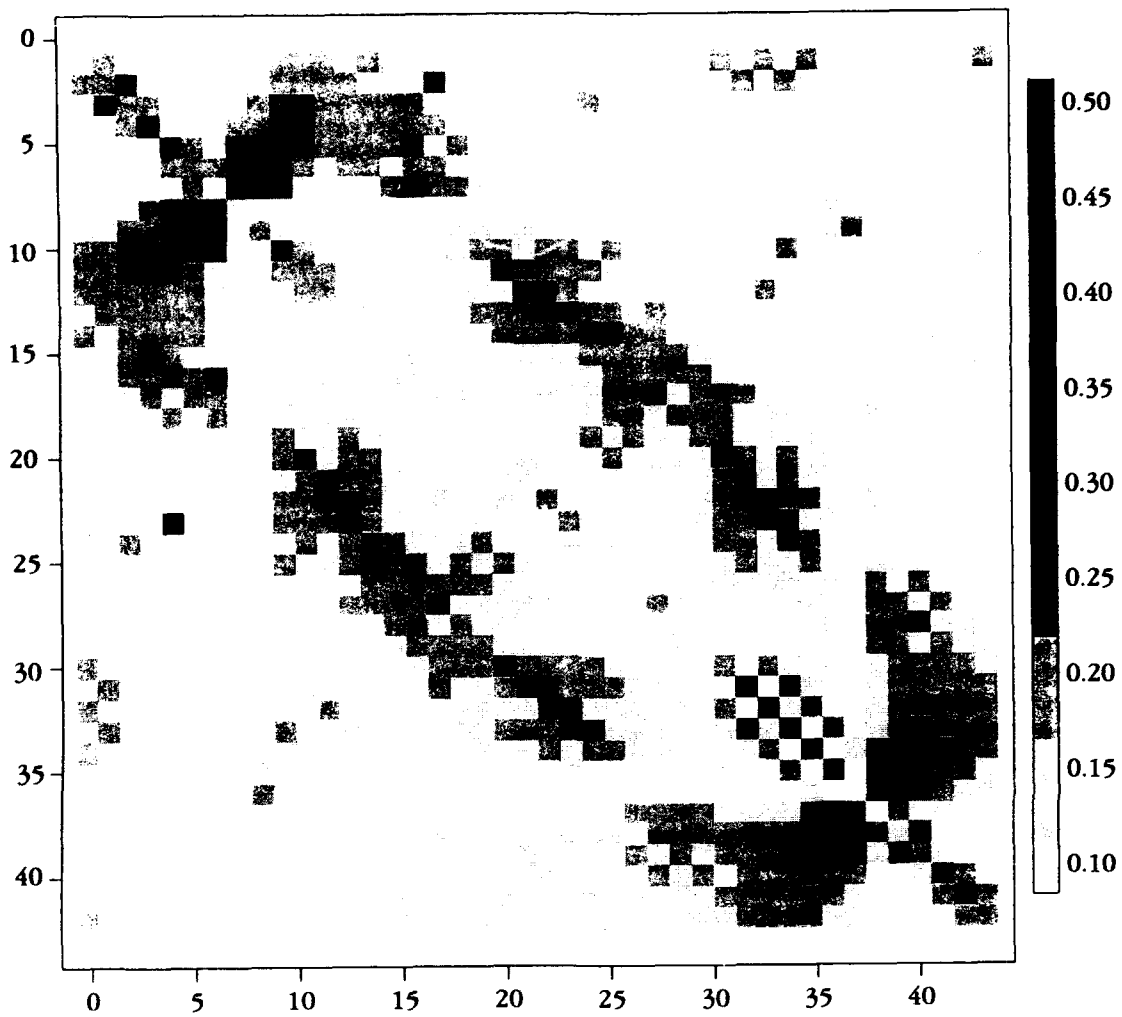


Figure 5. Magnitude difference between measured and theoretical data

port. The discrepancy between measured and theoretical results may be partially attributed to the fact that the effective dielectric constant of the substrate material is not known precisely. For example, an uncertainty of only $\pm 2\%$ in the relative permittivity could result in phase errors of 60 degrees between the array and focal ports. Additional *in situ* measurements may help clarify this uncertainty. A second source of error arises in the modeling of the tapered transitions, which were assumed to be "triangular" tapers [8] in the preliminary theoretical model instead of the Klopfenstein tapers actually used for lens fabrication. Although the two impedance functions are similar, their differences may have contributed to phase inaccuracies. The assumption that higher-order modes on a tapered microstrip having relatively narrow line width are completely uncoupled is an additional source of error, but it appears that little research has been done to date on the true behavior of higher-order modes under these conditions.

9. CONCLUSION

In summary, an integral equation formulation has been developed in order to predict the S-matrix associated with a Rotman lens fabricated from high dielectric substrate material, in this case TiO_2 . Preliminary theoretical results for a 42-port lens have been compared with measured data. Agreement between the theoretical model and measured data is dependent on accurate knowledge of the device parameters, especially the effective relative permittivity of the substrate material.

Future efforts will be directed toward reducing the difference between theoretical and measured S-parameters. A second lens has been fabricated from TiO_2 and will be the focus of a similar comparison. The theoretical model will ultimately be used as a design tool to enhance the performance of physically compact Rotman lenses.

ACKNOWLEDGEMENT

This work was supported by the U.S. Air Force Wright Laboratory at Dayton, Ohio under contract F33615-88-C-1728. The authors are also grateful to Mr. Michael Baden for supplying the image and phasor plotting software and for many valuable discussions.

REFERENCES

- [1] Konishi, Y. (1991) Novel dielectric waveguide components – microwave applications of new ceramic materials, Proc. IEEE 79:725-740
- [2] Rotman, W. and Turner, R. F. (1963) Wide-angle microwave lens for line source applications, IEEE Trans. Antennas Propagat., AP-11: 623-632
- [3] Gagnon, D. R. (1989) Procedure for correct refocusing of the Rotman lens according to Snell's law, IEEE Trans. Antennas Propagat., 37: 390-392
- [4] Chan, K. K. (1989) Field analysis of planar bootface lens feeds. Proc. International Conf. Radar, Paris, France: 273-278..
- [5] Okoshi, T. and Miyoshi, T. (1972) The planar circuit – an approach to microwave integrated circuitry, IEEE Trans. Microwave Theory Tech., MTT-20: 245-252
- [6] Okoshi, T. (1985) Planar Circuits for Microwaves and Lightwaves, Springer-Verlag, Berlin.
- [7] Pozar, D. M. (1990) Microwave Engineering, Addison-Wesley, New York.
- [8] Collin, R. E. (1966) Foundations for Microwave Engineering, McGraw-Hill, New York.

ADVANCES IN LENS-FED MULTIBEAM TECHNOLOGY

George J. Monser
The Raytheon Company
Electromagnetic System Division
Goleta, CA

ABSTRACT

The Rotman lens, or more appropriately the Gent lens, was first demonstrated in 1956 by Gent, Jones, and Brown. In 1958, Rotman and Turner applied multibeam technology in an Early Warning Radar as reported by Hatcher of Chu Associates in 1960.

Raytheon's Don Archer and George Monser applied the concept in 1969. In 1972, a system was flight-tested in the leading-edge of an F-4 aircraft. By then, the technology was advanced from the simple probe-feed lenses to the printed high-K lens of reduced size.

In 1977, Raytheon was selected to provide the design-to-price antennas for the U. S. Navy for shipboard use. This system later became the AN/SLQ-32. Over 250 systems were delivered to the U. S. Navy.

In 1979, the technology was demonstrated to the U. S. Air Force and, in 1980, successfully flight-tested in a 10-inch diameter pod under an F-4 aircraft. Since then, over 100 pods have been delivered to the U. S. Air Force.

In 1986, Raytheon's Analysis Group (Maybell, McInturff, and Simon) began to apply in-depth analyses to lenses. Computer-aided design and the application of the method-of-moments are in practice showing good correlation to measured data. Raytheon's growth and recognition as a prominent EW system supplier follows closely the development and advancements made in lens multibeam technology.

ADVANCES IN LENS-FED MULTIBEAM TECHNOLOGY

George J. Monser
The Raytheon Company
Electromagnetic Systems Division
Goleta, CA

SUMMARY

This paper traces the evolution of lens design over the past two decades at Raytheon. A short discussion of lens design is followed by a synopsis of the analysis model based upon the method-of-moments. Predicted model performance is given and shown to be in good agreement with calculated values.

1.0 INTRODUCTION

The evolution of lens-fed technology from inception¹ to the present may, more appropriately, be classified as a technological explosion. The first decade following inception addressed designs limited to less than an octave in bandwidth with a useful field-of-view on the order of 100°. The feed and array ports were either probe-fed or waveguide-fed. The lens proper was of parallel-plate design, generally air-filled.

Present technology addresses designs requiring multi-octave performance with useful fields-of-view of 120°. The feed and array ports are printed circuit horns. The lens feeds have been successfully modelled² using an extension of the method-of-moments formulation³.

2.0 OPTICAL DESIGN

Figure 1 shows the elements of a multibeam design. Four optical design features exist:

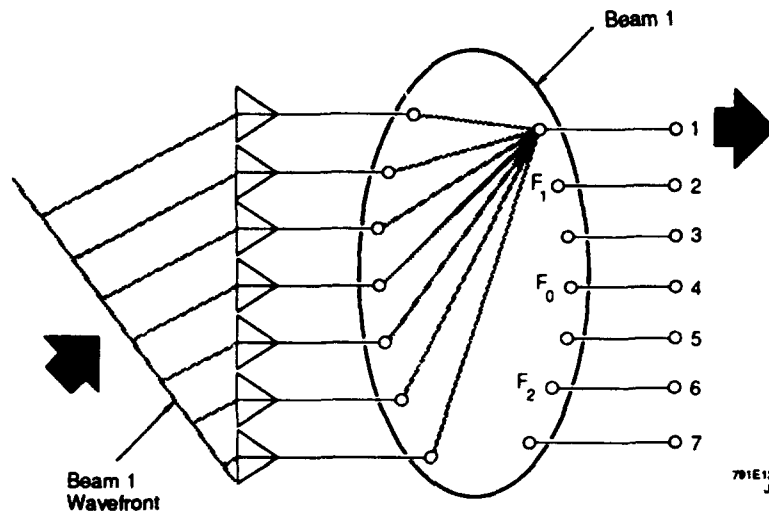


Figure 1. Rotman Lens

1. Shape of the input surface
2. Shape of the output surface
3. Positions of the pickup elements along each surface
4. Lengths of the transmission lines from the lens to the array

As a result of these features, three perfect focus points can be allocated on the input surface. The surface facing the array can be arbitrarily selected to match requirements of linear or curved array geometrics.

Beam pointing or positioning is derived by movement along the focal arc with one-to-one scan action or greater by shrinking array element spacing. The maximum number of beams are determined by the minimum antenna beamwidth and the cross-over level between adjacent beams readily found. For example, to cover a sector of $\pm 60^\circ$, the total sine-space (one-to-one) is 1.732. For a 10°

beamwidth, the sine value is 0.342, and five beams can be equally spaced over the full sector.

Raytheon frequently uses beam expansion to cover wide scan sectors with less inherent errors for the total scan can be achieved with minimum extension beyond the three points of perfect focus.

3.0 LENS DESIGN

Again, referring to Figure 1, the lens design consists of the lens proper and the associated cables to the array, here taken as a linear array. Beam steering is realized by movement along the focal arc. For any given position, the lens and the cables define a phase gradient along the array unique to the beam pointing direction. Since the system is true time-delay, the various path lengths can exceed thousands of degrees partitioned between the lens proper and the cables.* Cables, feeds, and array ports, phase-length tolerances must be maintained for optimum performance in low sidelobe systems. However, if sidelobes are not critical, the tolerances can be eased.

4.0 LENS FEEDS

In the early designs where the lens was constructed as a parallel-plate, the feed and array ports were realized using coaxial-to-waveguide probes with a back wall along each surface. Performance of this design was limited to about one octave.

The next evolution consisted of forming the lens in microstrip and using tapered horns for both the feed and array ports. The sizing and geometry of the horns were determined empirically yielding designs useful over two to three

*See Appendix A for added discussion.

octaves. Internal reflections were reduced to tolerable levels by judiciously placed resistive loading.

Microstrip designs were abandoned because of their unfavorable open design and the dispersion effects at the higher frequencies. The next and continuing generation utilized stripline construction. Again, the feed-horn geometries were empirically determined. Presently, the design can be examined and optimized analytically. The design steps, using the method-of-moments, are as follows:

1. Model each launcher as a unit cell (floquet cavity).
2. Remove the metal conductor and replace with surface current "J".
3. Find "J".

In order to find "J";

1. Develop a generalized impedance matrix and fill.
2. Use wide band Green's function to reduce matrix fill time.
3. Replace launcher by triangles and basis functions.

The analyses, which are rigorous, accurate and capable of handling arbitrary geometries (lumped and distributed), yield S_{11} , S_{22} , S_{12} , and S_{21} .

Figure 2 shows the results of a slot and stripline model. Figure 3 shows the results of a skewed notch and stepped stripline model. In both cases, reasonably good agreement to measured data is displayed. For a lens design, a typical program might require running 2,000 times to cover all scan angles and frequencies of interest. On a Cray supercomputer, the execution would be completed in about one and one-half days.

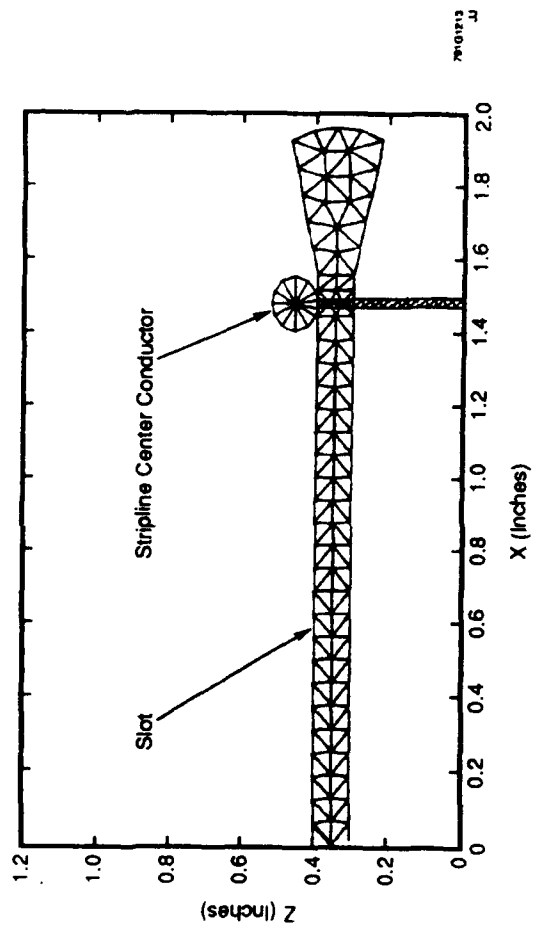
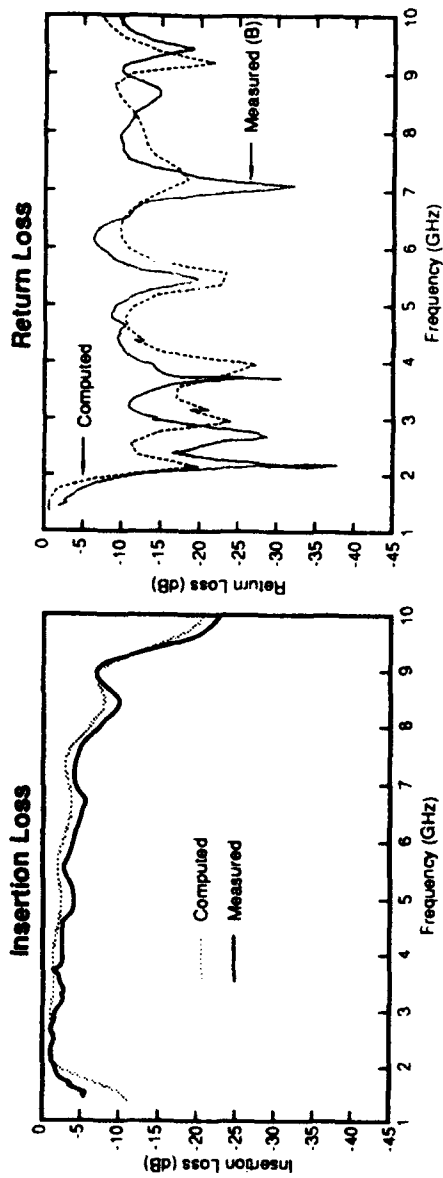


Figure 2. Slot and Stripline Model Results

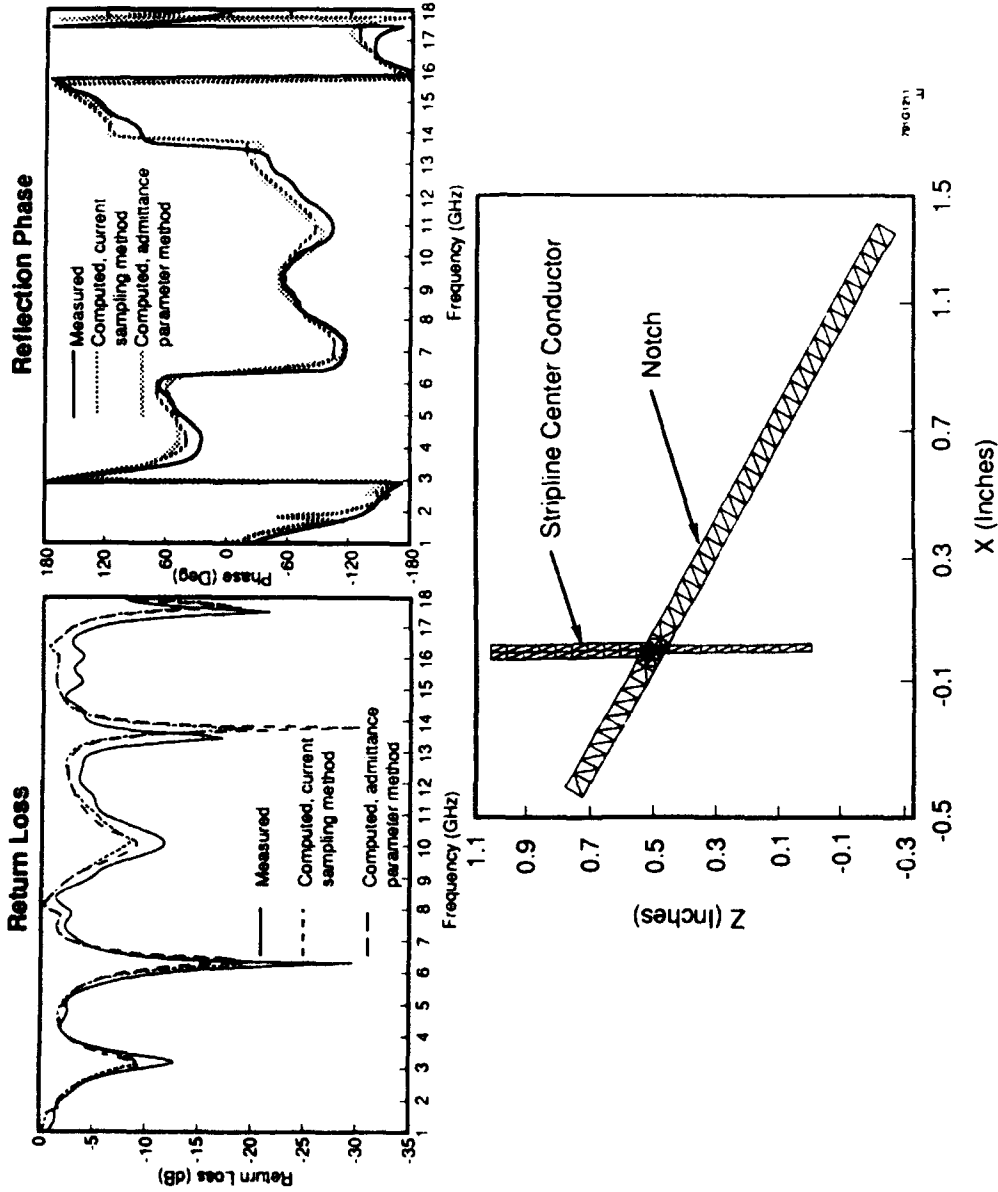


Figure 3. Skewed Notch and Stepped Stripline Model Results

5. THE EVOLUTION

The evolution at Raytheon is detailed in Table 1. Various configurations, test events, and application over the last two decades are displayed. Figure 4 shows a beam pattern designed to cover a full 180° sector, which exceeds the requirements for most systems.

TABLE 1. LENS CHRONOLOGY

TITLE	COMMENTS
Air-Dielectric Lens (1969)	1. 2 to 4 GHz 2. Parallel-plates and probe feeds for all ports
Isolation Test Set-up (1969)	1. TX and rec. lens/arrays in presence of fuselage (Section Contellation A/C)
1st K = 25 Lens/Array (1970)	1. Microstrip lens using K = 25 material
Leading-Edge F-4 A/C (1971)	1. Shrink factor 1/5 full-size
	1. Multibeam system in leading-edge of wing
AN/SLQ-32 in SLQ-32 (1978)	1. Chamber testing of SLQ-32
Transmit Array, SLQ-32 (1978)	1. Phys.: About 8" ht. and 12" in depth
F-16 A/C with Pod on Wing pylon (1982)	1. AN/ALQ-184 passive model tests
Ship Installation (1990)	1. Sidekick, a variant of SLQ-32

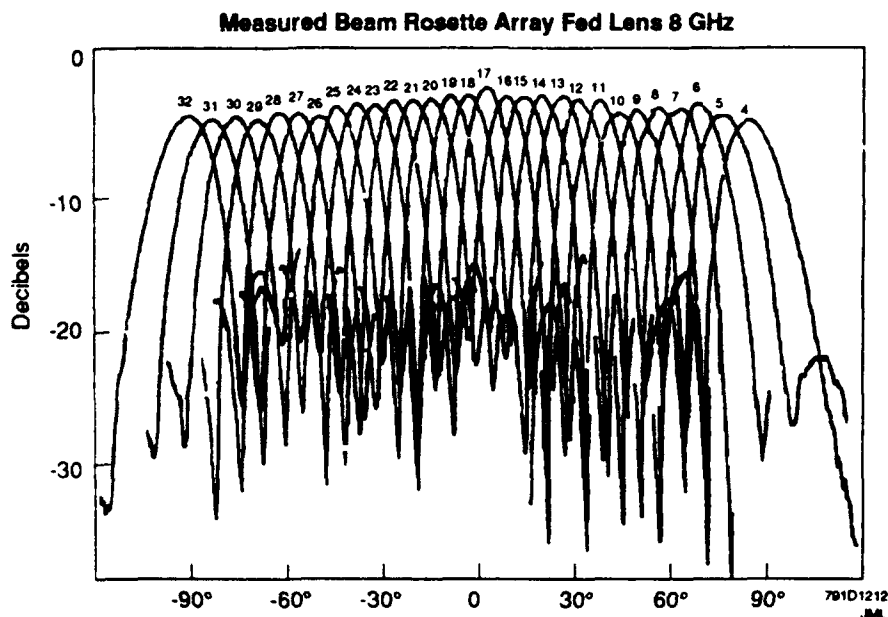


Figure 4. Multibeam Patterns

6. CONCLUDING REMARKS

Lens design technology has progressed such that today cost-effective, computer mechanization, and optimization can be effected.

Work is presently continuing to further develop the analytic model and extend it to other designs. (See Appendix B for further discussion.)

7. ACKNOWLEDGEMENTS

The analysis method presented in this paper represent principally the work of Dr. Peter Simon, Kim McInturff, and Deron Johnson under the direction of M. Maybell, Antenna Analysis Group, Raytheon Company, Electromagnetic Systems Division.

REFERENCES:

1. Gent, H. (1958) The Bootlace Aerial, Ministry of Technology, England.
2. Simon, P.S. et al (1989) Antenna CAD Final Report, Raytheon Company, Electromagnetic Systems Division, Goleta, CA.
3. Harrington, R. F. (1968) Field Computation by Moment Method, MacMillan, New York.
4. Simon, P.S. et al (1991) Full-Wave Analysis of an Infinite, Planar Array of Linearly Polarized, Stripline-Fed, Tapered Notch Elements, International IEEE/AP-S Symposium, Ontario, Canada, pp 334-337.
5. Simon, P.S. and McInturff, Kim (1991) Analysis of a Tapered Stripline Element in an Infinite Array Environment, International Union of Radio Science (URSI), Ontario, Canada, pp 186.
6. Johnson, D.L. et al (1991) Moment Method Analysis of an Array of Stripline-Fed Slot Elements, Progress in Electromagnetics Research Symposium, Cambridge, Massachusetts, pp 782.

Appendix A

Beam Steering Using a Rotman Lens

1.0 INTRODUCTION

Beam positioning is realized by moving along the focal arc as depicted in Figure A-1. Continuous beam positioning over the full focal arc (+) and (-), and slightly beyond, is possible. However, for most systems, a discrete number of beams are employed.

Each beam position corresponds to a particular angle of transmission (reception).

2.0 TYPICAL PATH LENGTHS

The phase gradient, depicted in Figure A-1 for beam Number 1 (extreme scan), will be used to illustrate the design. At the upper frequency, the array element spacing will typically be a one-half wavelength or 180° apart.

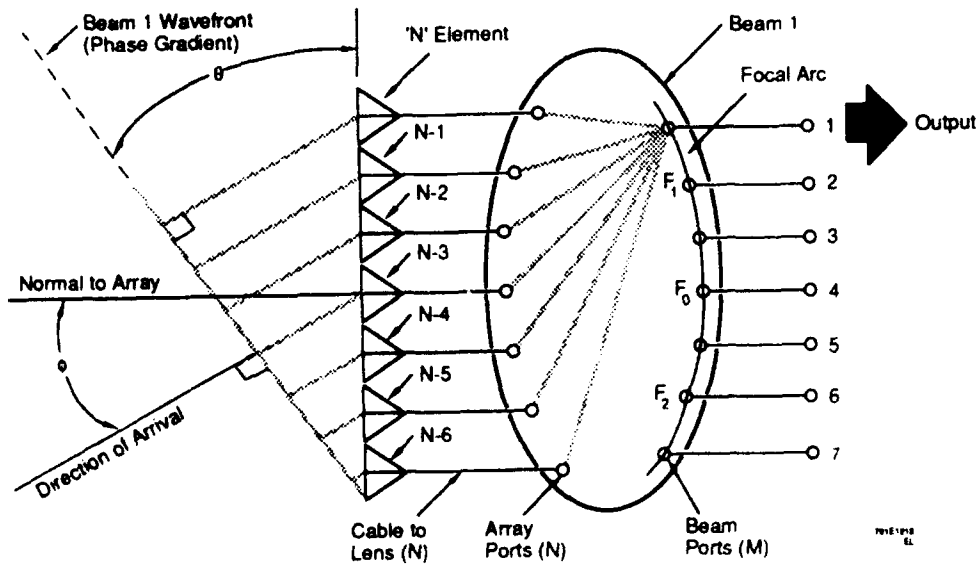


Figure A-1. Rotman Lens

The beam pointing angle ' θ ' is reflected as ' θ ' in the right phase-gradient triangle, with a total array length of $(N-1) \times 180^\circ$. The maximum delay of the signal to, or from, the last element is $[(N-1) \times 180^\circ] \times \sin \theta$.

As an example, if $(N - 1) = 7$ and $\theta = 60^\circ$, then the maximum delay would be 935° . The delay for the next element would be 779° , and so forth. Within the lens and the cables, the respective phase delays would be 935° , 779° , etc. If N is large, then the electrical lengths could easily reach several thousand degrees.

3.0 PHASE GRADIENTS AND PERFORMANCE

For optimum performance, each beam has a unique phase gradient which should be a perfect straight line (normal) to the direction of radiation (reception) for that beam. Any departure from a straight line will introduce phase errors and, if these are allowed to become significant, beam sidelobe levels will increase, clean nulls between lobes will fill in, and the main beam will broaden, yielding reduced gain.

A typical design may strive to limit the peak phase errors to $\pm 16^\circ$, with a budget of $\pm 10^\circ$ for the pair of lens feeds, and $\pm 6^\circ$ for the cable. These values translate to tight mechanical tolerances which are specified at the highest frequency where the wavelength may be as small as 0.66 inches, or less. For example, the 6° in air translates to an equivalent linear dimension of 0.011 inches.

4.0 DESIGN PROGRAM

Raytheon currently validates each new lens design using ANA beam programs. Beam quality, beam position, and array factor gain are determined.

In addition, total loss, return loss, phase, and transfer loss are measured for all ports yielding an $N \times M$ matrix of data where N is the number of ports on the array side, and M is the number of beam ports.

Appendix B

A Short Digest of a Tapered Stripline in an Infinite Array Environment⁵

1.0 INTRODUCTION

Work-in-process, as reflected in reference 5, is detailed briefly in this appendix. Recent test results are also included.

2.0 UNIT CELL FLOQUET CAVITY

Within the lens, to a first approximation, the array ports can be considered a linear array. Similarly, the beam ports can be considered a linear array as shown in Figure B-1.

The element under analysis can be considered as a unit cell with Floquet boundary conditions as depicted in Figure B-2.

Next, the Electric Field Integral Equation can be developed from the equation in Table B-1.

3.0 METHOD OF MOMENTS

Table B-2 shows the development for applying the method-of-moments.

4.0 GREEN'S FUNCTIONS

Table B-3 shows the development for reducing computational time by reducing Green's function to a three-term polynomial in frequency and summing the various frequency coefficient.

5.0 BASIS FUNCTION

Figure B-3 shows the basis function geometry and subsequent application to a lens port (Figure B-4).

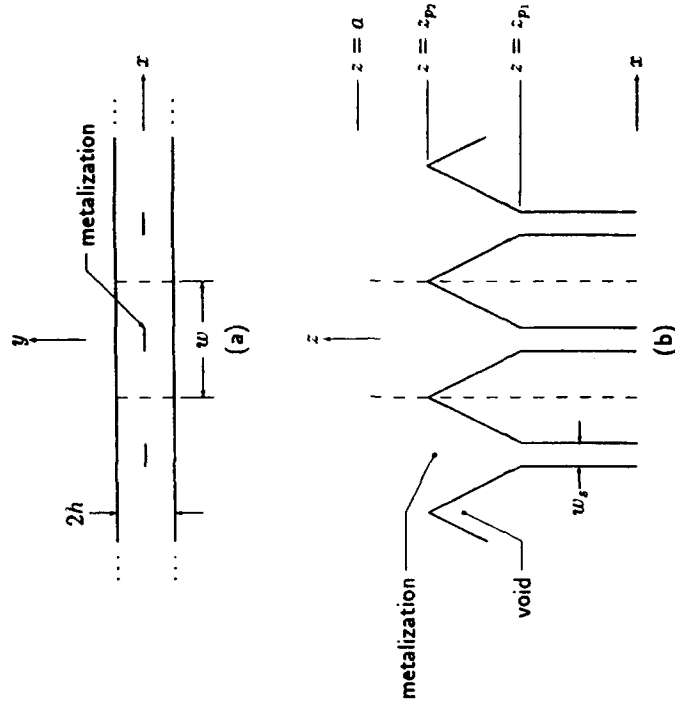
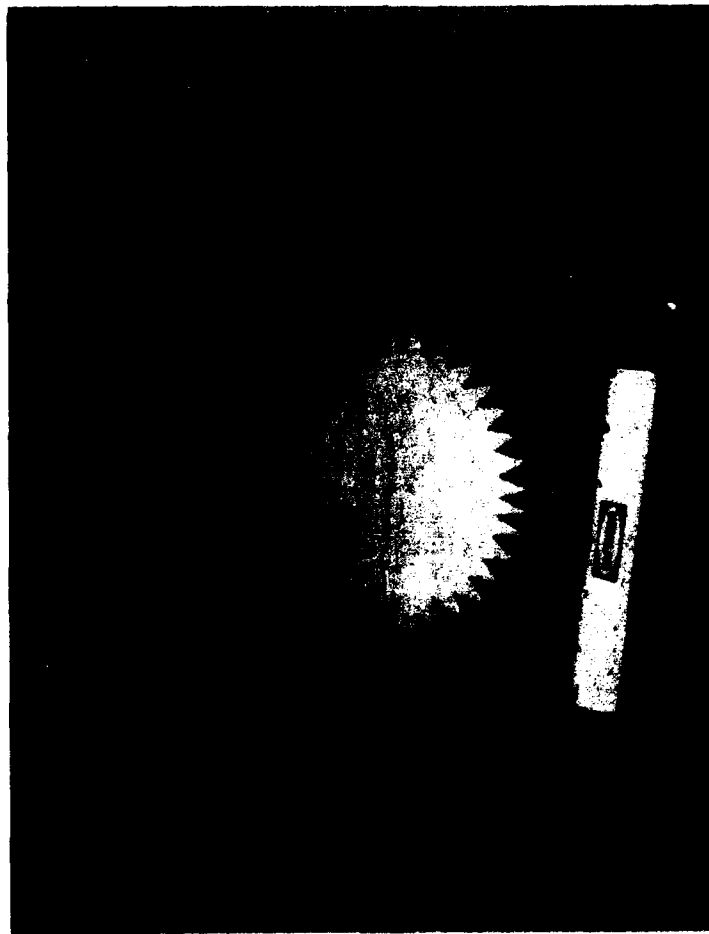


Figure B-1. Stripline Rotman Lens and Periodic Array of Tapered Striplines Feeding a Semi-Infinite Parallel-Plate Region

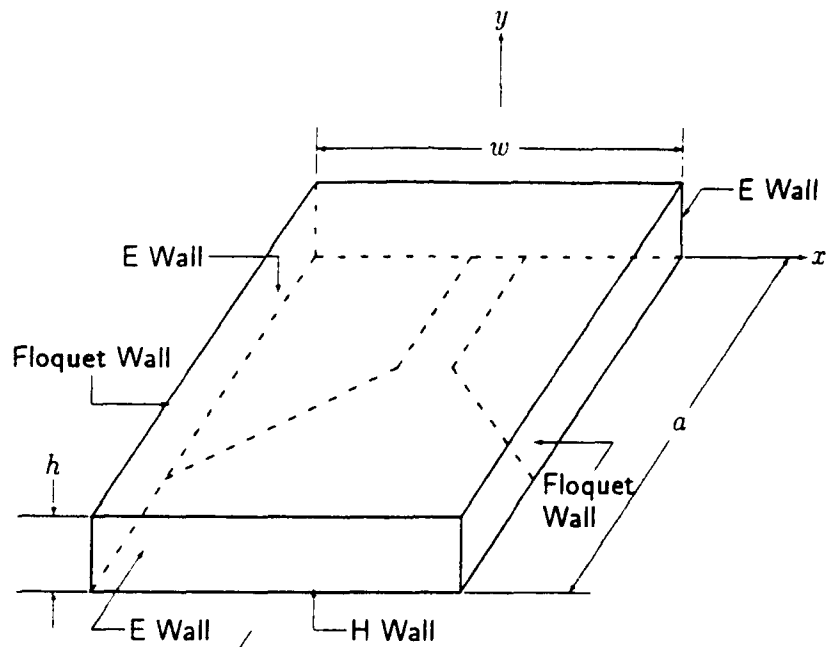


Figure B-2. Unit Cell Floquet Cavity

6.0 RESULTS

Figure B-5 through B-8 shows a few of the results. While reasonably good agreement between measured and predicted results is shown, work is continuing to refine the models for further improvements.

TABLE B-1. ELECTRIC FIELD INTEGRAL EQUATION

- Remove metal center conductor, replace with electric surface current \mathbf{J} (which is unknown).
- Total electric field in cavity is $\mathbf{E}^{\text{inc}} + \mathbf{E}^{\text{scat}}$. \mathbf{E}^{inc} is due to impressed source, \mathbf{E}^{scat} is due to induced source \mathbf{J} .
- Boundary condition on the conductor $\mathbf{E}_{\text{tan}} = \mathbf{0}$:

$$-\hat{\mathbf{n}} \times \mathbf{E}^{\text{scat}}\{\mathbf{J}\} = \hat{\mathbf{n}} \times \mathbf{E}^{\text{inc}} \text{ on center conductor}$$

where

$$\begin{aligned} \mathbf{E}^{\text{scat}}\{\mathbf{J}\} &= -j\omega\mathbf{A}\{\mathbf{J}\} - \nabla\Phi\{\mathbf{J}\}, \\ \mathbf{A}\{\mathbf{J}\}(\mathbf{r}) &= \iint \bar{\mathbf{G}}_A(\mathbf{r};\mathbf{r}') \cdot \mathbf{J}(\mathbf{r}') dS' \\ \Phi\{\mathbf{J}\}(\mathbf{r}) &= \iint G_\Phi(\mathbf{r};\mathbf{r}') \nabla'_s \cdot \mathbf{J}(\mathbf{r}') dS' \end{aligned}$$

- Task: find \mathbf{J} which satisfies above integro-differential equation.

TABLE B-2. METHOD OF MOMENTS FORMULATION APPROXIMATE, VARIATIONAL TECHNIQUE FOR LINEAR OPERATOR EQUATIONS

- Expand unknown \mathbf{J} in series of known basis functions with coefficients TBD.

$$\mathbf{J}(\mathbf{r}) \approx \sum_{n=1}^{N_j} \mathcal{J}_n \mathbf{f}_n(\mathbf{r}).$$

- By linearity

$$\mathbf{E}^{\text{scat}} \{ \mathbf{J} \} = \sum_{n=1}^{N_j} \mathcal{J}_n \mathbf{E}^{\text{scat}} \{ \mathbf{f}_n \}$$

- Define inner product:

$$\langle \mathbf{f}, \mathbf{g} \rangle \equiv \iiint \mathbf{f} \cdot \mathbf{g}^* dV.$$

- Choose testing (or weighting) functions $\{ \mathbf{T}_m \}$. For our case, use $\mathbf{T}_m = \mathbf{f}_m$.
- Inner product of EFIE with \mathbf{f}_m :

$$\langle -\mathbf{E}^{\text{scat}}, \mathbf{f}_m \rangle = \langle \mathbf{E}^{\text{inc}}, \mathbf{f}_m \rangle, \quad m = 1, 2, \dots, N_j.$$

- Substitute in expansion of currents to get matrix equation:

$$[\mathcal{Z}_{mn}] [\mathcal{J}_n] = [\mathcal{V}_m]$$

where

$$\begin{aligned} \mathcal{Z}_{mn} &= \langle -\mathbf{E}^{\text{scat}} \{ \mathbf{f}_n \}, \mathbf{f}_m \rangle \\ \mathcal{V}_m &= \langle \mathbf{E}^{\text{inc}}, \mathbf{f}_m \rangle. \end{aligned}$$

TABLE B-3. POTENTIAL GREEN'S FUNCTIONS WIDE-BAND EXPANSION

- Most costly part of moment method procedure is filling generalized impedance matrix.
- Fill time can be reduced dramatically by use of wide-band Green's function expansion.
- Example: Electric scalar potential Green's function satisfying Dirichlet BC at $y = h$, $z = 0$, and $z = a$; Neumann BC at $x = \pm w/2$, and the differential equation

$$(\nabla^2 + k^2)G_\Phi(\mathbf{r}; \mathbf{r}') = -\epsilon^{-1}\delta(\mathbf{r} - \mathbf{r}').$$

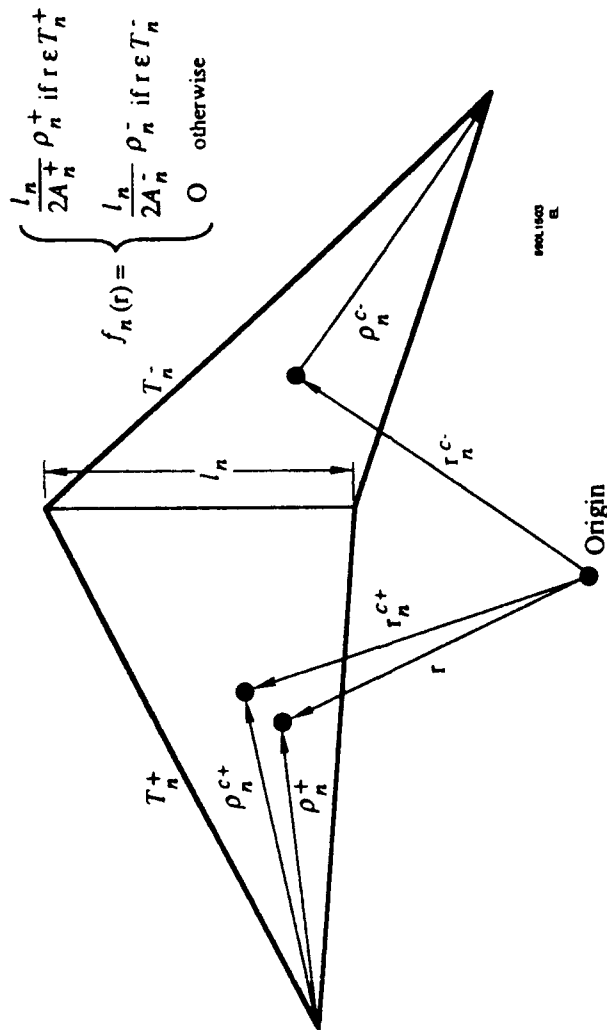
- Expand in series of eigenfunctions (resonant modes)

$$G_\Phi(\mathbf{r}; \mathbf{r}') = \sum_{mnl} \frac{\Phi_{mnl}(\mathbf{r})\Phi_{mnl}^*(\mathbf{r}')}{k_{mnl}^2 - k^2}$$

- All resonant frequencies (wavenumbers) are well above operating frequency (wavenumber) so that

$$\frac{1}{k_{mnl}^2 - k^2} = \frac{1}{k_{mnl}^2} \left[\frac{1}{1 - (k/k_{mnl})^2} \right] \approx \frac{1}{k_{mnl}^2} \left[1 + (k/k_{mnl})^2 + (k/k_{mnl})^4 \right]$$

- Result: A three term polynomial in frequency for the Green's function. Coefficients are slowly converging triply infinite series which must be (and have been) highly accelerated for efficient evaluation.
- By separately summing the contributions of the various frequency polynomial coefficients, the generalized impedance matrix assumes the form of a four-term rational function of frequency. The rational function coefficients need be computed only once.



PRO. 1500
E.

Figure B-3. Basic Function Geometry

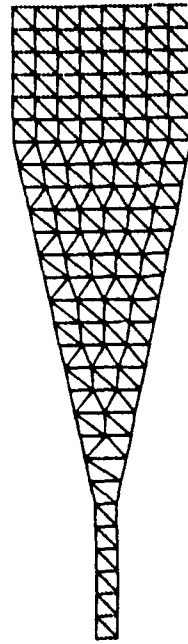


Figure B-4. PRLens Sim6d Triangulation

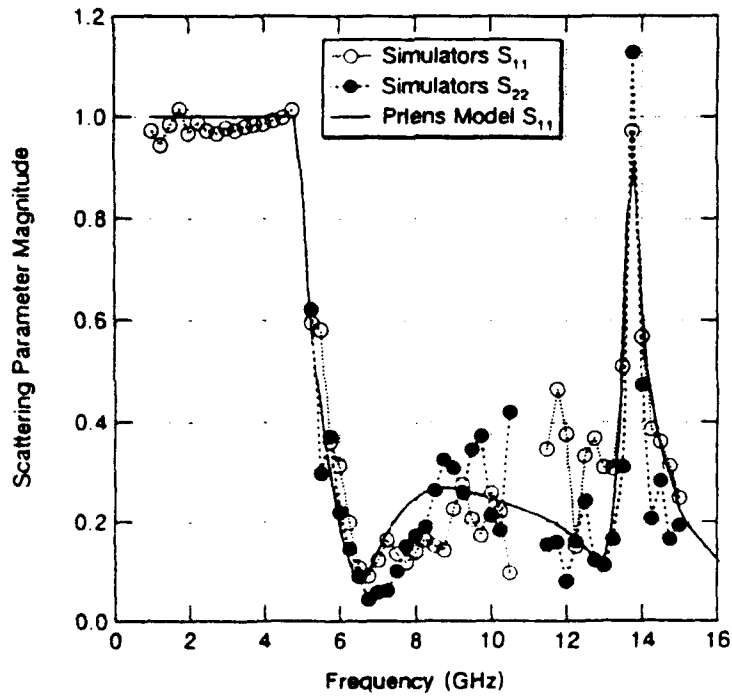


Figure B-5. PRLens versus Linear Taper Simulator Reflection Magnitude

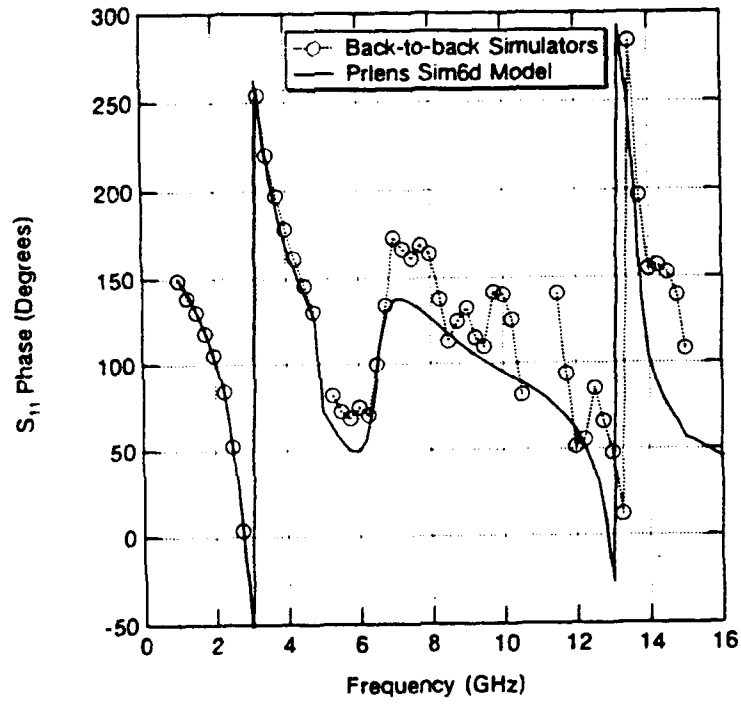


Figure B-6. PRLENS versus Linear Taper Simulator Reflection Phase, Port 1

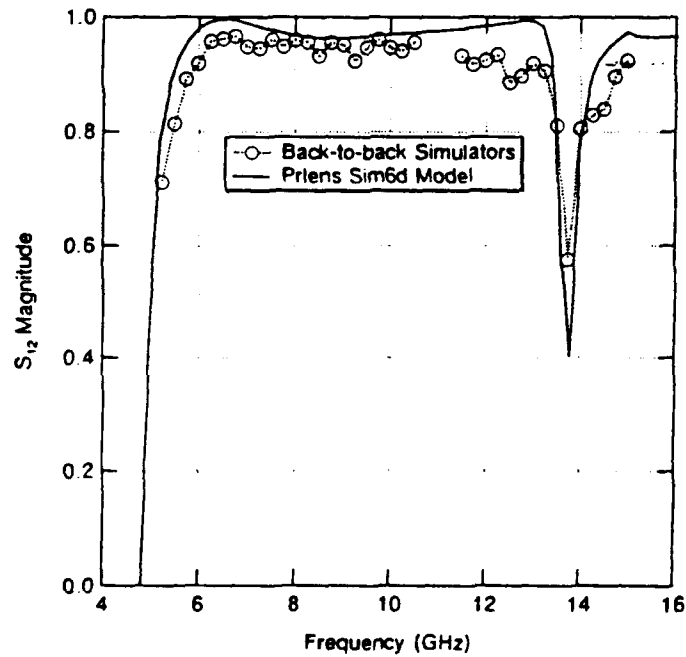


Figure B-7. PRLENS versus Linear Taper Simulator Transmission Magnitude

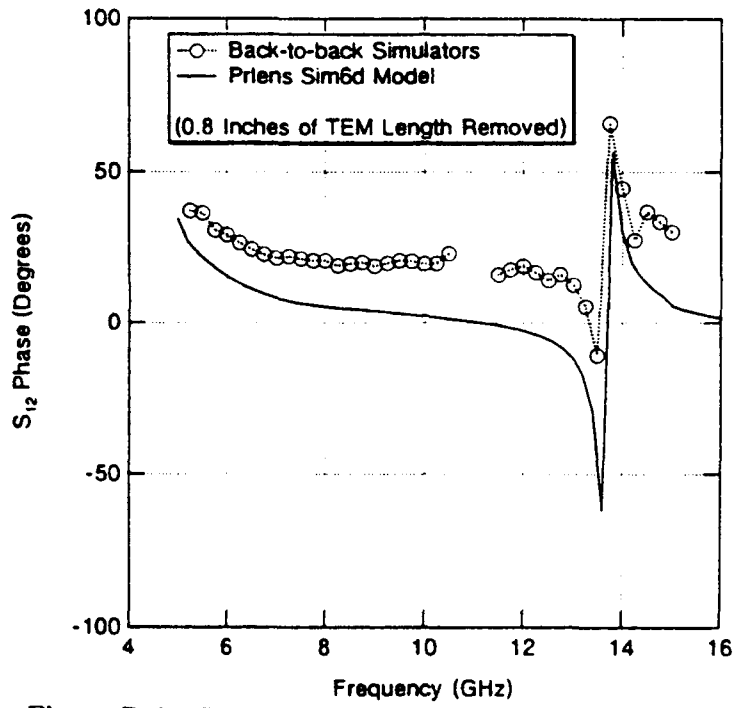


Figure B-8. PRLENS versus Linear Taper Simulator Transmission Phase

**MISSION
OF
ROME LABORATORY**

Rome Laboratory plans and executes an interdisciplinary program in research, development, test, and technology transition in support of Air Force Command, Control, Communications and Intelligence (C³I) activities for all Air Force platforms. It also executes selected acquisition programs in several areas of expertise. Technical and engineering support within areas of competence is provided to ESD Program Offices (POs) and other ESD elements to perform effective acquisition of C³I systems. In addition, Rome Laboratory's technology supports other AFSC Product Divisions, the Air Force user community, and other DOD and non-DOD agencies. Rome Laboratory maintains technical competence and research programs in areas including, but not limited to, communications, command and control, battle management, intelligence information processing, computational sciences and software producibility, wide area surveillance/sensors, signal processing, solid state sciences, photonics, electromagnetic technology, superconductivity, and electronic reliability/maintainability and testability.